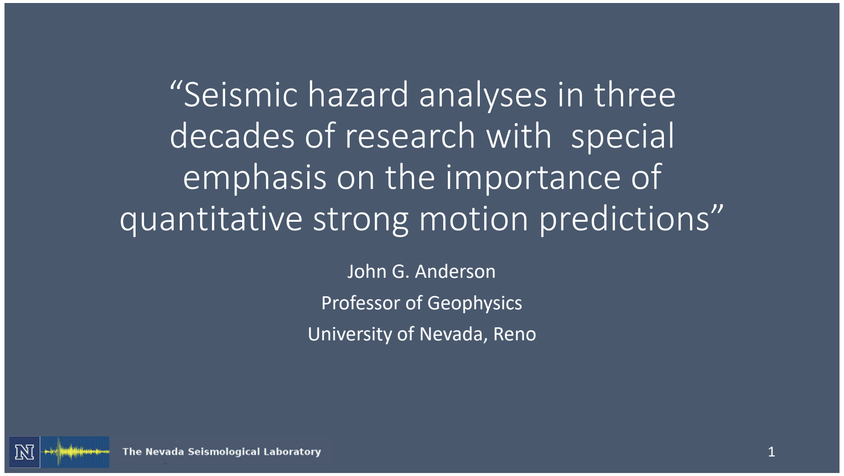

“Seismic hazard analyses in three decades of research with special emphasis on the importance of quantitative strong motion predictions”

John G. Anderson
Professor of Geophysics
University of Nevada, Reno

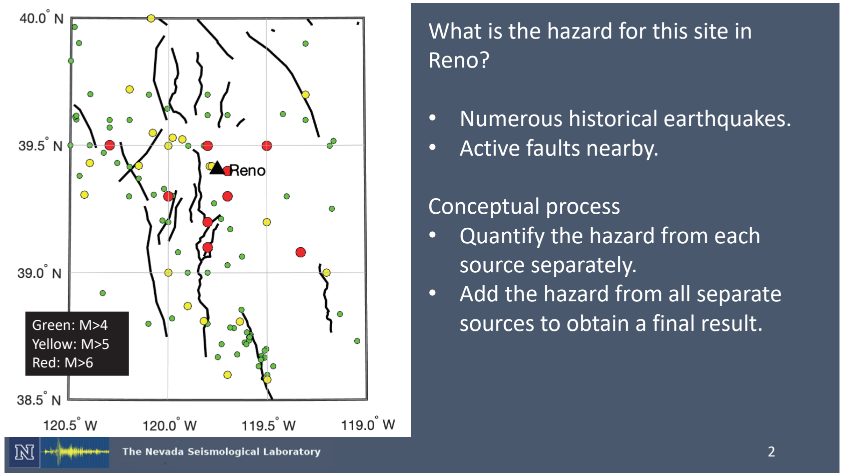

What is the hazard for this site in Reno?

- Numerous historical earthquakes.
- Active faults nearby.

Conceptual process

- Quantify the hazard from each source separately.
- Add the hazard from all separate sources to obtain a final result.

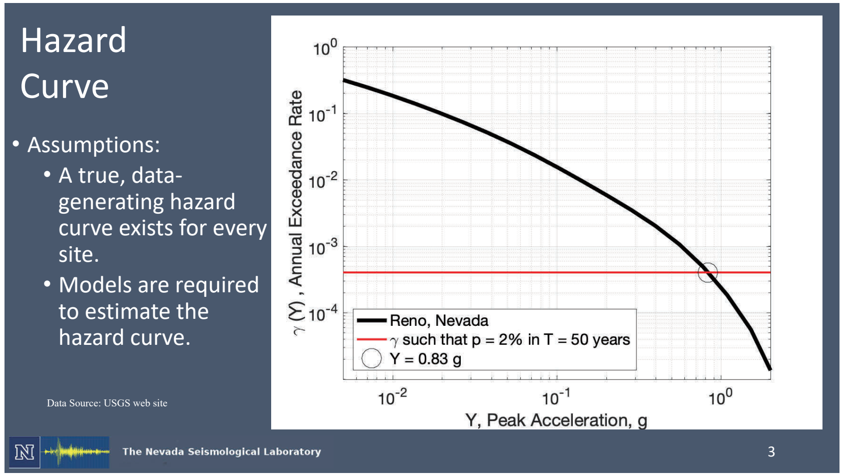

Hazard Curve

- Assumptions:
  - A true, data-generating hazard curve exists for every site.
  - Models are required to estimate the hazard curve.

Data Source: USGS web site

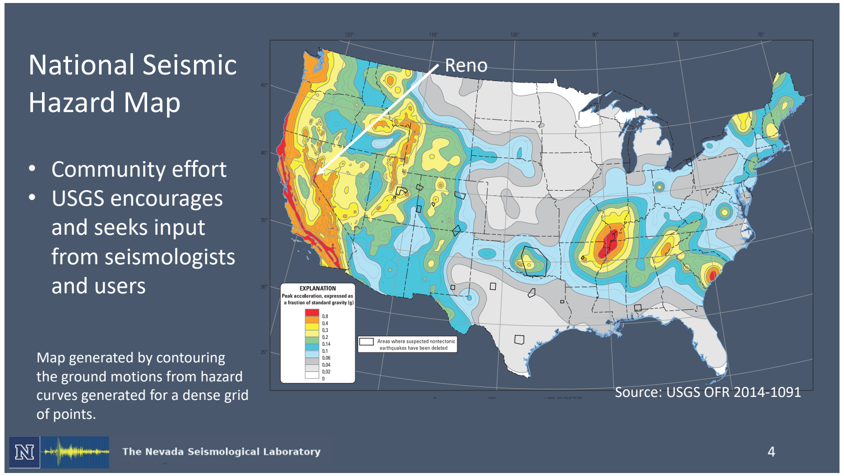

National Seismic Hazard Map

- Community effort
- USGS encourages and seeks input from seismologists and users

Map generated by contouring the ground motions from hazard curves generated for a dense grid of points.

Source: USGS OFR 2014-1091

Symbolic equation to build a hazard curve

$$\gamma_C\left(Y\right) = \iint n\left[M,\mathbf{x}\right]\Phi\left\{y \geq Y|\hat{Y},\sigma_T\right\} dM\,d\mathbf{x}$$

Y = ground motion
γ(Y) = the hazard curve, the rate of exceeding Y.
n = number of earthquakes, magnitude M, at location x
Φ = probability of the earthquake exceeding Y.

Outline

- Identify 15 key problems that need to be solved for seismic hazard studies.
- For some: just describe the problem.
- Others: discuss in more detail.

Seismicity Model

Declustered seismicity model

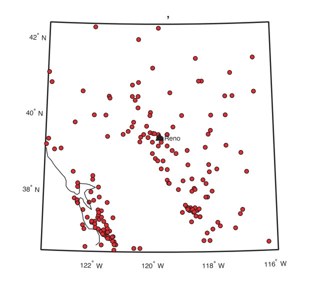

Faults

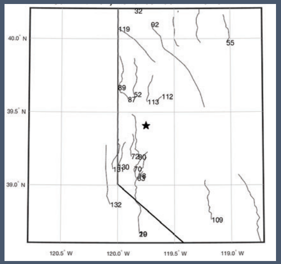

Should the seismicity catalog be declustered? If so, how?

- Purpose: to make the catalog Poissonian.
- Some information is not used. What are the tradeoffs?

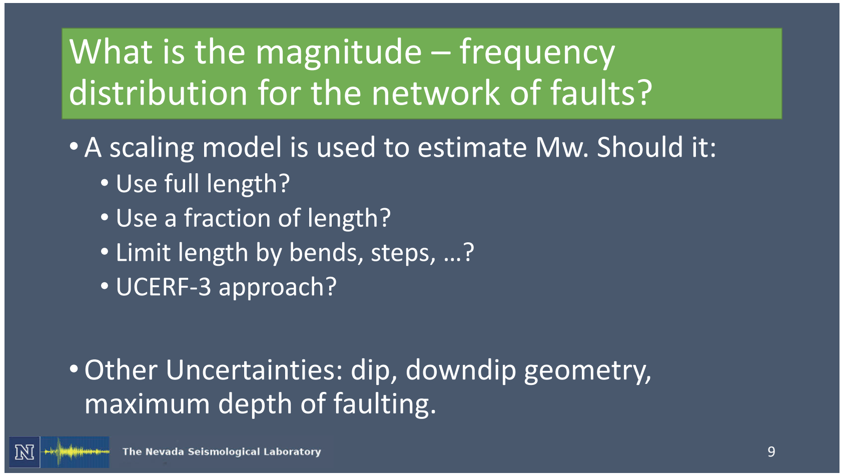

What is the magnitude – frequency distribution for the network of faults?

- A scaling model is used to estimate Mw. Should it:
  - Use full length?
  - Use a fraction of length?
  - Limit length by bends, steps, …?
  - UCERF-3 approach?
- Other Uncertainties: dip, downdip geometry, maximum depth of faulting.

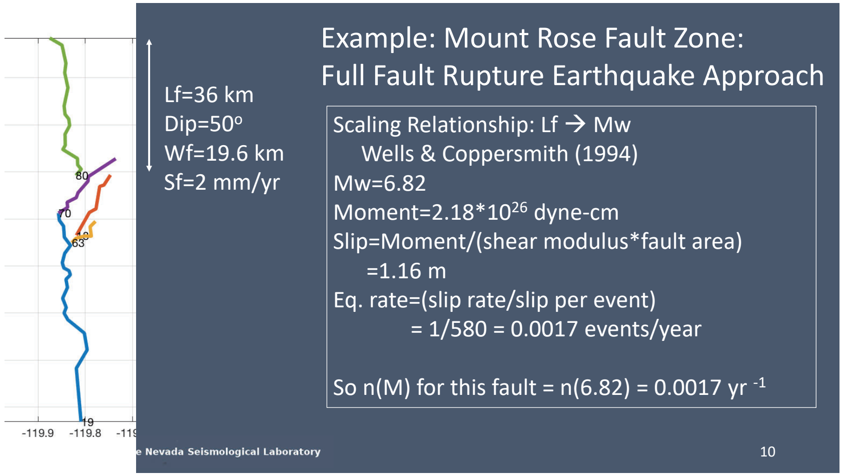

Example: Mount Rose Fault Zone: Full Fault Rupture Earthquake Approach

Lf=36 km
Dip=50°
Wf=19.6 km
Sf=2 mm/yr

Scaling Relationship: Lf → Mw
Wells & Coppersmith (1994)
Mw=6.82
Moment=2.18*10^{26} dyne-cm
Slip=Moment/(shear modulus*fault area)
=1.16 m
Eq. rate=(slip rate/slip per event)
= 1/580 = 0.0017 events/year

So n(M) for this fault = n(6.82) = 0.0017 yr^{-1}

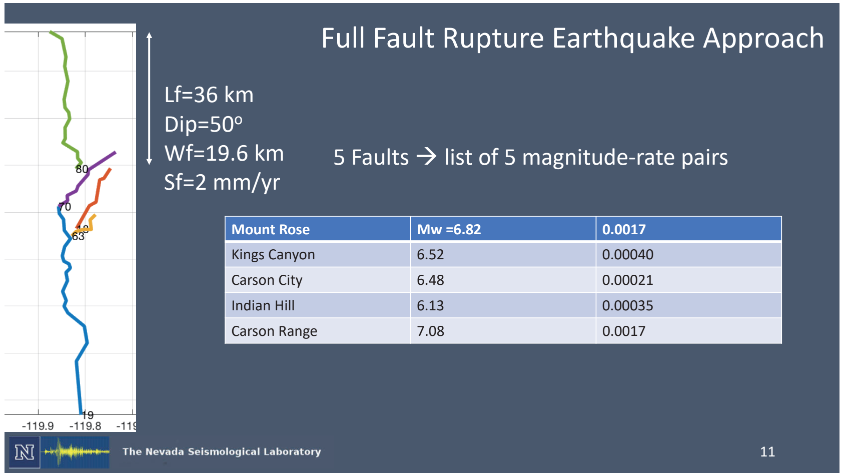

Full Fault Rupture Earthquake Approach

Lf=36 km
Dip=50°
Wf=19.6 km
Sf=2 mm/yr

5 Faults → list of 5 magnitude-rate pairs

Mount Rose	Mw =6.82	0.0017
Kings Canyon	6.52	0.00040
Carson City	6.48	0.00021
Indian Hill	6.13	0.00035
Carson Range	7.08	0.0017

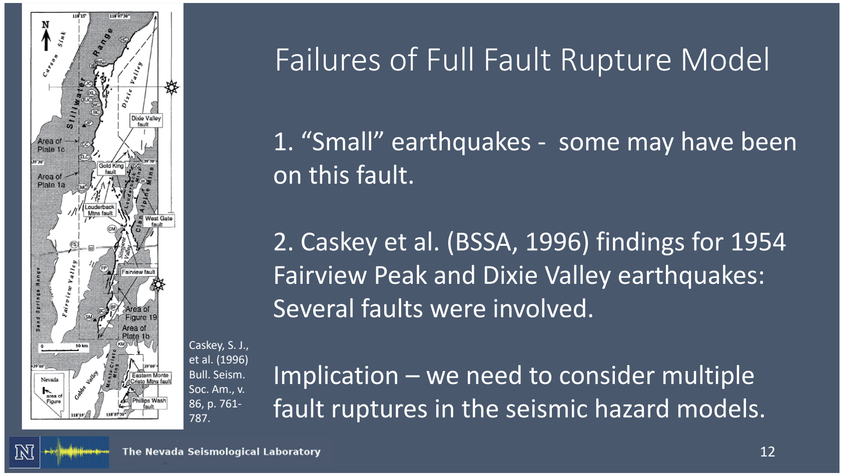

Caskey, S. J., et al. (1996) Bull. Seism. Soc. Am., v. 86, p. 761-787.

Failures of Full Fault Rupture Model

1. “Small” earthquakes - some may have been on this fault.

2. Caskey et al. (BSSA, 1996) findings for 1954 Fairview Peak and Dixie Valley earthquakes: Several faults were involved.

Implication – we need to consider multiple fault ruptures in the seismic hazard models.

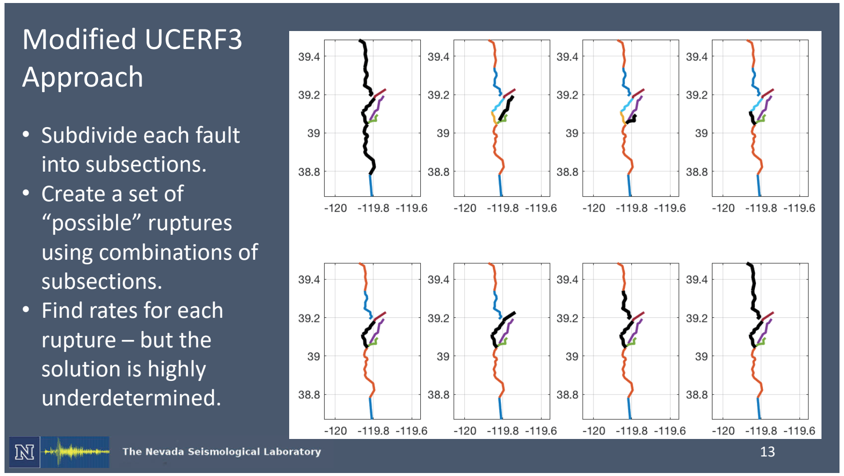

Modified UCERF3 Approach

- Subdivide each fault into subsections.
- Create a set of “possible” ruptures using combinations of subsections.
- Find rates for each rupture – but the solution is highly underdetermined.

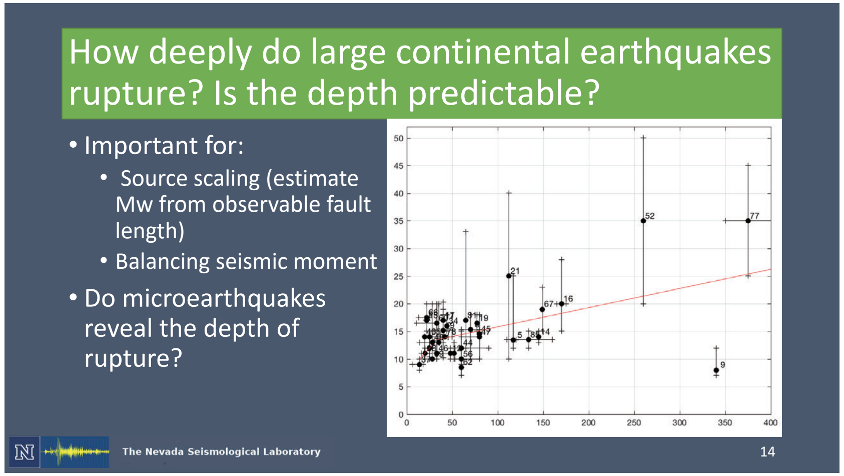

How deeply do large continental earthquakes rupture? Is the depth predictable?

- Important for:
  - Source scaling (estimate Mw from observable fault length)
  - Balancing seismic moment
- Do microearthquakes reveal the depth of rupture?

Is moment balancing based on slip/strain rate the best approach to estimate earthquake rates? Are there other methods?

- Doesn’t work for low-hazard areas, such as eastern North America.
- What controls the rate of earthquakes in “stable continental regions”?
- Quantify off-fault strain?
- Are there alternatives to background seismicity to quantify the role of minor, unmapped faults?

- References: Anderson (1979), Bird & Kreemer (2015)

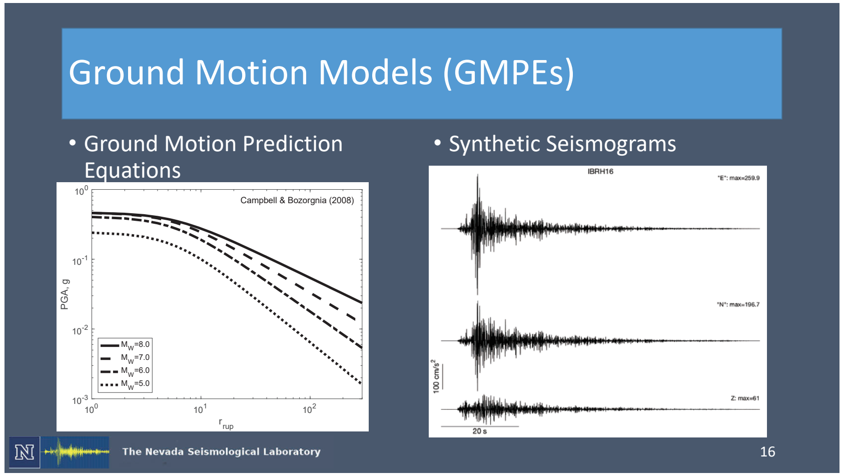

Ground Motion Models (GMPEs)

- Ground Motion Prediction Equations
- Synthetic Seismograms

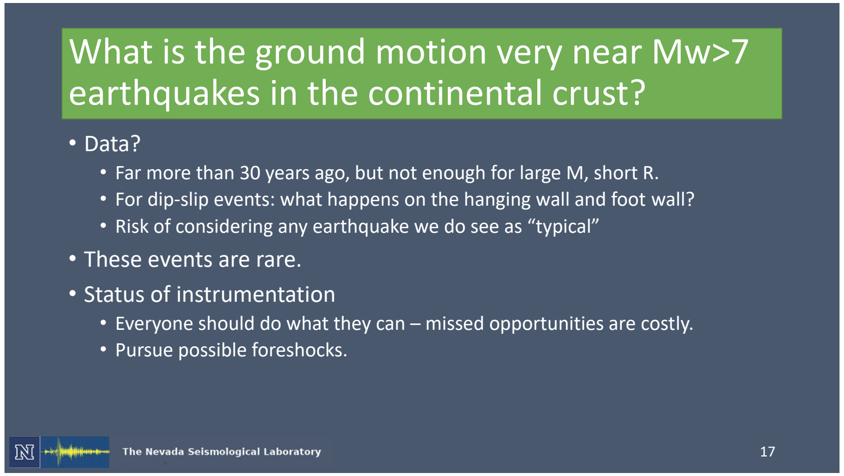

What is the ground motion very near Mw>7 earthquakes in the continental crust?

- Data?
  - Far more than 30 years ago, but not enough for large M, short R.
  - For dip-slip events: what happens on the hanging wall and foot wall?
  - Risk of considering any earthquake we do see as “typical”
- These events are rare.
- Status of instrumentation
  - Everyone should do what they can – missed opportunities are costly.
  - Pursue possible foreshocks.

The Nevada Seismological Laboratory

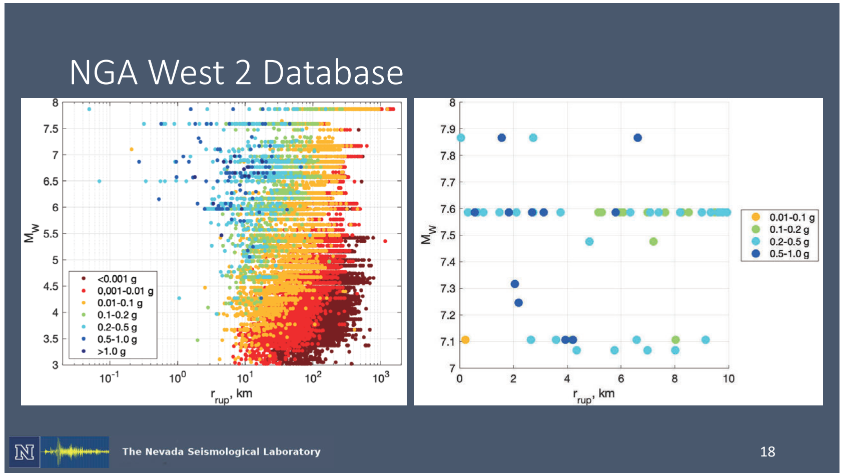

NGA West 2 Database

The Nevada Seismological Laboratory

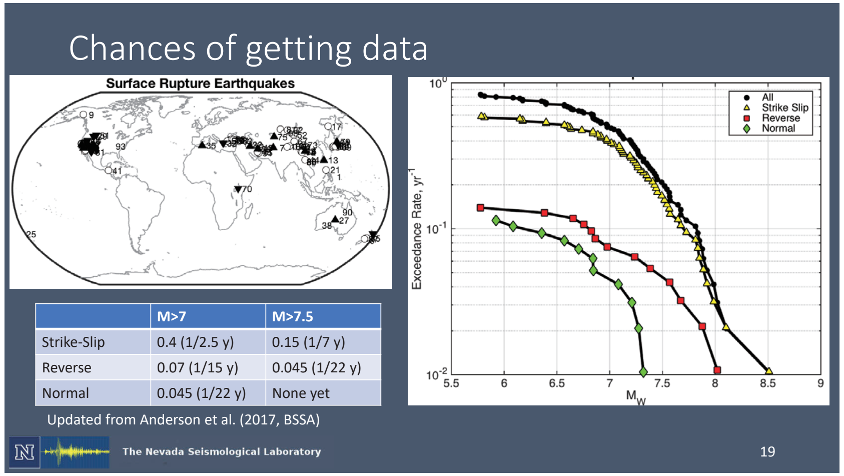

Chances of getting data

	M>7	M>7.5
Strike-Slip	0.4 (1/2.5 y)	0.15 (1/7 y)
Reverse	0.07 (1/15 y)	0.045 (1/22 y)
Normal	0.045 (1/22 y)	None yet

Updated from Anderson et al. (2017, BSSA)

The Nevada Seismological Laboratory

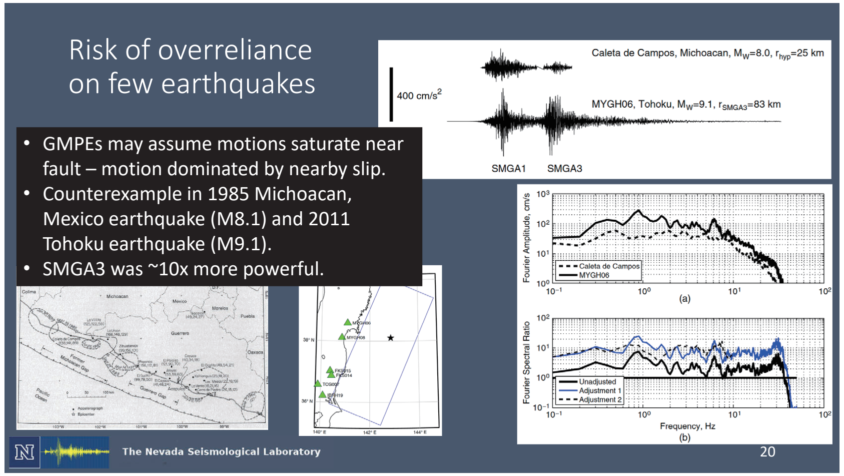

Risk of overreliance on few earthquakes

- GMPEs may assume motions saturate near fault – motion dominated by nearby slip.
- Counterexample in 1985 Michoacan, Mexico earthquake (M8.1) and 2011 Tohoku earthquake (M9.1).
- SMGA3 was ~10x more powerful.

The Nevada Seismological Laboratory

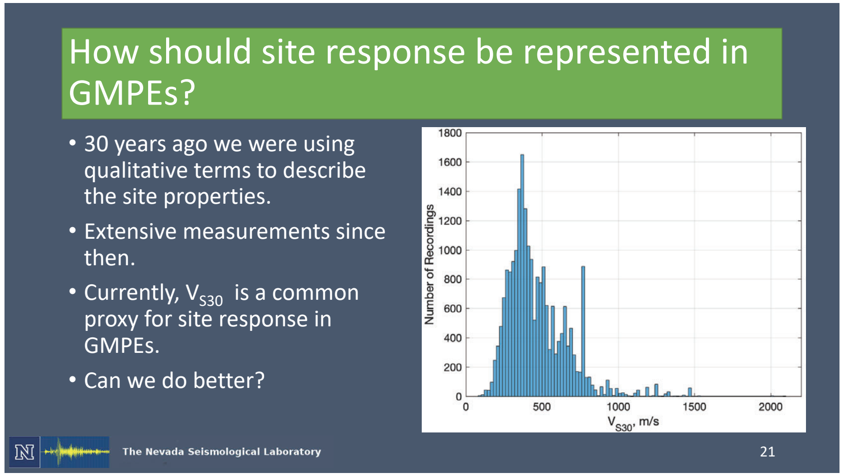

How should site response be represented in GMPEs?

- 30 years ago we were using qualitative terms to describe the site properties.
- Extensive measurements since then.
- Currently, V_{S30} is a common proxy for site response in GMPEs.
- Can we do better?

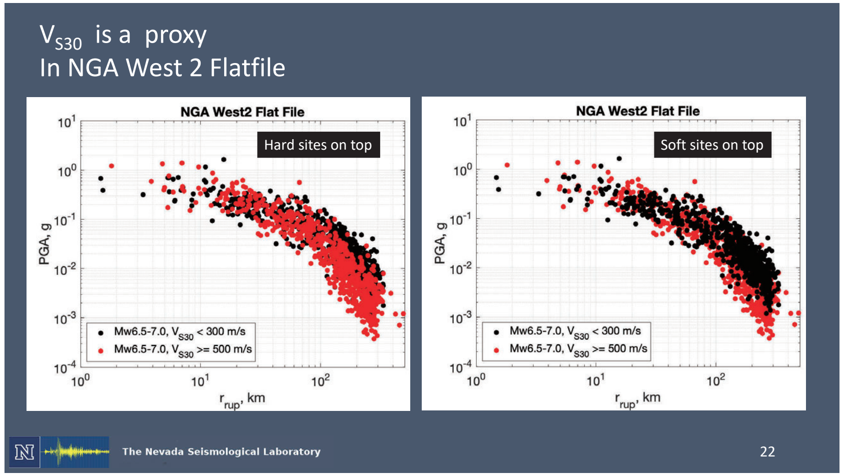

V_{S30} is a proxy
In NGA West 2 Flatfile

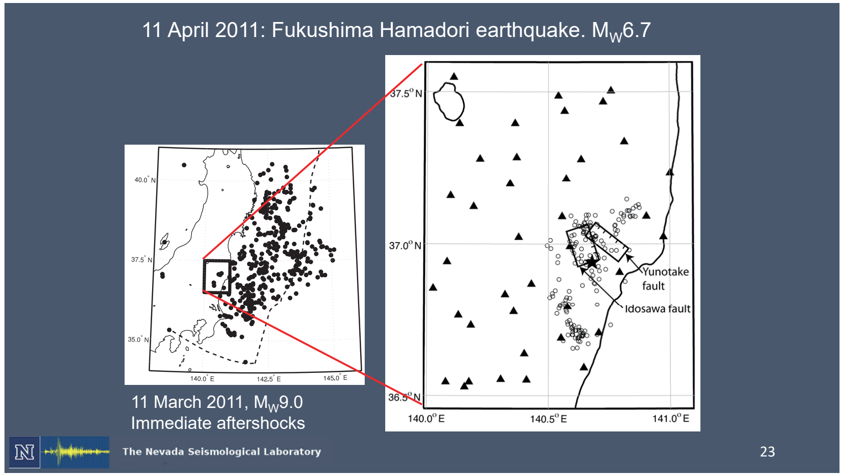

11 April 2011: Fukushima Hamadori earthquake. M_W6.7

11 March 2011, M_W9.0
Immediate aftershocks

11 April 2011: Fukushima Hamadori earthquake. M_W6.7
Images from Maruyama et al, 2011 (GSJ)

Cabin adjacent to fault that ruptured in the 1954 Dixie Valley earthquake (MW 6.9). The photograph was taken on 20 December 1954 by Karl Steinbrugge (NISEE, UCB).

Fault exposure during the 2011 Fukushima Hamadori earthquake. These photographs were taken by Tadashi Maruyama, Geological Survey of Japan.

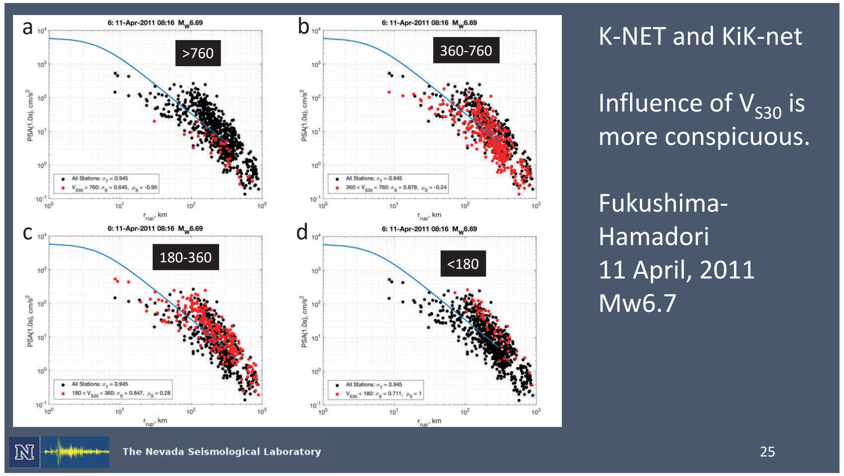

K-NET and KiK-net

Influence of V_{S30} is more conspicuous.

Fukushima-Hamadori
11 April, 2011
Mw6.7

Can sigma (σ) be reduced in GMPEs?

- Critical role of sigma for PSHA results at low probabilities.
- Ergodic assumption (Anderson & Brune, 1999, SRL)
- Single-station sigma

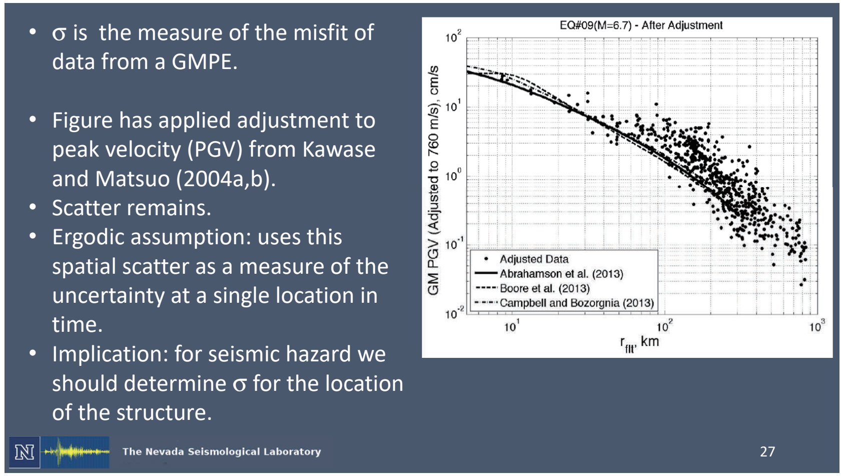

- σ is the measure of the misfit of data from a GMPE.
- Figure has applied adjustment to peak velocity (PGV) from Kawase and Matsuo (2004a,b).
- Scatter remains.
- Ergodic assumption: uses this spatial scatter as a measure of the uncertainty at a single location in time.
- Implication: for seismic hazard we should determine σ for the location of the structure.

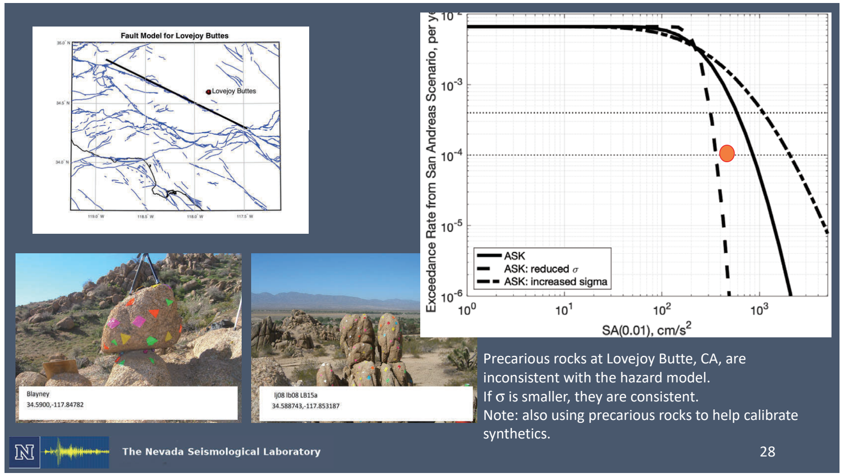

Precarious rocks at Lovejoy Butte, CA, are inconsistent with the hazard model.
If σ is smaller, they are consistent.
Note: also using precarious rocks to help calibrate synthetics.

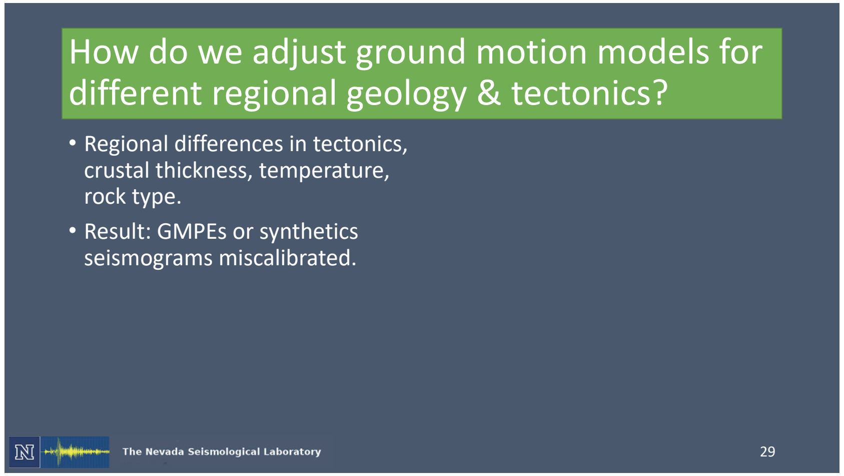

How do we adjust ground motion models for different regional geology & tectonics?

- Regional differences in tectonics, crustal thickness, temperature, rock type.
- Result: GMPEs or synthetics seismograms miscalibrated.

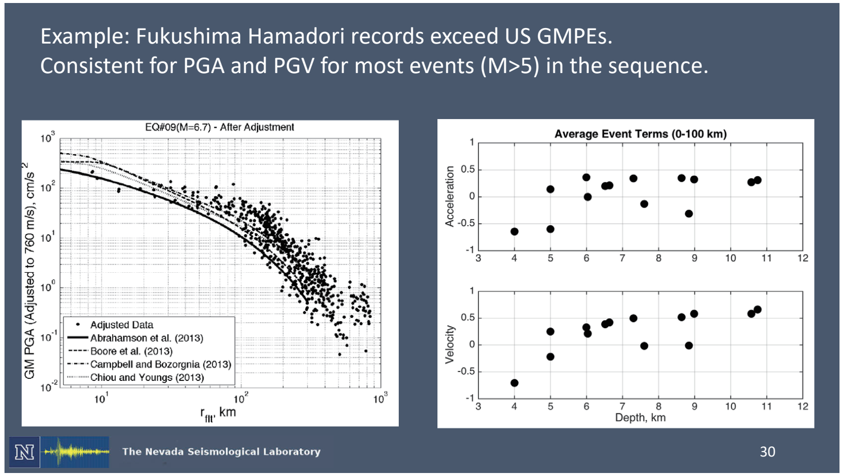

Example: Fukushima Hamadori records exceed US GMPEs.
Consistent for PGA and PGV for most events (M>5) in the sequence.

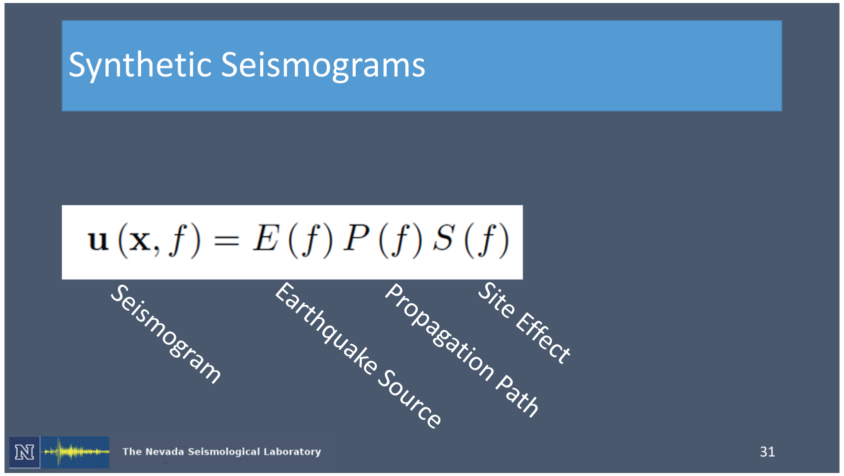

Synthetic Seismograms

$$\mathbf{u}(\mathbf{x}, f) = E(f)\,P(f)\,S(f)$$

Seismogram
Earthquake Source
Propagation Path
Site Effect

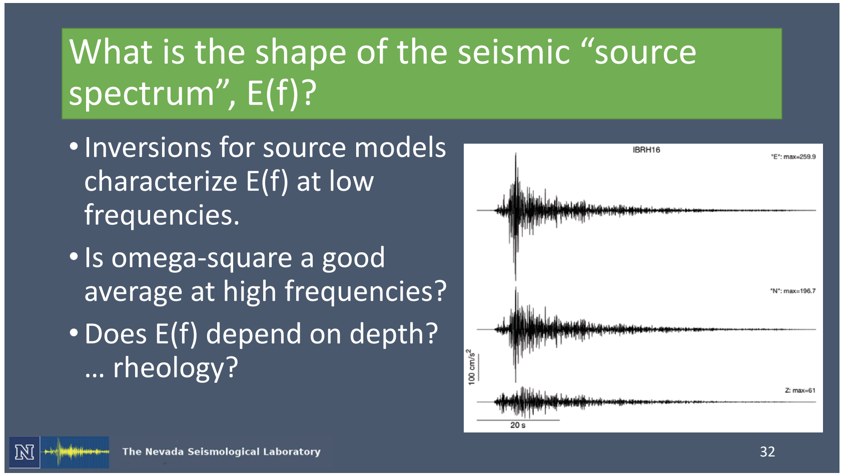

What is the shape of the seismic “source spectrum”, E(f)?

- Inversions for source models characterize E(f) at low frequencies.
- Is omega-square a good average at high frequencies?
- Does E(f) depend on depth? … rheology?

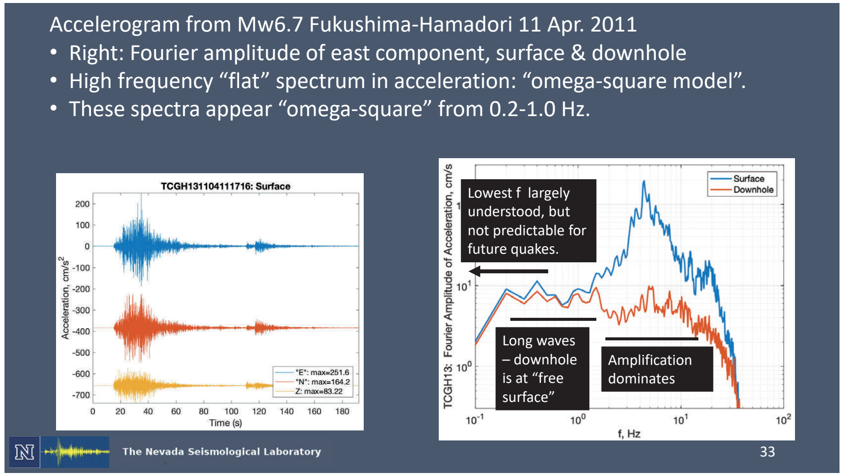

Accelerogram from Mw6.7 Fukushima-Hamadori 11 Apr. 2011
- Right: Fourier amplitude of east component, surface & downhole
- High frequency “flat” spectrum in acceleration: “omega-square model”.
- These spectra appear “omega-square” from 0.2-1.0 Hz.

Lowest f largely understood, but not predictable for future quakes.

Long waves – downhole is at “free surface”

Amplification dominates

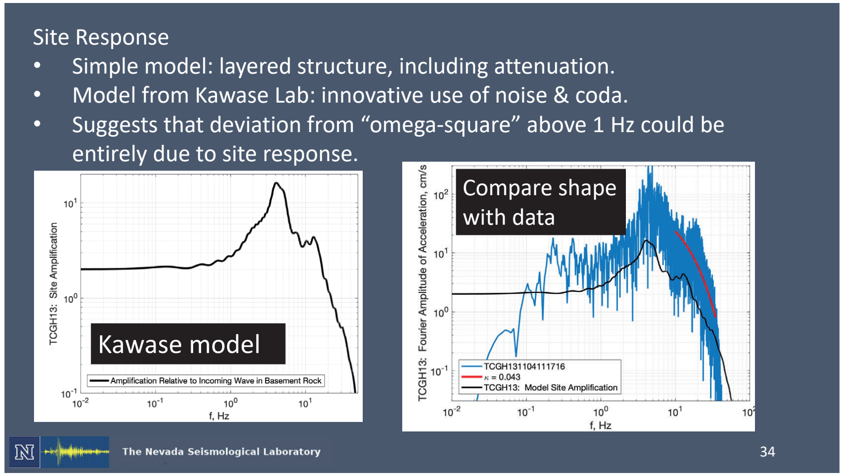

Site Response
- Simple model: layered structure, including attenuation.
- Model from Kawase Lab: innovative use of noise & coda.
- Suggests that deviation from “omega-square” above 1 Hz could be entirely due to site response.

Kawase model

Compare shape with data

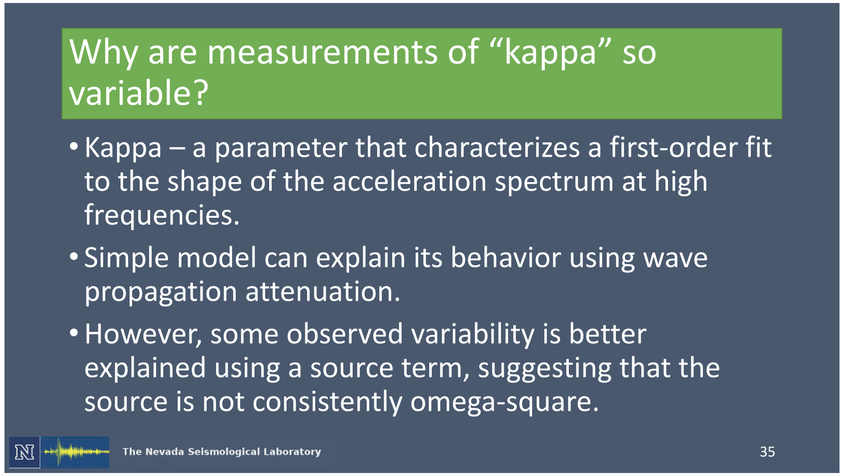

Why are measurements of “kappa” so variable?

- Kappa – a parameter that characterizes a first-order fit to the shape of the acceleration spectrum at high frequencies.
- Simple model can explain its behavior using wave propagation attenuation.
- However, some observed variability is better explained using a source term, suggesting that the source is not consistently omega-square.

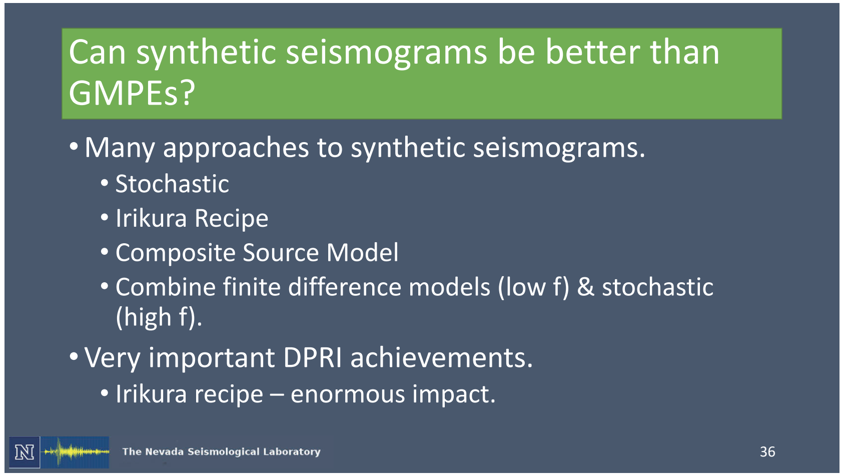

Can synthetic seismograms be better than GMPEs?

- Many approaches to synthetic seismograms.
  - Stochastic
  - Irikura Recipe
  - Composite Source Model
  - Combine finite difference models (low f) & stochastic (high f).
- Very important DPRI achievements.
  - Irikura recipe – enormous impact.

How effectively can site response be represented in synthetic seismograms?

- Illustrate with example of work I've done with Prof. Kawase and others in his lab.
  - The approach introduces site response through detailed model of shallow structure.

Synthetic Seismograms using a Composite Source Model

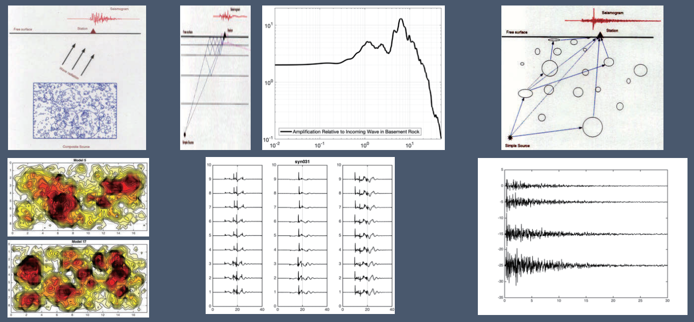

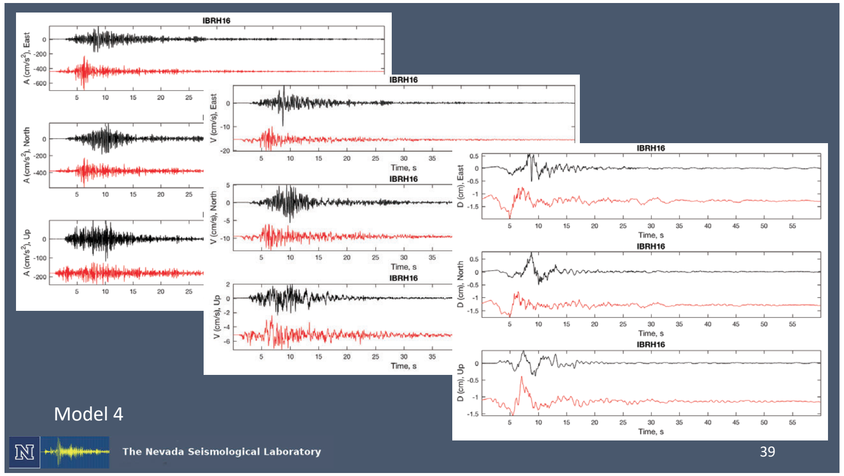

Model 4

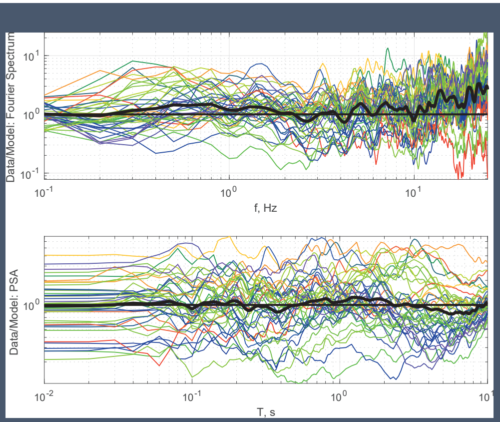

Model 4

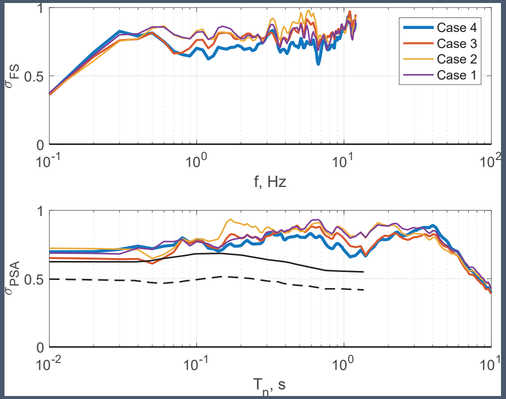

General Issues

Hazard maps should show uncertainties. How should those uncertainties be measured?

- Assumptions:
  - A true, data-generating hazard curve exists for every site.
  - However, estimates vary from one model to another.

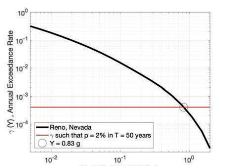

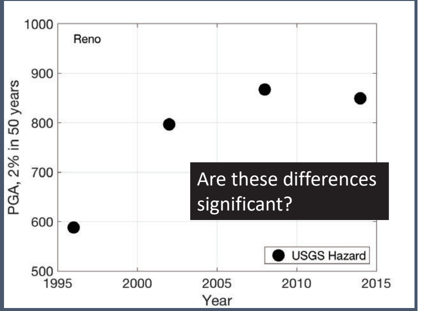

Are these differences significant?

Logic Tree for Epistemic Uncertainty

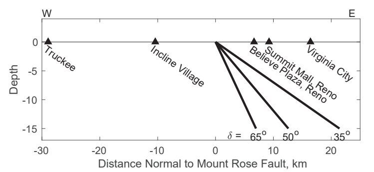

- MECE: Mutually Exclusive & Collectively Exhaustive.

gement, not

each node to
the end.
responding

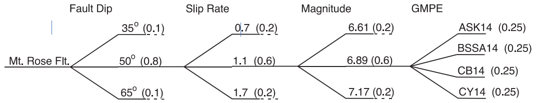

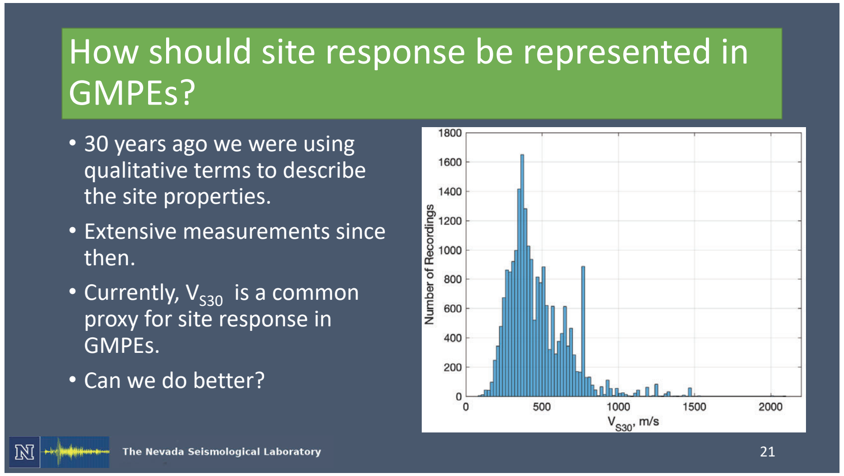

How should site response be represented in GMPEs?

- 30 years ago we were using qualitative terms to describe the site properties.
- Extensive measurements since then.
- Currently, V_{S30} is a common proxy for site response in GMPEs.
- Can we do better?

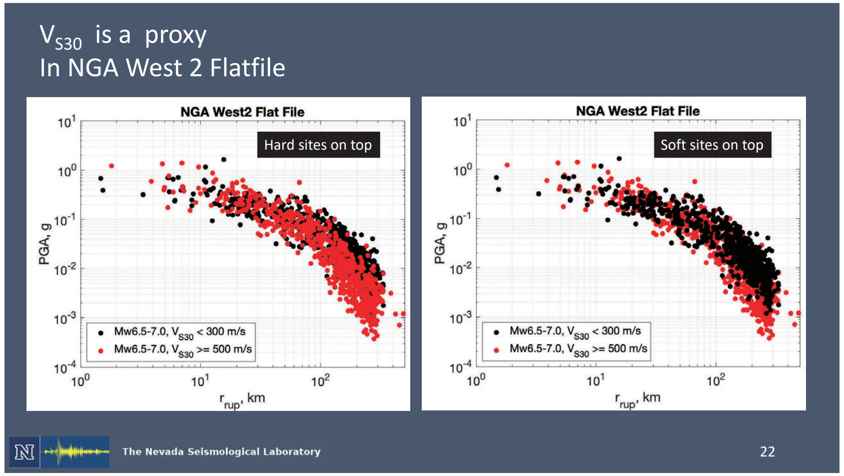

V_{S30} is a proxy
In NGA West 2 Flatfile

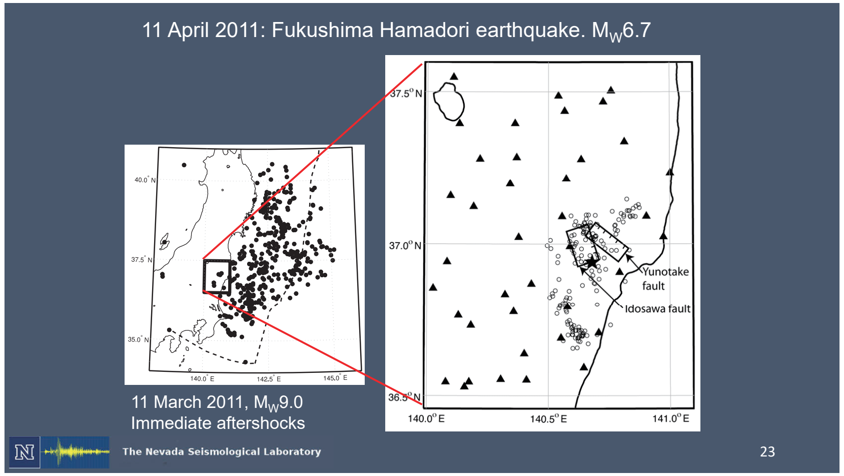

11 April 2011: Fukushima Hamadori earthquake. M_W6.7

11 March 2011, M_W9.0
Immediate aftershocks

11 April 2011: Fukushima Hamadori earthquake. M_W6.7
Images from Maruyama et al, 2011 (GSJ)

Cabin adjacent to fault that ruptured in the 1954 Dixie Valley earthquake (MW 6.9). The photograph was taken on 20 December 1954 by Karl Steinbrugge (NISEE, UCB).

Fault exposure during the 2011 Fukushima Hamadori earthquake. These photographs were taken by Tadashi Maruyama, Geological Survey of Japan.

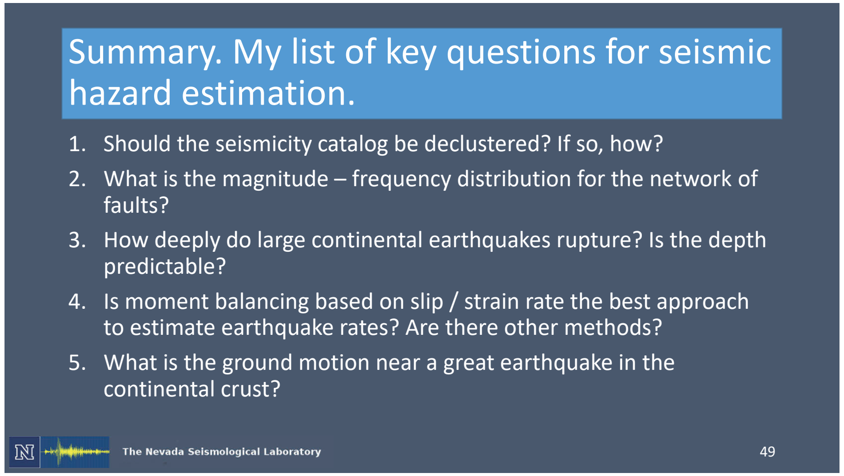

Summary. My list of key questions for seismic hazard estimation.

1. Should the seismicity catalog be declustered? If so, how?
2. What is the magnitude – frequency distribution for the network of faults?
3. How deeply do large continental earthquakes rupture? Is the depth predictable?
4. Is moment balancing based on slip / strain rate the best approach to estimate earthquake rates? Are there other methods?
5. What is the ground motion near a great earthquake in the continental crust?

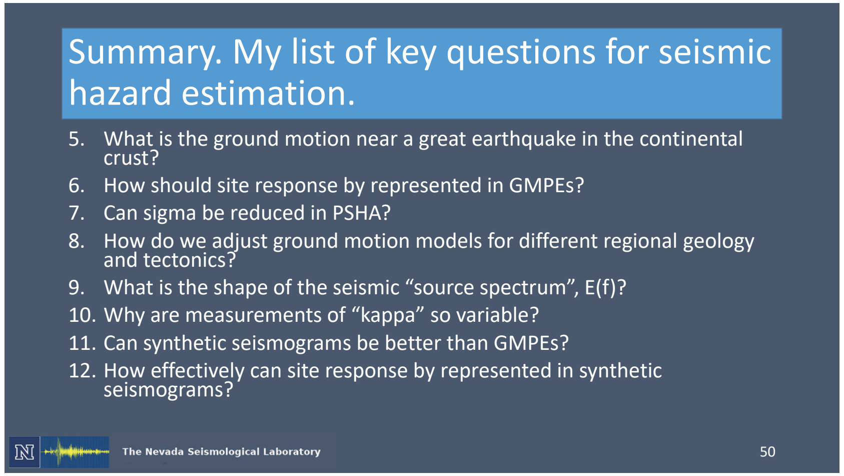

Summary. My list of key questions for seismic hazard estimation.

5. What is the ground motion near a great earthquake in the continental crust?
6. How should site response by represented in GMPEs?
7. Can sigma be reduced in PSHA?
8. How do we adjust ground motion models for different regional geology and tectonics?
9. What is the shape of the seismic “source spectrum”, E(f)?
10. Why are measurements of “kappa” so variable?
11. Can synthetic seismograms be better than GMPEs?
12. How effectively can site response by represented in synthetic seismograms?

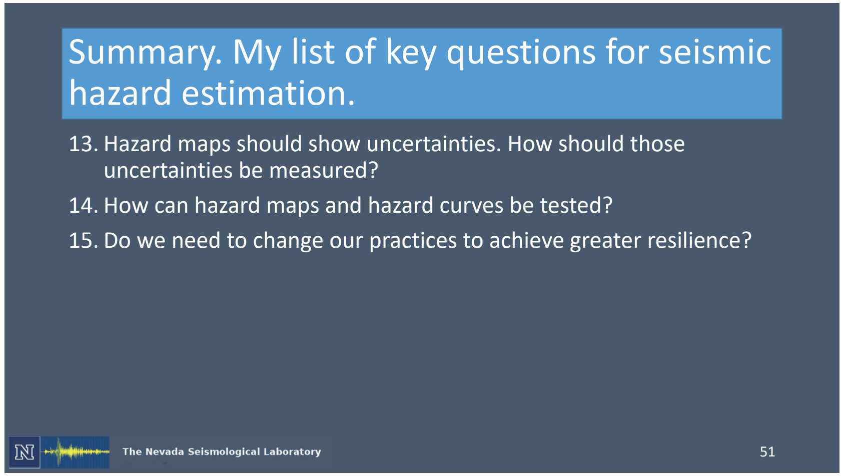

Summary. My list of key questions for seismic hazard estimation.

13. Hazard maps should show uncertainties. How should those uncertainties be measured?
14. How can hazard maps and hazard curves be tested?
15. Do we need to change our practices to achieve greater resilience?

We need to work together!

- Thank you.
  - For your attention today
  - For this generous recognition.
  - For welcoming me to DPRI so many times in the past.
  - For collaboration and friendship.

Bulletin of the Seismological Society of America, Vol. 74, No. 5, pp. 1969–1993, October 1984

A MODEL FOR THE SHAPE OF THE FOURIER AMPLITUDE SPECTRUM OF ACCELERATION AT HIGH FREQUENCIES

BY JOHN G. ANDERSON AND SUSAN E. HOUGH

ABSTRACT

At high frequencies f the spectrum of S-wave accelerations is characterized by a trend of exponential decay, $e^{-\pi\kappa f}$. In our study, the spectral decay parameter κ shows little variation at a single station for multiple earthquakes at the same distances, but it increases gradually as the epicentral distance increases. For multiple recordings of the San Fernando earthquake, κ increases slowly with distance, and κ is systematically smaller for sites on rock than for sites on alluvium. Under the assumption that the Fourier spectrum of acceleration at the source is constant above the corner frequency (an ω^{-2} source model), the exponential decay is consistent with an attenuation model in which Q increases rapidly with depth in the shallow crustal layers.

INTRODUCTION

The shape and amplitude of the Fourier amplitude spectrum of strong ground acceleration is recognized as useful for various applications to earthquake engineering (McGuire, 1978). This acceleration spectrum also contains fundamental information about physical processes at the earthquake source and wave propagation in the crust of the earth. Yet at high frequencies, we still do not have a satisfactory model for the shape of the acceleration spectrum. By the shape of a spectrum we refer to a smooth trend through the spectrum; the fine structure which is superimposed on this trend is not meant to be included.

At low frequencies and sufficiently far from the fault, the inevitable result of an elastic rebound source model is that the acceleration spectrum increases as ω^2, where $\omega = 2\pi f$ and f is the frequency of ground motion. For example, a widely employed model by Brune (1970) relates the coefficient of this ω^2 trend to the seismic moment, M_0, and relates the corner frequency (f_0) where this ω^2 trend terminates to a stress drop parameter at the source. Above the corner frequency, Trifunac (1976) and McGuire (1978) have carried out empirical regressions for the shape of the acceleration spectrum but these regressions do not yield much insight into the physical processes which are involved. Hanks (1979, 1982) suggests that, in general, the acceleration spectrum is flat above the corner frequency to a second corner frequency ($f_{\max}$) above which the spectrum decays rapidly.

In the next section, we propose a parametric shape for the acceleration spectrum at high frequency. Our model is characterized by one parameter, which we designate as the spectral decay parameter κ. Recognition and study of this parameter were motivated in part by the observations that most spectra observed in the 1981 Santa Barbara Island earthquake appear to fall off exponentially (Anderson, 1984). Subsequent sections explore the systematic behavior of κ for the S-wave portion of the accelerogram. We also recognize a plausible attenuation model to explain the observations but intentionally avoid introducing the terminology and notation of that model into the observation sections of this paper.

SPECTRAL SHAPE AT HIGH FREQUENCIES

Figure 1 shows the Fourier amplitude spectrum of acceleration for the S16°E component of the Pacoima Dam accelerogram from the 1971 San Fernando, California, earthquake. Figure 1A shows the spectrum plotted on log-log axes. Based on a figure of this type, Hanks (1982, Figure 2) selects f_{max} for this record to be near 10 Hz. In Figure 1B, the frequency axis is linear. On these axes, the dominant trend is a linear decrease of the log of spectral amplitude with frequency, and there is no apparent additional slope break in the vicinity of 10 Hz. In some cases, the dominant trend of exponential decay is initiated near f_0, but on other spectra it begins at some higher frequency. It is, therefore, useful to label the frequency above which the spectral shape is indistinguishable from exponential decay. Here we call this frequency f_E. We do not ascribe any fundamental importance to f_E, and pay little attention to it in the rest of this paper. Considering the amplitude of the fine structure to the spectrum (Figure 1), it is difficult to determine meaningful trends over narrow frequency bands (e.g., bandwidth less than about 3 to 5 Hz). Thus the identification of f_E, like that of f_{max}, is to some extent subjective. On Figure 1, f_E may occur between 2 and 5 Hz. Thus, on this spectrum, f_E is distinctly less than the value for f_{max} which was identified by Hanks (1982).

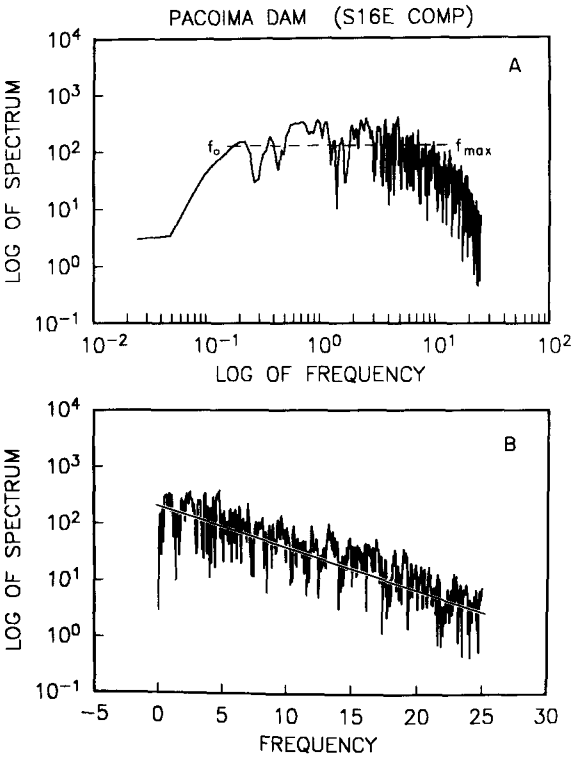

FIG. 1. Fourier amplitude spectrum of acceleration for the S16°E component of the Pacoima Dam accelerogram, San Fernando, California, earthquake of 9 February 1971. Accelerogram was digitzed by hand. (A) Log-log axes. (B) Linear-log axes.

Figure 2 is the equivalent of Figure 1, but for the spectrum of an accelerogram recorded at Cucapah, Baja California, Mexico, from the June 1980 earthquake (M_L = 6.1) in the Mexicali Valley, across the international border from the Imperial Valley, California. These data are described by Anderson *et al.* (1982). The accelerograph in this case is a digital recorder (Kinemetrics DSA-1) which samples the output of a force-balance accelerometer (natural frequency 50 Hz) at a rate of 200 samples/sec, so that the Nyquist frequency is 100 Hz. The least count is about 0.5

cm/sec^2. Because the response of the force-balance sensor is flat to 50 Hz, no instrument correction has been applied to this record. Because of the highly accurate digital recording, there is little uncertainty about the reliability of the digitization on this record, as there might be for hand-digitized data (e.g., Berrill and Hanks, 1974; Sacks, 1980; Cormier, 1982).

Figure 2A shows the same general properties as Figure 1A, although the window in this case was not long enough to establish a low-frequency asymptote at frequencies less than the corner frequency f_0. By analogy to Figure 1A, one would pick $f_{\max}$ at about 10 Hz for the spectrum in Figure 2A. Figure 2B again shows a predominantly exponential decrease in spectral amplitude, in this case from 1 to 40 Hz. Below about 6 Hz, there is again room to define, at a lower confidence level, a trend which diverges from the exponential trend which dominates over the full frequency band. At 40 Hz the exponential trend intersects spectral amplitudes of about 0.1 cm/sec, corresponding to the least count digitization level, and above 40 Hz the spectrum is flat, as is appropriate for a digitization process with random round-off errors at an amplitude of ±0.5 least count.

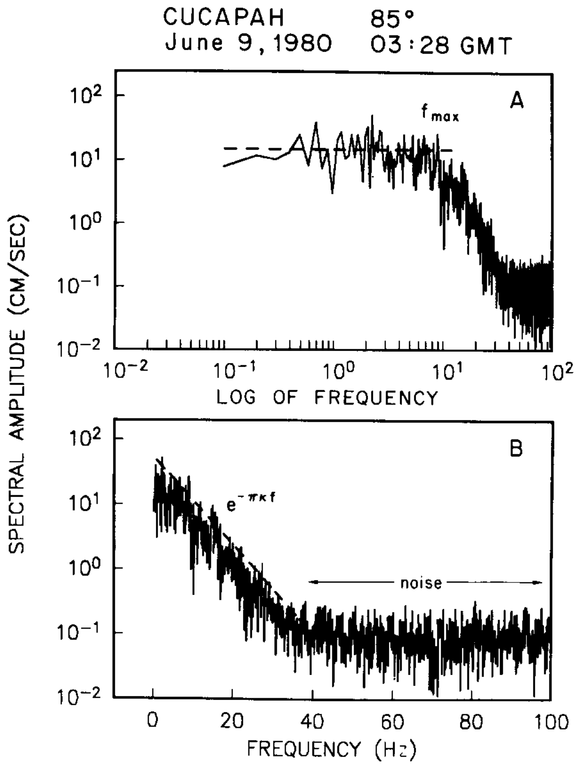

FIG. 2. Fourier amplitude spectrum of the N85°E component of strong ground acceleration recorded at Cucapah during the Mexicali Valley earthquake of 9 June 1980 ($M_L = 6.2$). Accelerograph was a digital recorder which samples at a rate of 200/sec. (A) Log-log axes. (B) Linear-log axes.

Based on Figures 1 and 2, and many comparable spectral plots, we hypothesize that to first order the shape of the acceleration spectrum at high frequencies can generally be described by the equation

$$a(f) = A_0 e^{-\pi\kappa f} \qquad f > f_E \tag{1}$$

where A_0 depends on source properties, epicentral distance, and perhaps other factors. The systematic behavior of the spectral decay parameter κ is explored in the next three sections of this paper.

METHOD

We studied shear-wave spectra for the horizontal components of strong ground acceleration from 98 sites around the 1971 San Fernando earthquake, ten events recorded at Ferndale, ten events recorded at El Centro, and five events recorded at Hollister. All records are corrected accelerograms from the Volume II data tape prepared by the Earthquake Engineering Research Laborartory of California Institute of Technology (EERL, 1971).

Fourier transforms of the shear waves were computed from accelerograms. The time window was chosen to include only direct S-wave arrivals. In cases where the transition from direct S-wave arrivals to coda was not readily apparent, our choice for the time window favored including coda rather than possibly eliminating direct arrivals. Spectral shape was found to be fairly insensitive to the time window length as long as it was reasonably chosen. The value of κ at stations ~40 km from the epicenter of the San Fernando earthquake showed no correlations with time window length. The transforms were computed with a standard Fast Fourier transform routine after a cosine taper was applied to the raw data and the time series were padded out to powers of two with zeroes. The spectra were plotted from 0 to 25 Hz (Nyquist frequency = 25 Hz).

To obtain the spectral decay parameter, linear least-squares fits to the spectra were obtained. A 2- to 12-Hz interval was used for the El Centro, Ferndale, and Hollister records. The corner frequencies for all of the earthquakes we considered are less than 2 Hz. Frequencies higher than 12 Hz were considered potentially unreliable on some of these records in these data sets for reasons to be discussed later. For the San Fernando records, the interval used for regression was 2 to 18 Hz.

Values of the slopes were converted to the spectral decay parameter, κ, and subsequently plotted against epicentral distance to evaluate distance-dependence. To quantify trends, we found a linear regression between κ and distance, R, even though we do not believe a linear relationship is the definitive dependence of κ on R. For the multiple event data, these straight lines were fit directly. The San Fernando data were averaged within 10-km distance bands and then fit with straight lines. This latter procedure reduces the weight of the distance ranges which are represented by large numbers of stations. Regression done on the complete data sets yielded similar results.

RESULTS: SINGLE STATION AND MULTIPLE EVENTS

Figures 3 through 9 illustrate results for records of earthquakes at multiple distances from a single station. Figure 3 is a map of the vicinity of the El Centro accelerograph, showing locations of the station, epicenters of ten earthquakes which were recorded on the accelerograph, and generalized surficial geology. Corresponding S-wave spectra and least-squares fits are shown in Figure 4. Figure 5 is a map of the Ferndale vicinity, and Figure 6 shows corresponding spectra for ten earthquakes which have been recorded there. Locations of the earlier earthquakes recorded at El Centro and Ferndale may have substantial errors. The 1934 and 1954 earthquakes at El Centro are shown at the relocated epicenters of Leeds (1979). These epicenters may be more reliable than others among the earlier earthquakes on these maps.

Figure 7 is a map of the Hollister vicinity and Figure 8 shows corresponding spectra for five earthquakes recorded at Hollister. Finally, Table 1 and Figure 9 show measured values of κ as a function of distance for all three stations.

Figure 4 shows spectra for both components of the El Centro station. On these spectra, a linear trend dominates the spectral shapes for frequencies between 2 and 12 Hz. Spectra for the 1934, 1940, and 1942 earthquakes (records B024, A001, and T286, respectively) have a nearly level trend starting at frequencies between 12 and 15 Hz. Likewise in Figure 6 many of the spectra, and most conspicuously the spectra for the earliest earthquakes, appear to assume a nearly level trend starting at

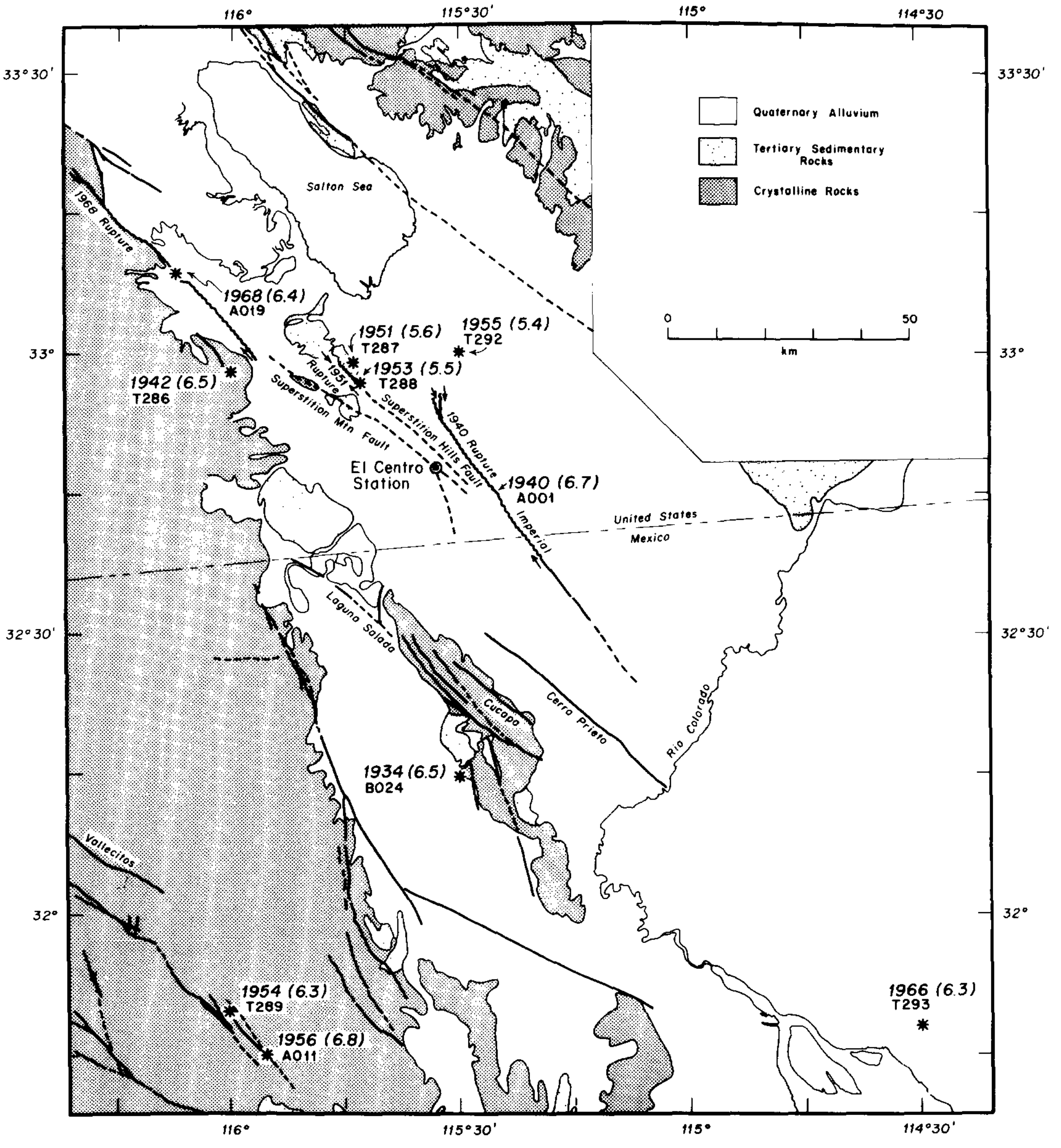

FIG. 3. Map of Imperial Valley, California-Mexico showing generalized geological features. Epicenters (asterisk) from Leeds (1979) or Hileman *et al.* (1973) are shown with year and magnitudes of earthquakes which have generated accelerograms at the El Centro station. Accelerogram number on the Caltech tapes is given below year. The 1940 and 1968 ruptures are from Jennings (1975).

frequencies as low as about 12 Hz. In Figure 8 all of the spectra deviate above the linear trend starting at between 12 and 15 Hz. In Figure 2, similar behavior resulted from the digitization, thus suggesting that digitization has also caused level spectral trends on these accelerograms.

An estimate for the typical range for the Fourier amplitude of digitization noise for these hand-digitized accelerograms has been presented by Berrill and Hanks (1974). Noise amplitudes under the digitization conditions of these accelerograms

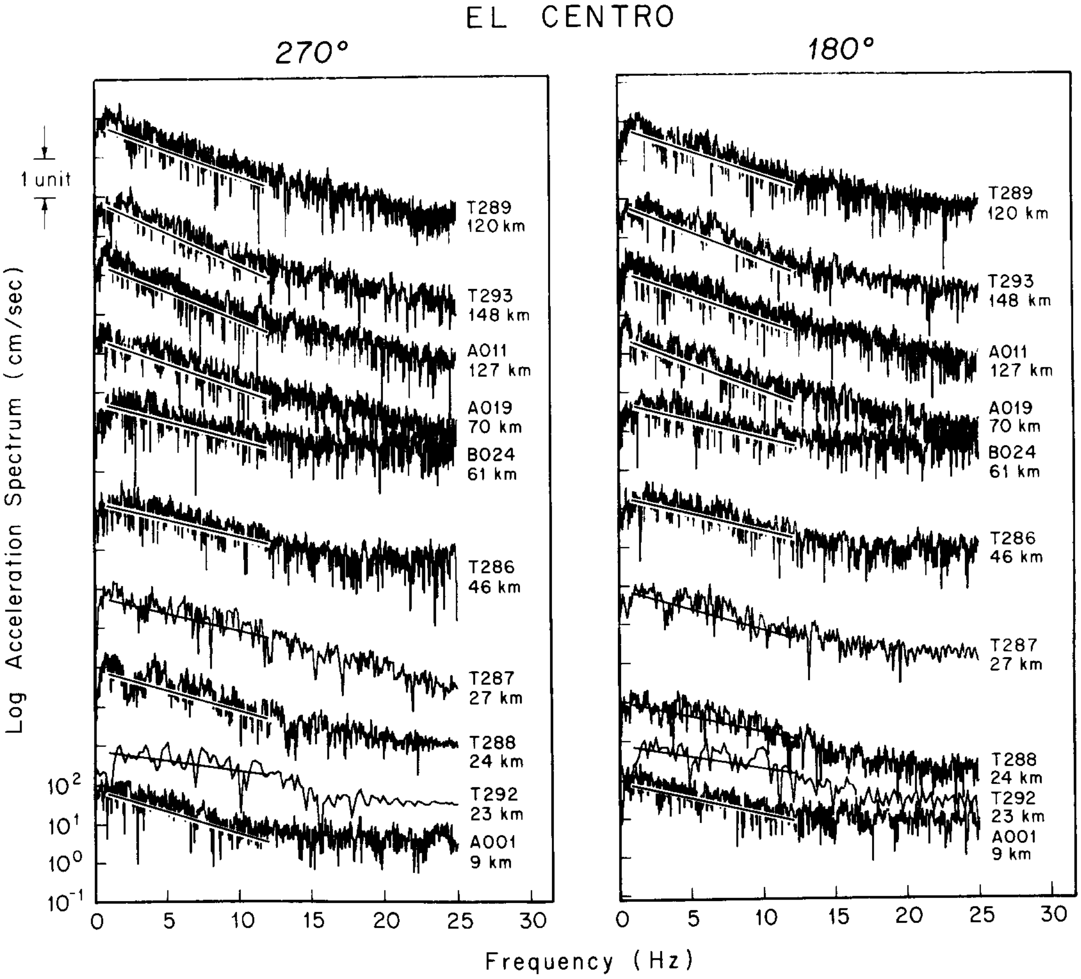

FIG. 4. Fourier amplitude spectra of S-wave accelerograms corresponding to epicenters from Figure 3. Record number and distance from the accelerograph are indicated to *right* of each spectrum. Each spectrum is offset by two logarithmic units from the spectrum immediately below. Superimposed on each spectrum is a linear, least-squares fit over the frequency band 2 to 12 Hz.

and the signal window employed in our study decrease smoothly from about 0.3 ± 0.07 cm/sec at 1 Hz to 0.18 ± 0.06 cm/sec at 12 Hz, and 0.11 ± 0.03 cm/sec at 24 Hz. Deviations of S-wave spectra above an exponential decay approximately coincide with these levels for all Hollister spectra (Figure 8) and for El Centro and Ferndale spectra of earthquakes recorded after 1949 (Figures 4 and 6).

All of the pre-1948 spectra from El Centro and Ferndale form a trend parallel to the digitization noise but the amplitude of this trend exceeds the amplitudes found by Berrill and Hanks (1974). It turns out that instrumental characteristics of the acclerographs at El Centro and Ferndale were modified once. Before the modification, the undamped natural frequency of each sensor was about 10 Hz (e.g., Bodel, 1944). Beginning in 1942, the U.S. Coast and Geodetic Survey began to modify its accelerographs to reduce the gain at selected stations. This modification was made at El Centro and at Ferndale in late 1948 or early 1949, based on a review of instrument constants published in the series *United States Earthquakes* (see Murphy and Ulrich, 1951a, b). Subsequently, the natural frequencies of the sensors were between 15 and 16 Hz. Thus, if we assume that the digitization and instrument correction procedure for the pre-1948 earthquakes leads to digitization noise above the level described by Berrill and Hanks (1974), the deviations of spectra in Figures 4, 6, and 8 above the model of exponential decay are all explained by digitization noise.

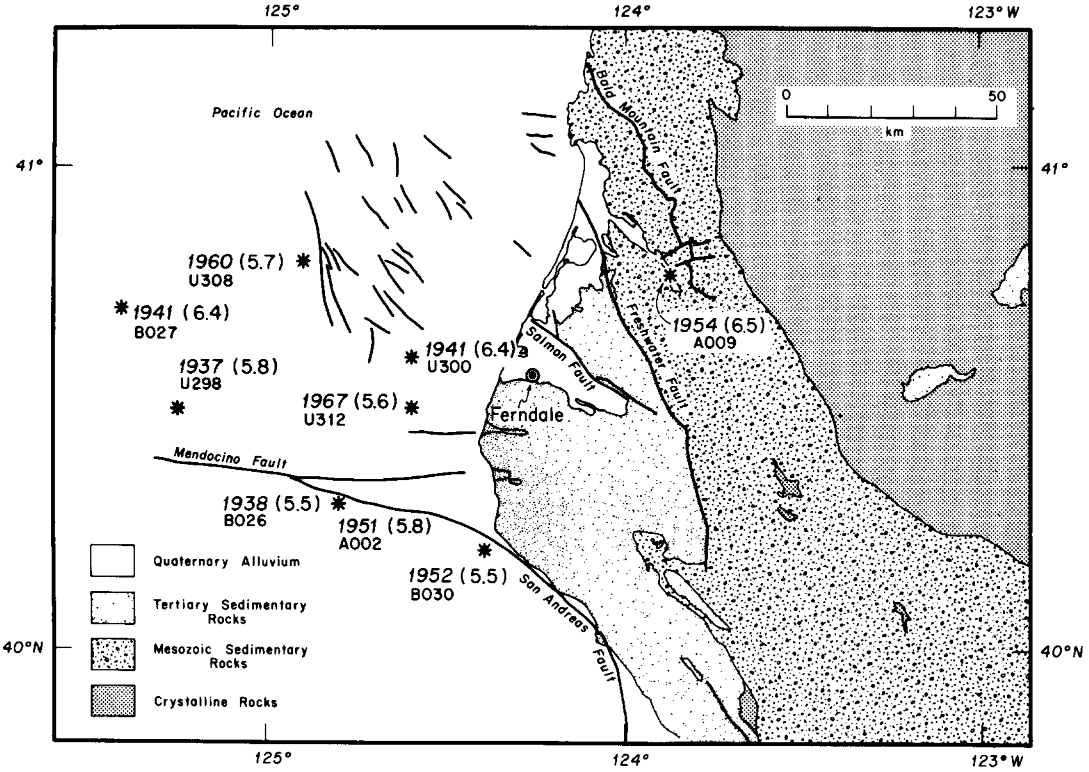

FIG. 5. Map of Cape Mendocino, California, showing generalized geological features. Epicenters from Trifunac and Lee (1978) are identified with the same notations as in Figure 3 and represent earthquakes which have produced accelerograms on the Ferndale accelerograph. The 1934, $M = 6.0$ earthquake (Record U294) was located off map at 41.7°N, 124.6°W. Real *et al.* (1978) location for the 1938 earthquake is 40°N, 124°W, about 75 km from the epicenter shown here.

For the 1953 event, the north-south component at El Centro may have been working improperly based on the appearance of the original accelerogram in Murphy and Cloud (1955) and spectral levels nearly an order of magnitude less than for the east-west component. The same trace was defective for the record of the 21 July 1952 Kern County earthquake (Murphy and Cloud, 1954). We have thus not included that measurement of κ on Figure 9, even though it is consistent with other values.

The El Centro station data in Figure 4 show that the spectral slopes of the two horizontal components of S waves from an earthquake are similar. Spectra in Figure 4, generally arranged from farthest to nearest, show a weak but clear distance dependence of the spectral shape, which is confirmed in Table 1 by the numerical values of the spectral decay parameters. The least-squares line through these data on Figure 9 has the equation $\kappa = 0.054$ sec + (0.00041 sec/km)R, where R is the source-to-station distance.

Accelerograms which have been recorded at Ferndale are primarily from offshore locations (Figure 5), and many of the epicenters are not well controlled. Spectra (Figure 6) show a less conspicuous increase of κ with distance than for El Centro records. The least-squares fit to the Ferndale data on Figure 9 is $\kappa = 0.075$ sec + (0.00016 sec/km)R. Spectra from Hollister (Figure 8) do not show a conclusive change in the spectral decay parameter with distance, but all the accelerograms were obtained at distances of less than 40 km.

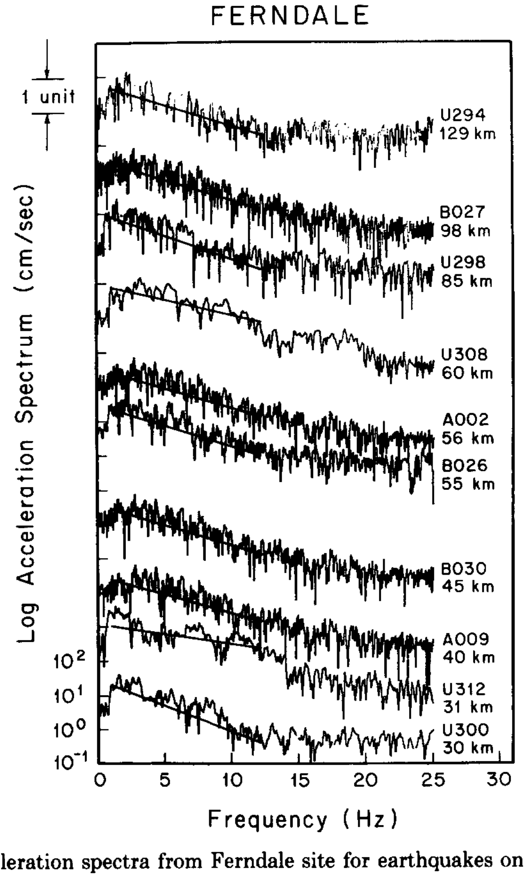

FIG. 6. S-wave acceleration spectra from Ferndale site for earthquakes on Figure 5. Please refer to Figure 4 caption for other notation.

Figure 9 summarizes the three studies of multiple recordings at a single station. At El Centro, Ferndale, and Hollister, the spectral decay parameter exhibits a common type of behavior. Within the resolution of the data, κ tends toward a finite value as epicentral distance approaches zero; we interpret this finite value as a characteristic of the subsurface geological structures. The term “subsurface geological structure” is used in the sense employed by Dobrin (1960) to refer to geological conditions below and near the site within distances on the order of hundreds of meters to a few kilometers. In addition to the subsurface geology effect, a path-distance effect also seems to be present and causes κ to increase gradually with distance. The existence of this systematic behavior suggests that the source spectral shapes of the several earthquakes probably had identical trends between the frequencies of 2 and 12 Hz.

TABLE 1

SPECTRAL DECAY PARAMETERS FOR ACCELEROGRAMS RECORDED AT HOLLISTER, FERNDALE, AND EL CENTRO

Date	Record	Distance	Magnitude	κ_1	κ_2
HOLLISTER					
03/09/49	U301	19.9	5.3	0.0850	
04/25/54	U305	29.1	5.3	0.0828	
01/19/60	U307	8.5	5.0	0.0865	
04/08/61	U309	19.8	5.6	0.0667	
12/18/67	U313	39.0	5.8	0.0880	
FERNDALE					
10/07/51	A002	56.3	5.8	0.0858	
12/21/54	A009	40.4	6.5	0.0821	
09/11/38	B026	55.3	5.5	0.0909	
02/09/41	B027	98.4	6.4	0.0909	
09/22/52	B030	45.2	5.5	0.0887	
07/06/34	U294	128.9	6.0	0.0923	
02/06/37	U298	85.1	5.8	0.1019	
10/03/41	U300	29.8	6.4	0.1114	
06/05/60	U308	60.3	5.7	0.0667	
12/10/67	U312	30.6	5.6	0.0447	
EL CENTRO					
05/19/40	A001	9.3	6.7	0.0608	0.0806
02/09/56	A011	126.9	6.8	0.0945	0.1077
04/08/68	A019	69.8	6.4	0.1011	0.0938
12/30/34	B024	60.8	6.5	0.0682	0.0711
10/21/42	T286	46.5	6.5	0.0645	0.0645
01/23/51	T287	27.5	5.6	0.0770	0.0630
06/13/53	T288	23.6	5.5	0.0591	0.0751
11/12/54	T289	119.8	6.3	0.0923	0.0975
12/16/55	T292	23.5	5.4	0.0452	0.0369
08/07/66	T293	148.1	6.3	0.1048	0.1217

RESULTS: SAN FERNANDO EARTHQUAKE

The San Fernando earthquake represents a situation in which multiple recordings have been made of a single event. Azimuthal variations in κ resulting from the source function were assumed negligible even though radiation at frequencies of 4 Hz and lower might be affected by source directivity (Berrill, 1975). This earthquake was used to study the effect of variable local geology and distance on κ. A map showing station locations and generalized geology has been prepared by Hanks (1975).

About 90 per cent of the spectra from the San Fernando records have an average trend which is modeled well by equation (1). The other 10 per cent of the records often appear to follow the same trend, except for a superimposed bulge which we tentatively identify as a site amplification effect. Figure 10 shows one of the more conspicuous examples of Fourier spectra with a relatively large apparent amplification of this type. Smaller broadband resonances may be unrecognized, and we conjecture that such resonances may add noise to determinations of κ.

Table 2 and Figure 11 summarize values of κ obtained from the San Fernando earthquake. Table 2 also lists the distance, the window length employed (T), and site classification, S. In Figure 11, the stations were grouped into three categories: alluvium ($S = 0$), consolidated sedimentary rock ($S = 1$), and hard (igneous or metamorphic) rock ($S = 2$), following the site classification of Trifunac and Brady (1975). Stations listed as being on sedimentary rocks actually include sites on shallow alluvium as well as those on consolidated sediments. In this manner, the site classifications of Trifunac and Brady (1975) attempt to account for subsurface geological structure as well as conditions in the immediate vicinity of the site.

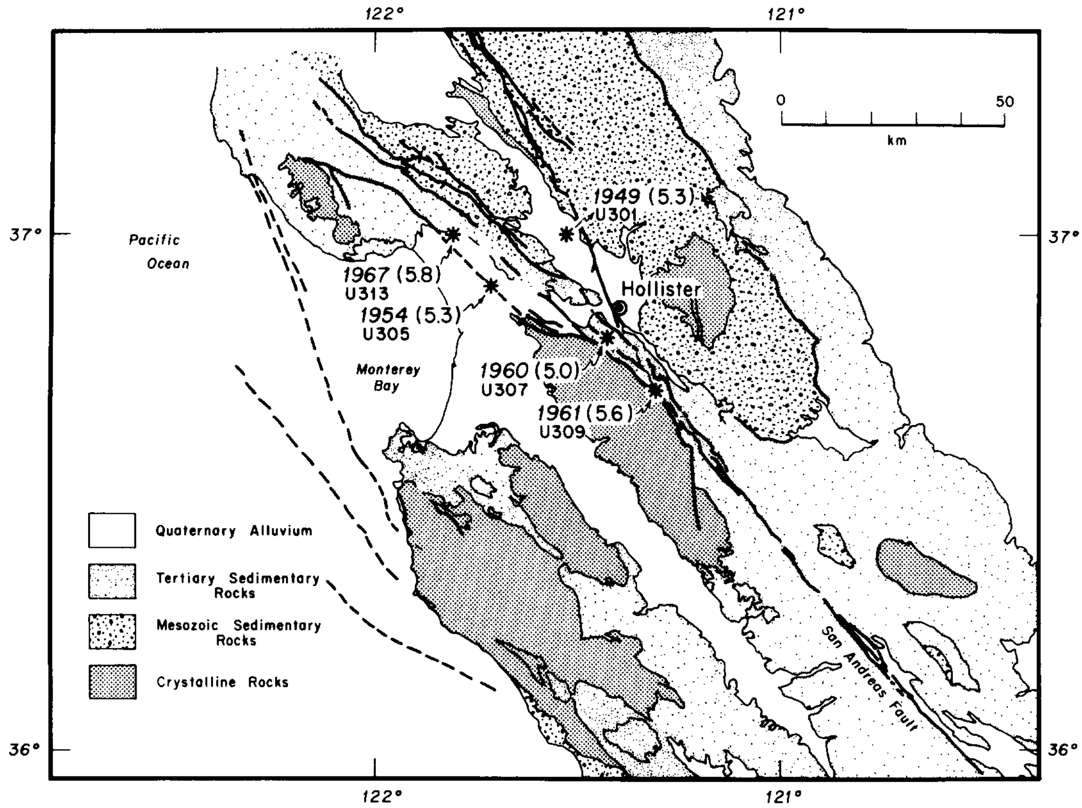

FIG. 7. Map of central California showing generalized geological features. Epicenters from Real *et al.* (1978) are identified with the same notation as in Figure 3 and represent earthquakes which have produced accelerograms on the Hollister accelerograph.

Trends in the raw data on Figure 11 resemble trends on Figure 9, except for a larger amount of scatter: κ tends toward a finite intercept and increases slowly with distance. The larger amount of scatter is predictable if a major contribution to κ results from a subsurface geologic structure effect, since subsurface geology is highly variable. Figure 11 also shows average values of κ over 10-km intervals and least-square linear regression through these averages. Numerical values of the regression lines between κ and R are in the figure caption. There is a factor of three difference between the slopes of these regressions for stations on alluvium and on rock. These differences result in part from different distance ranges involved in the regressions. Considering this and the scatter in the data, it is doubtful that the slope differences are significant. An observation which may be significant is that, averaged over the distance range to 70 km, stations on alluvium ($S = 0$) and consolidated sedimentary rock ($S = 1$) give indistinguishable values for κ while the values of κ for hard rock sites average about 25 per cent lower.

RESULTS: REGRESSIONS FOR FOURIER AMPLITUDE OF ACCELERATION

Spectral shapes which were obtained by the regressions of Trifunac (1976) and McGuire (1978) also show exponential decay with frequency. Discrete points at frequencies greater than 1 Hz from both regressions are illustrated in Figure 12 for a magnitude 6.5 earthquake at 25 and 100 km. For the Trifunac (1976) regression, the mean predicted spectra on soil conditions agree with exponential decay for frequencies from 2 to 15 Hz, and mean predicted spectra on rock conditions agree with exponential decay for frequencies from 5 to 15 Hz. The points at 25 Hz fall above the level consistent with exponential decay, but this may result from noise, as in some of the spectra shown in previous figures. The results from McGuire (1978), shown in Figure 13B, confirm this result. This regression indicates that exponential decay persists to frequencies of 20 Hz at 25 km and for rock sites at 100 km. The results by Trifunac (1976) at 25 km and at 100 km, and results of McGuire (1978) at 100 km anticipate the lower values of the spectral decay

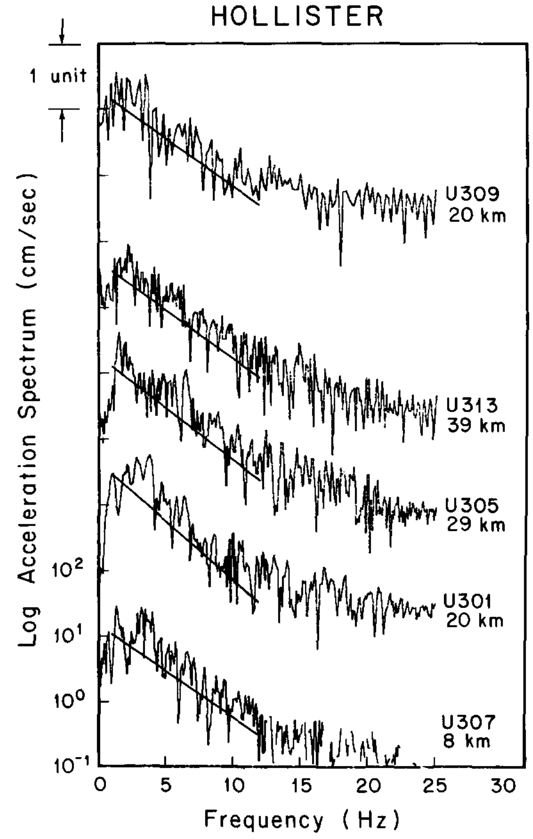

FIG. 8. S-wave acceleration spectra from Hollister site for earthquakes on Figure 7. Please refer to Figure 4 caption for other notation.

parameter on rock sites, as found in our study. The McGuire results for soil sites anticipate the observed increase of the spectral decay parameter with distance. Numerical values of spectral decay parameters for all lines on Figure 12 are between 0.077 and 0.090 sec, and are slightly higher than values which would have been anticipated based on our results. However, spectra studied by Trifunac and by McGuire were whole record spectra, while we used S-wave spectra.

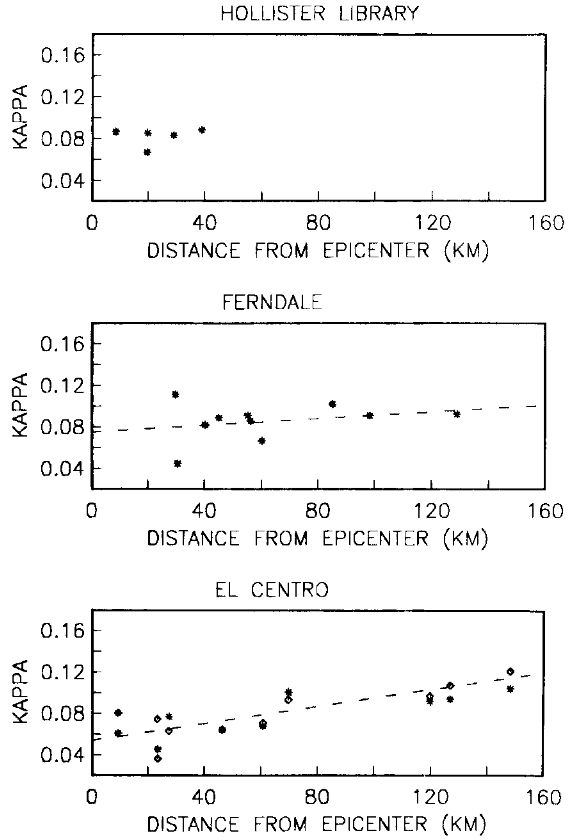

FIG. 9. Values of κ for frequency band 2- to 12-Hz derived from spectra in Figures 4, 6, and 8, shown as a function of distance. Data are also listed in Table 1. On El Centro plot, asterisk represents 180° component and diamond represents 270° component. Least-squares line through El Centro data, shown dashed, has equation κ = 0.054 sec + (0.00041 sec/km)R, where R is the distance from epicenter. Least-squares line through Ferndale data has the equation κ = 0.075 sec + (0.00016 sec/km)R.

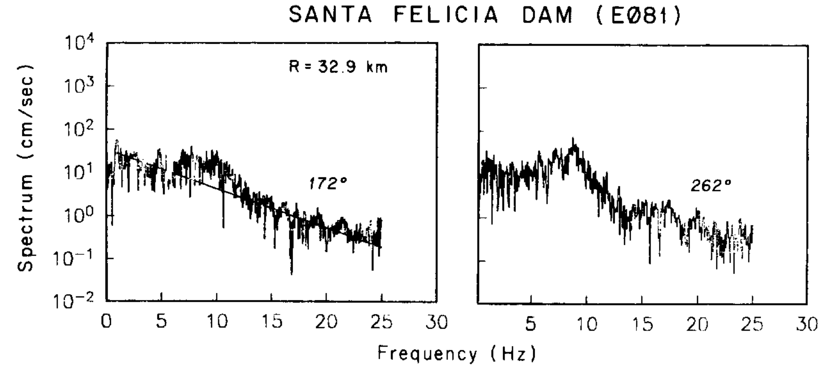

FIG. 10. S-wave acceleration spectra from Santa Felicia Dam for the San Fernando earthquake, showing a conspicuous site resonance superimposed on average linear trend.

These regressions suggest that exponential decay might be a general feature of the acceleration spectrum and not an artifact of the limited data set which we have studied in detail in the previous section.

A MODEL FOR THE OBSERVATIONS

Two alternative models have been proposed to explain the decay of the high frequencies in the strong motion acceleration spectrum, a phenomenon referred to by Hanks (1982) as "$f_{\max}$." Hanks (1982) leans toward a model in which high frequencies are generated at the seismic source, and in which attenuation, primarily caused by subsurface geological structure near the site, is responsible for the observed rapid decay of high frequencies. Papageorgiou and Aki (1983a, b) have proposed an alternative model in which the high frequency energy is not generated by the earthquake. The most straightforward explanation for the observations presented above is more in line with the Hanks (1982) model. If the S-wave displacement spectrum at the earthquake source has an ω^{-2} behavior at frequencies higher than the corner frequency (ω-square model), then attenuation within the earth is sufficient to explain the observations.

Hanks (1979) has reviewed some of the evidence for ω-square behavior and also argues that the strong motion spectra generally support this hypothesis. Modiano and Hatzfeld (1982) and Sipkin and Jordan (1980) have previously used these assumptions to study attenuation. One can define an attenuation time, t^*, for seismic phases which are modeled by rays as (Cormier, 1982)

$$t^* = \int \frac{dr}{Q_\beta(r)\beta(r)}, \tag{2}$$

and the amplitude spectrum of that phase is multiplied by the factor $e^{-\pi f t^*}$. In (2), $Q_\beta(r)$ is the spatial quality factor of shear wave attenuation, $\beta(r)$ is the shear velocity, and the integral in equation (2) is along the ray path. In general, Q_β is a function of both frequency and depth, and regional lateral variations have been observed. Converting the source spectral behavior to acceleration and incorporating the effect of attenuation leads to a spectral shape at high frequencies of

$$a(f) = A_0 e^{-\pi f t^*}. \tag{3}$$

If Q_β, and thus t^*, is independent of frequency, the effect of attenuation on an ω-square source spectrum will yield a spectral shape like equation (1).

In addition, to explain the observations, it is necessary to recognize that Q_β is a strong function of depth. The finite intercept of the trends of κ with distance (Figures 9 and 11) would then correspond to the attenuation which the S-waves all encounter in traveling through the subsurface geological structure to the surface of the earth, while the slope of the mean trend would correspond to the incremental attenuation due to predominantly horizontal propagation of S waves through the crust. Under this model, from Figures 9 and 11, attenuation caused by the subsurface geology appears to dominate the total contribution to attenuation to distances greater than 100 km.

Figure 13 illustrates several combinations of source spectral shapes and Q models. Figure 13A illustrates the ω-square spectrum behavior with four models for Q: $Q = \infty$, $Q = Q_0$, $Q = Q_1 f^1$, and $Q = Q_2 f^{0.5}$. The constants Q_1 and Q_2 are chosen so that for these two cases, $Q = Q_0$ at $f = 15$ Hz. Figure 13B illustrates the effects of the

TABLE 2

SPECTRAL DECAY PARAMETERS FOR ACCELEROGRAMS OF THE 9 FEBRUARY 1971 SAN FERNANDO, CALIFORNIA, EARTHQUAKE

Rec.	Dist. (km)	T	S	Kappa1	Peak Accel1	Kappa2	Peak Accel1	Rec.	Dist. (km)	T	S	Kappa1	Peak Accel1	Kappa2	Peak Accel2
041	9.1	10	2	0.04779	1054.9	0.04675	1148.1	157	42.5	12	0	0.06392	168.2	0.06008	116.1
048	22.4	15	0	0.08971	250.0	0.08817	131.7	166	30.8	9	1	0.05897	164.2	0.06264	147.6
051	42.8	8	0	0.05699	97.8	0.04631	122.7	171	139.8	17	1	0.08033	11.8	0.08143	16.2
054	41.9	8	0	0.06874	147.1	0.07277	117.0	176	42.9	12	0	0.05869	83.4	0.06363	115.7
056	28.6	8	1	0.07872	309.4	0.07011	265.4	179	70.7	4	1	0.03292	19.7	0.04108	49.1
057	37.1	9	0	0.09294	103.8	0.09059	148.2	180	84.3	20	0	0.08663	23.8	0.09352	29.7
058	37.1	9	0	0.06295	167.3	0.07219	207.0	183	70.8	15	1	0.05593	43.2	0.05558	56.5
059	39.8	8	0	0.07439	133.8	0.08040	147.1	184	70.8	16	1	0.06284	43.1	0.05887	57.2
062	42.8	13	0	0.06945	118.0	0.08282	130.3	185	75.6	13	1	0.08348	67.3	0.08348	67.3
065	40.0	8	1	0.09059	146.7	0.09140	155.7	186	54.1	15	0	0.08202	95.7	0.07542	96.8
068	35.0	9	0	0.07079	81.2	0.06168	98.0	187	72.1	14	0	0.06144	75.8	0.07842	56.2
071	86.0	12	0	0.03704	26.9	0.04829	25.5	188	38.9	13	0	0.06968	114.4	0.09352	126.8
072	39.5	8	1	0.05829	82.2	0.06585	115.0	191	67.8	19	1	0.10598	24.8	0.09711	40.1
075	40.1	9	0	0.08253	133.8	0.09279	111.8	192	40.7	12	1	0.04946	96.6	0.04525	98.7
078	42.5	9	1	0.05721	120.5	0.05418	189.2	195	122.6	32	0	0.08905	41.0	0.07996	30.9
081	32.9	14	1	0.06929	213.0	0.05894	198.3	196	75.4	17	0	0.09396	35.1	0.09873	31.2
083	40.0	10	0	0.07754	158.2	0.06231	161.9	197	185.7	20	0	0.08678	24.9	0.09462	34.8
086	49.4	10	0	0.07681	104.6	0.08803	80.5	198	34.0	12	2	0.05185	176.9	0.05022	167.4
087	88.5	15	0	0.08839	26.8	0.09448	28.2	199	42.0	15	0	0.05691	137.8	0.07081	238.6
088	34.1	8	1	0.07989	265.7	0.08978	209.1	204	73.8	23	0	0.08803	26.0	0.09242	20.8
089	44.0	13	0	0.06279	139.9	0.05830	139.0	205	73.6	28	0	0.09799	28.4	0.06009	28.1
092	43.1	9	1	0.05726	64.2	0.05475	79.1	206	108.2	20	0	0.08964	37.4	0.09389	44.1

095	37.4	13	0	0.06588	96.2	0.07290	83.9	207	32.8	15	2	0.06582	65.1	0.05861	97.1
098	42.7	12	0	0.05991	236.4	0.05312	192.0	208	133.4	23	1	0.08385	16.5	0.07659	17.1
101	107.6	10	0	0.09088	36.5	0.08744	29.6	210	151.4	13	0	0.06873	35.0	0.07366	39.2
102	68.5	10	2	0.05820	25.4	0.06617	21.8	214	36.2	10	1	0.07142	154.1	0.07251	156.3
103	45.4	12	0	0.04756	91.5	0.05441	120.5	217	40.0	12	0	0.08231	108.3	0.07307	88.2
104	52.2	10	1	0.07579	85.1	0.07952	103.1	220	95.8	17	1	0.09462	24.2	0.08869	34.3
105	38.7	12	0	0.07762	83.1	0.06872	77.6	221	43.3	13	2	0.04982	137.7	0.03745	165.8
106	36.1	12	2	0.05605	87.4	0.07842	188.7	222	79.3	20	0	0.09132	25.9	0.09792	25.2
107	39.8	14	0	0.05036	93.5	0.07150	107.1	223	65.0	15	2	0.08436	69.7	0.07586	53.9
108	39.8	15	0	0.08341	198.1	0.09623	181.4	231	51.7	16	0	0.06543	41.2	0.06607	37.9
110	31.5	13	1	0.05216	207.9	0.03243	138.9	233	29.3	13	0	0.06690	243.3	0.04534	197.3
112	42.5	10	0	0.04680	78.7	0.04438	101.9	236	34.9	14	0	0.06931	122.4	0.05461	167.1
114	32.3	13	0	0.06990	110.8	0.07417	136.1	239	38.4	15	0	0.06180	119.4	0.07469	161.6
115	29.3	12	0	0.07373	220.5	0.08605	146.0	241	41.8	15	1	0.05381	86.9	0.06607	137.8
118	50.2	17	0	0.08048	33.7	0.07432	32.6	244	41.9	15	1	0.07240	149.1	0.07886	126.9
121	43.1	13	0	0.05157	119.5	0.04509	112.2	246	35.7	13	0	0.05526	115.9	0.06757	107.1
124	76.2	16	0	0.09689	35.2	0.08517	34.5	248	35.7	13	0	0.06393	184.0	0.06155	174.2
128	37.1	13	0	0.05878	60.9	0.06735	91.6	249	39.2	15	0	0.05755	80.0	0.06029	84.1
131	38.2	14	0	0.07476	184.3	0.09228	160.5	251	41.8	12	1	0.07960	195.7	0.08319	188.2
134	38.9	13	0	0.06123	97.8	0.05604	82.1	253	42.0	15	0	0.06888	220.8	0.06031	242.0
137	29.0	13	0	0.04750	140.2	0.04027	128.9	255	38.9	12	1	0.08018	124.1	0.07505	128.4
141	29.6	8	2	0.07200	145.5	0.05393	108.6	258	44.6	16	0	0.06178	56.1	0.05408	83.1
142	26.8	7	2	0.03432	168.1	0.04046	143.5	261	39.6	10	0	0.05781	98.0	0.06025	107.9
143	26.6	6	2	0.02957	119.3	0.01954	109.4	262	39.0	14	1	0.09000	68.5	0.08231	93.9
144	23.3	7	1	0.06374	346.2	0.05216	277.9	265	39.9	15	1	0.06550	104.2	0.05625	125.3
145	24.9	12	0	0.08011	113.9	0.07637	103.9	266	40.0	15	0	0.05469	153.5	0.06297	129.8
148	39.9	12	1	0.06003	107.6	0.06183	112.1	267	52.0	18	0	0.05696	55.4	0.06615	61.5

same four attenuation models for a source with a displacement spectrum displaying ω^{-3} behavior (ω-cubed model). Figure 13C is for a source with ω-square behavior out to a second corner frequency $f_{\max}$; at higher frequencies the behavior is ω^{-6}. (Boore, 1983; Hanks, 1982). Among these combinations only the model with an ω^{-2} displacement spectrum falloff and constant Q gives the spectral trend which is modeled by equation (1). However, over finite frequency bands, the other models closely approximate exponential decay in some cases. The ω-cubed model with frequency-dependent Q is dominated by the attenuation effect at frequencies above about 5 Hz. Below 5 Hz, however, this model diverges to a level considerably above an exponential trend in contrast to data which if anything diverge below the exponential trend. The *ad hoc* model with the second corner frequency, $f_{\max}$, is also below the exponential trend at low frequencies, but $f_{\max}$ would then be estimated to be around 5 Hz or less, rather than 10 to 15 Hz as has been suggested by Hanks (1982) and Boore (1983). Figure 13 also illustrates that if Q is proportional to f, attenuation does not affect the spectral decay parameter κ. If the dependence of Q on f is some power of f less than 1 along part of the path, then the spectral shape

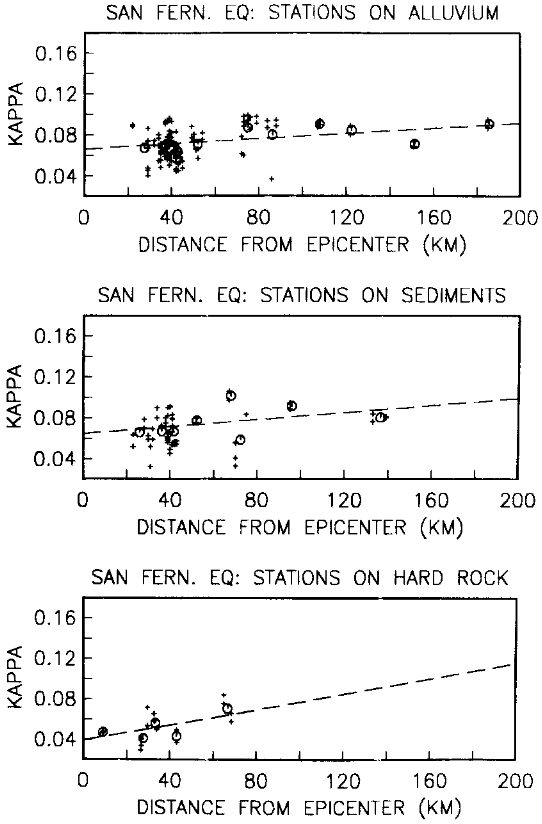

FIG. 11. Values of κ (small "+") for the frequency band 2 to 18 Hz derived from both components of San Fernando earthquake accelerograms. Data are listed in Table 2. Stations are classified as alluvium, consolidated sediments, or hard rock as in Trifunac and Brady (1975). Larger circles are at average values of both κ and distance (R) for 10-km intervals. Least-squares lines (dashed) have the following equations

alluvium $\kappa = 0.066 \text{ sec} + (0.000126 \text{ sec/km}^{-1})R$
consolidated sediments $\kappa = 0.065 \text{ sec} + (0.000172 \text{ sec/km}^{-1})R$
rock $\kappa = 0.040 \text{ sec} + (0.000380 \text{ sec/km}^{-1})R$

may not be easily resolvable from an exponential decay. For example, if the source model is ω-square, an attenuation model with $Q \sim f^{0.25}$ (e.g., Thouvenot, 1983) would closely approximate pure exponential decay. If Q_β depends on frequency along any part of the path, then κ is not exactly t^*.

Wave propagation phenomena may also be playing a role in the determination of κ. As examples, Heaton and Helmberger (1978) have shown a theoretical example of the way plane layering and differences in the earthquake source depth can cause the spectrum to be perturbed. Correlations by Trifunac (1976) and by McGuire (1978) indicate the presence of soil amplification at low frequencies. Results by Liu (1983) suggest that the low-frequency amplification observed in alluvial valleys during the San Fernando earthquake may be a result of excitation of surface waves by the S waves incident on intervening ridges. Such phenomena are probably not sufficiently universal to explain our observations, but they probably contribute to the scatter, particularly in Figure 11. The dependence of κ on distance undoubtedly is influenced by multiple S-wave arrivals (Richter, 1958) with differing paths through the crust.

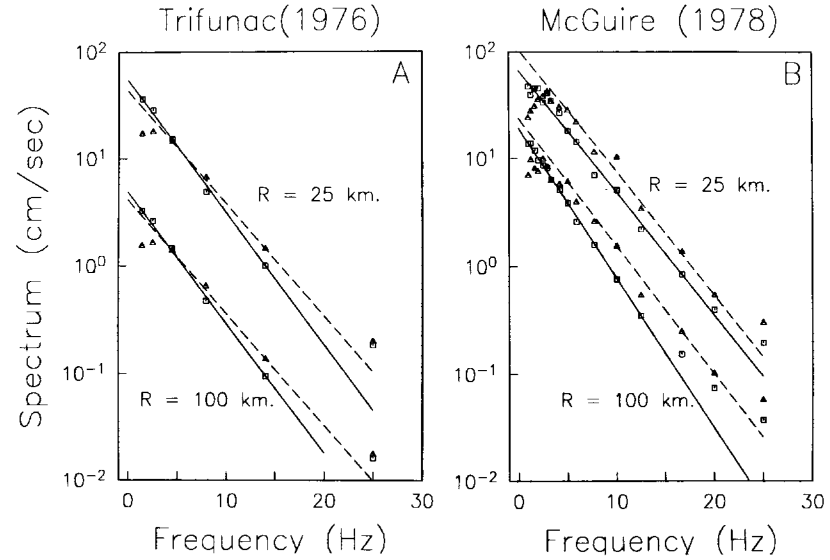

FIG. 12. (A) Discrete points are mean Fourier spectral amplitudes for a magnitude 6.5 earthquake from the regression of Trifunac (1976) at frequencies greater than 1 Hz. Lines are shown to illustrate the extent of agreement of regression points with exponential decay of the spectrum with frequency. Squares and solid lines apply to soil sites; triangles and dashed lines apply to rock sites. (B) Equivalent of (A) for the regression of McGuire (1978).

Papageorgiou and Aki (1983b) have applied several alternative models to extrapolate observations of strong motion back to the source of five earthquakes. The source models which they obtain fall off at high frequencies relative to the ω-square model. However, we do not consider that these results are sufficient to invalidate the ω-square model. If, as this paper and as Hanks (1982) have inferred, there is a highly attenuating zone near the surface, this zone will introduce a systematic effect which is not removed by the extrapolation to zero epicentral distance employed by Papageorgiou and Aki (1983a, b). For example, we observe that for the San Fernando earthquake, the source spectra derived by Papageorgiou and Aki (1983b) are consistent with exponential decay. For the attenuation model which they describe by "Q_β = free", all points on the source amplitude spectrum are within 25 per cent of an exponentially decaying shape characterized by $\kappa = 0.063$ sec. Numerically, this coincides with the intercept of our linear approximations to κ as a function of distance for that earthquake for sites on alluvium (0.066 sec) and sedimentary rock (0.065 sec). This verifies that the same feature of the data which we suggest is caused by vertical propagation through shallow layers is explained by Papageorgiou and Aki as a source effect.

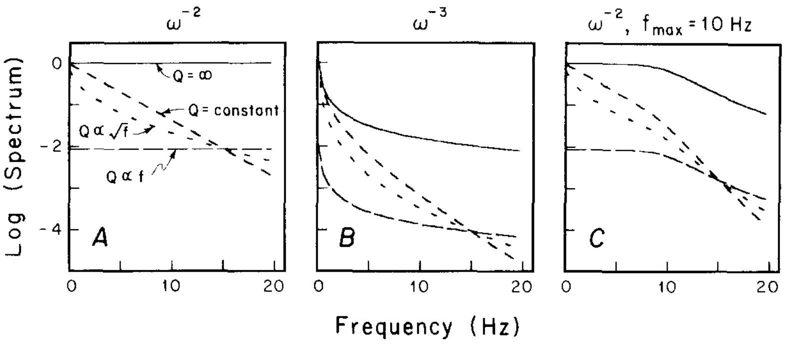

FIG. 13. Idealized acceleration spectral shapes at an accelerograph site for three source-spectral models and various attenuation models. The source spectra are described, following tradition, by falloff at high frequencies on a displacement spectrum. Thus ω^{-2} models yield a constant acceleration spectrum (A) and ω^{-3} models yield an acceleration spectrum with ω^{-1} falloff (B). Source model on right (C) consists of ω^{-2} model, but with a second corner at 10 Hz, and ω^{-4} falloff in acceleration at frequencies higher than the second corner. Attenuation models are no attenuation ($Q = \infty$), constant Q attenuation, attenuation with $Q \propto f$, and with $Q \propto f^{1/2}$.

COMPARISON WITH MODELS FOR Q IN THE CRUST

As discussed previously, it is possible to explain our observations with an ω-square source and an earth model with low, frequency-independent Q in the shallow crust. However, our model must be consistent with other recent observations that seem to show that Q depends on frequency at greater depths within the earth (e.g., Sipkin and Jordan, 1980; Aki, 1980; Singh *et al.*, 1982; Papageorgiou and Aki, 1983a, b; Dwyer *et al.*, 1983). One plausible explanation would be to appeal to models in which Q is separated into two components

$$\frac{1}{Q} = \frac{1}{Q_i} + \frac{1}{A_s f} \tag{4}$$

where the terms Q_i and $Q_s = A_s f$ represent attenuation caused by different physical mechanisms (e.g., Dainty, 1981; Rovelli, 1982). If this is true, our method would only detect the term in $1/Q_i$, and the dependence of Q_i on depth would be adjusted to fit our observations. Another possible explanation is that the frequency dependence of Q is also a function of depth (Lundquist and Cormier, 1980; Singh *et al.*, 1982). If Q is independent of frequency in the shallow crust, which dominates the attenuation of direct S waves at the distances employed in this study, then a frequency-dependent contribution to Q at depths greater than, say, 5 km would not cause a large perturbation to the exponential trend which dominates these data. In this case t^*, as a function of frequency, would be nearly equal to κ for frequencies and distances at which the shallow attenuation dominates. Of course, our analysis procedure did not allow for detection of possible frequency dependence. On these data, digitization noise could cause the same type of perturbation as frequency dependence in Q, and therefore, since our noise levels are somewhat uncertain, interpretation of a frequency dependent perturbation to the dominant exponential trend would be unreliable.

There is some independent evidence, obtained in conjunction with seismic exploration techniques, indicating that Q is independent of frequency in the shallow crust. These studies consist of *in situ* measurements of attenuation which have employed shallow artificial sources and vertical arrays of seismometers mounted in drill holes (vertical-seismic profiles). Several studies which have concluded that Q is independent of frequency from *in situ* measurements are cited by Knopoff (1964). Additional studies which reach this conclusion include Tullos and Reid (1969), Hamilton (1972; 1976), Ganley and Kanasewich (1980), and Hauge (1981). In general, these studies have concentrated on attenuation of P waves, but McDonal *et al.* (1958) conclude that both Q_α and Q_β are independent of frequency in the Pierre Shale formation, Colorado. Frequencies considered in these studies have generally been broadband, somewhat higher (e.g., 20 to 400 Hz) than the strong-motion frequencies which we are considering. Studies which have attempted to separate the contributions from dissipation and from dispersion due to layering have concluded that dispersion is variable and sometimes important (e.g., Schoenberger and Levin, 1978), but that dissipation always makes a significant contribution (Schoenberger and Levin, 1978; Ganley and Kanasewich, 1980; Hauge, 1981; Spencer *et al.*, 1982).

Several studies, most of which employ downhole sensors have also obtained results for the attenuation as a function of depth in the shallow crust. McDonal *et al.* (1958) estimated that attenuation between the depths of 250 and 750 feet was three times as rapid as the average over the entire depth range to 4000 feet. Tullos and Reid (1969) found severe attenuation (corresponding to $Q_\alpha \sim 2$) over the depth range 1 to 10 feet in Gulf Coast sediments, but attenuation was 1 to 2 orders of magnitude less severe at depths from 10 to 100 feet. Hamilton (1976) has summarized attenuation measurements as a function of depth in sea-floor sediment. These data show a trend toward less attenuation at greater depths, but also a considerable dependence on lithology, and Hamilton suspected that lithology differences caused the overall trend of the data. Wong *et al.* (1983) find that attenuation is highly variable in the depth range 100 to 350 m of a granite pluton in Manitoba, but the overall trend is an order of magnitude decrease in attenuation rate between the top and the bottom of the hole. Thouvenot (1983) finds that Q_α increases from 40 near the surface to 600 at 7 km depth in a granite terrane in central France. Joyner *et al.* (1976) found that $Q_\beta \approx 16$ applies to the upper 186 m of sediments for a site near San Francisco Bay, and Kurita (1975) found $Q_\beta \approx 20$ for the upper crust northeast of the San Andreas fault near Hollister. Barker and Stevens (1983) found that Q_β increases rapidly with depth in the upper 50 m of sediments at three sites near El Centro in the Imperial Valley of California. A low Q surface layer for both P- and S-waves is evidently a typical, if not universal, phenomenon.

In summary, the seismic exploration results are consistent with a model that κ is closely related to t^*, and that the intercept of the trend of κ with distance is a result of relatively intense attenuation experienced by the propagation of seismic waves through subsurface geological structure below each station. This also appears to be reasonable based on the agreement of observed values of κ and calculated values of t^* based on velocity profiles and Q models. At Hollister, taking $Q = 20$ (Kurita, 1975), in conjunction with P-wave velocity models for the shallow crust northeast of the San Andreas fault in central California (e.g., Eaton *et al.*, 1970; Mayer-Rosa, 1973) and assuming Poisson's ratio is 0.25, equation (2) gives t^* between 0.088 and

0.091 sec for the upper 4 to 5 km. This range is only slightly higher than typical values of κ, about 0.085 sec, which were determined for Hollister. At El Centro, assuming κ is t^*, the intercept (Figure 9) gives $t^* = 0.054$ sec. Singh *et al.* (1982) found $t^* = 0.049$ sec for the shallow crust in the Imperial Valley and an ω-square model. These correspond to an average $Q_\beta \approx 30$ distributed over a sediment thickness of 3.8 km, using the velocity model given by curve 17 of Fuis *et al.* (1982). The slope of the least-squares line with distance, 0.00041 sec/km, corresponds to an average $Q_i \approx 800$ for shear waves below the sediments if Q is decomposed by equation (4). The slope of the least-squares line through the Ferndale data (0.00016 sec/km) suggests an average $Q_i \approx 2000$ below the high attenuation zone near the surface.

The values of κ derived for San Fernando accelerograms might suggest that the picture is not quite so simple. We observe first that if the dominant contribution to κ is from subsurface geology near the site but the increase of κ with distance is a result of propagation at depth, then one would not expect the subsurface geology to affect the slope of the relationship between κ and R. By this inference, the possibly different slopes which are derived for different types of site conditions would have to result from sample differences. It was pointed out previously that this may be the case. We notice that the slope is greatest for rock sites which are only represented at relatively short distances, while the slope is smallest for alluvium sites which are represented to the greatest distances. These observations suggest the possibility that the slope, $d\kappa/dR$, is a decreasing function of distance. There is no theoretical reason for $d\kappa/dR$ to be independent of distance, and our linear regressions were intended only to illustrate general trends. It may be possible to invert κ and $d\kappa/dR$ as a function of distance to derive Q_i as a function of depth. The average slopes shown in Figure 11 correspond to Q_i greater than 1000 at depth.

A visual survey of the spectra which we have employed does allow the possibility that a frequency dependence in Q at depth contributes to the spectral shape at low frequencies ($f < f_E \approx 5$ Hz). Such frequency dependence might cause some spectra to appear flat or to increase with frequency at these lowest frequencies. We have indicated previously that a deviation from exponential decay might be present in Figures 1 and 2 at $f < 5$ Hz. This frequency band might instead be characterized by the source spectrum not yet approaching its asymptotic ω-square form due to a complex source mechanism which introduces a second corner frequency (e.g., Joyner, 1984). A thorough study focused on these frequencies seems appropriate. A model in which Q is strictly proportional to frequency at all depths would seem to be ruled out, however, since such a model is not consistent with the observed increase of κ with distance.

RELATIONSHIP TO $f_{\max}$

We have designated the observational range of validity of equation (1) as $f > f_E$, where f_E is a label for the low frequency limit of agreement. On some spectra f_E is closely related to f_0 while in others it seems to be a conspicuous feature occurring at a distinctly larger frequency than f_0, Where f_0 and f_E differ significantly, the processes which dominate the spectrum between f_0 and f_E remain to be determined.

The frequency f_E is distinguishably smaller than $f_{\max}$. $f_{\max}$ is recognized on log-log axes as a frequency above which spectral amplitudes appear to diminish abruptly. For California accelerograms from moderate- to large-sized earthquakes, f_E is generally less than 5 Hz (examples are in Figures 1, 2, 4, 6, and 8) while $f_{\max}$ generally occurs in the frequency band 10 to 20 Hz (Hanks, 1982). $f_{\max}$, in the sense used by Hanks, has been employed as an integration limit to derive root-mean-square acceleration from a parametric model for the acceleration spectrum (Hanks, 1979; McGuire and Hanks, 1980; Hanks and McGuire, 1981; Boore, 1983). To preserve this function $f_{\max}$ needs to be at a frequency where the spectral trend has fallen to a value of the order of 0.1 to 0.3 of its peak. This implies that $f_{\max} \approx$ constant/κ or perhaps $f_{\max} \approx f_E +$ constant/κ where the constant is on the order of 0.2 to 0.7 depending on the shape of the spectrum. If $f_{\max}$ is chosen in this manner, the mathematical properties of the exponential curve make the spectrum observationally indistinguishable from a constant for frequencies greater than f_E but less than some fraction, on the order of 0.2 to 0.5, of $f_{\max}$.

As recognized on the source spectra which have been derived by Papageorgiou and Aki (1983a, b), $f_{\max}$ is generally smaller, with numerical values between 2.5 and 5 Hz. Thus, this usage of $f_{\max}$ is consistent with the frequency range found for f_E on some spectra. However, our interpretations are opposite. While Papageorgiou and Aki (1983a, b) suggest that the source acceleration spectrum is a constant for $f < f_{\max}$ and falls off above $f_{\max}$, our interpretation is that the source spectrum is a constant for $f > f_E$, but may not be constant for f between f_0 and f_E.

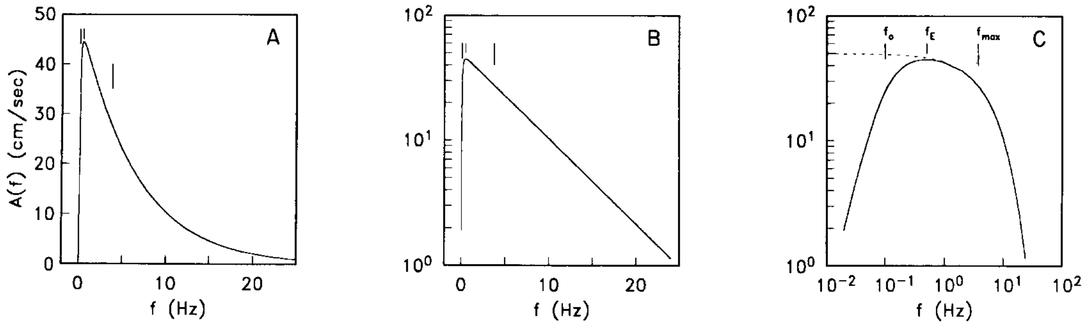

FIG. 14. A particular spectral shape plotted on three types of axes. Fiducials identify f_0, f_E, and $f_{\max}$ in each frame.

Figure 14 shows a Brune (1970) spectrum modified by exponential decay at all frequencies

$$a(f) = (\text{constant}) \frac{f^2}{1 + \left(\dfrac{f}{f_0}\right)^2} e^{-\pi\kappa f}. \tag{5}$$

In Figure 14, the parameters which have been employed are $f_0 = 0.1$ Hz and $\kappa = 0.05$ sec. Figure 14A uses algebraic axes, 14B uses semi-logarithmic axes, and 14C uses logarithmic axes. An exponential function, starting at $f = 0$ and with the same high-frequency asymptote, is shown as a dashed line in Figure 14C. In 14B, the frequency f_E is recognized by a deviation from the straight line defined at higher frequencies. In 14C, $f_{\max}$ is picked according to the convention described above: the integral from 0 to $f_{\max}$ of a constant spectrum with amplitude equal to the peak of this spectrum gives the same value of a_{rms} as the spectrum plotted in Figure 14. Qualitative picks of $f_{\max}$ as the corner of the exponential curve may differ from the value shown. At the value of f_E shown, the spectrum described by equation (5) differs from the exponential curve by about 4 per cent.

For spectra described by (5), f_E is related to f_0. For more complex spectra, such as the two-corner source spectra proposed by Joyner (1984), a direct relationship no longer exists.

CONCLUSIONS

At high frequencies, the Fourier acceleration spectrum of S waves decays exponentially in a majority of existing California accelerograms. The spectral decay parameter, κ, was defined in equation (1), and a study of its properties was pursued in this paper. The principal features of the spectral decay parameter are: (1) it can be used to describe the shape of the Fourier amplitude spectrum of acceleration in the frequency band from ~2 Hz to at least 20 Hz; (2) it seems to be primarily an effect caused by subsurface geological structure near the site because it is only a weak function of distance; and (3) it seems to be smaller on rock sites than on sites of less competent geology. These observations suggest that the spectral decay parameter is related to attenuation within the earth, and that all of the earthquake sources employed for our study produce the same asymptotic behavior of the spectral shape at high frequencies.

We have attributed deviations from a trend of exponential decay at high frequencies to two sources, broadband site resonances and noise. The obvious site resonances, such as in Figure 10, appear on about 10 per cent of the San Fernando accelerograms. Weaker resonances may add some noise to determinations of κ. Figure 2 shows a clear example of the effect of digitization noise on the spectrum, and we have inferred that spectra in Figures 4, 6, and 8 approach a level trend because of digitization or instrumental noise. At low frequencies, it is possible that frequency dependence in Q is also causing a deviation from the exponential decay on some records.

Our model for the origin of the spectral decay parameter envisions a frequency-independent contribution to the attenuation parameter Q which modifies the shape of source displacement spectrum obeying an ω^{-2} asymptotic behavior at high frequencies. The dominant contribution to κ would be attenuation close to the accelerograph site; this contribution is less severe for more competent site geologies. There is also a small incremental attenuation which results from lateral propagation in the crust. This attenuation mechanism implies that the source spectrum is modified by $e^{-\pi\kappa f}$ at low frequencies ($f < f_E$) also, but that other processes dominate the shape. Based on the data presented in this paper, we cannot rule out a hybrid model in which the spectrum falls off due to both source and attenuation effects, but significantly smaller values of κ will be forthcoming from sites on more competent rock than those studied here. Thus, future studies of this type will eventually place constraints on the extent to which the source spectrum deviates from the ω-square model.

Several research topics remain to be addressed. These include the relationship of κ to site geology including research into nonlinear effects, studies to reduce scatter about attenuation equations, and elaboration of the relationship between κ and attenuation including possible inversion of κ-distance observations for attenuation as a function of depth.

ACKNOWLEDGMENTS

K. Aki, J. E. Luco, O. W. Nuttli, and M. Reichle provided helpful critical reviews of this manuscript. We thank T. C. Hanks for calling our attention to the article by Berrill and Hanks, as well as for a thoughtful review of the manuscript. We also wish to acknowledge helpful discussions with J. N. Brune, T. H. Heaton, A. H. Olson, and D. M. Boore. P. Bodin provided much assistance in gathering information for this study. This research was supported by National Science Foundation Grant CEE 81-20096.

REFERENCES

Aki, K. (1980). Attenuation of shear-waves in the lithosphere for frequencies from 0.05 to 25 Hz, *Phys. Earth Planet. Interiors* **21,** 50-60.

Anderson, J. G. (1984). The 4 September 1981 Santa Barbara Island, California, earthquake: interpretation of strong motion data, *Bull. Seism. Soc. Am.* **74,** 995-1010.

Anderson, J. G., J. Prince, J. N. Brune, and R. S. Simons (1982). Strong motion accelerograms, in J. G. Anderson and R. S. Simons, Editors, The Mexicali Valley Earthquake of 9 June 1980, *Newsletter Earthquake Eng. Res. Inst.* **16,** 79-83.

Barker, T. G. and J. L. Stevens (1983). Shallow shear wave velocity and Q structures at the El Centro strong motion accelerograph array, *Geophys. Res. Letters* **10,** 853-856.

Berrill, J. B. (1975). A study of high-frequency strong ground motion from the San Fernando earthquake, *Ph.D. Thesis*, California Institute of Technology, Pasadena, California.

Berrill, J. B. and T. C. Hanks (1974). High frequency amplitude errors in digitized strong motion accelerograms, in *Analysis of Strong Motion Earthquake Accelerograms*, volume IV—Fourier Amplitude Spectra, Parts Q, R, S—Accelerograms IIQ 233 through IIS 273, Report EERL 74-104, Earthquake Engineering Research Laboratory, California Institute of Technology, Pasadena, California.

Bodle, R. R. (1944). *United States Earthquakes 1942*, Serial 662, U.S. Dept. of Commerce, Coast and Geodetic Survey, Washington, D.C.

Boore, D. M. (1983). Stochstic simulation of high frequency ground motions based on seismological models of the radiated spectra, *Bull. Seism. Soc. Am.* **73,** 1865-1894.

Brune, J. N. (1970). Tectonic stress and the spectra of seismic shear waves from earthquakes, *J. Geophys. Res.* **75,** 4997-5009.

Cormier, V. F. (1982). The effect of attenuation on seismic body waves, *Bull. Seism. Soc. Am.* **72,** S169-S200.

Dainty, A. M. (1981). A scattering model to explain seismic Q observations in the lithosphere between 1 and 30 Hz, *Geophys. Res. Letters* **8,** 1126-1128.

Dobrin, M. B. (1960). *Introduction to Geophysical Prospecting*, 2nd ed., McGraw-Hill, New York, 446 pp.

Dwyer, J. J., R. B. Hermann, and O. W. Nuttli (1983). Spatial attenuation of the L_g wave in the central United States, *Bull. Seism. Soc. Am.* **73,** 781-796.

Earthquake Engineering Research Laboratory (1971). Strong Motion Earthquake Accelerograms Volume II—Corrected accelerograms and integrated ground velocity and displacement curves, Report EERL 71-50, California Institute of Technology, Pasadena, California.

Eaton, J. P., M. E. O'Neill, and J. N. Murdock (1970). Aftershocks of the 1966 Parkfield-Cholame, California, earthquake: a detailed study, *Bull. Seism. Soc. Am.* **60,** 1151-1197.

Fuis, G. S., W. D. Mooney, J. H. Healey, G. A. McMechan, and W. J. Lutter (1982). Crustal structure of the Imperial Valley region, in The Imperial Valley, California, earthquake of October 15, 1979, *U.S. Geol. Surv. Profess. Paper 1254*, 25-50.

Ganley, D. C. and E. R. Kanasewich (1980). Measurement of absorption and dispersion from check shot surveys, *J. Geophys. Res.* **85,** 5219-5226.

Hamilton, E. L. (1972). Compressional-wave attenuation in marine sediments, *Geophysics* **37,** 620-646.

Hamilton, E. L. (1976). Sound attenuation as a function of depth in the sea floor, *J. Acoust. Soc. Am.* **59,** 528-535.

Hanks, T. C. (1975). Strong ground motion of the San Fernando, California, earthquake: ground displacements, *Bull. Seism. Soc. Am.* **65,** 193-226.

Hanks, T. C. (1979). b-values and $\omega^{-\gamma}$ seismic source models: implications for tectonic stress variations along active crustal fault zones and the estimation of high-frequency strong ground motion, *J. Geophys. Res.* **84,** 2235-2242.

Hanks, T. C. (1982). $f_{\max}$, *Bull. Seism. Soc. Am.* **72,** 1867-1880.

Hanks, T. C. and R. K. McGuire (1981). The character of high-frequency strong ground motion, *Bull. Seism. Soc. Am.* **71,** 2071-2096.

Hauge, P. S. (1981). Measurements of attenuation from vertical seismic profiles, *Geophysics* **46,** 1548-1558.

Heaton, T. H. and D. V. Helmberger (1978). Predictability of strong ground motion in the Imperial Valley: modeling the M 4.9, November 4, 1976 Brawley earthquake, *Bull. Seism. Soc. Am.* **68,** 31-48.

Hileman, J. A., C. R. Allen, and J. M. Nordquist (1973). *Seismicity of the southern California region.* 1 January 1932 to 31 December 1972, Seismological Laboratory, California Institute of Technology, Pasadena, California.

Jennings, C. W. (1975). *Fault Map of California*, Map No 1, Faults, Volcanos, Thermal Springs and Wells, California Division of Mines and Geology, Sacramento, California.

Joyner, W. B. (1984). A scaling law for the spectra of large earthquakes, *Bull. Seism. Soc. Am.* **74,** 1167-1188.

Joyner, W. B., R. E. Warrick, and A. A. Oliver, III (1976). Analysis of seismograms from a downhole array in sediments near San Francisco Bay, *Bull. Seism. Soc. Am.* **66,** 937-958.

Knopoff, L. (1964). *Q*, *Rev. Geophys.* **2,** 625-660.

Kurita, T. (1975). Attenuation of shear waves along the San Andreas fault zone in central California, *Bull. Seism. Soc. Am.* **65,** 277-292.

Leeds, A. (1979). The locations of the 1954 northern Baja California earthquake, *Masters Thesis*, University of California at San Diego, La Jolla, California.

Liu, H.-S. (1983). Interpretation of near-source ground motion and implications, *Ph.D. Thesis*, California Institute of Technology, Pasadena, California, 184 pp.

Lundquist, G. M. and V. C. Cormier (1980). Constraints on the absorption band model of *Q*, *J. Geophys. Res.* **85,** 5244-5256.

Mayer-Rosa, D. (1973). Travel-time anomalies and distribution of earthquakes along the Calaveras fault zone, California, *Bull. Seism. Soc. Am.* **63,** 713-729.

McDonal, F. J., F. A. Angona, R. L. Mills, R. L. Sengbush, R. G. Van Nostrand, and J. E. White (1958). Attenuation of shear and compressional waves in Pierre Shale, *Geophysics* **23,** 421-439.

McGuire, R. K. (1978). A simple model for estimating Fourier amplitude spectra of horizontal ground acceleration, *Bull. Seism. Soc. Am.* **69,** 803-822.

McGuire, R. K. and T. C. Hanks (1980). RMS accelerations and spectra amplitudes of strong ground motion during the San Fernando, California, earthquake, *Bull. Seism. Soc. Am.* **70,** 1907-1919.

Modiano, T. and D. Hatzfeld (1982). Experimental study of the spectra content for shallow earthquakes, *Bull. Seism. Soc. Am.* **72,** 1739-1758.

Murphy, L. M. and F. P. Ulrich (1951a). *United States Earthquakes 1948*, U.S. Dept. of Commerce, Serial 746, Coast and Geodetic Survey, Washington, D.C.

Murphy, L. M. and F. P. Ulrich (1951b). *United States Earthquakes 1949*, Serial 748, U.S. Dept. of Commerce, Coast and Geodetic Survey, Washington, D.C.

Murphy, L. M. and W. K. Cloud (1954). *United States Earthquakes 1952*, Serial 773, U.S. Dept. of Commerce, Coast and Geodetic Survey, Washington, D.C.

Murphy, L. M. and W. K. Cloud (1955). *United States Earthquakes 1953*, U.S. Dept. of Commerce, Coast and Geodetic Survey, Washington, D.C.

Papageorgiou, A. S. and K. Aki (1983a). A specific barrier model for the quantitative description of inhomogeneous faulting and the prediction of strong ground motion. Part I. Description of the model, *Bull. Seism. Soc. Am.* **73,** 693-722.

Papageorgiou, A. S. and K. Aki (1983b). A specific barrier model for the quantitative description of inhomogeneous faulting and the prediction of strong ground motion. Part II. Applications of the model, *Bull. Seism. Soc. Am.* **73,** 953-978.

Real, C. R., T. R. Toppozada, and D. L. Parke (1978). *Earthquake Epicenter Map of California*, Map Sheet 39, California Division of Mines and Geology, Sacramento, California.

Richter, C. F. (1958). *Elementary Seismology*, W. H. Freeman and Co., San Francisco, California.

Rovelli, A. (1982). On the frequency dependence of *Q* in Friuli from short-period digital records, *Bull. Seism. Soc. Am.* **72,** 2369-2372.

Sacks, I. S. (1980). Mantle *Q* from body waves—Difficulties in determining frequency dependence, (abstract), *EOS*, *Trans. Am. Geophys. Union* **61,** 299.

Schoenberger, M. and F. K. Levin (1978). Apparent attenuation due to intrabed multiples. II. *Geophysics* **43,** 730-737.

Singh, S. K., R. J. Apsel, J. Fried, and J. N. Brune (1982). Spectral attenuation of *SH* waves along the Imperial fault, *Bull. Seism. Soc. Am.* **72,** 2003-2016.

Sipkin, S. A. and T. H. Jordan (1980). Regional variation of Q_{ScS}, *Bull. Seism. Soc. Am.* **70,** 1071-1102.

Spencer, T. W., J. R. Sonnad, and T. M. Butler (1982). Seismic *Q* Stratigraphy or dissipation, *Geophysics* **47,** 16-24.

Thouvenot, F. (1983). Frequency dependence of the quality factor in the upper crust: a deep seismic sounding approach, *Geohys. J. R. Astr. Soc.* **73,** 427-447.

Trifunac, M. D. (1976). Preliminary empirical model for scaling Fourier amplitude spectra of strong ground accelerations in terms of earthquake magnitude, source to station distance, and recording site conditions, *Bull. Seism. Soc. Am.* **66,** 1343-1373.

Trifunac, M. D. and V. W. Lee (1978). Uniformly processed strong earthquake ground accelerations in the western United States of America for the period from 1933 to 1971: corrected acceleration, velocity and displacement curves, Report CE 78-01, Department of Civil Engineering, University of Southern California, Los Angeles, California.

Trifunac, M. D. and A. C. Brady (1975). On the correlation of seismic intensity scales with peaks of recorded strong ground motion, *Bull. Seism. Soc. Am.* **65,** 139–162.

Tullos, F. N. and A. C. Reid (1969). Seismic attenuation of Gulf Coast sediments, *Geophysics* **34,** 516–528.

Wong, J., P. Hurley, and G. F. West (1983). Crosshole seismology and seismic imaging in crystalline rocks, *Geophys. Res. Letters* **10,** 686–689.

INSTITUTE OF GEOHYSICS AND PLANETARY PHYSICS (A-025)
SCRIPPS INSTITUTION OF OCEANOGRAPHY
UNIVERSITY OF CALIFORNIA, SAN DIEGO
LA JOLLA, CALIFORNIA 92093

Manuscript received 11 October 1983

Articles

Strong Ground Motion from the Michoacan, Mexico, Earthquake

J. G. ANDERSON, P. BODIN, J. N. BRUNE, J. PRINCE, S. K. SINGH,
R. QUAAS, M. ONATE

The network of strong motion accelerographs in Mexico includes instruments that were installed, under an international cooperative research program, in sites selected for the high potential of a large earthquake. The 19 September 1985 earthquake (magnitude 8.1) occurred in a seismic gap where an earthquake was expected. As a result, there is an excellent description of the ground motions that caused the disaster.

ON 19 SEPTEMBER 1985, AN EARTHQUAKE OF MAGNITUDE 8.1 occurred with the epicenter near the Pacific coast of Mexico (*1*). Some damage occurred in the epicentral area, in Ciudad Guzman, and elsewhere outside of Mexico City. In Mexico City, 350 kilometers from the epicenter, the earthquake destroyed or badly damaged 300 (*2*) to 3,300 (*3*) buildings, and caused $4 billion damage (*3*). The human toll was at least 8,000 dead or missing, 30,000 injured, and 50,000 homeless (*3*), out of a population of more than 18 million people. The earthquake occurred at 7:17 a.m. local time; had it occurred during business and school hours, the toll in lives could have been far greater because of the number of severely damaged school and office buildings. Damage in Mexico City was most concentrated in tall structures, with earthquake-resistant design features, which were subjected to shaking that was amplified by soft sediments below part of the city.

The earthquake came as no scientific surprise. It was caused by subduction of the Cocos Plate beneath Mexico (Fig. 1), the most active subduction thrust fault in the Westen Hemisphere. Mexico has had 42 earthquakes with magnitude greater than 7 in this century associated with the subduction zone (*4, 5*), whereas California has had five associated with its correspondingly long San Andreas fault system. The 19 September earthquake occurred in the Michoacan seismic gap, which had been identified as a zone with high seismic potential by a variety of investigators (*4, 6–13*) with, however, speculation that the gap was permanently aseismic (*4, 10, 12, 13*).

The 19 September earthquake was documented by an array of strong motion accelerographs installed in the source region in expectation of this earthquake and what was considered an even more likely event in the nearby Guerrero seismic gap (Fig. 2).

International Cooperative Studies of Earthquake Ground Motion

The near-source recording of the 19 September Mexico earthquake is a success story in international cooperation. Before 1975, it was realized that international cooperative projects were crucial to increase the number of earthquake zones available for collecting data. Since earthquakes are relatively frequent in Mexico, the University of California, San Diego (UCSD), and the National Autonomous University of Mexico (UNAM) initiated in 1975 strong motion research in northern Baja California, Mexico, with National Science Foundation (NSF) support, resulting in important near-source recordings from two moderate earthquakes—the magnitude 6.6 Imperial Valley, California, earthquake of 15 October 1979, and the magnitude 6.1 Victoria, Baja California (Mexicali Valley), earthquake of 9 June 1980.

The importance of international cooperation was discussed at a workshop in 1978 in Honolulu, Hawaii (*14*). Several favorable array locations were identified, including the subduction zone of Oaxaca, Mexico, which, along with Taiwan, was given the highest probability (0.9) of recording accelerations greater than $0.2g$ in 10 years (*15*). It seemed reasonable and important to extend the international program to the subduction zone along the west coast of Mexico. A large earthquake (magnitude 7.8) occurred in Oaxaca, Mexico, on 29 November 1978, making another large earthquake in that region less likely in the near future. After studying the seismicity pattern, we proposed to install an array in the Guerrero and Michoacan seismic gaps, northwest of Acapulco. The array of 29 instruments was being installed when the 19 September 1985 earthquake occurred. Twenty stations were in place and 16 high dynamic range digital records of ground motion were obtained (Fig. 2). The magnitude 7.5 aftershock, 36 hours later, was also recorded by the array.

Seismic Prognosis for the Guerrero Gap

Repeat times of large earthquakes along a given portion of the Mexican subduction zone apparently average about 30 to 75 years (*4, 12*). However, successive large earthquakes can occur at shorter intervals in the same or nearby regions. Four large earthquakes occurred along the trench southeast of the 19 September event between 1899 and 1911; that region is now called the Guerrero seismic gap (Fig. 2), since it has not been the source of any large events since 1911.

In anticipation of large earthquakes recurring here, we concentrated the strong motion array southeast of the 19 September

---

J. G. Anderson, P. Bodin, and J. N. Brune are at the Institute of Geophysics and Planetary Physics, Scripps Institution of Oceanography, University of California at San Diego, La Jolla, CA 92093. J. Prince, S. K. Singh, R. Quaas, and M. Oñate are at the Instituto de Ingeniería, Universidad Nacional Autónoma de México, Coyoacan 04510, C.U., México, D.F.

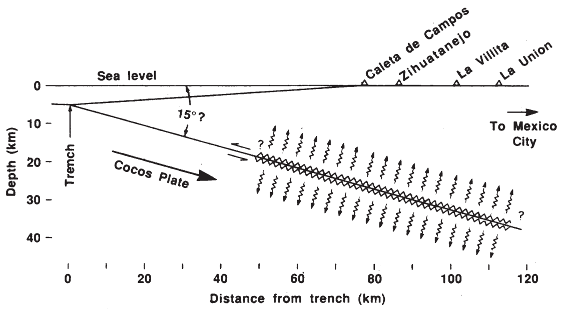

Fig. 1. Cross section of subduction of the Cocos Plate beneath the Mexican mainland. The illustrated extent of faulting corresponds to the aftershock zone in Fig. 3.

epicenter. Since the 19 September event did not fill the Guerrero gap, the likelihood of one or several large events there remains high, and recording the large earthquakes that will inevitably fill the gap remains an important short-term objective.

Teleseismic Analysis

From free oscillations of the earth, the seismic moments were estimated to be 10.3×10^{27} dyne-cm and 2.8×10^{27} dyne-cm for the main shock and aftershock, respectively (*16*). The fault plane orientations for these solutions are estimated to strike 105° and dip 18°. The long-period *P*-waves recorded at Akureyri, Iceland (AKU), for the 19 and 21 September earthquakes are shown in Fig. 3. The pulse from the 21 September event is simple; the 19 September event appears to be approximately the sum of two such sources with a time lag of about 26 seconds. The occurrence of the second event was in part responsible for the long source duration, but such long durations may be typical of earthquakes with magnitudes of at least 8 in this region.

In common with most Mexican earthquakes, aftershock activity was minimal from a teleseismic perspective: only 12 aftershocks with body wave magnitude (m_b) of at least 3.7 were located in the 24 hours after the main shock; in the next 24 hours there were only four, including the aftershock with surface wave magnitude (M_S) of 7.5; only one aftershock was recognized from teleseisms on 22 and 23 September.

Immediately after the earthquake, field crews went to the epicentral region to deploy sensitive instruments to record small aftershocks that would outline the rupture zone. Figure 2 shows preliminary determinations of the aftershock zones for the main event and large aftershock based on these data (*17*). The aftershock area of the 25 October 1981 earthquake ($M_S = 7.3$) and the area to the south are relatively free of aftershocks (*18*).

Strong Motion Recordings Near the Source

The locations of strong motion accelerographs on which the main shock on 19 September was recorded are shown in Fig. 2. These instruments are state-of-the-art digital recording accelerographs (*19*) and, like all accelerographs, are designed to operate remotely and unattended for months. When an earthquake occurs they sense the motion, turn on, record three components of ground motion including 2.5 seconds from pre-trigger memory, and turn off a few seconds after ground motion is below the trigger threshold. The

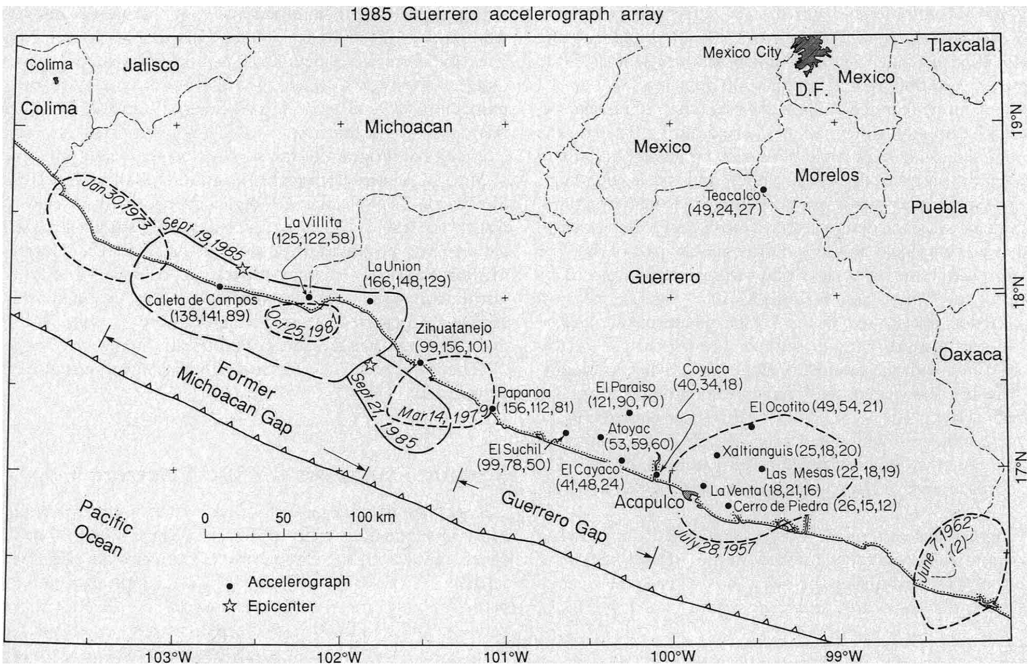

Fig. 2. Map of coastal Mexico, epicenters and aftershock zones of 1985 events, and locations of strong motion stations in Guerrero array on 19 September 1985. Short dashed lines show limits of aftershocks of large earthquakes in this region since 1951. Peak accelerations (cm/sec^2) are given for each station for the north, east, and vertical components, respectively, in parentheses.

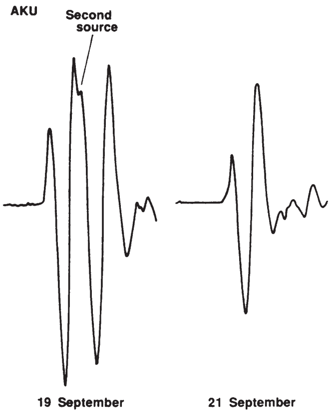

Fig. 3. Long-period vertical *P*-wave for the 19 and 21 September earthquakes recorded at station AKU (Akureyri, Iceland).

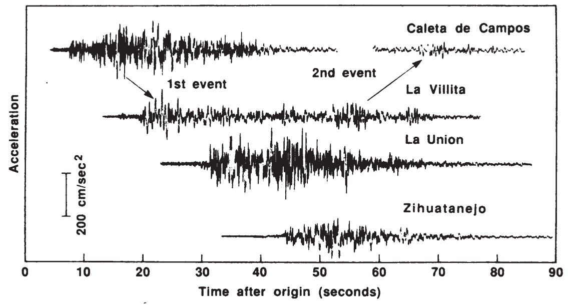

Fig. 4. North-south component of acceleration for stations above the aftershock zone. Vertical separation of traces is proportional to separation of the projection of stations onto the trench. Time, T_0, is the origin time of the earthquake (*1*). The clock correction at Caleta de Campos is uncertain.

accelerograph stations were purposely located on hard crystalline basement rock to reduce near-surface effects. Thus motions in sediment-covered regions were probably considerably higher. All stations are equipped with clocks synchronized to Universal Time by Omega navigation signals.

Accelerographs at Caleta de Campos, La Villita, La Union, and possibly Zihuatanejo, were situated directly above the aftershock zone and inferred ruptured area (Fig. 2). Figure 4 shows the north-south component of acceleration from these four stations (*20*). Peak values (*21*) are listed on Fig. 2, about 0.15*g* (150 gals) in the rupture region; durations of shaking in excess of 0.1*g* were about 20 seconds. These accelerograms confirm that there were two "subevents" in which energy release was relatively more intense, one near the epicenter and the second, starting about 24 seconds later, near La Union, separated by the aftershock zone of the October 1981 earthquake. At La Union and stations farther southeast, the energy from the two subevents arrived almost simultaneously. At La Villita and Caleta de Campos the two pulses were separated by about 20 seconds and 40 seconds, respectively. Caleta de Campos indicated a 3.2-second difference between the arrival times of the compressional and shear waves from the initiating event—that implies a hypocentral distance of less than 25 km. The gradual beginning suggests that the faulting was not immediately large.

Figures 5 and 6 show velocity and displacement at Caleta de Campos from the integrated accelerograms, and Fig. 7 shows north-south displacement at the stations directly above the fault. The integrations use a baseline correction proposed by Iwan *et al.* (*22*), and indicate a permanent displacement of the ground. At Caleta de Campos, displacements occurred over about a 10-second interval with ground velocity on each component averaging between 10 and 13 cm/sec, and the westward motion ceasing first. Such dynamic offsets during a major earthquake have never before been reliably recorded.

The directions of the offset (south, west, and up) are what one would expect from the plate tectonic model; the magnitudes are consistent with the average slip (~230 cm) obtained from the moment and fault area although we expected a smaller ratio of horizontal to vertical offsets. The vertical uplift at Caleta de Campos, 93 cm, is confirmed by the observation of about 1 m of permanent uplift along the coast (*23*). Caleta de Campos is located on a coastal terrace that might have formed seismically (*10*). This uplift generated a small tsunami (approximately 3 m locally at the coast).

On the basis of the data shown in Fig. 7 and the separations of the stations, the rupture front propagated with a velocity estimated at 3.8 km/sec from Caleta de Campos to La Villita, and 3.5 km/sec from La Villita to La Union. The major offset at Caleta de Campos begins about 8 seconds after the first *S*-wave arrived at the stations, suggesting some delay in the major faulting after the initiating event. The surface displacement took place over a time interval of about 10 seconds at Caleta de Campos and 20 seconds at La Union. At La Villita, integrations to displacement have higher relative uncertainties, but it appears that most displacement occurred in the initial 20 seconds, with some offset continuing until after the effects from faulting near La Union would have propagated back past the station. There are no indications of important precursory slip or post-rupture slip.

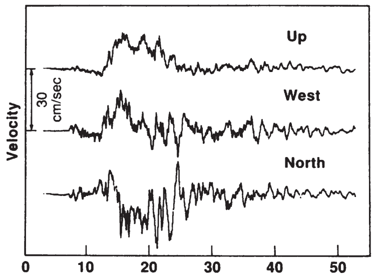

Fig. 5. Ground velocity at Caleta de Campos during the 19 September earthquake derived from accelerograms.

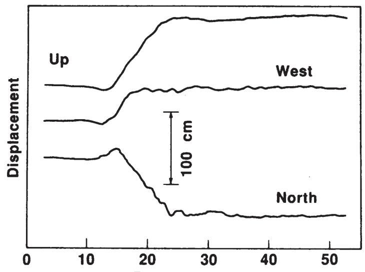

Fig. 6. Ground displacement at Caleta de Campos during the 19 September earthquake derived from accelerograms.

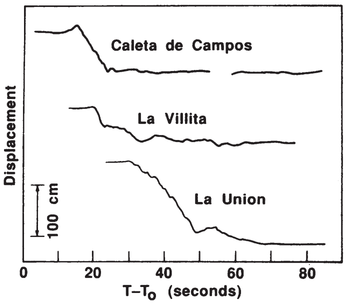

Fig. 7. North component of displacement at three stations above the aftershock zone.

Fourier Spectra

Fourier spectra from surface stations above a fault rupture of this size have not been observed before. Spectral ordinates (Fig. 8) increase with frequency from 0.1 to about 0.5 Hz, are relatively level to about 2 Hz, and generally decrease above 2 Hz, due to attenuation. At frequencies above 4 Hz, the spectrum from La Villita is smaller than those at the other two stations, consistent with less energetic rupture below La Villita and the attenuation of high frequencies which were radiated elsewhere on the fault. These spectra do not show a conspicuous peak at 0.5 Hz like spectra from the lake zone in Mexico City, although there is a relative maximum in the spectra from Caleta de Campos and La Union at that frequency, corresponding to visible oscillations on displacement traces (Fig. 7). From teleseisms the *P*-wave spectrum on 19 September resembles *P*-wave spectra from other recent large Mexican earthquakes; all are depleted from 0.1 to 1.0 Hz relative to a worldwide average (*24*). Near-field records from more earthquakes are needed to determine whether the source spectral amplitudes at 0.5 Hz are unusual, or typical, for this size of earthquake in Mexico. At frequencies higher than 0.1 Hz, the shape qualitatively resembles the far-field shape predicted by Gusev (*25*), although it differs in details.

For comparison, Fig. 8 shows the acceleration spectrum calculated for a synthetic seismogram consisting of a ramp displacement function, with displacement of 100 cm and a rise time of 10 seconds. Below 0.1 Hz, this generally agrees with the observed spectra, but from 0.3 to 3 Hz the observations are much larger, a consequence of fault-roughness causing radiation from relatively small areas on the fault surface that have stress drops perhaps exceeding 100 bars. A possible envelope for the roughness spectrum has a corner frequency of 0.5 Hz, corresponding to a source dimension with a 3- to 4-km radius (*26*) and, incidentally, to the resonant frequency of the sediments in Mexico City. From another viewpoint, relative to the high frequencies, which represent a higher stress drop over patches of the fault, the fault roughness can be thought of as introducing barriers, which cause partial stress drop averaged over the entire rupture (*27*), decreasing radiation at long periods.

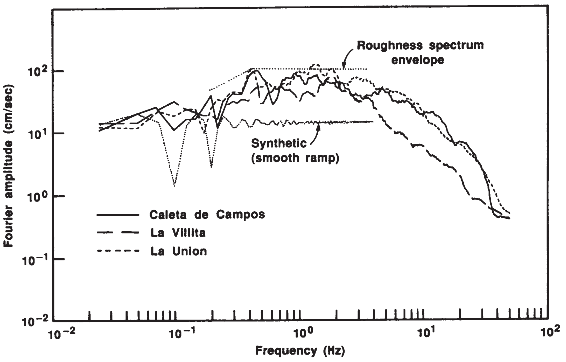

Fig. 8. Fourier amplitude spectra (smoothed) for the north-south components of acceleration above the aftershock zone.

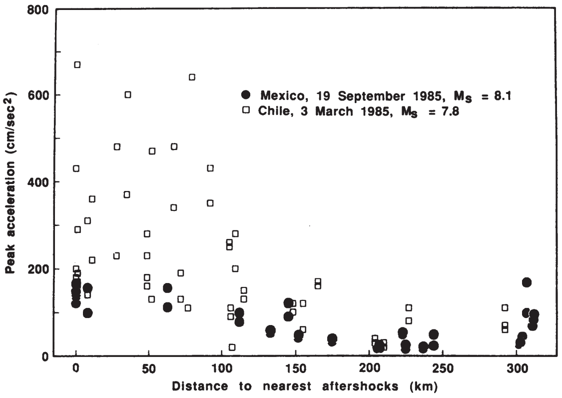

Fig. 9. Peaks of horizontal components of acceleration plotted against distance outside the boundary of the aftershock zone (Fig. 2).

Energy and Stress Drop

The radiated seismic energy, E_S, is estimated by

$$E_S = \tfrac{1}{2} A\, \rho c \int v^2(t)\,dt \tag{1}$$

where A is the fault area, ρ and c are density and seismic wave velocity at the surface, and $v(t)$ is the ground velocity. The integral is evaluated over the duration of the strong ground motion. Equation 1 assumes that the accelerograph, at which the surface velocity is amplified by a factor of 2 compared to the full space, is sufficiently near a uniformly radiating fault of area A that the limits of faulting do not affect the integral. Kinematic models and some modeling experiments suggest that Eq. 1 overestimates the energy radiated to the far field (*28*).

Energy estimates based on the strong motions observed at Caleta de Campos, La Villita, La Union, and Zihuatanejo indicate values for radiated energy of 1.2, 0.8, 1.3, and 0.8 × 10^{23} ergs, respectively. For c we used a shear-wave velocity of 2.9 km/sec and ρ of 2.8 g cm^{-3} as values appropriate for unweathered granite at the surface. The fault area, 50 by 170 km^2, is derived from the aftershock zone on Fig. 2. About 50% of the energy on the north component at Caleta de Campos is associated with the smooth ramp, and 50% comes from the roughness; the roughness contributes less on other components.

The Gutenberg and Richter (*29, 30*) formula for energy gives, for $M_S = 8.1$, $E_S = 9 \times 10^{23}$ ergs. Our estimate is considerably smaller and suggests a relatively low dynamic stress drop in comparison with average earthquakes used to derive the formula.

We calculate three stress-change parameters for this earthquake. The static stress drop, 19 bars, is proportional to the average strain drop (approximation for a long, narrow dip-slip fault) (*30*). The apparent stress, obtained from radiated energy, is 6 bars or less since the energy may be overestimated. Apparent stress is expected to be 0.5 times the static stress (*31*). The effective dynamic stress, 6 to 12 bars (*26, 32*), relates particle velocity adjacent to a fault and the stresses that drive the faulting (*32*). These three estimates of stress drop are remarkably consistent, and indicate a relatively low stress drop and low energy release, which correlates with the relatively low values of peak ground acceleration recorded in the near field. None of the above estimates of stress drop can be used as a direct indication of absolute stress on the fault, since an unknown amount of energy goes into frictional heat generation. However, a profile of heat flow holes perpendicular to the coast (*33*) showed no evidence of any frictional heat generation along the fault. That study probably indicates an upper limit on frictional stresses of about 100 bars, consistent with estimates for the San Andreas fault (*34*). Therefore, the stress estimates from the seismic data, when combined with the observation of low heat flow, indicate low absolute stresses, probably less than 100 bars and perhaps as low as 20 bars. These low values of absolute stress have an important bearing on the physics of plate motion, since some plate tectonic models involve high absolute stresses at subduction zones.

Attenuation with Distance

Figure 9 shows the peak horizontal accelerations recorded during the main shock, as a function of distance from the edge of the aftershock zone (Fig. 2). Peak values decrease with distance except for Mexico City and are considerably lower than expected based on extrapolation of the strong motion data gathered from shallower (5 to 15 km deep) earthquakes in California. For example, one empirical relation (*35*) extrapolates to 1200 cm/sec^2 above the aftershock zone of a magnitude 8.0 earthquake, but predicts values less than half the values observed in Mexico at distances between 200 and 250 kilometers. However, the depth of faulting in Mexico on 19 September is greater than that for shallow strike-slip and thrust earthquakes in California (Fig. 1); it is not surprising that the peak accelerations at short distances from the epicenter in this earthquake are less than estimates based on California data, although we would not have expected them to be so much lower. Further study is needed to determine what factors, in addition to the differences in the depth of faulting and the low stress drop, might contribute to these lower levels of ground motion.

For comparison, Fig. 9 also shows peak accelerations recorded during the Chile earthquake (M_S = 7.8, 3 March 1985) (*36*), another subduction thrust earthquake with a geometry similar to the 19 September event. Peak accelerations for the Mexico data show much less scatter than the Chile data, and seem to be almost a lower bound. The depths to faulting in Chile and Mexico may be similar, but site conditions for the two sets of data are different. The Mexican stations at distances less than 300 km are generally on small piers on competent rock outcrops. The Chile site conditions are less uniform, generally in one- and two-story buildings and on a variety of volcanic or sedimentary rocks and alluvial deposits; these conditions result in resonances and amplification relative to basement rock, contributing to the scatter and higher values in peak accelerations. The scatter and the large amplitudes in Mexico City and at points beyond 300 km are obviously caused by site conditions. Other factors that might contribute to the higher accelerations in Chile than in Mexico are higher overall stress drop, failure of higher stress drop asperities, or triggered slip in the upper plate.

Higher peak accelerations have been observed in other Mexico subduction zone earthquakes. In the 21 September aftershock they reached 245 cm/sec^2 at Papanoa (*21*). A shallow magnitude 5 earthquake produced 522 cm/sec^2 accelerations in Acapulco at an epicentral distance of about 35 km (*37*). The 19 March 1978 earthquake (M_S = 6.5), located directly below Acapulco at a depth of 15 km, produced a peak acceleration of 834 cm/sec^2 in Acapulco (*38*). An empirical relation for peak acceleration based on earlier Mexican data (*38*) predicts larger values at all distances except at Mexico City. Considering these results, and the Chile data, it would be premature to infer that the 19 September earthquake was typical of subduction thrust earthquakes, either in general or in Mexico.

Strong Motion in Mexico City

The subsoil structure played an important role in determining the pattern and extent of damage in the Valley of Mexico. The near-surface geology of Mexico City, site of the former Lake Texcoco, may be classified into three general zones: the old lake bed, a hill zone, and a transition zone between the two (Fig. 10) (*2*). The firmest near-surface materials are found in the hill zone, the southern edge of which is capped by 5 to 30 m of lava less than 2500 years old. The transition zone consists of river delta and shoreline deposits with interbedded intervals of clay. The lake bed zone is characterized by a deposit of very soft clay with high water content in the upper 30 to 40 meters.

Nearly all buildings that collapsed during the earthquakes of 19 and 21 September were located on the lake zone (Fig. 10). Ground motion was digitally recorded at four free-field sites on the hill and lake zones—UNAM, VIV (Viveros de Coyoacan), CDA (Central de Abastos), and SCT (Secretaria de Comunicaciones y Transportes). Other city sites were in buildings and may have been influenced by building response. The characteristics of the shaking at the various sites are related to the observed damage. Peak recorded accelerations are given in Fig. 10; Fig. 11 shows the most significant segment of the east-west components of acceleration. Not surprisingly, accelerograms on the hill zone (UNAM and VIV) show lower amplitudes and higher frequencies than accelerograms in the lake zone (CDA and SCT). The UNAM and VIV accelerograms are typical of prior observations in the hill zone, and the accelerograms from CDA and SCT are characteristic of prior observations in the lake zone (*39, 40*). Peak accelerations on 19 September are larger, possibly primarily a result of the larger magnitude.

The lake zone accelerograms have a long duration (5 minutes)

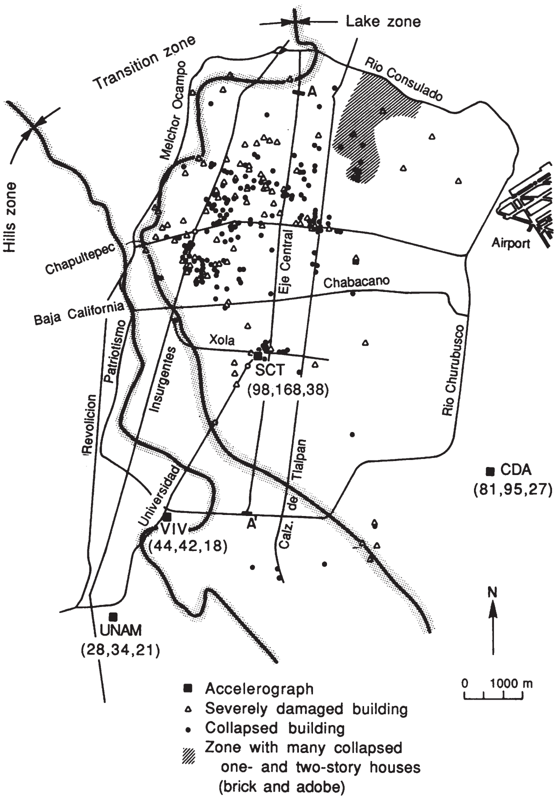

Fig. 10. Mexico City map showing free-field accelerograph stations, generalized soil classification, and sites of worst building damage from (*2*). Peak accelerations (cm/sec^2) for the north, east, and vertical components, respectively, are given in parentheses by each station.

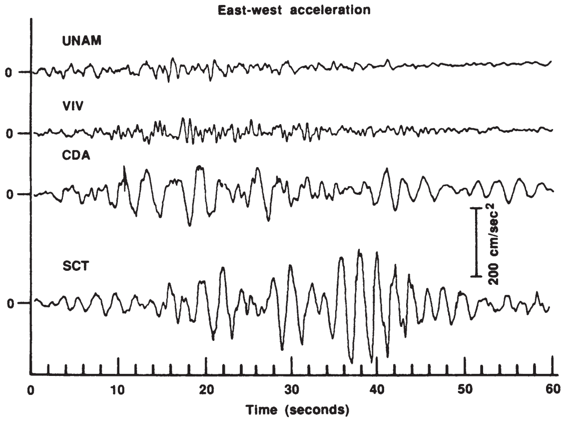

Fig. 11. Most significant 1-minute segments of the east-west acceleration recorded on the free-field accelerographs in Mexico City. Complete accelerograms are longer; 100 seconds of motion preceded the segment of the SCT record shown here. No time correlation exists among these traces.

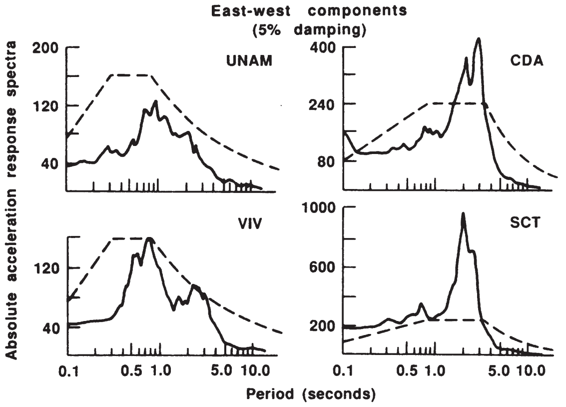

Fig. 12. Absolute acceleration response spectra (5% damping) for the accelerogram components in Fig. 11. Dashed lines are the applicable design spectra for the locations of each instrument.

with conspicuous long-period oscillations. Accelerograms from previous earthquakes at lake zone stations invariably are similar, with the low-frequency oscillations explained as resonant excitation of the shallow sedimentary structure (*40, 41*). Gravity anomalies indicate a buried, north-south ridge east of the heavily damaged area (*42*) which may also have modified the ground motion. Based on proximity and stronger similarities in the shallow geology, the SCT accelerogram is probably most representative of the excitation applied to building foundations in the heavily damaged area of the city. However, during the 14 March 1979 earthquake, an accelerograph in the basement of the Loteria Nacional building 4 km north of SCT showed accelerations 50 to 80% larger than the 1979 records at SCT. The Loteria record may have been modified by soil-structure interaction, but it reminds us that during the 19 September event some areas of the former lake bed may have experienced long-period shaking with amplitudes even larger than those recorded at SCT.

Response Spectra

Structures in Mexico City are designed under a building code that requires earthquake-resistant features. As in the United States, this code provides for dynamic design of significant structures. The most common procedure is based on the concept of a design "response spectrum." A building with a given fundamental period of vibration is designed to resist a force proportional to the design "response spectrum" at that period. This may be compared with the actual "response spectrum," calculated from an observed accelerogram, which is proportional to the actual force to which the building was subjected (*43*).

Absolute acceleration response spectra (5% damping) for the four east-west accelerograms are compared in Fig. 12 with the corresponding design spectrum according to the latest revision (1977) of the Mexico City Building Code (*44*). Response spectra for UNAM and VIV do not exceed the design spectrum, correlating with the lack of damage in the hill zone. For CDA the spectrum is exceeded between from about 1.6 to 3.3 seconds by factors of up to 2.6, but there are no buildings higher than seven stories within a few kilometers of CDA, and the area was unscathed. At SCT the design spectrum is more significantly exceeded by the response spectrum; at 2 seconds the factor is almost 4.2; this and the long time the spectral ordinate exceeded the design spectrum (over 25 seconds at a period of 2 seconds) were clearly excessive for many buildings. Within 300 m of SCT, eight buildings collapsed and several others were heavily damaged and had to be abandoned.

Within the primary damage zone, one estimate is that about 20% of the structures over six stories high suffered structural damage (*2*). For typical construction in Mexico the period in seconds of the fundamental mode of building vibration (fixed foundation) is usually about 0.1 times the number of stories. One effect of ductile behavior is to decrease the building stiffness and further increase the period during the shaking. Thus the high percentage of tall buildings that collapsed or were severely damaged correlates with the periods at which the design spectrum was exceeded by the earthquake motions.

Conclusion

Because the epicentral regions of the tragic Mexican earthquakes were a well-instrumented seismic gap, a wealth of new observations on the mechanism of earthquake faulting and strong motion generation was obtained. More observations under similar conditions are needed before it can be known whether the observed low accelerations in the source region are anomalous or typical of such great earthquakes. Ground motion amplitudes had decreased with distance of propagation to harmless levels on rock sites near Mexico City, but selected frequencies were greatly amplified by the soft sediments of the Valley of Mexico. The worst damage occurred to structures that were near resonance with these amplified wave frequencies. Many of the questions left unanswered for this earthquake can be resolved if the Guerrero gap, which may rupture in the next decade or so, is properly instrumented.

REFERENCES AND NOTES

1. "Preliminary determination of epicenters, No. 38–85" (National Earthquake Information Service, National Oceanic and Atmospheric Administration, Boulder, CO, 10 October 1985). The main shock epicenter is located at 18.182°N, 102.573°W, origin time 1300 hours 17 minutes 47.8 seconds Universal Time (UT), $M_S = 8.1$, $m_b = 7.0$. From teleseisms, the primary aftershock is located at 17.823°N, 101.671°W, origin time 0100 hours 37 minutes 13.8 seconds UT,

$M_S = 7.5$, $m_b = 6.3$. On the basis of local stations already in place, we have relocated the aftershock at 17.618°N, 101.815°W.

2. Instituto de Ingenieria de la Universidad Nacional Autónoma de México, *Informe Preliminar* (Mexico City, 1985).
3. United Nations Economic Commission for Latin America and the Caribbean, *ECLAC, Report 85-10-1528* (1985).
4. S. K. Singh, L. Astiz, J. Havskov, *Bull. Seismol. Soc. Am.* **71**, 827 (1981).
5. S. K. Singh, M. Rodriguez, J. M. Espindola, *ibid.* **74**, 267 (1984).
6. J. Kelleher, L. Sykes, J. Oliver, *J. Geophys. Res.* **78**, 2547 (1973).
7. W. McCann, S. Nishenko, L. Sykes, J. Krause, *U.S. Geol. Surv. Open File Rep. 78-943* (1978).
8. A. Reyes, J. N. Brune, C. Lomnitz, *Bull. Seismol. Soc. Am.* **69**, 1819 (1979).
9. R. P. Meyer *et al.*, *Geophys. Res. Lett.* 7, 97 (1980).
10. K. C. McNally and J. B. Minster, *J. Geophys. Res.* **86**, 4949 (1981).
11. J. Havskov, S. K. Singh, E. Nava, T. Dominguez, M. Rodriguez, *Bull. Seismol. Soc. Am.* **73**, 449 (1983).
12. L. Astiz and H. Kanamori, *Phys. Earth Planet. Int.* **34**, 24 (1984).
13. L. V. LeFevre and K. C. McNally, *J. Geophys. Res.* **96**, 4495 (1985).
14. W. D. Iwan, Ed., *Proceedings of the International Workshop on Strong Motion Instrument Arrays* (California Institute of Technology, Pasadena, 1978).
15. University of California at Berkeley submitted a proposal in cooperation with investigators from Taiwan to install a strong motion array there. In 4 years it has recorded 35 earthquakes over a range of depths and distances and has been cost-effective in terms of quantity and quality of data acquired [B. A. Bolt and N. Abrahamson, *Bull. Seismol. Soc. Am.* **75**, 1247 (1985)]. Other arrays are planned in India, China, and Turkey.
16. K. Priestley and G. Masters, *Geophys. Res. Lett.* **13**, 601 (1986).
17. UNAM Seismology Group, *ibid.*, p. 573.
18. There is a possibility of systematic offshore bias in our locations and in the locations of previous aftershock zones because of the complex structure of the downgoing slab (C. Stolte *et al.*, *ibid.*, p. 577).
19. R. Quaas *et al.*, *Preliminary Report GAA-1B* (Instituto de Ingenieria, UNAM, Mexico City, 1985).
20. At Caleta de Campos the instrument turned off before the intense energy from the southern source had arrived and started after a 6-second quiescence.
21. J. G. Anderson *et al.*, *Preliminary Report GAA-1A* (Instituto de Ingenieria, UNAM, Mexico City, 1985).
22. W. D. Iwan, M. Moser, C.-Y. Peng, *Bull. Seismol. Soc. Am.* **75**, 1225 (1985).
23. P. Bodin and T. Klinger, *Science* **233**, 1071 (1986).
24. H. Houston and H. Kanamori, *Geophys. Res. Lett.* **13**, 597 (1986).
25. A. A. Gusev, *Geophys. J. R. Astron. Soc.* **74**, 787 (1983).
26. A. Papageorgiou and K. Aki, *Bull. Seismol. Soc. Am.* **73**, 693 (1983).
27. J. N. Brune, *J. Geophys. Res.* 75, 4997 (1970).
28. N. A. Haskell, *Bull. Seismol. Soc. Am.* **59**, 869 (1969); S. H. Hartzell and R. J. Archuleta, *J. Geophys. Res.* **84**, 3623 (1979); R. J. Archuleta and S. H. Hartzell, *Bull. Seismol. Soc. Am.* **71**, 939 (1981).
29. B. Gutenberg and C. F. Richter give E_s (ergs) = $10^{(11.8 + 1.5m)}$ [*Bull. Seismol. Soc. Am.* **46**, 105 (1956)].
30. H. Kanamori and D. Anderson, *ibid.* **65**, 1073 (1975). The uncertainty in estimating static stress drop, $(8/3\pi)\mu(D/w)$, where μ is shear modulus, D is average slip and w is fault width, is proportional to the uncertainty in estimating the width of the rupture zone based on aftershocks.
31. Apparent stress is given by $\mu E_S/M_0$, where μ is shear modulus. E_s is radiated energy, and M_0 is moment [K. Aki, *Bull. Earthquake Res. Inst. Tokyo Univ.* **44**, 2388 (1966); M. Wyss and P. Molnar, *J. Geophys. Res.* 77, 1433 (1972)].
32. The effective dynamic stress is calculated from the equation of Brune (*27*), $[(\mu/\beta)\bar{v}]$, where β is shear velocity and $\bar{v}$ is approximated by 0.5 times the average velocity at the surface during the ramp offset. Subsequent studies which remove simplifying assumptions of Brune find the rupture velocity replace the shear velocity β. The rupture velocity is unknown but is likely to be near the shear velocity. Foam rubber modeling of dynamic ruptures [J. N. Brune, *Bull. Seismol. Soc. Am.* **63**, 2105 (1973)] and calculations by H. Kanamori [*Phys. Earth Planet. Int.* **5**, 426 (1972)] indicate that the equations may give estimates of stress drop as much as a factor of 2 low.
33. J. P. Ziagos, D. D. Blackwell, F. Mooser, *J. Geophys. Res.* **90**, 5410 (1985).
34. J. N. Brune, T. L. Henyey, R. F. Roy, *ibid.* **74**, 3821 (1969); A. H. Lachenbruch and J. H. Sass, *ibid.* **85**, 6185 (1980).
35. W. B. Joyner and D. M. Boore, *Bull. Seismol. Soc. Am.* 71, 2011 (1981).
36. G. H. Saragoni, *Secc. Ing. Estruct. Univ. Chile* (1985); B. Bolt and N. A. Abrahamson, *Earthquake Eng. Res. Inst. Rep. 3 March 1985 Chile Earthquake* (1986).
37. S. H. Hartzell, J. N. Brune, J. Prince, *Bull. Seismol. Soc. Am.* **68**, 1663 (1978).
38. M. A. Bufaliza, thesis, Facultad de Ingenieria, Universidad Nacional Autónoma de México, Mexico City (1984).
39. L. Alonso, J. M. Espinosa, I. Mora, D. Muria, J. Prince, *Inst. Ing. IPS-5A* (Universidad Nacional Autónoma de México, Mexico City, 20 March 1979).
40. L. Zeevaert, *Bull. Seismol. Soc. Am.* **54**, 209 (1964).
41. E. Rosenblueth, "Teoría del diseño sísmico sobre mantos blandos," *Ediciones ICA, B14* (Mexico, 1953); E. Faccioli and D. Resendiz, *Seismic Risk and Engineering Decisions*, C. Lomnitz and E. Rosenblueth, Eds. (Elsevier, New York, 1976), pp. 71–141.
42. R. Alvarez, *Eos* **67**, 85 (1986).
43. However, suitability of design criteria cannot be judged solely by the level of the design spectrum. The effects of ductility (ability of the structure to deform beyond the limits of elastic behavior without failure), differences between the true damping of the structure and assumed damping in the design spectrum, and durations of shaking are three other important effects that must be considered [G. W. Housner and P. C. Jennings, *Earthquake Design Criteria* (Earthquake Engineering Research Institute, Berkeley, CA, 1982)].
44. In actual practice, the design spectra are reduced by a ductility factor ranging from 1 to 4. A large proportion of engineered structures in Mexico were undoubtedly designed with spectral ordinates one-half or less than those shown in Fig. 12.
45. Supported by NSF grant CEE 82 19432. We thank D. Agnew and J. Berger for providing the very high quality IDA data used to determine the moment. D. Almora and P. Perez provided technical and field support, and E. Mena is responsible for computer processing of the data. We thank F. Vernon for his efforts in the aftershock studies. We also thank B. Bolt and N. Abrahamson for making their manuscript available to us in advance of publication and for sharing data on the 1985 Chile earthquake. J. E. Luco and E. Rosenblueth reviewed the manuscript.

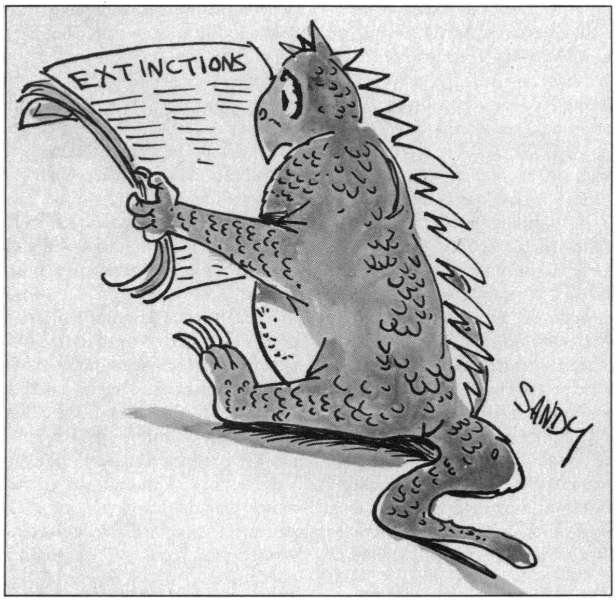

Bulletin of the Seismological Society of America, Vol. 103, No. 3, pp. 1935–1951, June 2013, doi: 10.1785/0120120252

Ground Motions in the Fukushima Hamadori, Japan, Normal-Faulting Earthquake

by John G. Anderson,* Hiroshi Kawase, Glenn P. Biasi, James N. Brune, and Shin Aoi

Abstract A crustal normal-faulting earthquake (M_{JMA} 7.0; M_{w} 6.7) occurred in eastern Tohoku, Japan, on 11 April 2011. K-NET and KiK-net stations recorded 82 records from within 100 km of fault rupture. These data and data from associated foreshocks and aftershocks will make a critical contribution to future improvements of ground-motion prediction for normal-faulting earthquakes.

Peak ground accelerations (PGA) and peak ground velocities (PGV) are compared with four ground-motion prediction equations (GMPEs) that include the style of faulting as a predictor parameter. For distances under 100 km, and using a network average value of V_{S30}, the average ratio of PGA to the selected GMPEs (the event term) is high by factors of 2.3–3.7. Event terms for PGV are high by factors of 1.4–1.8. Adjusting PGA and PGV with customized site terms (Kawase and Matsuo, 2004a,b), the standard deviations of PGA and PGV residuals are reduced from 0.59 to 0.43, and from 0.53 to 0.35, respectively. The event terms decreased to relatively small factors of 1.1–1.8 for PGA and increased slightly to 1.5–2.0 for PGV. Thus, site terms are very important, but positive event terms remain. The remaining positive event terms are not explained by high stress drop, which was typical of crustal events of all mechanisms globally or in Japan. Two subparallel faults ruptured, but source inversions, which we reviewed, revealed that they ruptured sequentially, so simultaneous contributions from the two faults did not cause high motions. Although these observations may tend to suggest that ground motions in large normal-faulting events are larger than predicted by the tested models, we are not aware of any observations from this event that contradict the precarious rock evidence of Brune (2000) that ground shaking is low on the footwall near the rupture.

Introduction

Strong-motion records from the near field of earthquakes with a normal-faulting mechanism (Fig. 1) are sparse, even by comparison with crustal earthquakes with a strike-slip or reverse-faulting mechanism. For instance, a search of the Next Generation Attenuation (NGA) relation flatfile (Chiou *et al.*, 2008) finds that only 91 records (out of 3551 total used for the NGA) have a normal-faulting mechanism. There are only 25 records from three normal-faulting earthquakes with $M_{\mathrm{w}} \geq 6.5$ (Irpinia, Italy, 23 November 1980, M_{w} 6.9, 12 records; Borah Peak, Idaho, 20 October 1983, M_{w} 6.9, 11 records [in a fairly small area]; Edgecumbe, New Zealand, 2 March 1987, M_{w} 6.6, 2 records). The NGA compilation, of course, does not include the entire set of ground motions from normal-faulting earthquakes. It has the obvious limitation that the most recent event in that compilation occurred in 2003. Furthermore, it did not benefit from recent efforts to improve the quality and accessibility of strong-motion data from Italy (e.g., Luzi *et al.*, 2010; Massa *et al.*, 2010; Pacor *et al.*, 2011) and Greece (Theodulidis *et al.*, 2004), where normal faulting is dominant.

Within these modest constraints, several ground-motion prediction equations (GMPEs) have concluded that on average, ground motions in normal-faulting events are slightly smaller than in strike-slip or thrust events (e.g., Spudich *et al.*, 1999; Abrahamson and Silva, 2008; Boore and Atkinson, 2008; Campbell and Bozorgnia, 2008; Chiou and Youngs, 2008). The last four of these are collectively known as NGA relations. A recent model by Bindi *et al.* (2011) using the Italian database finds that ground motions in Italy are generally consistent with the NGA predictions for normal-faulting events, but near-source records from earthquakes with $M_{\mathrm{w}} \geq 6$ are sparse in that data set as well. The NGA relations, developed under the NGA Project (Power *et al.*, 2008), are used extensively in hazard analysis in the United States. Applications include use of Boore and Atkinson (2008),

---

*Also at Department of Geological Sciences and Engineering.

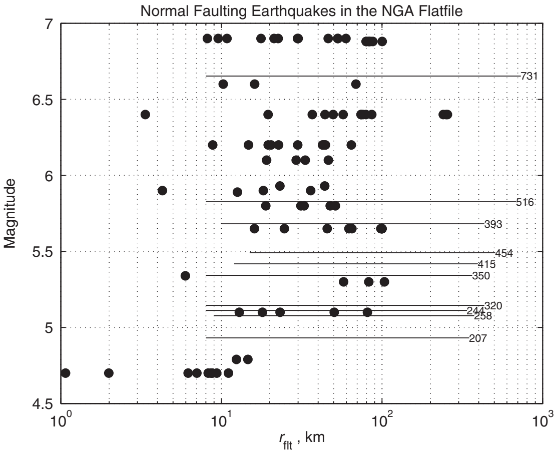

Figure 1. Distribution of magnitude and distance of strong-motion data for normal faulting earthquakes in the NGA database, as a function of r_{flt}. For events in which r_{flt} is not given in the database, r_{epi} is substituted. The solid horizontal lines are drawn at magnitudes of normal faulting earthquakes associated with the Fukushima Hamadori earthquake. The numbers to the right give the number of strong-motion accelerograms recorded in each event, and the extent of the lines give a preliminary estimate of the distance range of each event. Distances are based on epicenter as given in the K-NET or KiK-net files obtained from NIED.

Campbell and Bozorgnia (2008), and Chiou and Youngs (2008) by the U.S. Geological Survey to develop the 2008 revision of the National Hazard Map (Petersen *et al.*, 2008). These three models are used to estimate the ground motions from earthquakes in the Intermountain West region, where normal faulting dominates.

In this context, the Fukushima Hamadori earthquake of 11 April 2011 (M_w 6.7, M_{JMA} 7.0) is extremely significant, as the strong ground motions are by far the most extensively recorded of any normal-faulting earthquake of any magnitude. About 82 stations are within 100 km of the nearer of the two fault surfaces, at a wide range of azimuths, and over 730 stations altogether recorded the event. Besides the mainshock, the Global Centroid Moment Tensor (Global CMT) project (see Data and Resources) identified at least nine other normal-faulting events in this sequence with $M_w > 5$, as indicated in Figure 1. This analysis, which evaluates only the mainshock, finds that the recorded strong motion in the Fukushima Hamadori mainshock had significantly stronger peak ground accelerations (PGA) and peak ground velocities (PGV) than the prediction of the NGA equations cited above, and considers four hypotheses that might help explain the discrepancy.

Fukushima Hamadori Earthquake

The Fukushima Hamadori earthquake, and associated events with smaller magnitudes, was apparently triggered by the 11 March 2011 Tohoku (M_w 9.0) earthquake. The Fukushima Hamadori earthquake occurred in the continental crust of Japan, and caused surface rupture. Large shallow aftershocks with extensional mechanisms also followed the M_w 8.8 Maule, Chile, earthquake in 2010 (Ryder *et al.*, 2012). The general location of the Fukushima Hamadori event, in the context of the Tohoku aftershocks, is shown in Figure 2, and some teleseismic parameters for the earthquake are given in Table 1. Although Kato *et al.* (2011) suggested that the entire Tohoku region, including the source area of the Fukushima Hamadori earthquake, was under compression prior to the Tohoku earthquake, Imanishi *et al.* (2012) found 23 focal mechanisms of smaller earthquakes with normal-faulting mechanisms in the region between 2003 and 2010.

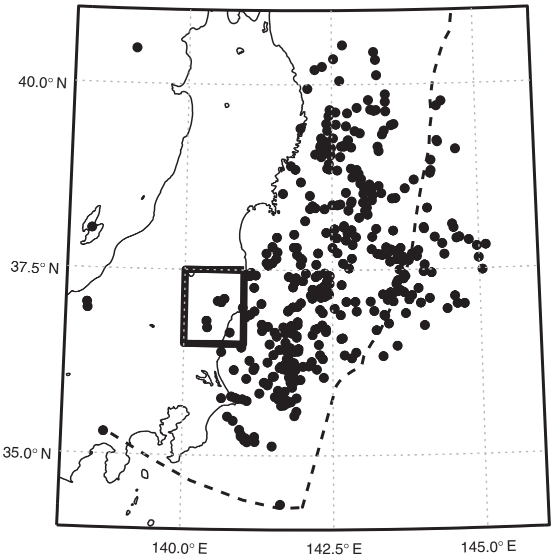

Figure 2. Location map, showing the region affected by the Fukushima Hamadori earthquake (outlined by heavy box) in the context of the region affected by the Tohoku earthquake. Epicenters shown are events located by the U.S. Geological Survey National Earthquake Information Center (USGS NEIC) in the first 12 days following the M_w 9.0 Tohoku mainshock. Dashed black lines indicate the boundary between the Pacific or Philippine Sea plates and the crustal block including Tohoku.

The Fukushima Hamadori earthquake caused surface rupture on two faults. Faulting is described by Maruyama *et al.* (2011). The Idosawa fault ruptured for a distance of 14 km, with a maximum offset of about 200 cm (Maruyama *et al.*, 2011). The Yunotake fault ruptured for about 15 km, with maximum slip of about 80 cm. Table 2 gives the parameters used in this paper to describe the locations and orientations of these two faults. A model of the faulting is needed to determine the fault distance for comparisons of observed ground motions with GMPEs. Figure 3 shows the location of the fault planes as modeled in Table 2. Both faults are approximated by a planar surface, with the surface trace approximating the location of observed rupture as given by Maruyama *et al.* (2011) and Geology Research Team (2011). The dip of the Idosawa fault is constrained so that the fault

Table 1

Catalog Parameters for the Fukushima Hamadori Earthquake of 11 April 2011

Data Source	Origin Time	Location	Depth, km	M_0 dyn·cm	Magnitude
K-NET and KiK-net data files	17:16 JST	36.945° N 140.672° E	6.0		7.0M_{JMA}
PDE	08:16:12.73 UTC	37.001° N 140.401° E	11.0		6.6$M_{\mathrm{w}}W$
Global CMT *	08:16:19.5 UTC (centroid time)	37.00° N 140.54° E	12.0	1.2×10^{26}	6.69M_{w} 6.4m_{b} 6.6M_{S}

*Fault planes: FP1: Strike = 139, Dip = 56, Rake = −75; FP2: Strike = 295, Dip = 39, Rake = −109; FP1 is most consistent with the observed surface faulting.

Table 2

Geometry of Fault Planes Used in This Study to Describe the Idosawa and Yunotake Faults

Parameter	Idosawa	Yunotake
Reference point latitude*	36.9488	36.9855
Reference point longitude*	140.7082	140.8302
Reference point depth (km)*	0	0
Strike†	162	128
Dip†	66	66
Total Rupture Length (km)†	13.4	15.3
Total Rupture Width (km)†	20	15
Length in +strike direction from reference point (km)‡	0	0
Length in −strike direction from reference point (km)‡	13.4	15.3
Shallowest depth of faulting (km)	0	0
Maximum depth of faulting (km)	18.27	13.70
Fault area (km^2)	268	229.5
Maximum Surface Slip (m)	2.0	0.8

*The reference points are at the south end of the surface traces of each fault.

†The strike and fault length are chosen to be a close approximation to the location of surface faulting. The strike uses the Aki and Richards (2002) convention that when facing in the +strike direction, the fault dips to the right. The dip of the Idosawa fault is determined so that the dipping plane will go through the hypocenter, whereas the dip of the Yunotake fault is taken to be the same. The down-dip width is wide enough to reach the depth and horizontal offset of the deepest aftershocks. Cross sections of the faults show that these planes are not inconsistent with the aftershock locations.

‡Because of the convention for fault geometry and the location of the reference points, the fault traces are in the opposite direction from the positive-strike direction.

will pass through the hypocenter, and the same dip is then applied to the Yunotake fault. Associated smaller events that were also recorded on strong-motion instruments include immediate aftershocks, and the fault width in Table 2 was set so as to be consistent with the deepest of those events. Based on aftershocks, Hikima (2012) and Shiba and Noguchi (2012) model the Idosawa fault as longer than its surface rupture, 26 and 23.8 km, respectively, mainly extending the fault towards the north compared with Figure 3. The kinematic models by both authors find most of the slip took place within the part of the fault shown in the figure.

Strong-Motion Data

Strong-motion data in this study was obtained from the NIED K-NET and KiK-net strong-motion networks (Kinoshita, 1998, 2005; Okada *et al.*, 2004). Data from all stations recording the event were downloaded from the NIED websites. There are 82 stations within 100 km of the faults shown in Figure 3, 298 within 200 km, 477 stations within 300 km, 608 stations within 400 km, and 715 stations altogether, with the most distant at 876 km distance. Data were high-pass filtered with a Butterworth causal filter, 2 pole, with corner frequency of 0.05 Hz, and then integrated to velocity and displacement. The geometric mean horizontal acceleration and geometric mean horizontal velocity, determined from the horizontal components oriented as recorded, are shown as a function of distance in Figures 4 and 5, respectively. Four NGA models (Abrahamson and Silva, 2008; Boore and Atkinson, 2008; Campbell and Bozorgnia, 2008; Chiou and Youngs, 2008) are also shown in Figures 4 and 5. These four NGA relations use V_{S30}, the time-average shear velocity in the upper 30 m, as a predictor variable. The stations contributing data on Figures 4 and 5, of course, come from a variety of site conditions. Therefore, the intention on these figures is to use a value of V_{S30} that is a reasonable median for the ensemble of stations. All of the K-NET sites have velocity logs posted by NIED, giving compressional and shear velocities and densities at one meter intervals from the surface to 20 m depth. A reasonable lower bound to V_{S30}, say $V_{S30}^{\min}$, is to project the velocity at the base of the provided log to the depth of 30 m. The median value of $V_{S30}^{\min}$ is 340 m/s. We also estimated an upper bound, say $V_{S30}^{\max}$, by projecting a velocity of 2000 m/s from the base of velocity log to 30 m. The median value of $V_{S30}^{\max}$ estimated in this manner is 470 m/s. Therefore, the median V_{S30} is bounded between 340 and 470 m/s. The value $V_{S30} = 400$ m/s is used in Figures 4 and 5. It is worth noting that based on the correlation of Boore *et al.* (2011), a median value of $V_{S20} = 340$ m/s corresponds to a median value of $V_{S30} = 407$ m/s.

The data are offset above the predictions in Figures 4 and 5. A different choice of V_{S30} can not help significantly to reduce the discrepancy. For several spot checks for both PGA and PGV at distances of 10, 50, and 100 km,

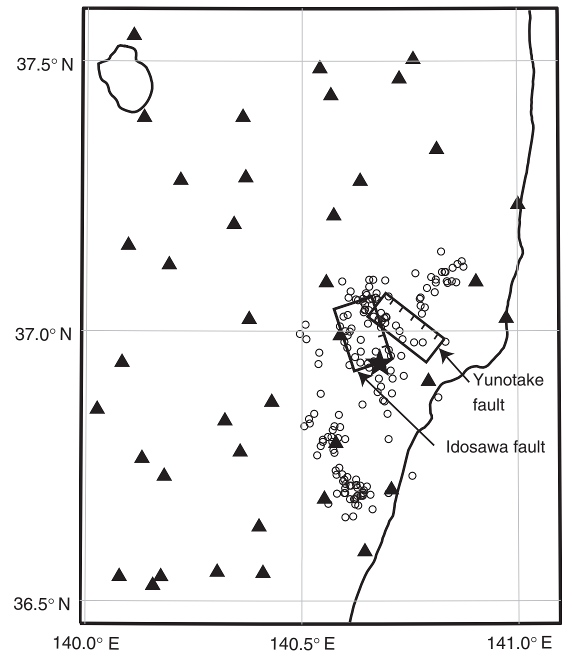

Figure 3. Detailed map of the area around the Fukushima Hamadori earthquake. Black rectangles show the surface projection of the two contributing faults, as modeled in Table 2. The fault edges with tick marks indicate the approximate locations of surface rupture. Triangles show locations of strong-motion stations. The star shows the epicenter of the mainshock. Circles are associated crustal earthquakes, which have generated strong-motion accelerograms. Earthquake locations are NIED locations from the headers of strong-motion records obtained at station IBRH13 from shallow, nearby earthquakes.

the difference between curves generated with $V_{S30} = 400$ m/s and the predictions at either bound on median V_{S30} is under 6%. This difference is negligible compared with the offset of the data.

The GMPE model by Si and Midorikawa (1999, 2000) is used in the development of the national seismic hazard map of Japan. It is not shown in Figures 4 and 5 because that model is developed for PGA and PGV on records that have been low-pass filtered with a corner frequency of 10 Hz, and it predicts the value of the larger horizontal component. In contrast, the accelerograms used to develop Figures 4 and 5 show the geometric mean of the two horizontal peaks without applying a low-pass filter to the data. The Si and Midorikawa (1999, 2000) model predicts larger amplitudes of PGA and PGV, for distances smaller than 100 km, than the NGA models, but the observations of both PGA and PGV are still somewhat higher (Si *et al.*, 2012). Because the Si and Midorikawa (1999, 2000) model does not include an adjustment for fault mechanism, this implies that ground motions in the Fukushima Hamadori earthquake are somewhat stronger than the average reverse and strike-slip earthquakes that dominate in development of the Si and Midorikawa (1999, 2000) model.

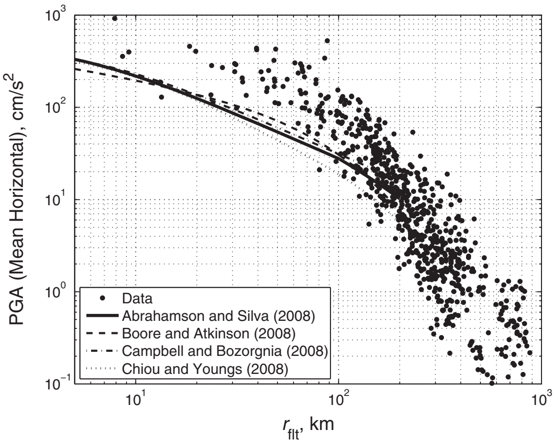

Figure 4. PGA, compared with four different GMPEs. Curves assume $V_{S30} = 400$ m/s, as explained in the text.

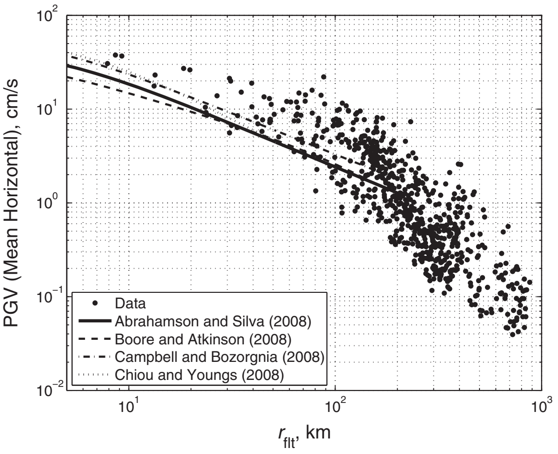

Figure 5. PGV compared with four different GMPEs. Curves assume $V_{S30} = 400$ m/s, as explained in the text.

Event Terms

The value of an individual ground-motion observation, using the notation of Anderson and Uchiyama (2011), can be written as

$$\ln Y_{es} = f_M(\cdot) + \delta^I_{es}, \qquad (1)$$

where Y_{es} is the observation (either PGA or PGV), $f_M(\cdot)$ is the value predicted by the GMPE, and δ^I_{es} is the residual. The subscripts e and s identify the earthquake (just one in this case) and the station. The function $f_M(\cdot)$ will be different for

Table 3
Event Terms for the NGA GMPEs Determined from Stations at Distances under 100 km

	Acceleration				Velocity			
GMPE	E_e	ε_a	σ^{IIE}	e^{E_e}	E_e	ε_v	σ^{IIE}	e^{E_e}
Abrahamson and Silva (2008) $\sigma^I_a = 0.573$, $\sigma^I_v = 0.583$ $\sigma_{\text{Events},a} = 0.326$, $\sigma_{\text{Events},v} = 0.319$	1.08	3.3	0.59	2.95	0.60	1.9	0.52	1.82
Boore and Atkinson (2008) $\sigma^I_a = 0.564$, $\sigma^I_v = 0.560$ $\sigma_{\text{Events},a} = 0.260$, $\sigma_{\text{Events},v} = 0.256$	0.84	3.2	0.57	2.32	0.51	2.0	0.53	1.67
Campbell and Bozorgnia (2008) $\sigma^I_a = 0.515$, $\sigma^I_v = 0.525$ $\sigma_{\text{Events},a} = 0.219$, $\sigma_{\text{Events},v} = 0.203$	0.98	4.5	0.59	2.66	0.32	1.6	0.52	1.37
Chiou and Youngs (2008) $\sigma^I_a = 0.549$, $\sigma^I_v = 0.540$ $\sigma_{\text{Events},a} = 0.271$, $\sigma_{\text{Events},v} = 0.241$	1.32	4.8	0.62	3.74	0.54	2.2	0.54	1.71
Average	1.05			2.87	0.49			1.63

PGA and PGV. Higher roman numeral superscripts are used to indicate standard deviations after removal of potential epistemic terms. The standard deviation corresponding to equation (1) is

$$\sigma^I = \sqrt{\frac{1}{N_{es} - 1} \sum_{e,s} (\delta^I_{es})^2}, \tag{2}$$

where the total number of data is N_{es}. The event term E_e is the mean of the residuals in a single event over all stations:

$$E_e = \frac{1}{N_s} \sum_{s=1}^{N_s} \delta^I_{es}, \tag{3}$$

where N_s is the number of stations observing the event. As a measure of the variability of events used to develop the GMPE, it is convenient to define σ_{Events} as the standard deviation of E_e, and the deviation of a single event from average as

$$E_e = \varepsilon \sigma_{\text{Events}}, \tag{4}$$

(in the notation of Rodriguez-Marek *et al.*, 2011, the event term E_e is the between-event residual or interevent residual, and $\sigma_{\text{Events}} = \tau$). Because the main hazard is at close distances, Table 3 gives E_e for PGA and PGV, for stations at distances under 100 km. GMPEs considered are the NGA relations of Abrahamson and Silva (2008), Chiou and Youngs (2008), and Campbell and Bozorgnia (2008) at $r_{\text{flt}} < 100$ km, and for Boore and Atkinson (2008) with $r_{\text{JB}} < 100$ km. The unexplained residual, $\delta^{IIE}_{es} = \delta^I_{es} - E_e$ (δW_{es} in the notation of Rodriguez-Marek *et al.*, 2011) has zero mean and standard deviation σ^{IIE} (ϕ in the notation of Rodriguez-Marek *et al.*, 2011), also given in Table 3. The σ^{IIE} corresponds to the within-event standard deviations of the GMPEs. These σ^{IIE} are not optimized because the site conditions are not treated on a station-by-station basis.

The GMPE column in Table 3 gives the average standard deviation, σ^I for PGA and PGV, and σ_{Events}, the standard deviation of the event terms as determined by each respective model. For models in which the standard deviation depends on distance and amplitude, σ^I is the average of the value appropriate for each datum. This is a reasonable approximation because the distance dependence of σ^I is weak, if present, in the models. The columns with ε_a and ε_v in Table 3 are the event terms normalized by σ_{Events} as in equation 4. For instance, the event term for PGA relative to the Abrahamson and Silva (2008) relationship is +3.3 standard deviations of the event term, determined from all earthquakes used to develop the model, above the median curve. The columns with e^E convert the log values of the event terms into numerical ratios. Thus, the mean PGA observation is 2.95 times the prediction of Abrahamson and Silva (2008).

Table 3 finds that for PGA the range of σ^{IIE}, from 0.57–0.62, is similar to that found by Anderson and Uchiyama (2011) in Guerrero (0.61), similar to the estimate of Rodriguez-Marek *et al.* (2011) for Japan (0.62), and similar to the standard deviations of the NGA models. For PGV the range of σ^{IIE} from 0.52–0.54 is slightly smaller than the Guerrero estimate (0.57), but similar to the standard deviations of the NGA models. Thus, the variability of these uncorrected data are in a reasonable range.

On the other hand, Table 3 finds that the event terms are high for all four NGA models. PGAs are 3.2–4.8 standard deviations above the NGA models, with an average of about 4 times greater than the respective models ($\sim +4\sigma_{\text{Event},a}$). PGVs average about 2 times greater ($\sim +2\sigma_{\text{Event}}$). The deviations of PGV would have a low probability, but the deviations for PGA would seem to have such a low probability as to demand further study.

Discussion: What Causes the High Event Terms?

We consider four possible explanations for the high event terms of this earthquake at short distances: (1) site

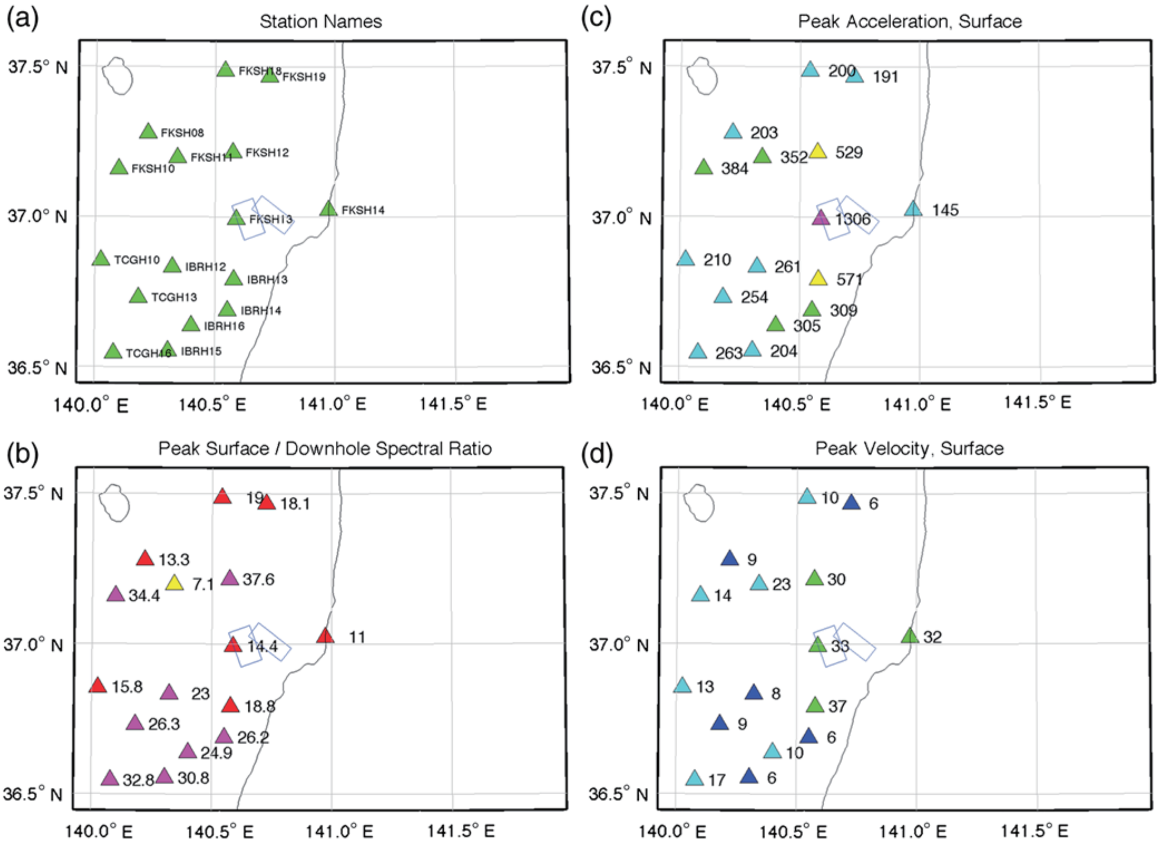

Figure 6. KiK-net maps showing (a) station name, (b) peak surface/downhole spectral ratio, (c) surface PGA (cm/s^2), and (d) surface PGV (cm/s). Peaks of acceleration and velocity are the peak amplitude of the vector sum of the two horizontal components. The color version of this figure is available only in the electronic edition.

effects are inadequately explained using V_{S30}; (2) the source has a high stress drop, or is otherwise radiating excessive energy at the frequencies controlling PGA; (3) the two subparallel faults are radiating simultaneously, increasing the amplitudes of shaking; or (4) the GMPEs are underpredicting the ground motions. Directivity was not considered because the source is surrounded by stations. The different slopes of the NGA curves and the data beyond 100 km (Figs. 4 and 5), probably result from differences in attenuation but large event terms at short distances are difficult to explain by differences in attenuation.

Site Effects

The comparisons in Figures 4 and 5 already incorporate parameter choices in the NGA relations appropriate for the median value of V_{S30}. However, there are reasons to expect that V_{S30} by itself is not sufficient to characterize the site conditions. For instance, Atkinson and Casey (2003) compared amplitudes of pseudoacceleration response spectra (5% damping) at four oscillator frequencies from earthquakes in southern Japan and Washington State of similar mechanism and magnitude. Noting that different velocity profiles can have the same value of V_{S30}, they explained higher average amplitudes at 10 Hz in the Japanese event by the differences in average site profiles. Amplification was calculated using the quarter-wavelength method (Boore and Joyner, 1997). This method does not recognize resonant peaks, but for constant V_{S30} a site with a thin low-velocity layer will have higher amplification than a site with a low-velocity gradient. Thus, characterizing the site response using V_{S30} alone is inadequate to fully characterize site response.

Before adjusting for site effects, we view some seismograms and their spectra. Figure 6 shows maps of KiK-net stations within about 50 km of the Fukushima Hamadori source. All stations in KiK-net have downhole accelerometers at a typical depth of 100 m in addition to surface accelerometers. Although the downhole instrument may be affected by site response to some extent, the differences between the surface and downhole records provide much information about site response at these stations. Figure 6 also maps the peak vector acceleration, peak vector velocity, and

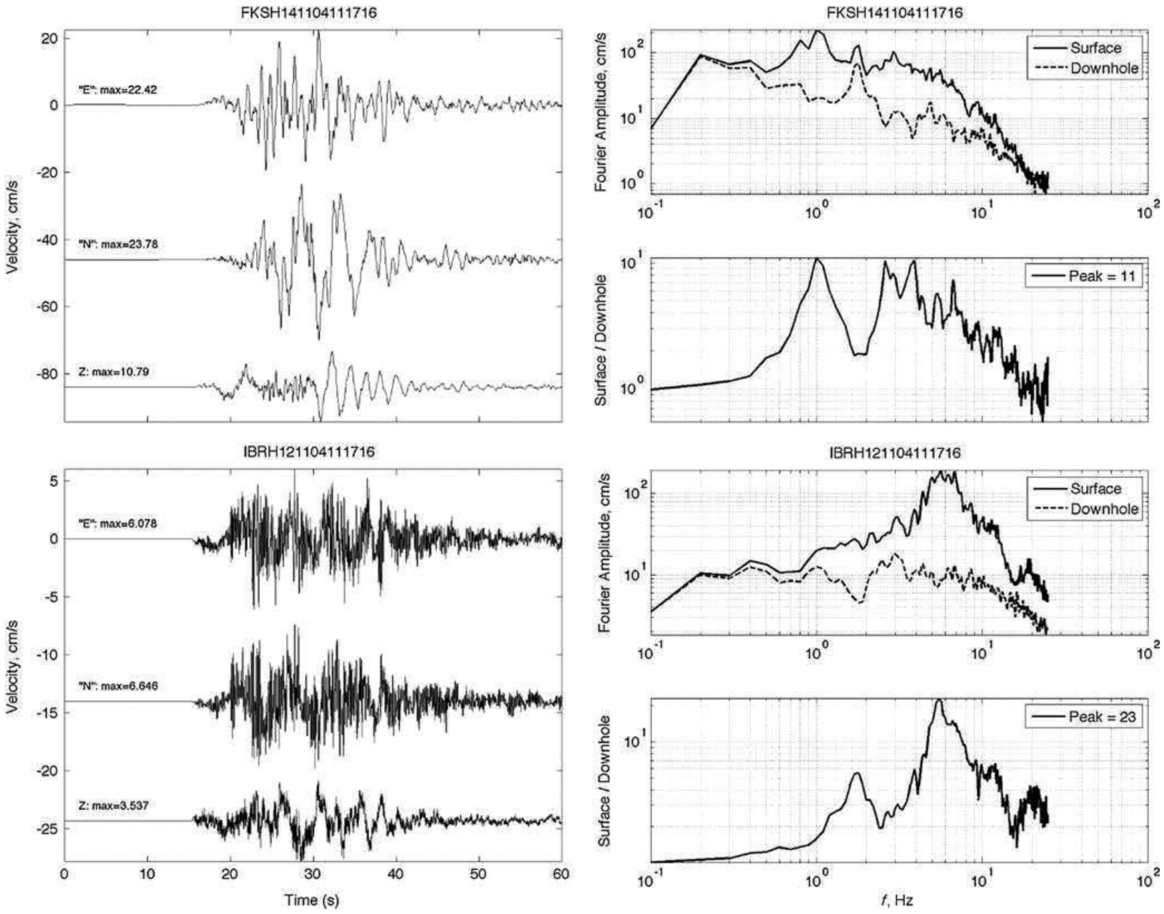

Figure 7. Velocity seismograms and Fourier amplitude spectra at two KiK-net stations. Station locations are shown in Figure 6. The velocity seismograms are from the surface components. For FKSH14, $r_{\mathrm{flt}} = 13.4$ km, $a_{\mathrm{GM}} = 129$ cm/s^2, and $v_{\mathrm{GM}} = 23.1$ cm/s. For IBRH12, $r_{\mathrm{flt}} = 33.5$ km, $a_{\mathrm{GM}} = 208$ cm/s^2, and $v_{\mathrm{GM}} = 6.3$ cm/s. Fourier spectra show Fourier amplitudes of acceleration. Spectra of the two horizontal components are smoothed in a way that approximately conserves the energy (or to be more precise, the Arias intensity) of the spectrum, and then the vector sum of the two horizontal components is formed. Spectra processed in this way are shown for both the surface and downhole components, along with the ratio of surface/downhole.

the peak of the ratio of smoothed surface to downhole spectral amplitudes. A peak spectral ratio of under 6.0 was used by Anderson (2013) to recognize sites with a minimum distortion from surface layers. Figure 6 indicates that none of the sites in this region meet that criterion for the Fukushima Hamadori earthquake, but some are close.

Figure 7 shows velocity seismograms and Fourier spectra of acceleration for two of the KiK-net sites. Station FKSH14 has one of the lower surface/downhole ratios on Figure 6b. The surface spectrum is relatively flat to first order, with some fine structure superimposed on the overall spectral shape. In contrast, station IBRH12 has a prominent narrow peak at about 5–7 Hz. The high peak is associated with conspicuous ringing that dominates the surface accelerogram and is even conspicuous on the surface-velocity seismograms. This record contrasts sharply with the record from station FKSH14 in which the velocity seismogram shows relatively very little high-frequency shaking. Inspection of seismograms and spectra at the KiK-net sites suggest that IBRH12 is more typical of accelerograms from this region. Stations with high surface/downhole spectral ratios in Figure 6b show similar phenomena to the resonance at IBRH12, and contribute high positive residuals in Figure 4.

Figure 8 shows maps of K-NET stations, at which there are only surface accelerometers. Instead of spectral ratios, this figure shows $V_{S30}^{\min}$ for each station. Perusal of Figure 8 shows that there is a correlation between high values of $V_{S30}^{\min}$ and low PGA. Some of the Fourier spectra show prominent peaks like the peak at station IBRH12 in Figure 7; others do not. Figure 9 shows velocity seismograms and Fourier spectra for two stations, FKS011 and FKS014, which do not have prominent resonances. The residuals at stations FKSH14,

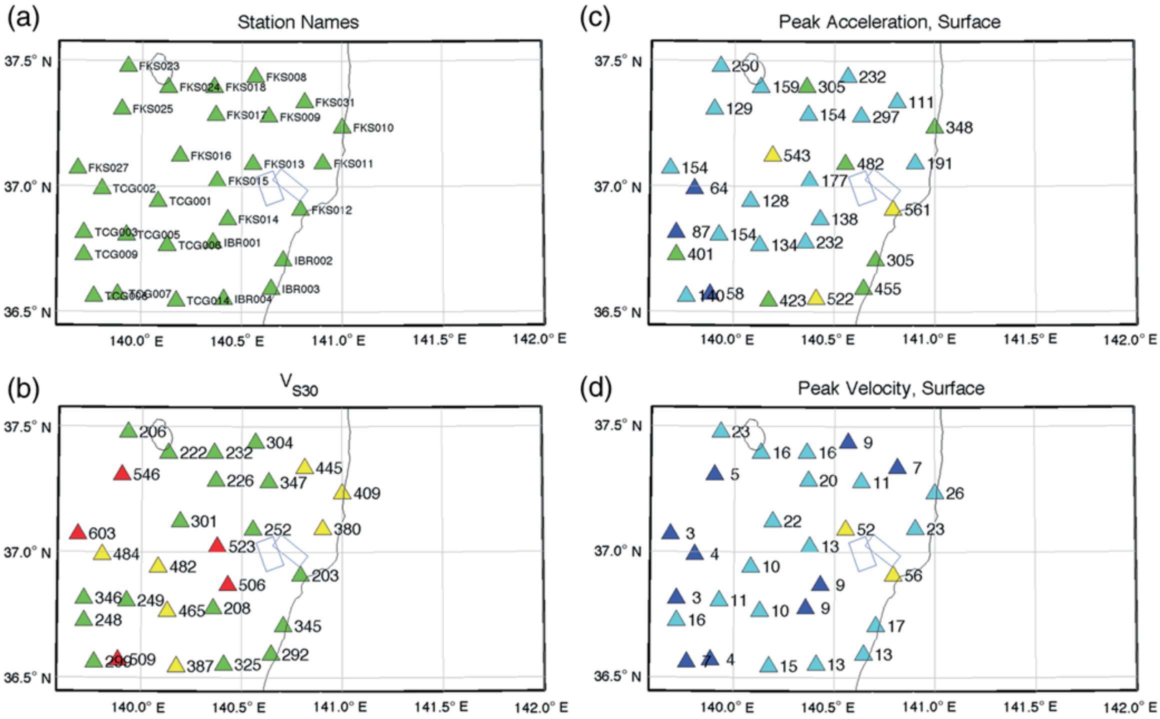

Figure 8. K-NET composite figure showing (a) station name, (b) estimates of V_{S30} in m/s, (c) PGA in cm/s^2, and (d) PGV in cm/s. Peaks of acceleration and velocity are the peak amplitude of the vector sum of the two horizontal components. The estimates of V_{S30} are lower bounds based on profiles provided by NIED. The site profiles are available to depths of up to 20 m, so these estimates extend the deepest measured value to 30 m. Any station, for which velocity increases between the bottom of the borehole and 30 m, will have a larger value of V_{S30} than the value given here. The color version of this figure is available only in the electronic edition.

FKS011, and FKS014 are all reasonably consistent with the GMPEs.

First Adjustment for Site Response. The results shown in Figures 7 and 9 suggest that, as in the case of Atkinson and Casey (2003), a systematic adjustment for site response at all the stations might reduce or even eliminate the discrepancy between the data and models. They further suggest that the ground motions on the most rock-like stations might be relatively consistent with the NGA relations.

Several models have already been developed to characterize the site response, including nonlinear behavior, at all or most of the individual K-NET and KiK-net stations (e.g., Moya and Irikura, 2003; Kawase and Matsuo, 2004a,b; Wu *et al.*, 2009). In this section, we therefore apply one of these models that applies station-specific adjustments found using prior earthquakes to reduce each of the KiK-net and K-NET peak motion observations in the Fukushima Hamadori earthquake to motion expected on rock site conditions. This differs from Atkinson and Casey (2003), who used corrections for large site classes rather than using site factors that are customized on a station-by-station basis.

The model we use is described in Kawase and Matsuo (2004a,b) and Kawase (2006). Kawase and Matsuo (2004a) defined a reference site with shear velocity of 3.45 km/s that extends to the surface. Then using moderate-sized earthquakes for each station separately, they found correction factors that adjust the observed PGA and PGV of a record to the peak acceleration and velocity at the reference site with the shear velocity of 3.45 km/s.

GMPEs used in this paper are defined as a function of V_{S30}, but $V_{S30} = 3450$ m/s is outside of their ranges of validity. Thus, we select $V_{S30} = 760$ m/s for the comparison, because that is the reference site condition for the U.S. National Hazard Map. To adjust the difference of a reference site between $V_{S30} = 3450$ m/s and $V_{S30} = 760$ m/s, we use the empirical relationship for average amplification as a log-linear function of V_{S30} (Kawase and Matsuo, 2004b). Thus, the observed value of PGA and PGV is divided by the site-specific adjustment, and then multiplied by the reference correction factor (1.91 for PGA and 2.66 for PGV).

Figure 10 shows adjustments from raw PGA and PGV to a site with $V_{S30} = 760$ m/s, as a function of estimates of V_{S30}. The estimates of V_{S30} are not used in our procedure, but they provide a convenient parameter to use for displaying the adjustments. For K-NET stations, Figure 10 uses $V_{S30}^{\min}$. For KiK-net stations, the NIED website gives measured values of shear velocity to depths of 100 m or more that are used

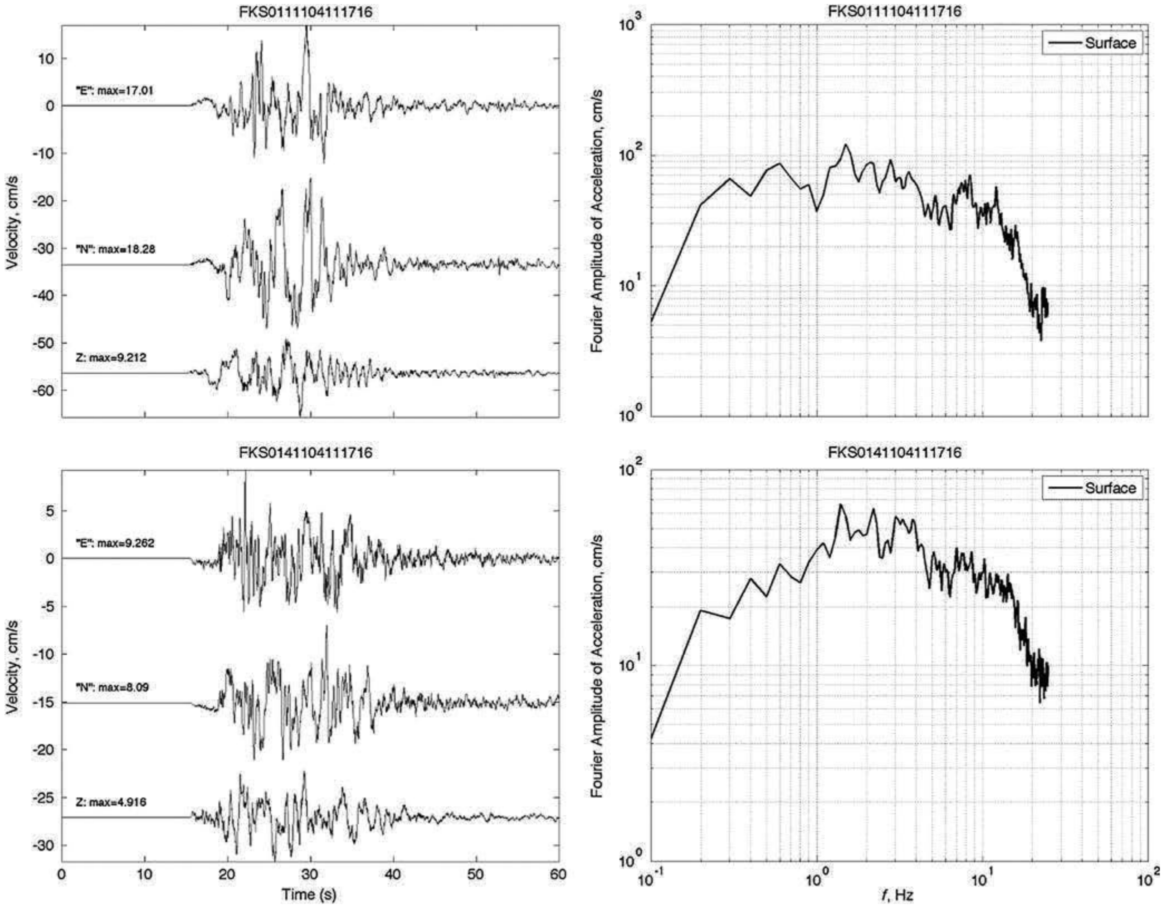

Figure 9. Velocity seismograms and Fourier amplitude spectra at two K-NET stations. Station locations are shown in Figure 8. For station FKS011, $r_{\rm flt} = 13.3$ km, $a_{\rm GM} = 188$ cm/s^2, and $v_{\rm GM} = 17.6$ cm/s and for station FKS014, $r_{\rm flt} = 24.0$ km, $a_{\rm GM} = 111$ cm/s^2, and $v_{\rm GM} = 8.7$ cm/s. Fourier spectra are smoothed as in Figure 7.

to calculate V_{S30}. Figure 10 also shows adjustments used by Atkinson and Casey (2003), which do depend on estimates of V_{S30}. Notable features of Figure 10 are the high variability of the adjustments within small ranges of V_{S30}, the tendency of adjustments to decrease as V_{S30} increases, and that the adjustments appear on average to be smaller than those of Atkinson and Casey (2003).

Although the adjustments in Figure 10 are determined from a different data set, this step can be considered approximately equivalent to the station correction step in Anderson and Uchiyama (2011). Designating the Kawase and Matsuo (2004a,b) corrections as S_s ($\delta S2S_s$ in the notation of Rodriguez-Marek *et al.*, 2011), the new residuals are

$$\delta_{es}^{IIS} = \delta_{es}^{I} - S_s. \tag{5}$$

New estimates of the event terms ($E_e^{(2)}$) can be found by averaging δ_{es}^{IIS}. The residuals after removing these event terms are

$$\delta_{es}^{III} = \delta_{es}^{IIS} - E_e^{(2)} \tag{6}$$

($\delta W_{o,es}$ in the notation of Rodriguez-Marek *et al.*, 2011) and the standard deviation of these residuals is σ^{III} (ϕ_{SS} in the notation of Rodriguez-Marek *et al.*, 2011).

The adjustments in Figure 10 have been applied to the PGAs on Figure 4 and the PGVs on Figure 5. In Figures 11 and 12, the adjusted points are compared with four NGA models for $V_{S30} = 760$ m/s.

Figure 13 shows the residuals (δ_{es}^{IIS}) and the event term ($E_e^{(2)}$) for one of the NGA relations, Campbell and Bozorgnia (2008), as a function of distance. Table 4 gives, for the adjusted peak values, statistical parameters equivalent to those for the unadjusted residuals in Table 3.

One surprising result is that the adjustment has significantly reduced the standard deviation of the residuals. The decrease is made possible because the adjustments are customized to the stations. The change can be seen by

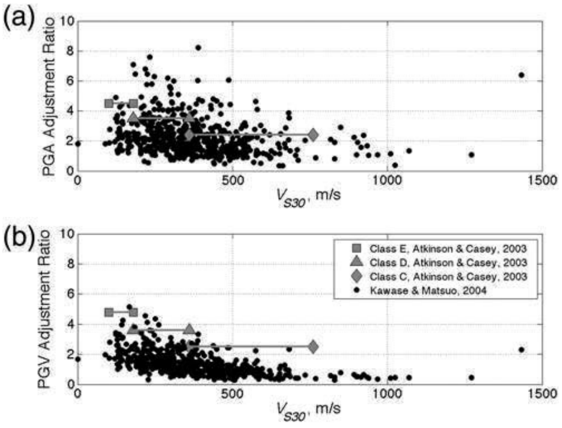

Figure 10. Custom station adjustments for PGA and PGV from Kawase and Matsuo (2004a,b), used in this paper to adjust observed values to a site with $V_{S30} = 760$ m/s. The adjustments are plotted as a function of estimated values of V_{S30} for each site, as explained in the text. Estimates of V_{S30} are not used in this paper, but are used by Atkinson and Casey (2003). Adjustment factors attributed to Atkinson and Casey (2003) are developed for response spectra, not PGA or PGV. For PGA, (a) their adjustments for 5 Hz, and for PGV, (b) their adjustments for 2.5 Hz.

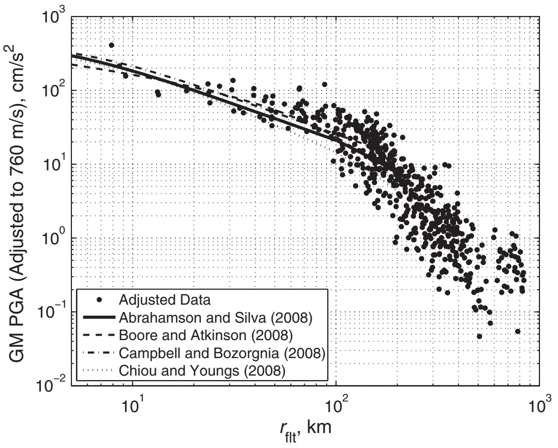

Figure 11. PGA, adjusted to $V_{S30} = 760$ m/s, using the adjustment factors from Kawase and Matsuo (2004a,b). The NGA model predictions in this figure also use $V_{S30} = 760$ m/s.

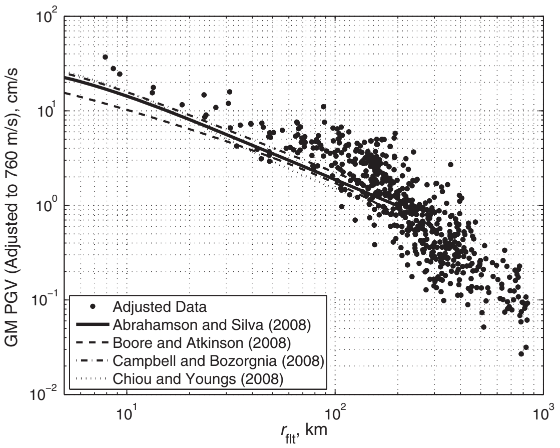

Figure 12. PGV, adjusted to $V_{S30} = 760$ m/s, using the adjustment factors from Kawase and Matsuo (2004a,b). The NGA model predictions in this figure also use $V_{S30} = 760$ m/s.

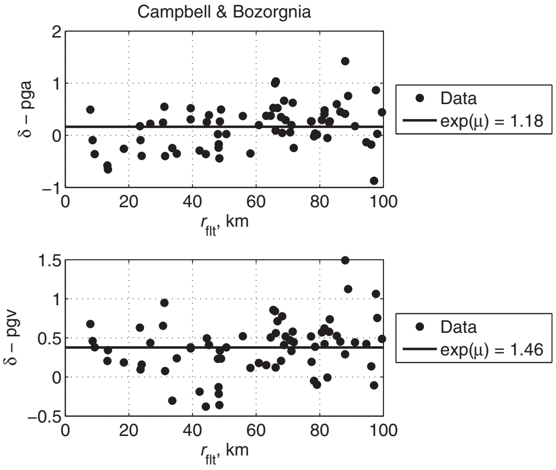

Figure 13. Residuals of PGA and PGV to the Campbell and Bozorgnia (2008) ground-motion prediction equation. As shown in Table 4, this model has the lowest residuals of the four NGA relations.

comparing σ^{IIE} in Table 3 with σ^{III} in Table 4. The standard deviations decrease from ~0.59 to ~0.42 for PGA, and from ~0.53 to ~0.35 for PGV. In their pilot study of peak motions recorded in Mexico, Anderson and Uchiyama (2011) found a comparable $\sigma^{III} = 0.42$ for PGA, and larger $\sigma^{III} = 0.46$ for PGV. Rodriguez-Marek *et al.* (2011) found a larger value for PGA (0.497). Overestimates of seismic hazard can result from the ergodic assumption (Anderson and Brune, 1999a), and examples such as this of single-station sigma provide annecdotal examples on the lower limits of sigma for future GMPE development.

This adjustment also has a significant effect on the event terms. For PGA and PGV, the mean event terms have been decreased by a factor of ~2.1 and increased by ~10% respectively. In spite of these adjustments, the event terms are still positive. Table 4 finds that the PGAs average about 1.3 times greater than the model ($\sim + 1.7\sigma_{\mathrm{Events},a}$), and that the PGVs average about 1.7 times greater than the model ($\sim + 2.2\sigma_{\mathrm{Events},v}$). These event terms are still high, but the estimates of median acceleration are greatly improved. It is worth noting that the adjustment by site class of Atkinson

Table 4
Event Terms for the NGA GMPEs, after Adjusting for the Kawase and Matsuo (2004a) Site Response Terms

GMPE	Acceleration				Velocity			
	E_e	ε_a	σ^{III}	e^{E_e}	E_e	ε_v	σ^{III}	e^{E_e}
Abrahamson and Silva (2008)	0.35	0.60	0.42	1.42	0.52	0.90	0.35	1.69
$\sigma_a^I = 0.586$ $\sigma_v^I = 0.583$								
$\sigma_{\text{Events},a} = 0.326$ $\sigma_{\text{Events},v} = 0.319$								
Boore and Atkinson (2008)	0.11	0.20	0.41	1.12	0.59	1.05	0.34	1.80
$\sigma_a^I = 0.564$ $\sigma_v^I = 0.560$								
$\sigma_{\text{Events},a} = 0.260$ $\sigma_{\text{Events},v} = 0.256$								
Campbell and Bozorgnia (2008)	0.16	0.31	0.42	1.18	0.38	0.72	0.35	1.46
$\sigma_a^I = 0.524$ $\sigma_v^I = 0.525$								
$\sigma_{\text{Events},a} = 0.219$ $\sigma_{\text{Events},v} = 0.203$								
Chiou and Youngs (2008)	0.58	1.04	0.47	1.79	0.69	1.26	0.37	2.00
$\sigma_a^I = 0.557$ $\sigma_v^I = 0.545$								
$\sigma_{\text{Events},a} = 0.271$ $\sigma_{\text{Events},v} = 0.241$								
Average	0.30			1.35	0.54			1.72

and Casey (2003), which on average exceed our adjustments (Fig. 10), reduced event terms to near zero for the event in their study.

All four of the NGA relations have a term for normal-faulting mechanisms. The terms for normal faulting modify the predicted log (base e) of the PGA in the Abrahamson and Silva (2008), Boore and Atkinson (2008), Campbell and Bozorgnia (2008), and Chiou and Youngs (2008) models by −0.06, −0.25, −0.12, and −0.25, respectively, in which the negative sign indicates reduction. The respective adjustments for PGV are −0.06, −0.45, 0.0, and −0.06. For PGA, without the normal-faulting adjustments the Boore and Atkinson (2008) model would have essentially no residual, and Campbell and Bozorgnia (2008) event term would be smaller than the interevent standard deviation, $\sigma_{\text{Events},a}$. For PGV, without the normal-faulting term the Boore and Atkinson (2008) model would overestimate the adjusted data. With these exceptions, the normal-faulting adjustments are not, by themselves, possible explanations for underestimating the ground motions in the Fukushima Hamadori earthquake.

Stress Drop

There are several ways that stress drop is measured. Studies of the Fukushima Hamadori earthquake allow estimates of the static stress drop, and provide estimates and comparisons with other earthquakes of stress drop determined from energy and high-frequency spectral amplitudes.

To evaluate the static stress drop we consider how the seismic moment might be divided between the two overlapping ruptures. With overlapping ruptures, it is unclear how to estimate the static stress drop for this event, so we consider some alternative models. These are presented in Table 5. The two most commonly used rupture models are the circular fault model and the dip-slip fault model (Kanamori and Anderson, 1975). The model for a dip-slip earthquake assumes that the fault is long compared to its width. Because that is not the case for either of the faults that ruptured in the Fukushima Hamadori earthquake, we use the equation for a circular fault,

$$\Delta\tau_S = \frac{7\pi}{16}\mu\frac{\bar{D}_E}{R_E}, \tag{7}$$

where $\Delta\tau_S$ is the static stress drop, $\bar{D}_E$ is the mean slip, and R_E is the radius of a circular fault with the same area as the rectangular approximations given in Table 2. With these assumptions, Table 5 gives the mean slip and the stress drop for five alternative distributions of the seismic moment from Table 1 between the two active faults.

Because they overlap, extreme models would be to put all the moment on one, and to consider the other to be sympathetic (Fraction = 1.0 cases in Table 5). These lead to $\Delta\tau_S = 6.7$ MPa if all the moment is released on the Idosawa fault, and $\Delta\tau_S = 8.4$ MPa if entirely on the Yunotake fault. A model that divides the moment in proportion to the maximum surface slip, which was 2.0 m on the Idosawa fault and 0.8 m on the Yunotake fault, would have $f_{\text{slip}} = 2.0/(2.0 + 0.8) = 0.71$ of the slip would be on the Idosawa fault. This is close to dividing the moment 75:25 between the Idosawa and Yunotake faults, and leads to $\Delta\tau_S = 5.0$ MPa and $\Delta\tau_S = 2.1$ MPa, respectively. Dividing the moment equally between the two faults leads to $\Delta\tau_S = 3.3$ and 4.2 MPa, respectively. In summary, assuming both faults contributed

Table 5
Mean Slip and Stress-Drop Estimates for the Two Faults Active in the Fukushima Hamadori Earthquake

		Fraction of Total Moment on the Idosawa Fault				
Fault		1.0	0.75	0.5	0.25	0.0
Idosawa	$\bar{D}_E$, cm	149	112	75	37	
	$\Delta\tau_S$, MPa	6.7	5.0	3.3	1.7	
Yunotake	$\bar{D}_E$, cm		43	87	131	174
	$\Delta\tau_S$, MPa		2.1	4.2	6.3	8.4

to the moment, the static stress drops on each fault are in the range from 2–5 MPa.

A global study of earthquakes based on teleseismic observations (Allmann and Shearer, 2009) found that the stress drop for normal-faulting mechanisms is distributed primarily from 1–10 MPa, with a mean value apparently about 3 MPa. This suggests that the static stress drop on the two primary faults in the Fukushima Hamadori earthquake is similar to other normal faults.

Another potentially useful way to compare with other results would be based on results of Hecker *et al.* (2010). This study determines the ratio of maximum displacement to rupture length. From Table 2, this ratio is 1.5×10^{-4} for the Idosawa fault, and 0.5×10^{-4} for the Yunotake fault. The former is in a range of ratios typical of faults with smaller cumulative displacement in Hecker *et al.* (2010), whereas the latter is lower than most faults in their data set. In summary, the static stress drop associated with the Fukushima Hamadori earthquake is in a range that is typical of other earthquakes with normal-faulting mechanisms.

Nakano (2013) determined stress drop for several of the earthquakes in the Fukushima Hamadori sequence. Extending the approach of Kawase and Matsuo (2004a), they combined the seismic moment determined from regional recordings based on F-NET data (Okada *et al.*, 2004) and corner frequency measured from local stations to find the stress drop using the equations in Brune (1970). By their results, $\Delta\sigma_{\mathrm{Brune}} = 3.1$ MPa. This is within the range of the stress parameters found by Nakano (2013) for other Japanese earthquakes with $M_{\mathrm{w}} \gtrsim 5.3$, with reverse or strike-slip mechanisms.

Satoh and Tsutsumi (2012) measured the short-period spectral level of the Hamadori earthquakes and compared that with other Japanese events. According to their model, the short-period level is proportional to the product of a stress-drop parameter (not necessarily the same as $\Delta\sigma_{\mathrm{Brune}}$) and fault radius. They find that their stress parameter is approximately constant for events with $M_{\mathrm{w}} \gtrsim 5.7$, with reverse-faulting earthquakes having a higher stress parameter, on average, than strike-slip-faulting earthquakes. They find that the Fukushima Hamadori mainshock has a stress parameter, which is intermediate between the overlapping populations of reverse and strike-slip stress parameters.

Finally, Somei *et al.* (2012) find stress drop using the spectra of coda waves to find seismic moment and corner frequency, following the approach of Mayeda and Walter (1996). They find relatively small scatter in stress-drop estimates for $M_{\mathrm{w}} \gtrsim 4.5$. In this range, and by this method, they find that the stress drop of strike-slip- and reverse-mechanism earthquakes overlap almost completely, and that the Fukushima Hamadori normal faulting event is near the center of that range.

In summary, it appears that the static stress drop of the Fukushima Hamadori earthquake is consistent with the global population of normal-faulting earthquakes and that the other stress parameters are consistent with the Japanese population of strike-slip and reverse earthquakes.

Simultaneous Rupture of the Two Main Faults

The results presented in the previous section indicate that the static stress drop of the two faults, taken individually, is fairly typical of normal-faulting earthquakes. However, given the overlap of the geometry, if the two faults ruptured simultaneously the combined radiation from the two ruptures might be a cause of the above-average ground motions.

Hikima (2012) inverted the strong-motion waveforms to find a kinematic model of slip in the earthquake. He finds that the Idosawa fault slipped first, and the Yunotake fault slipped second. In this model, the Idosawa fault slip takes place in the first 8 seconds after the origin time, with the largest slip in the time interval from 3–7 seconds. The major rupture on the Yunotake segment takes place in the interval from about 9–13 seconds.

Shiba and Noguchi (2012) also found a kinematic model for the source based on waveform inversion. In their model, slip also occurs first on the Idosawa fault, and has largely ended on that fault after about 6 s. Rupture on the Yunotake fault in this model starts at about 5 s and ends at about 13 s after the origin. Thus, their model allows simultaneity of rupture during only a small part of the earthquake.

Both of these studies, then, find sequential rupture of the two segments, rather than simultaneous rupture. Given the small separation of the two faults, there would be little overlap in ground motion from the two segments, probably not significantly more than the overlap in ground motion from multisegment ruptures of faults in which subsequent segments follow a more linear geometry.

GMPE Calibrations

The fourth hypothesis for the high event terms that needs to be considered closely is the calibration of the GMPEs. As noted in Figure 1, the data at large magnitude and small distance used to calibrate the GMPEs for the effect of normal faulting in the NGA relations is sparse. In the preliminary findings above, other obvious factors do not seem to explain the somewhat high event terms, leaving the calibration of the GMPEs as an obvious potential contributor.

Additional Considerations

There are two themes of evidence that might support the idea that the NGA relations are reasonably correct and the event terms are high for this particular event.

Precarious Rocks. Brune (2000, 2003) discusses precariously balanced rocks (PBRs) in normal-faulting and transtensional environments. For the sake of this discussion, a PBR is a rock that is balanced on, but not mechanically attached to, its pedestal, and has a high enough ratio of height to width that it is easily toppled by strong ground motions (Anderson *et al.*, 2011). For instance, some of the PBRs that have been cited to constrain ground motions 15 km from the San Andreas fault are expected to topple in ground motions with PGAs exceeding ~0.4*g*. Brune (2000) observed equally fragile PBRs located on the footwall close to several normal faults with Quaternary activity. Based on this, and supported by the physical model results of Brune and Anooshehpoor (1999), he proposed the hypothesis that normal-faulting events at short distances on the footwall (e.g., less than 3 km from the fault trace) do not, in general, cause ground motions sufficient to topple many precarious rocks, as they would at a comparable distance from the trace of a strike-slip or thrust fault. Brune (2003) suggests that ground motions also tend to be low near transtensional stepovers of strike-slip faults. Of the three examples presented there, the Honey Lake zone of precarious rocks is most relevant (Briggs *et al.* [2013]). The rocks there are on the footwall of a normal fault associated with a major extensional stepover of strike-slip faults.

Unfortunately, none of the ground motions observed in the Fukushima Hamadori earthquake are located in a position to test the hypothesis in Brune (2000), and this earthquake has the wrong mechanism to test the Brune (2003) hypothesis. Only two K-NET stations (FKS010 and FKS011; Fig. 8) and one KiK-net station (FKSH14; Fig. 6) are at an azimuth, which can be considered to sample the footwall ground motions, and all three are over 10 km from the vertical projection of the fault. The K-NET stations both have relatively high values of V_{S30}, and the KiK-net station has a relatively low surface/downhole ratio. Thus, all three are expected to have somewhat lower ground motions based on site condition properties. To the extent that these three stations have below-average ground motions, the cause is ambiguous at best and would require more study.

A loose extrapolation of the Brune (2000, 2003) studies, however, leads one to consider the hypothesis that ground motions in normal and transtensional environments are generally lower than in strike-slip environments. This hypothesis is consistent with the normal-faulting adjustments that were discussed previously. Thus, it is reasonable to ask whether the observed ground motions imply that precarious rocks any place would be toppled. Precarious rocks are situated on solid rock pedestals, so correction of ground motions to rock site conditions ($V_{S30} = 760$ m/s) is essential to compare with their hypothesis.

All but one of the PGAs are corrected to below 0.3*g* (Fig. 11). The lone exception is station FKSH13. This station is above the deepest part of the fault on the hanging wall (Fig. 6), and thus does not test the Brune (2000) hypothesis. We consider whether ground motion on rock at this location would have caused precarious rocks to be toppled. The initial adjustment for site response would seem to suggest ground motions capable of causing at least some precarious rocks to topple. The geometric mean horizontal PGA at site FKSH13 is adjusted from 922 cm/s^2 to 709 cm/s^2. The geometric mean horizontal PGV at site FKSH13 is practically unchanged, adjusting from 30.6 cm/s to 30.5 cm/s^2. The toppling of precarious rocks depends on both parameters. The value of PGA is essential as a threshold to initiate rocking and depends on the shape of the rock. The additional PGV threshold (or a related measure of longer period motions such as spectral acceleration for an oscillator period of 1.0 s) depends on the size of the rock. A PGV of 30 cm/s is sufficient to cause smaller precarious rocks to topple, but large rocks (e.g., more than 2 m high) may require higher velocities.

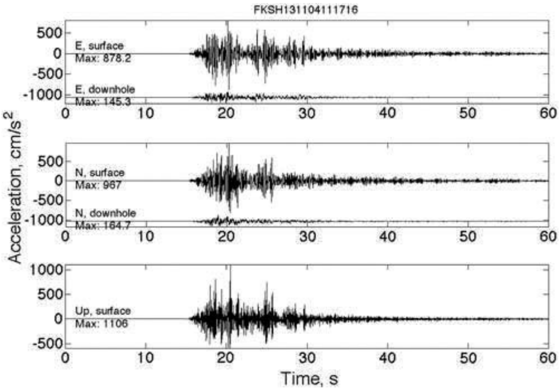

Figure 14. Surface and downhole accelerogram from surface sensors at FKSH13. The vertical component of the downhole sensor did not produce a seismogram.

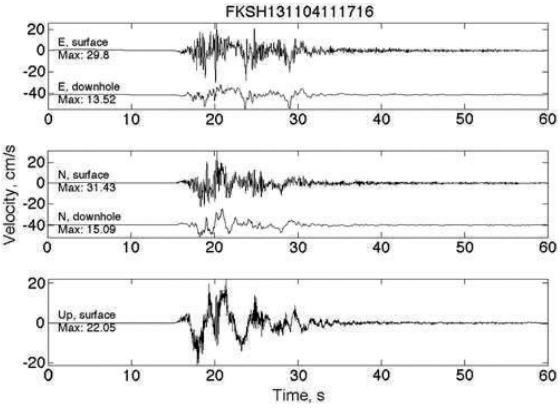

Figure 15. Surface and downhole velocity at FKSH13. The vertical downhole sensor did not produce a seismogram.

Figure 14 shows the surface and downhole acceleration, Figure 15 shows the surface and downhole velocity, and Figure 16a shows the Fourier spectra of the record from station FKSH13. The vector horizontal PGA at the surface was 1306 cm/s^2, whereas downhole it was 179 cm/s^2 (Fig. 16b). The Fourier spectra show a very broad peak of amplification from 3–12 Hz, peaking at 6–7 Hz, that is responsible for the large surface acceleration. The velocity seismogram shows prominent high-frequency energy at this spectral peak, similar to IBRH12 in Figure 7. Thus, this location appears to have a contribution to shaking from resonant site conditions. A station on solid rock might have expected acceleration two–three times the downhole value, but the peak may be

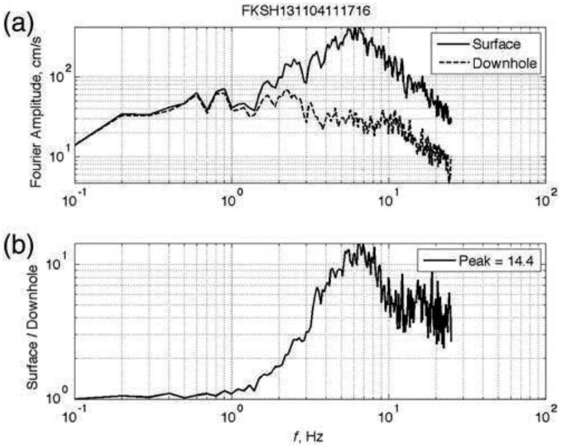

Figure 16. (a) Smoothed horizontal surface and downhole spectra at FKSH13. (b) Ratio of horizontal surface to horizontal downhole Fourier spectra.

smaller than the adjusted PGA based on the Kawase and Matsuo (2004a,b) correction. A correction of the seismogram in the frequency domain would be needed to more accurately predict these effects, but such a correction is beyond the scope of this paper. All of these things considered, a solid rock outcrop at the location of this station would likely have accelerations capable of toppling most precarious rocks. Thus, an extrapolation of the Brune (2000, 2003) hypotheses to infer reduced shaking at all distances from a normal fault would not be supported by this data.

1954 Cabin. Finally, we consider Figure 17, a classic picture of a normal-fault scarp in Nevada, formed in the M_w 6.9 Dixie Valley earthquake of 16 December 1954. Figure 18 shows a different view of the cabin, which shows that the cabin is in a graben caused by the faulting. A remarkable observation by the scientists investigating the faulting was that except for the tilt due to differential settlement near the fault, the structure was essentially undamaged. Furthermore, inside the structure a tin cup had not even been shaken off the shelf (Slemmons, 1957; Steinbrugge and Moran, 1957). As with the precarious rocks discussed by Brune (2000), this evidence suggests that motions near the fault were not particularly severe, even as the ground failed on the hanging wall. Slemmons (1957) also noted that in the Dixie Valley settlement three miles (~5 km) east of this cabin, above the hanging wall, "the up-and-down motion was so strong as to throw some of the residents out of bed and then repeatedly knock them to the floor as they made their way outdoors." He also notes that the movement of objects inside buildings was spatially inconsistent. At the Dixie Valley settlement, on sediments, Slemmons reports at least one home in which essentially everything that could be moved was shaken to the floor, as would be expected from an acceleration of the nature of what was observed at FKSH13.

Figure 17. Cabin adjacent to fault that ruptured in the 1954 Dixie Valley earthquake (M_w 6.9). The photograph was taken on 20 December 1954 by Karl Steinbrugge. The man in the photo is Vincent Bush, a member of the team investigating the earthquake. Source: Karl V. Steinbrugge Collection: S653, National Information Service for Earthquake Engineering (NISEE), University of California, Berkeley. The color version of this figure is available only in the electronic edition.

Figure 18. Karl Steinbrugge standing next to the cabin at the 1954 Dixie Valley rupture (M_w 6.9). The photograph was taken on 20 December 1954 by Donald Moran. Source: Karl V. Steinbrugge Collection: S662, National Information Service for Earthquake Engineering (NISEE), University of California, Berkeley. The color version of this figure is available only in the electronic edition.

Accelerations and velocities that are much stronger above the hanging wall are predicted by a lattice model of normal faulting (Shi *et al.*, 2003). The lattice model also predicts that these strong motions extend all the way to the fault scarp. Thus, the inferred low amplitudes very near the fault trace at the cabin may be a local effect brought about by highly nonlinear response of the sediments in the fault zone (as can be observed by the shattered surface around the cabin in Fig. 17), whereas motions farther away may be larger.

Indeed, besides this anecdotal evidence of strong shaking on the hanging wall a few kilometers from the fault trace, the lack of precarious rocks provides some support for the suggestion that low accelerations do not persist to larger distances on the hanging wall. Purvance *et al.* (2008) find precarious rocks that constrain past ground motions in a granite outcrop on the hanging wall of one splay of the active Genoa fault in western Nevada. However, one of us (JNB) has found that similar granites located 5–10 km from the fault on the hanging wall have no precarious rocks, and indeed rather have the appearance of extensive rockfalls such as might be expected to be triggered by strong shaking. All of this evidence is consistent with the idea that the frictional forces, which must be overcome at depth to cause a normal-faulting earthquake, and the consequent seismic radiation, are comparable to the forces associated with other mechanisms.

We are not aware of any detailed intensity surveys near the faults that broke in the Fukushima Hamadori earthquake. Koarai and Okaya (2011) and Hisada (2012) reported a small number of Japanese wooden houses, which were heavily damaged, but almost all of them seem to be associated with either fault movement or ground failure (including liquefaction) so that they are not indicative of severe ground motions. At first glance, this lack of heavy damage to wooden houses elsewhere may suggest weak ground motions, contrary to the Dixie Valley observation. However, to create heavy damage to Japanese wooden houses we need both high PGA and high PGV, namely PGA $\geq 0.8g$ and PGV ≥ 100 cm/s based on the damage survey in Kobe (Kawase, 2011). From the KiK-net and K-NET records (Figs. 6 and 8) PGV in the source region is not observed in excess of 53 cm/s, which is well below 100 cm/s, so the absence of severe damage to wooden houses is exactly what we should expect. So far as we know, a detailed survey of the effect of the shaking on contents of the structures in the region has not been carried out yet, so a basis for comparison with Dixie Valley apparently does not exist.

Summary

To sample two parts of the seismic spectrum in a preliminary assessment of the potential impact of this event on prediction of median estimates of ground motion in normal-faulting earthquakes, this paper compared observed PGA and PGV with the median values of four NGA relations. The models for PGA are generally lower than the observations in the Fukushima Hamadori earthquake by a factor of ~2.3–3.7, depending on the GMPE, at all distances to 100 km. For PGV the differences are smaller, with the data exceeding the predictions by factors of 1.4–1.8.

We consider four hypotheses to explain this. The first is that the Fukushima Hamadori earthquake is unusual for normal faulting. The case for this is perhaps easily made; it is triggered by a large subduction-zone earthquake, so it might be easy to presume it should be different from other events. However, aside from this unusual triggering, we are unable to identify physical parameters describing the faulting that set this earthquake apart. Several stress-drop measurements of the Fukushima Hamadori earthquake are similar to measurements from other crustal earthquakes in Japan. The comparison events predominantly have strike-slip or reverse mechanism. Second, we find that the available kinematic models of the Fukushima Hamadori earthquake show the two participating faults ruptured sequentially, so simultaneous contributions from those two faults does not appear to be a viable explanation for the high event terms.

Another alternative is that the records of the event have higher motions than average due to a prevalence of sites with strong resonances. Our corrections are based on customized station terms found by Kawase and Matsuo (2004a,b). These station terms cause a significant reduction in the standard deviation of corrected data from the GMPEs, and thus provide strong support for the idea that corrections based on data from smaller earthquakes can improve ground-motion prediction over models based on simplified site parameters such as V_{S30}. These corrections also strongly reduced the event term for PGA, indicating the power of customized site terms to impact mean ground-motion predictions. The event terms remaining after this correction are sensitive to the empirical adjustment of Kawase and Matsuo between $V_{S30} = 3450$ m/s and $V_{S30} = 760$ m/s. Because the data used by Kawase and Matsuo (2004a,b) are scattered, an objective for future studies could be to seek additional theoretical guidance for the form and size of that adjustment, and to understand the differences from adjustments used by Atkinson and Casey (2003).

More sophisticated site correction is still possible, such as adjustment of records for Fourier spectral amplifications determined by joint inversions for source, path, and site effects (e.g., Kawase, 2006). Thus, the test of the effect of site response in this paper is incomplete, but if we accept the preliminary results we would conclude that site effects account for a large part of the large event term for PGA. If we presume that adjustments for site resonance could completely explain the high event term, it raises complex issues for ground-motion prediction. It casts doubt on the efficacy of V_{S30} alone to model these effects even to first order, and implies resonance needs to be built into the models. To achieve that, the model will need to be based on perterbations from a reference-site velocity and density profile.

The last alternative is that GMPEs have underestimated accelerations for large normal-faulting events at distances larger than about 5 km, for which the instrumental data from the Fukushima Hamadori earthquake provide control. Observational geologic data, mainly from precariously balanced rocks, suggest that this may not be the case at closer distances. An underestimate of ground motions at high frequencies would primarily affect hazard estimates on the U.S. National Seismic Hazard Map in regions dominated by normal faulting, such as the Basin and Range region. To the extent that these Japanese data influence future GMPEs, this might result in a small increase in the hazard in a future version of the U.S. national map.

Data and Resources

The NIED website for site velocity profiles and accelerograms from K-NET and KiK-net stations is now (http://www.kyoshin.bosai.go.jp/), last accessed November 2012. We accessed the same data from predecessors to the current site: for K-NET: (http://www.k-net.bosai.go.jp/, last accessed January 2012) and for KiK-net (http://www.kik.bosai.go.jp/kik/index_en.shtml, last accessed January 2012). GMPEs of Abrahamson and Silva (2008), Boore and Atkinson (2008), Chiou and Youngs (2008), and Campbell and Bozorgnia (2008) were calculated using the Attenuation Relationship Plotter in OPEN_SHA (Field *et al.*, 2003; http://www.opensha.org/, last accessed January 2012). The NGA flatfile is available from PEER (http://peer.berkeley.edu/nga/flatfile.html, last accessed August 2012). Strong-motion data from Italy is available from http://itaca.mi.ingv.it/ItacaNet/itaca10_links.htm (last accessed January 2013), and from Greece is available from http://www.itsak.gr/en/page/data/strong_motion/ (last accessed January 2013). The Global Centroid Moment Tensor Project database was searched using www.globalcmt.org/CMTsearch.html (last accessed January 2013).

Acknowledgments

The authors thank Hiroe Miyake and Hongjun Si for providing information, which was not otherwise available, and for several very helpful interactions. John Anderson thanks the Earthquake Research Institute of the University of Tokyo for supporting a sabbatical visit and a return visit to Tokyo, which provided invaluable insights and interactions making this paper possible. Burt Slemmons identified critical references for the 1954 earthquake, and helped identify the man in the cabin-fault photo. Adrian Rodriguez-Marek provided helpful comments on an early version of this paper. This paper also benefited from helpful reviews by Gail Atkinson, Ivan Wong, and an anonymous reviewer. We thank the National Research Institute for Earth Science and Disaster Prevention for the making the K-NET and KiK-net strong-motion data and downhole profiles freely available. This study was completed with partial support from the U.S. Geologial Survey NEHRP External Grants Program, under Award Number G12AP20024.

References

Abrahamson, N. A., and W. Silva (2008). Summary of the Abrahamson & Silva NGA ground-motion relations, *Earthq. Spectra* **24,** 67–97.

Aki, K., and P. G. Richards (2002). *Quantitative Seismology*, Second Ed., University Science Books, Sausalito, California, 700 pp.

Allmann, B. P., and P. M. Shearer (2009). Global variations of stress drop for moderate to large earthquakes, *J. Geophys. Res.* **114,** B01310, doi: 10.1029/2008JB005821.

Anderson, J. G. (2013). Surface motions on near-distance rock sites in the 2011 Tohoku earthquake, *Earthq. Spectra* **29,** no. S1, S23–S35.

Anderson, J. G., and J. N. Brune (1999a). Probabilistic seismic hazard analysis without the ergodic assumption, *Seismol. Res. Lett.* **70,** 19–28.

Anderson, J. G., and Y. Uchiyama (2011). A methodology to improve ground-motion prediction equations by including path corrections, *Bull. Seismol. Soc. Am.* **101,** no. 4, 1822–1846, doi: 10.1785/0120090359.

Anderson, J. G., J. N. Brune, G. Biasi, A. Anooshehpoor, and M. Purvance (2011). Workshop report: Applications of precarious rocks and related fragile geological features to U. S. National Hazard Maps, *Seismol. Res. Lett.* **82,** no. 3, 431–441, doi: 10.1785/gssrl.82.3.431.

Atkinson, G. M., and R. Casey (2003). A comparison of ground motions from the 2001 M 6.8 in-slab earthquakes in Cascadia and Japan, *Bull. Seismol. Soc. Am.* **93,** 1823–1831.

Bindi, D., F. Pacor, L. Luzi, R. Puglia, M. Massa, G. Ameri, and R. Paolucci (2011). Ground motion prediction equations derived from the Italian strong motion database, *Bull. Earthq. Eng.* **9,** 1899–1920, doi: 10.1007/s10518-011-9313-z.

Boore, D. M., and G. M. Atkinson (2008). Ground-motion prediction equations for the average horizontal component of PGA, PGV, and 5%-damped PSA at spectral periods between 0.01 s and 10 s, *Earthq. Spectra* **24,** 99–138.

Boore, D. M., and W. B. Joyner (1997). Site amplifications for generic rock sites, *Bull. Seism. Soc. Am.* **87,** 327–341.

Boore, D. M., E. M. Thompson, and H. Cadet (2011). Regional correlations of V_{S30} and velocities averaged over depths less than and greater than 30 meters, *Bull. Seismol. Soc. Am.* **101,** 3046–3059.

Briggs, R. W., S. G. Wesnousky, J. N. Brune, M. D. Purvance, and S. A. Mahan (2013). Low footwall accelerations and variable surface rupture behavior on the Fort Sage Mountains fault, northeast California, *Bull. Seism. Soc. Am.* **103,** no. 1, 157–168.

Brune, J. N. (1970). Tectonic stress and the spectra of seismic shear waves from earthquake, *J. Geophys. Res.* **75,** 4997–5009.

Brune, J. N. (2000). Precarious rock evidence for low ground shaking on the footwall of major normal faults, *Bull. Seismol. Soc. Am.* **90,** 1107–1112.

Brune, J. N. (2003). Precarious rock evidence for low near-source accelerations for transtensional strike-slip earthquakes, *Phys. Earth Planet. In.* **137,** 229–239.

Brune, J. N., and A. Anooshehpoor (1999). Dynamic geometrical effects on strong ground motion in a normal fault model, *J. Geophys. Res.* **104,** 809–815.

Campbell, K. W., and Y. Bozorgnia (2008). NGA ground motion model for the geometric mean horizontal component of PGA, PGV, PGD and 5% damped linear elastic response spectra for periods ranging from 0.01 to 10 s, *Earthq. Spectra* **24,** 137–171.

Chiou, B. S.-J., and R. R. Youngs (2008). An NGA model for the average horizontal component of peak ground motion and response spectra, *Earthq. Spectra* **24,** 173–215.

Chiou, B., R. Darragh, N. Gregor, and W. Silva (2008). NGA Project strong-motion database, *Earthq. Spectra* **24,** 23–44.

Field, E. H., T. H. Jordan, and C. A. Cornell (2003). OpenSHA: A developing community-modeling environment for seismic hazard analysis, *Seismol. Res. Lett.* **74,** no. 4, 406–419.

Geology Research Team (2011). *Landforms, geology, and active faults* (in Japanese), Powerpoint presentation, download from http://www.pwri.go.jp/eng/news/2011/0602/ (last accessed 4 May 2012).

Hecker, S., T. E. Dawson, and D. P. Schwartz (2010). Normal-faulting slip maxima and stress-drop variability, *Bull. Seismol. Soc. Am.* **100,** 3130–3147.

Hikima, K. (2012). Rupture process of the April 11, 2011 Fukushima Hamadori earthquake (M_j 7.0), *Zishin* **64,** 243–256 (in Japanese).

Hisada, Y., T. Kubo, K. Matsuzawa, T. Matsumoto, A. Tanabe, and A. Morikawa (2012). Investigation of building damage near the surface faults of 2011 Fukushima-ken-Hama-Dori earthquake, special issue, *J. Japan Assoc. Earthq. Eng.* **12,** no. 4, 104–126, doi: 10.5610/jaee.12.4_104.

Imanishi, K., R. Ando, and Y. Kuwahara (2012). Unusual shallow normal-faulting earthquake sequence in compressional northeast Japan activated after the 2011 off the Pacific coast of Tohoku earthquake, *Geophys. Res. Lett.* **39,** L09306, doi: 10.1029/2012GL051491.

Kanamori, H., and D. L. Anderson (1975). Theoretical basis of some empirical relations in seismology, *Bull. Seismol. Soc. Am.* **65,** 1073–1095.

Kato, A., S. Sakai, and K. Obara (2011). A normal-faulting seismic sequence triggered by the 2011 off the Pacific coast of Tohoku earthquake: Wholesale stress regime changes in the upper plate, *Earth Planets Space* **63,** no. 7, 745–748, doi: 10.5047/eps.2011.06.014.

Kawase, H. (2006). Site effects derived from spectral inversion method for K-NET, KiK-net, and JMA strong-motion network with special reference to soil nonlinearity in high PGA records, *Bull. Earthq. Res. Inst. Tokyo Univ.* **81,** 309–315.

Kawase, H. (2011). Strong motion characteristics and their damage impact to structures during the Off Pacific Coast of Tohoku Earthquake of March 11, 2011: How extraordinary was this M 9.0 earthquake?, in *Proc. of the 4th IASPEI/IAEE International Symposium on Effects* *of Surface Geology on Seismic Motion, August 23–26, 2011*, University of California Santa Barbara, Santa Barbara, California.

Kawase, H., and H. Matsuo (2004a). Amplification characteristics of K-NET, KiK-NET, and JMA Shindokei network sites based on the spectral inversion technique, in *13th World Conference on Earthquake Engineering*, Vancouver, Canada, Paper No. 454.

Kawase, H., and H. Matsuo (2004b). Relationship of S-wave velocity structures and site effects separated from the observed strong motion data of K-NET, KiK-net, and JMA network, *J. Japan Assoc. Earthq. Eng.* **4**, no. 4, 126–145 (in Japanese).

Kinoshita, S. (1998). Kyoshin net (K_NET), *Seismol. Res. Lett.* **69,** 309–332.

Kinoshita, S. (2005). Development of strong-motion observation network constructed by NIED, in *Directions in Strong Motion Instrumentation*, P. Gulkan and J. G. Anderson (Editors), NATO Science Series IV, Earth and Environmental Sciences, Vol. 58, Springer, Dordrecht, the Netherlands, 181–196.

Koarai, M., and T. Okaya (2011). *Field Survey Report (Supplement) on the Seismic Damage around Iwaki City* (in Japanese), downloaded from http://www.gsi.go.jp/common/000060960.pdf (last accessed 24 June 2012).

Luzi, L., F. Sabetta, F. Mele, and B. Castello (2010). Italian strong motion database relative to the period 1972–2004: Motivations and aims, *Bull. Earthq. Eng.* **8,** 1159–1174, doi: 10.1007/s10518-009-9140-7.

Maruyama, T., A. Saito, T. Azuma, K. Taniguchi, M. Yoshimi, and T. Hayashida (2011). *Reconnaissance Survey Report on the Surface Ruptures along the Idosawa Fault Associated with the Fukushima Hamadori Earthquake of April, 11, 2011* (in Japanese), downloaded from http://unit.aist.go.jp/actfault-eq/Tohoku/report/idosawa/idosawa.pdf (last accessed 4 May 2012).

Massa, M., F. Pacor, L. Luzi, D. Bindi, G. Milana, F. Sabetta, A. Gorini, and S. Marcucci (2010). The ITalian ACcelerometric Archive (ITACA): Processing of strong-motion data, *Bull. Earthq. Eng.* **8,** 1175–1187, doi: 10.1007/s10518-009-9152-3.

Mayeda, K., and W. R. Walter (1996). Moment, energy, stress drop, and source spectra of western U.S. earthquakes, *J. Geophys. Res.* **101,** 11,195–11,208.

Moya, A., and K. Irikura (2003). Determination of site effects and Q factor using a reference event, *Bull. Seismol. Soc. Am.* **93,** 1730–1745.

Nakano, K. (2013). Statistical properties of strong ground motions based on the spectral inversion method, *Master's Thesis*, 28 February 2013, Dept. of Engineering, Kyoto University, Kyoto, Japan (in Japanese).

Okada, Y., K. Kasahara, S. Hori, K. Obara, S. Sekiguchi, H. Fujiwara, and A. Yamamoto (2004). Recent progress of seismic observation networks in Japan, Hi-net, F-net, K-NET and KiK-net, *Earth Planets Space* **56,** xv–xxviii.

Pacor, F., R. Paolucci, L. Luzi, F. Sabetta, A. Spinelli, A. Gorini, M. Nicoletti, S. Marcucci, L. Filippi, and M. Dolce (2011). Overview of the Italian strong motion database ITACA 1.0, *Bull. Earthq. Eng.* **9,** 1723–1739, doi: 10.1007/s10518-011-9327-6.

Petersen, M. D., A. D. Frankel, S. C. Harmsen, C. S. Mueller, K. M. Haller, R. L. Wheeler, R. L. Wesson, Y. Zeng, O. S. Boyd, D. M. Perkins, N. Luco, E. H. Field, C. J. Wills, and K. S. Rukstales (2008). Documentation for the 2008 Update of the United States National Seismic Hazard Maps, *U.S. Geological Survey Open-File Report 2008–1128*, 61 pp.

Power, M., B. Chiou, N. Abrahamson, Y. Bozorgnia, T. Shantz, and C. Roblee (2008). An overview of the NGA project, *Earthq. Spectra* **24,** 3–21.

Purvance, M. D., J. N. Brune, N. A. Abrahamson, and J. G. Anderson (2008). Consistency of precariously balanced rocks with probabilistic seismic hazard estimates in southern California, *Bull. Seismol. Soc. Am.* **98,** 2629–2640.

Rodriguez-Marek, A., G. A. Montalva, F. Cotton, and F. Bonilla (2011). Analysis of single-station standard deviation using the KiK-net data, *Bull. Seismol. Soc. Am.* **101,** no. 3, 1242–1258, doi: 10.1785/0120100252.

Ryder, I., A. Rietbrock, K. Kelson, R. Burgmann, M. Floyd, A. Socquet, C. Vigny, and D. Carrizo (2012). Large extensional aftershocks in the continental forearc triggered by the 2010 Maule earthquake, Chile, *Geophys. J. Int.* **188,** 879–890.

Satoh, T., and H. Tsutsumi (2012). Short-period spectral level, path and site-amplification derived from strong motion records during the normal-faulting earthquakes in Hamadori, Fukushima Prefecture in 2011, *J. Japan Assoc. Earthq. Eng.* **12,** no. 7, 1–18 (in Japanese).

Shi, B., J. N. Brune, Y. Zeng, and A. Anooshehpoor (2003). Dynamics of earthquake normal faulting: Two-dimensional lattice particle model, *Bull. Seismol. Soc. Am.* **93,** 1179–1197.

Shiba, Y., and S. Noguchi (2012). Statistical characteristics of seismic source parameters controlling broadband strong ground motions—Investigation based on source inversion analysis, *CRIEPI Rept. N11054*, 28 pp. (in Japanese).

Si, H., and S. Midorikawa (1999). New attenuation relationships for peak ground acceleration and velocity considering effects of fault type and site condition, *J. Struct. Constr. Eng.*, Architectural Institute of Japan, no. 523, 63–70 (in Japanese).

Si, H., and S. Midorikawa (2000). New attenuation relations for peak ground acceleration and velocity considering effects of fault type and site condition, in *Proceedings, 12th World Conference on Earthquake Engineering*, 30 January–4 February 2000, Auckland, New Zealand, New Zealand Society for Earthquake Engineering, Upper Hutt, New Zealand, Paper 0532.

Si, H., T. Kawasato, M. Ohba, T. Ishikawa, T. Masatsuki, and A. Sawaii (2012). A comparison of existing ground motion prediction equation to normal faulting earthquake, in *Summaries of Technical Papers of Annual Meeting, Architectural Institute of Japan, B-2*, 177–178 (in Japanese).

Slemmons, D. B. (1957). Geological effects of the Dixie Valley-Fairview Peak, Nevada, earthquakes of December 16, 1954, *Bull. Seism. Soc. Am.* **47**, 353–375.

Somei, K., K. Asano, T. Iwata, and K. Miyakoshi (2012). Comparisons of source characteristics between recent inland crustal earthquake sequences inside and outside of Niigata-Kobe tectonic zone, Japan, Poster S53A-2488, *American Geophysical Union Fall Annual Meeting*, San Francisco.

Spudich, P., W. B. Joyner, A. G. Lindh, D. M. Boore, B. M. Margaris, and J. B. Fletcher (1999). SEA99: A revised ground motion prediction relation for use in extensional regimes, *Bull. Seismol. Soc. Am.* **89,** 1156–1170.

Steinbrugge, K. V., and D. F. Moran (1957). Engineering aspects of the Dixie Valley-Fairview Peak earthquakes, *Bull. Seism. Soc. Am.* **47,** 335–348.

Theodulidis, N., I. Kalogeras, C. Papazachos, V. Karastathis, B. Margaris, Ch. Papaioannou, and A. Skarlatoudis (2004). HEAD 1.0: A unified HEllenic accelerogram database, *Seismol. Res. Lett.* **75,** 36–45.

Wu, C., Z. Peng, and D. Assimaki (2009). Temporal changes in site response associated with the strong ground motion of the 2004 Mw 6.6 Mid-Niigata earthquake sequences in Japan, *Bull. Seismol. Soc. Am.* **99,** no. 6, 3487–3495, doi: 10.1785/0120090108.

Nevada Seismological Laboratory
University of Nevada
Reno, Nevada 89557
jga@unr.edu
(J.G.A., G.P.B., J.N.B.)

DPRI
Kyoto University
Gokasho, Uji
Kyoto 611-0011, Japan
kawase@zeisei.dpri.kyoto-u.ac.jp
(H.K.)

Natl Res Inst Earth Sci & Disaster Prevention (NIED)
3-1 Tennodai, Tsukuba
Ibaraki 305-0006, Japan
aoi@bosai.go.jp
(S.A.)

Manuscript received 8 August 2012

The Composite Source Model for Broadband Simulations of Strong Ground Motions

by John G. Anderson

INTRODUCTION

My goal is to generate synthetic strong ground motions that are sufficiently realistic to be useful for engineering applications. The composite source model (CSM) uses a kinematic source model for rupture on a finite fault. This source is propagated to the station using a flat-layered velocity model, scattering, and attenuation that can be measured from independent seismological observations. A key objective is to reproduce the wave propagation within the constraints of the measured velocity and Q structure. This article summarizes the CSM as implemented for the Southern California Earthquake Center (SCEC) Broadband Platform validation exercise (Goulet *et al.*, 2015).

HISTORY

The CSM was first described by Yu (1994) and Zeng *et al.* (1994). Motivated by Frankel (1991), the model describes the source slip function as a superposition of overlapping circular subevents of random sizes, located randomly on the fault. Multiple source realizations naturally result in different seismograms. Zeng and Anderson (1996) and Zeng and Chen (2001) demonstrated that it is possible to find a specific realization of the CSM that reproduces the low-frequency accelerograms in Northridge and Chi-Chi earthquakes and that the slip functions resemble the slip function determined by other methods. Additional applications of the model include Khattri *et al.* (1994), Yu *et al.* (1995), Anderson and Yu (1996), and Su, Anderson, Ni, *et al.* (1998), Su, Anderson, Zeng (1998), and Hartzell *et al.* (2011).

Variations of the original model have been proposed (e.g., Zeng *et al.*, 1991, 1995). For simplicity, the current implementation is close to the basic version, although some aspects of the Broadband platform implementation have not been described elsewhere. For this reason, this article gives a brief summary of the model on the Broadband Platform.

THEORETICAL BASIS

Representation Theorem

The theoretical basis for understanding ground motion from a finite fault is the representation theorem (e.g., Aki and Richards, 2002). Through the representation theorem, the problem of predicting ground motions is reduced to specification of the offset on the fault as a function of location and time, and calculations of the Green' s function.

Composite Source Model Description

The slip function on the fault is treated as a superposition of subevents that are located at random on the fault. Each subevent can be visualized as having a circular cross section, where subevents can overlap. The rupture time of each subevent is determined by its distance from the hypocenter, using a constant rupture velocity, V_r. The moment of each subevent depends on the subevent radius R_i and the subevent stress drop $\Delta\tau_S$. V_r and $\Delta\tau_S$ are model parameters, whereas the radii R_i are chosen at random from a probability distribution. The moment of the ith subevent, with radius R_i, is, from Kanamori and Anderson (1975)

$$M_{0i} = \frac{16}{7}\Delta\tau_S R_i^3. \tag{1}$$

The time function of slip on each subevent is the source time function given by Brune (1970, 1971). To be specific, for a subevent with radius R_i the corner frequency of the subevent is

$$f_c^i = \frac{2.34\beta}{2\pi R_i}, \tag{2}$$

and the time function is then given by

$$\dot{M}_{0i} = (2\pi f_{ci})^2 M_{0i} H(\tau)\tau e^{-2\pi f_c \tau}, \tag{3}$$

in which $\tau = t - t_i$, in which t_i is the start time of the subevent: $t_i = x_{\text{hyp}}/v_r$ in which x_{hyp} is the path distance of the subevent center to the hypocenter measured along the fault, and v_r is the rupture velocity. Zeng *et al.* (1991) implemented the Sato and Hirasawa (1973) pulse instead of the Brune pulse. The Sato and Hirasawa pulse is an option controlled by input on the Broadband Platform, but in this article all results use the Brune pulse.

The distribution of subevent sizes, and thus of rise times among the subevents, motivated by Frankel (1991) is controlled by fractal dimension D. Specifically, the distribution of subevents with radius R or greater is given by Zeng *et al.* (1994) as

doi: 10.1785/0220140098

$$N(R) = \frac{P}{D}\left(R^{-D} - R_{\max}^{-D}\right), \qquad (4)$$

in which P is determined by the constraint that the sum of the moments of the subevents equals M_0, the moment of the earthquake being modeled. Consequently,

$$P = \frac{7M_0}{16\Delta\tau_S}\frac{3-D}{(R_{\max}^{3-D} - R_{\min}^{3-D})}\,(D \neq 3). \qquad (5)$$

My calculations use $D = 2$, because then the distribution of subevent sizes follows a Gutenberg–Richter distribution with the b-value $b = D/2 = 1$. The parameter $R_{\max}$ in equation (4) is the maximum subevent radius. My practice is to set $R_{\max}$ equal to half of the smaller fault dimension. The minimum subevent radius $R_{\min}$ is currently chosen by $R_{\min} = R_{\max}/20$. The moment of a subevent with radius $R_{\max}$ is 8000 times greater than a subevent with radius $R_{\min}$, and the magnitude difference is 2.6 magnitude units. Even though there are 400 times as many earthquakes of this size, they have little numerical significance.

Only $\Delta\tau_S$ is varied when the goal is to find a model-matching statistical properties of a suite of strong-motion observations from an earthquake. Increasing the value of $\Delta\tau_S$ has two effects. The first is that each subevent has a higher average slip, so the amplitude of the radiation from each subevent is increased. Countering that trend, the number of subevents needed to match M_0 decreases. Because M_0 is not changed, the low-frequency radiation of the fault is not affected by $\Delta\tau_S$. However, the net effect of increasing $\Delta\tau_S$ is an increase of the amplitude of the high frequencies in the seismogram. Beyond the variability in the locations and sizes of subevents, some source variability arises when a random realization does not match the target seismic moment. In this case, the moment is matched by adjusting $\Delta\tau_S$ in equation (1) without changing the number, location, or radii of subevents. Anderson (1997) found that $\Delta\tau_S$ is proportional to radiated energy and apparent stress, so the CSM has the flexibility to match both of the important stress parameters.

Figure 1 illustrates the source in three ways: the point location of subevents with contours showing rupture time, subevent locations with circles of radius R_i showing the part of the rupture represented by each subevent, and with contours illustrating the spatial distribution of slip represented by the sum of all subevents. Figure 2 shows the moment rate represented by this model and its displacement and acceleration spectra. In Figure 2, the source time function is slightly longer than 11 s, in which 11 s is the largest rupture time contoured in Figure 1. The corner frequency corresponding to $R_{\min}$ is about 3 Hz, and the acceleration spectrum of this model is essentially flat at higher frequencies. The acceleration spectrum also shows two corner frequencies, at about 0.2 Hz and about 3 Hz.

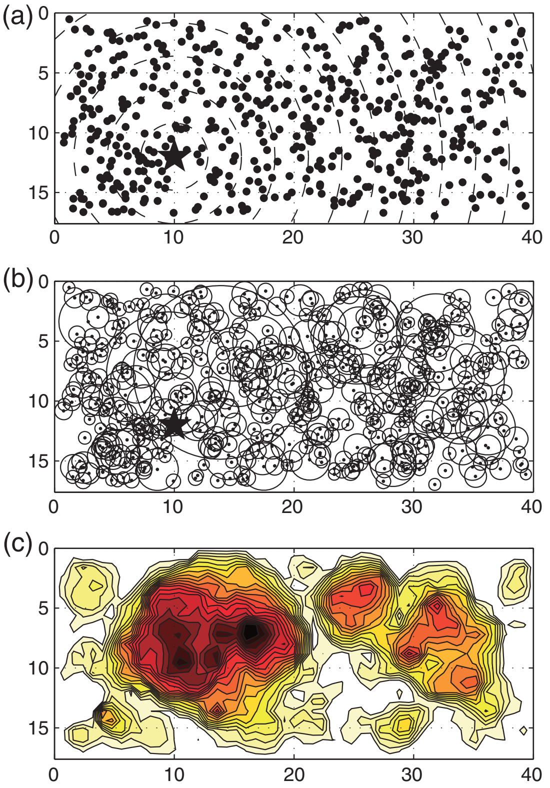

▲ **Figure 1.** Composite source illustrated in three ways to emphasize different features. (a) Locations of the 528 subevents for one realization of an M_w 6.9 earthquake on a fault that is 40 km long and 17.5 km wide. The dashed lines indicate the locations of the rupture front in 1 s intervals. Radiation of each subevent is triggered when the rupture front reaches its center. (b) The source radiation from each subevent is visualized as originating from a crack bounded by a circle centered on each subevent. The subevent radii are chosen randomly from the distribution in equation (4). Subevents are not allowed to overlap the fault borders. (c) The slip modeled in each subevent is displayed here with an elliptical cross section for each subevent, superimposed and contoured.

Green's Function

The Green's function is calculated using the approach of Luco and Apsel (1983), using a FORTRAN code written by Y. Zeng. Luco and Apsel derive the response of a layered half-space using propagator matrices in the frequency–wavenumber domain, organized in a way that has very good numerical stability. The inverse transform over wavenumber is performed by a numerical integration. The time series is then recovered using an inverse fast Fourier transform. Static offset is included in the synthetic seismograms. It is possible to implement a frequency-dependent Q in the Luco and Apsel (1983) model, but in the present version Q is independent of frequency. The treatment of the frequency dependence observed in Q is described subsequently. A typical application calculates the synthetic Green's functions from 0 to 25 Hz. For the SCEC Broadband implementation, all seismograms are found for a common site condition, but for other applications the shallow layers in the velocity model can be tailored to the local site.

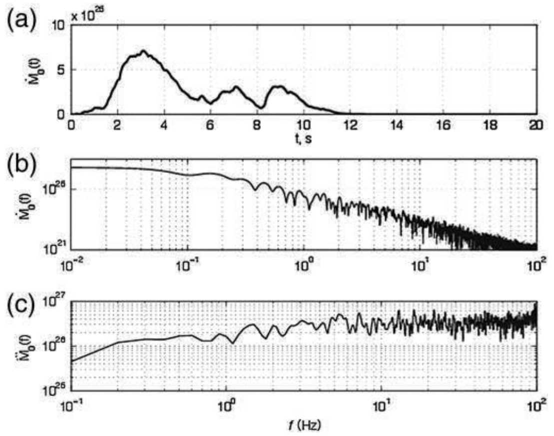

▲ **Figure 2.** (a) Moment rate function of the source in Figure 1. Units are in dyn·cm/s. (b) Fourier amplitude spectrum of moment rate function. The Fourier amplitude of displacement seismograms is similar but depends on azimuth because of radiation pattern and directivity. Units are in dyn·cm. Seismic moment of the source, 2.9×10^{26} dyn·cm, can be read from the intercept at $f = 0.01$ Hz. (c) Smoothed acceleration spectrum corresponding to the displacement spectrum in the center plot.

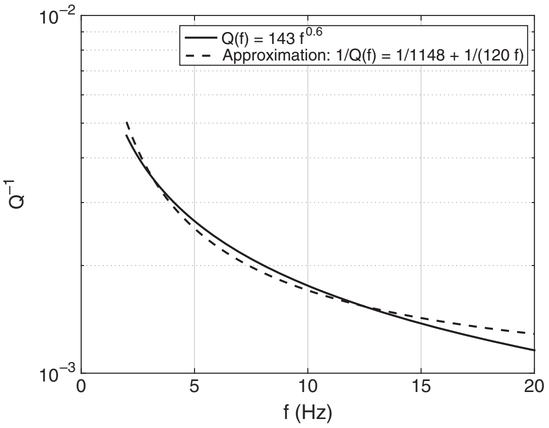

▲ **Figure 3.** Example of the approximation to the Q model given by equation (9).

The Model for *Q*

The model for Q needs to satisfy several criteria. First, it should be consistent with Q observations that find Q increasing with frequency at high frequencies. Second, amplitudes of seismic waves should have the same distance dependence as data. Third, the S-wave Q and coda Q, measured from the synthetic seismograms, should match observations. Finally, the trend of the high-frequency shape should behave as $\exp(-\pi\kappa f)$ (Anderson and Hough, 1984). Considering that the spectrum of the source model has a high-frequency asymptote of f^{-2} in displacement, or f^0 in acceleration (Fig. 2), a frequency-independent Q can cause this dependence. Also, I have modeled the distance dependence of κ as

$$\kappa(r) = \kappa_0 + \tilde{\kappa}(r) \approx \kappa_0 + \frac{d\kappa}{dr} r \tag{6}$$

(Anderson, 1986). The linear approximation in equation (6) was proposed by Anderson and Hough (1984) as a first approximation to the distance dependence.

Many regional Q models at high frequencies are modeled by a function of the form:

$$Q(f) = Q_0 f^{\gamma}, \tag{7}$$

in which Q_0 is the value of Q at 1 Hz, and γ is usually in the range $0 < \gamma < 1$. For instance, in the SCEC Broadband Platform simulations for California, the default Q structure is given by Bayless:

$$Q_{\mathrm{SCEC}}(f) = (41 + 34\beta) f^{0.6}, \tag{8}$$

in which β is the shear velocity in the layer. For $0 \le \gamma \le 1$, equation (7) can be approximated as

$$\frac{1}{Q_0 f^{\gamma}} \approx \frac{1}{Q_i} + \frac{1}{Q_d f} \tag{9}$$

(e.g., Anderson, 1986). Q_i and Q_d in equation (9) can be found so that the mismatch is under about 10% for the range of $2 \le f \le 25$ Hz (e.g., Fig. 3). Often, as in Figure 3, Q_i is very large. These high values are needed to model observations of $d\kappa/dr$ (e.g., Hough and Anderson, 1988).

To understand the effect of this approximation, consider the attenuation of a plane wave propagating a distance x for the model of Q given in equation (9):

$$A(x) = \exp\left(-\frac{\pi x f}{Q_0 f^{\gamma} \beta}\right) \approx \exp\left(-\frac{\pi x f}{Q_i \beta}\right) \exp\left(-\frac{\pi x}{Q_d \beta}\right). \tag{10}$$

The first term on the right side causes the high frequencies to decay, and one can associate $\kappa = x/Q_i\beta$. The second term on the right side has no effect on the spectral shape, but it reduces the amplitude uniformly across the spectrum.

To model κ_0, one needs low values of Q in the shallow sediments. An initial assignment is given in Table 1. To match a target value of κ_0, the values of Q for the upper 3 km are adjusted based on the slope of the Fourier SH response to an impulse at 5 km depth. These low Q values in the shallow crust rapidly damp any short-period surface waves so that even at moderate distances the synthetic seismograms are dominated by near-vertical propagating S waves.

Velocity Model Example

Figure 4 shows the velocity and Q model used for northern California as modified from Goulet *et al.* (2015). All layers

Table 1
Assignment of Q_i for S Waves in Shallow Layers, Based on Assimaki *et al.* (2008)

Shear Velocity for Layers Shallower Than 30 m (km/s)	Q_i	Depth Range	Q_i
0	5	$z_b \le 0.1$ km	20
0.1	5	0.1 km $\le z_b \le 0.5$ km	25
0.5	7	0.5 km $\le z_b \le 1.0$ km	30
1.0	10	1.0 km $\le z_b \le 2.0$ km	50
2.0	10	2.0 km $\le z_b \le 5.0$ km	100
10.0	10		

For the upper 30 m, Q_i is interpolated from the first two columns. From 30 m to 3 km, Q_i is determined from the depth z_b of the bottom of the layer (third and fourth columns). Q_i is generally defined in equation (9), but for these depths Q is treated as independent of frequency.

shallower than 30 m have been consolidated into a single layer with 30 m thickness. Below the Moho, several 5 km thick layers are introduced to bring the base of the model to 75 km depth; velocity in each of these layers is increased using the Earth flattening approximation for *SH* waves (Aki and Richards, 2002), $\beta_f(z) = [a/(a-z)]\beta(z)$, in which $a = 6371$ km is the radius of the Earth and z is the layer depth. The *P*-wave velocity is increased proportionately. The intent is to allow some of the energy that is refracted into the mantle to return to the crustal waveguide. Also note the high values of Q_i in the crustal waveguide and low values in the upper 5 km.

One expects a trade-off between the velocity model and $Q(f)$. A result of addressing this trade-off is that Figure 4 has a small velocity gradient in the crustal waveguide created by replacing the two thick original layers between 9 and 25 km with eight layers of 2 km thickness each, thus providing a smoother approximation to a velocity gradient in this depth range. Without this gradient, the synthetic seismograms attenuate too rapidly. An alternative way to overcome that systematic effect is to increase Q more in those layers (to ~4000), but when that is done the distance dependence of κ does not match the trend of the measurements, at least for the Loma Prieta earthquake, as discussed subsequently.

Coda

The coda in this implementation is calculated using the single-scattering model of Aki and Chouet (1975). It is applied as a convolution with the Green's functions. The coda function begins with a filtered impulse in which the filter incorporates the effect of Q_d from equation (10). It also adds reflections from randomly placed scatterers in the crustal waveguide. Figure 5 shows one of the Green's functions for one station without and with the coda. In this example, and in general, with the coda the Green's functions are beginning to take the realistic appearance of a small earthquake.

EXAMPLE: LOMA PRIETA CALCULATION

Synthetic Seismograms

Figures 6 and 7 show, respectively, the unfiltered synthetic acceleration, velocity, and displacement at station 0734, and the pseudorelative response spectra. The reader may judge their realism.

The average ground-motion amplitudes over multiple source models are fairly stable, but individual realizations show variability. The standard deviation, say σ_{fault}, is due to the variability of

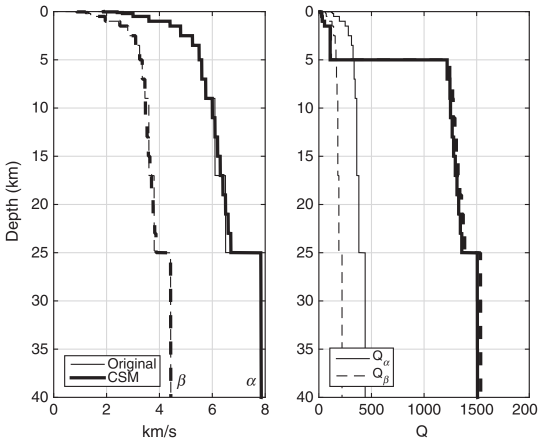

▲ **Figure 4.** Original and modified velocity and Q model for northern California. Original models are shown with narrow lines, and model used for the CSM are shown with heavy lines. α and β refer to P and S waves, respectively.

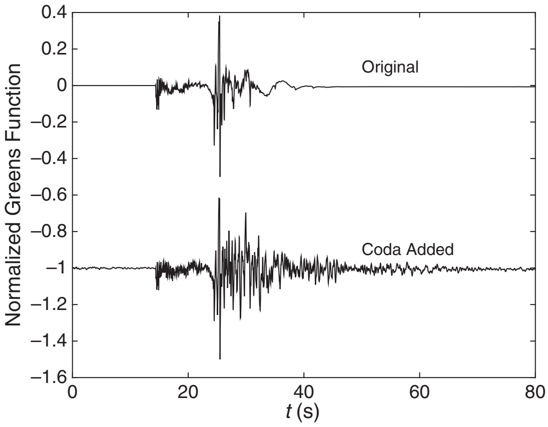

▲ **Figure 5.** Example of a Green's functions for station 0734 in the Loma Prieta earthquake. This is the north component for a fault element near the south end of the rupture. (Top) As computed for the velocity and Q model in Figure 4. (Bottom) The same component after convolution with a coda scattering function.

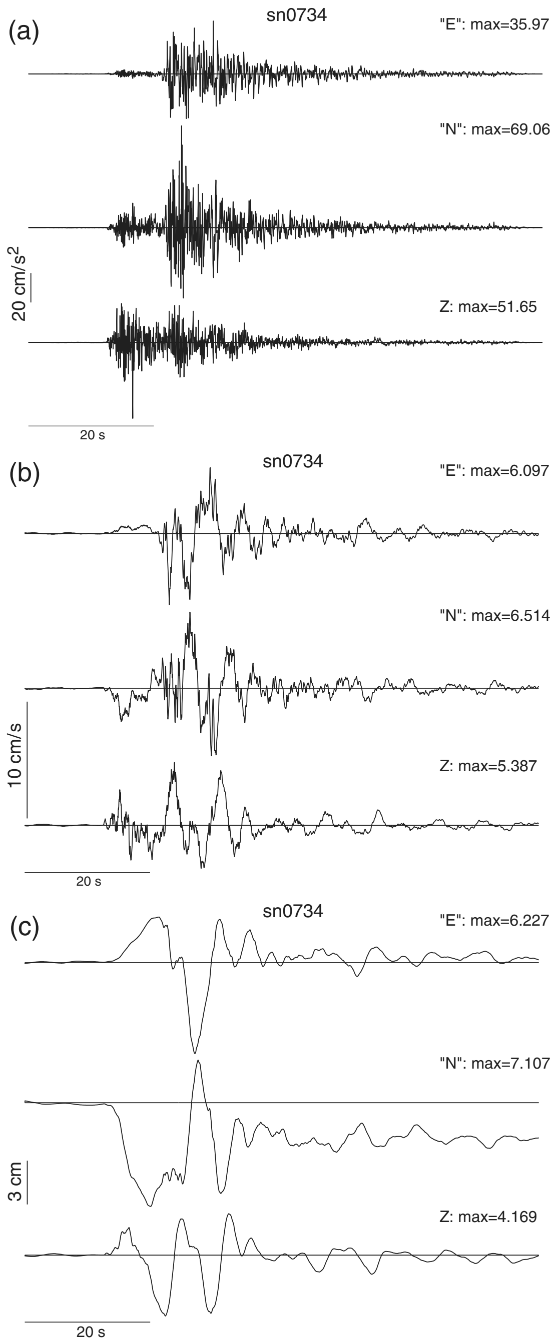

▲ **Figure 6.** Unfiltered synthetic realization of (a) acceleration, (b) velocity, and (c) displacement at station 0734. Notice the small static offset in the horizontal displacements.

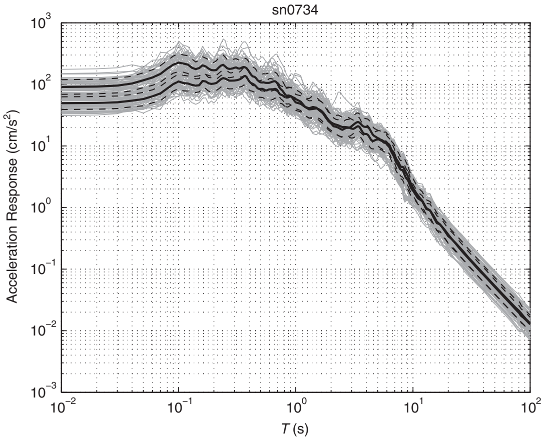

▲ **Figure 7.** East and north components of the pseudoacceleration response spectra (5% damping) for 50 realizations at station 0734. Black solid lines show averages for the two components, and dashed lines show ± one standard deviation.

the fault alone. For this Loma Prieta example, for 50 realizations of peak acceleration at each station, σ_{fault} decreases from ∼0.36 at short distances to ∼0.24 at ∼80 km. For peak velocity, σ_{fault} decreases from ∼0.32 to ∼0.2 in the same distance range. In the future, controlling the variability of $\Delta\tau_S$ can be used to control the variability of σ_{fault}.

Figure 8 compares data with the values of κ measured from whole-record synthetics using this model. Whole-record spectra are used because direct *P* waves overlap direct *S* waves at many of the stations, so the whole-record window is a straightforward way to measure the same thing at all distances; the

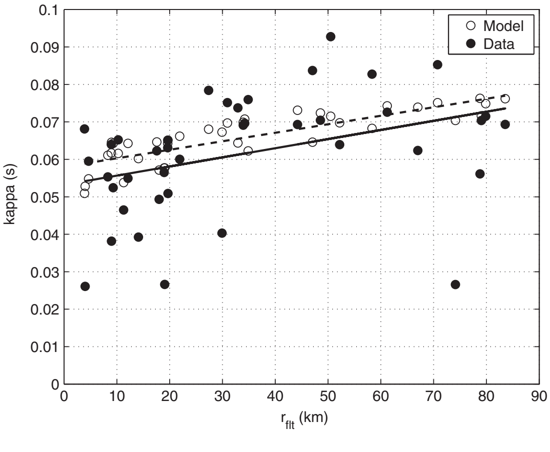

▲ **Figure 8.** Whole-record measurements of κ for both observed seismograms (open points, dashed line) and corresponding synthetic seismograms (black points, solid line). The lines both have slope $\sim 2.4 \times 10^{-4}$ s/km. Observed spectra are not adjusted for V_{S30}.

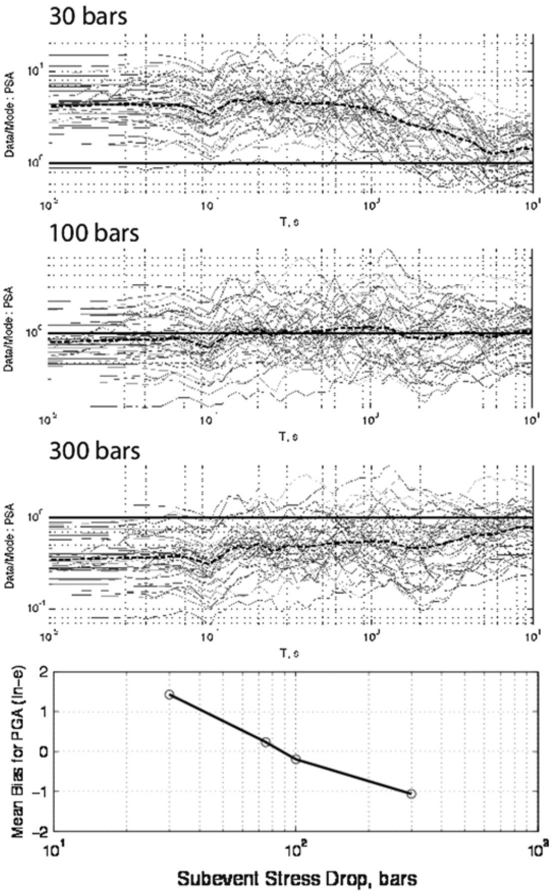

▲ **Figure 9.** Loma Prieta summary results. Each of the top three frames uses a different target subevent stress drop to find amplitudes at each station. The light lines show the corresponding residuals averaged over 50 realizations. The heavy lines show the average over the 40 stations. This figure shows how the residuals for the response spectrum change as the subevent stress drop is increased. The bottom frame shows how the residual for peak acceleration ($T = 0.01$ s) depends on the value of $\Delta\tau_S$.

presence of the coda in these windows has increased κ above the targeted value of $\kappa_0 = 0.04$ s for the S waves. The model shows an increase of κ with distance similar to the data. Anderson (1991) averaged kappa estimates at several stations in southern California, and an average trend through that model for $\tilde{\kappa}(r)$ has the slope 2.9×10^{-4} s/km, which is similar to the slope in Figure 8. The distance dependence in Figure 8 is also predicted by ray theory. As mentioned earlier, the slope $(d\kappa/dr)$ in Figure 8 is controlled by Q_i in the deeper parts of the crust. The attenuation is controlled by Q_i, Q_d, and the velocity model. The introduction of the gradient in the lower crust in Figure 4 achieved the right attenuation for Loma Prieta data without violating the observed slope $(d\kappa/dr)$. A full exploration of this trade-off is ongoing.

Calibration

When the average amplitudes of the CSM have a nonzero residual for an event, the residual can be adjusted by changing $\Delta\tau_S$. Figure 9 shows an example. The high-frequency residuals decrease as the subevent stress drop increases. The lower frame plots the average residual for peak acceleration, taken to represent the high frequencies in general for the sake of this example, as a systematic function of $\Delta\tau_S$. Generating plots like this for individual earthquakes identifies the optimal subevent stress drop for each. With measurements of $\Delta\tau_S$ from multiple earthquakes, appropriate values can be determined for future earthquakes.

At present, the SCEC calibration has not run enough cases to determine if there is a dependence of $\Delta\tau_S$ on magnitude, focal mechanism, or region. At present, for California events the CSM uses $\Delta\tau_S = 75$ bars, even though $\Delta\tau_S = 100$ bars would be optimal for Loma Prieta.

SUMMARY

This paper has summarized the theory behind the CSM for generating synthetic seismograms and given one example of the synthetics that are generated. For version 13.6 of the SCEC Broadband Platform, used for 2013 gauntlet, the CSM was below the target range for GMPEs at 50 km. The new version, with all of the features described in this article, had not been formally evaluated as part of the version 14.3 gauntlet. Features described here that were added subsequent to version 13.6 include the gradients in the crust and mantle, which are physically motivated adjustments to the velocity model, the addition of the coda, and the systematic evaluation of residuals and κ as a function of distance. Rules for the parameters controlling each of these features will be incorporated into the next version on the Broadband Platform.

ACKNOWLEDGMENTS

I thank D. Dreger and an anonymous reviewer for useful comments that improved this manuscript. This research was supported by the Southern California Earthquake Center (SCEC). SCEC is funded by NSF Cooperative Agreement EAR-1033462 and U.S. Geological Survey Cooperative Agreement G12AC20038. The SCEC contribution number for this paper is 1997.

REFERENCES

Aki, K., and B. Chouet (1975). Origin of coda waves: Source, attenuation and scattering effects, *J. Geophys. Res.* **80,** 3322–3342.

Aki, K., and P. G. Richards (2002). *Quantitative Seismology*, Second Ed., University Science Books, Sausalito, California, 700 pp.

Anderson, J. G. (1986). Implication of attenuation for studies of the earthquake source, *Earthquake Source Mechanics*, Geophysical Monograph 37, Maurice Ewing Series 6, American Geophysical Union, Washington, D.C., 311–318.

Anderson, J. G. (1991). A preliminary descriptive model for the distance dependence of the spectral decay parameter in southern California, *Bull. Seismol. Soc. Am.* **81,** 2186–2193.

Anderson, J. G. (1997). Seismic energy and stress drop parameters for a composite source model, *Bull. Seismol. Soc. Am.* **87,** 85–96.

Anderson, J. G., and S. Hough (1984). A model for the shape of the Fourier amplitude spectrum of acceleration at high frequencies, *Bull. Seismol. Soc. Am.* **74,** 1969–1994.

Anderson, J. G., and G. Yu (1996). Predictability of strong motions from the Northridge, California, earthquake, *Bull. Seismol. Soc. Am.* **86,** S100–S114.

Assimaki, D., W. Li, J. H. Steidl, and K. Tsuda (2008). Site amplification and attenuation via downhole array seismogram inversion: Study of the 2003 Miyagi-Oki aftershock sequence, *Bull. Seismol. Soc. Am.* **98,** 301–330.

Brune, J. N. (1970). Tectonic stress and spectra of seismic shear waves from earthquakes, *J. Geophys. Res.* **75,** 4997–5009.

Brune, J. N. (1971). Correction. Tectonic stress and spectra of seismic shear waves from earthquakes, *J. Geophys. Res.* **76,** 5002.

Frankel, A. (1991). High-frequency spectral falloff for earthquakes, fractal dimension of complex rupture, *b*-value, and the scaling of strength on faults, *J. Geophys. Res.* **96,** 6291–6302.

Goulet, C., N. A. Abrahamson, P. G. Somerville, and K. E. Wooddell (2015). The SCEC Broadband Platform validation exercise for pseudo-spectral acceleration: Methodology for code validation in the context of seismic hazard analyses, *Seismol. Res. Lett.* **86,** no. 1, doi: 10.1785/0220140104.

Hartzell, S., A. Frankel, P. Liu, Y. Zeng, and S. Rahman (2011). Model and parametric uncertainty in source-based kinematic models of earthquake ground motion, *Bull. Seismol. Soc. Am.* **101,** 2431–2452.

Hough, S. E., and J. G. Anderson (1988). High-frequency spectra observed at Anza, California: Implications for Q structure, *Bull. Seismol. Soc. Am.* **78,** 692–707.

Kanamori, H., and D. L. Anderson (1975). Theoretical basis of some empirical relations in seismology, *Bull. Seismol. Soc. Am.* **65,** 1073–1095.

Khattri, K. N., G. Yu, J. G. Anderson, J. N. Brune, and Y. Zeng (1994). Seismic hazard estimation using modelling of earthquake strong ground motions: A brief analysis of 1991 Uttarkashi earthquake, Himalaya and prognostication for a great earthquake in the region, *Curr. Sci.* **67,** 343–353.

Luco, J. E., and R. J. Apsel (1983). On the Green's function for a layered half-space, part I, *Bull. Seismol. Soc. Am.* **73,** 909–929.

Sato, T., and T. Hirasawa (1973). Body wave spectra from propagating shear cracks, *J. Phys. Earth* **21,** 415–431.

Su, F., J. G. Anderson, S.-D. Ni, and Y. Zeng (1998). Effect of site amplification and basin response on strong motion in Las Vegas, Nevada, *Earthq. Spectra* **14,** 357–376.

Su, F., J. G. Anderson, and Y. Zeng (1998). Study of weak and strong ground motion including Nonlinearity from the Northridge, California, earthquake sequence, *Bull. Seismol. Soc. Am.* **88,** 1411–1425.

Yu, G. (1994). Some aspects of earthquake seismology: Slip partitioning along major convergent plate boundaries; composite source model for estimation of strong motion; and nonlinear soil response modeling, *Ph.D. Thesis*, University of Nevada, Reno, 144 pp.

Yu, G., K. N. Khattri, J. G. Anderson, J. N. Brune, and Y. Zeng (1995). Strong ground motion from the Uttarkashi, Himalaya, India earthquake: Comparison of observations with synthetics using the composite source model, *Bull. Seismol. Soc. Am.* **85,** 31–50.

Zeng, Y., and J. G. Anderson (1996). A composite source model of the 1994 Northridge earthquake using genetic algorithms, *Bull. Seismol. Soc. Am.* **86,** no. 1B, S71–S83.

Zeng, Y., and C. Chen (2001). Fault rupture process of the 20 September 1999 Chi-Chi, Taiwan, earthquake, *Bull. Seismol. Soc. Am.* **91,** 1088–1098.

Zeng, Y., J. G. Anderson, and F. Su (1995). Subevent rake and random scattering effects in realistic strong ground motion simulation, *Geophys. Res. Letters* **22,** 17–20.

Zeng, Y., J. G. Anderson, and G. Yu (1994). A composite source model for computing realistic synthetic strong ground motions, *Geophys. Res. Lett.* **21,** 725–728.

Zeng, Y., F. Su, and K. Aki (1991). Scattered wave energy propagation in a random isotropic scattering medium, *J. Geophys. Res.* **96,** 607–619.

John G. Anderson
University of Nevada
Reno, Nevada 89557 U.S.A.
jga@unr.edu

Bulletin of the Seismological Society of America, Vol. 107, No. 6, pp. 2561–2577, December 2017, doi: 10.1785/0120160361

Ⓔ

Fault-Scaling Relationships Depend on the Average Fault-Slip Rate

by John G. Anderson, Glenn P. Biasi,* and Steven G. Wesnousky

Abstract This study addresses whether knowing the slip rate on a fault improves estimates of magnitude (M_w) of shallow continental surface-rupturing earthquakes. Based on 43 earthquakes from the database of Wells and Coppersmith (1994), Anderson *et al.* (1996) suggested previously that the estimates of M_w from rupture length (L_E) are improved by incorporating the slip rate of the fault (S_F). We re-evaluate this relationship with an expanded database of 80 events, which includes 56 strike-slip, 13 reverse-, and 11 normal-faulting events. When the data are subdivided by fault mechanism, magnitude predictions from rupture length are improved for strike-slip faults when slip rate is included but not for reverse or normal faults. Whether or not the slip-rate term is present, a linear model with $M_w \sim \log L_E$ over all rupture lengths implies that the stress drop depends on rupture length—an observation that is not supported by teleseismic observations. We consider two other models, including one we prefer because it has constant stress drop over the entire range of L_E for any constant value of S_F and fits the data as well as the linear model. The dependence on slip rate for strike-slip faults is a persistent feature of all considered models. The observed dependence on S_F supports the conclusion that for strike-slip faults of a given length, the static stress drop, on average, tends to decrease as the fault-slip rate increases.

Electronic Supplement: Table of earthquakes and parameters.

Introduction

Models for estimating the possible magnitude of an earthquake from geological observations of the fault length are an essential component of any state-of-the-art seismic-hazard analysis. The input to either a probabilistic or deterministic seismic-hazard analysis requires geological constraints because the duration of instrumental observations of seismicity is too short to observe the size and to estimate the occurrence rates of the largest earthquakes (e.g., Allen, 1975; Wesnousky *et al.*, 1983). Thus, wherever evidence in the geological record suggests earthquake activity, it is essential for the seismic-hazard analysis to consider the hazard from that fault, and an estimate of the magnitude of the earthquake (M_w) that might occur on the fault is an essential part of the process. The primary goal of this study is to determine if magnitude estimates that are commonly estimated from fault length (L_E) can be improved by incorporating the slip rate (S_F) of the fault.

Numerous models for estimating magnitude from rupture length have been published. Early studies were by Tocher (1958) and Iida (1959). Wells and Coppersmith (1994) published an extensive scaling study based on 244 earthquakes. Some of the more recent studies include Anderson *et al.* (1996), Hanks and Bakun (2002, 2008), Shaw and Wesnousky (2008), Blaser *et al.* (2010), Leonard (2010, 2012, 2014), and Strasser *et al.* (2010). For probabilistic studies and for earthquake source physics, it is valuable to try to reduce the uncertainty in these relations. Motivated by Kanamori and Allen (1986) and Scholz *et al.* (1986), Anderson *et al.* (1996; hereafter, AWS96) investigated whether including the fault-slip rate on a fault improves magnitude estimates given rupture length. They found that it does, and proposed the relationship $M_w = 5.12 + 1.16 \log L_E - 0.20 \log S_F$, thus indicating that slip rate is a factor. A physical interpretation of a significant dependence on slip rate is that, for a common rupture length, faults with higher slip rates tend to have smaller static stress drop. Since the publication of AWS96, the number of earthquakes with available magnitude, rupture length, and slip-rate estimates has approximately doubled. This article considers whether these new data improve or modify the conclusions from the earlier study.

One consideration in developing a scaling model is that seismological observations have found stress drop in earthquakes to be practically independent of magnitude. Kanamori and Anderson (1975) is one of the early papers to make this observation. Recent studies that have supported

---

*Now at U.S. Geological Survey, 525 S. Wilson Avenue, Pasadena, California 91106; gbiasi@usgs.gov.

Table 1
Earthquakes from 1968–2011 Used in This Study

Event Number	Event Name	Event Date (yyyy/mm/dd)	M_w	Rupture Length (km)	Slip Rate (mm/yr)	Mechanism*
2	Fukushima-Hamadori, Japan	2011/04/11	6.7	15	0.02	N
4	Yushu, China	2010/04/14	6.8	52	12	S
5	El Mayor–Cucapah	2010/04/04	7.3	117	2.5	S
6	Wenchuan, China	2008/05/12	7.9	240	1.3	R
7	Kashmir, Pakistan	2005/10/08	7.6	70	3.1	R
8	Chuya, Russia (Gorny Altai)	2003/09/27	7.2	70	0.5	S
9	Denali, Alaska	2002/11/03	7.8	340	12.4	S
10	Kunlun, China	2001/11/14	7.7	450	10	S
11	Düzce, Turkey	1999/11/12	7.1	40	15	S
12	Hector Mine, California	1999/10/16	7.1	48	0.6	S
13	Chi-Chi, Taiwan	1999/09/21	7.7	72	12.9	R
14	İzmit, Turkey	1999/08/17	7.5	145	12	S
15	Fandoqa, Iran	1998/03/14	6.6	22	2	S
16	Manyi, China	1997/11/08	7.4	170	3	S
17	Sakhalin Island (Neftegorsk), Russia	1995/05/27	7.0	40	4	S
18	Northridge, California	1994/01/17	6.7	21	0.4	R
19	Landers, California	1992/06/28	7.2	77	0.4	S
20	Luzon, Philippines	1990/07/16	7.7	112	15	S
21	Rudbar, Iran	1990/06/20	7.4	80	1	S
22	Loma Prieta, California	1989/10/17	6.8	35	3.2	R
25	Superstition Hill, California	1987/11/24	6.6	25	3	S
26	Edgecumbe, New Zealand	1987/03/02	6.4	15.5	2	N
28	Marryat, Australia	1986/03/03	5.8	13	0.005	R
29	Morgan Hill, California	1984/04/24	6.1	20	5.2	S
30	Borah Peak, Idaho	1983/10/28	6.9	36	0.15	N
31	Coalinga, California	1983/05/02	6.4	25	1.4	R
32	Sirch, Iran	1981/07/29	7.1	65	4.3	S
33	Corinth, Greece	1981/02/25	6.1	14	1.7	N
34	Corinth, Greece	1981/03/04	5.9	15	0.3	N
35	Daofu, China	1981/01/24	6.7	44	12	S
36	El Asnam (Ech Cheliff), Algeria	1980/10/10	6.9	36	0.8	R
37	Imperial Valley, California	1979/10/15	6.4	36	17	S
38	Coyote Lake, California	1979/08/06	5.8	14	11.9	S
40	Tabas, Iran	1978/09/16	7.4	90	1.3	R
41	Bob-Tangol, Iran	1977/12/19	5.8	19.5	4	S
42	Motagua, Nicaragua	1976/02/04	7.5	230	12	S
43	Luhuo, China	1973/02/06	7.5	90	14	S
44	San Fernando, California	1971/02/09	6.8	19	1.8	R
45	Tonghai, China	1970/01/04	7.2	60	2	S
46	Dasht-e-Bayaz, Iran	1968/08/31	7.1	80	5	S
47	Borrego Mtn, California	1968/04/09	6.6	33	6.7	S

*N, normal, S, strike slip, R, reverse.

this result include Allmann and Shearer (2009) and Baltay *et al.* (2011). Apparent exceptions have been reported based on Fourier spectra of smaller earthquakes, but as magnitude decreases, attenuation can cause spectral shapes to behave the same as they would for decreasing stress drop (e.g., Anderson, 1986). Studies that have taken considerable care to separate these effects have generally concluded that the average stress drop remains independent of magnitude down to extremely small magnitudes (e.g., Abercrombie, 1995; Ide *et al.*, 2003; Baltay *et al.*, 2010, 2011). However, all of these studies find that for any given fault dimension, the range of magnitudes can vary considerably (e.g., Kanamori and Allen, 1986). Despite this variability, it seems reasonable to evaluate a scaling relationship that is based on a constant stress drop before considering the additional effect of the fault-slip rate. This vision guides the development of the considered scaling relationships. Details of these models for the relationship of stress drop and the fault dimensions are deferred to the Appendix. The following sections describe the data, present the summary equations for three alternative models, fit the alternative models to the data, and discuss the results.

Data

Tables 1 and 2 give the preferred estimates of M_w, L_E, and S_F for the earthquakes used in this analysis. These values and their corresponding uncertainty ranges are given in Table S1 (Ⓔ available in the electronic supplement to this

Table 2
Earthquakes from 1848–1967 Used in This Study

Event Number	Event Name	Event Date (yyyy/mm/dd)	M_w	Rupture Length (km)	Slip Rate (mm/yr)	Mechanism*
48	Mudurnu Valley, Turkey	1967/07/22	7.3	80	18	S
49	Parkfield, California	1966/06/28	6.2	28	30	S
51	Alake Lake or Tuosuohu Lake or Dulan, China	1963/04/19	7.0	40	12	S
52	Ipak or Buyin-Zara, Iran	1962/09/01	7.0	100	1	R
53	Hebgen Lake, Montana	1959/08/18	7.3	25	0.5	N
54	Gobi-Altai, Mongolia	1957/12/04	8.1	260	1	S
55	San Miguel, Mexico	1956/02/14	6.6	20	0.3	S
56	Fairview Peak, Nevada	1954/12/16	7.1	46	0.14	N
57	Dixie Valley, Nevada	1954/12/16	6.6	47	0.5	N
58	Yenice–Gonen, Turkey	1953/03/18	7.3	60	6.8	S
60	Gerede-Bolu, Turkey	1944/02/01	7.3	155	18	S
61	Tosya, Turkey	1943/11/26	7.6	275	19	S
62	Tottori, Japan	1943/09/10	6.9	33	0.3	S
63	Niksar-Erbaa, Turkey	1942/12/20	6.8	50	19	S
64	Imperial Valley, California	1940/05/19	7.1	60	17	S
65	Erzincan, Turkey	1939/12/25	7.8	330	19	S
66	Tuosuo Lake, Huashixia, China	1937/01/07	7.6	150	11	S
67	Parkfield, California	1934/06/08	6.2	25	30	S
68	Long Beach, California	1933/03/10	6.4	22	1.1	S
69	Changma, China	1932/12/25	7.6	149	5	S
70	Fuyun, China	1931/08/10	7.9	160	0.3	S
71	North Izu, Japan	1930/11/25	6.9	28	2.4	S
72	Laikipia, Kenya	1928/01/06	6.8	38	0.18	N
73	Tango, Japan	1927/03/07	7.0	35	0.3	S
74	Luoho-Qiajiao (Daofu), China	1923/03/24	7.3	80	10	S
75	Haiyuan, China	1920/12/16	8.0	237	7	S
76	Pleasant Valley, Nevada	1915/10/03	7.3	61	0.1	N
77	Chon-Kemin (Kebin), Kazakhstan	1911/01/03	8.0	177	2	R
78	San Francisco, California	1906/04/18	7.9	497	21	S
79	Bulnay, Mongolia	1905/07/23	8.5	375	3	S
80	Laguna Salada, Mexico	1892/02/23	7.2	42	2.5	S
81	Rikuu, Japan	1896/08/31	7.2	40	1	R
82	Nobi/Mino-Owari, Japan	1908/06/28	7.4	80	1.6	S
83	Canterbury, New Zealand	1888/09/01	7.1	65	14	S
84	Sonora, Mexico	1887/05/13	7.2	101.8	0.08	N
85	Owens Valley, California	1872/03/26	7.4	110	3.5	S
86	Hayward, California	1868/10/01	6.9	61	8	S
87	Fort Tejon, California	1857/01/09	7.8	339	25	S
88	Marlborough, New Zealand	1848/10/16	7.5	134	5.6	S

*N, normal, S, strike slip, R, reverse.

article), along with the references for all estimates. Events considered for analysis come from AWS96 and Biasi and Wesnousky (2016). Some AWS96 events were not used because uncertainties in one or more of the magnitude, length, or slip-rate parameters were considered too large or too poorly known to contribute to the parametric regressions. Events in Biasi and Wesnousky (2016) were selected on the basis of having a well-mapped surface rupture and nongeologically estimated magnitude. Their list builds on the list of fault ruptures of Wesnousky (2008) by adding more recent events and by including surface ruptures newly documented by geologic field work. Interested readers are referred to these previous papers for further description of each event. Overall, the database is heavily weighted toward surface-rupturing earthquakes. Some events in Biasi and Wesnousky (2016) were not included for lack of a resolved fault-slip rate, or because their rupture lengths were too short. Events with $L_E < 15$ km were generally not included. The smallest preferred estimate of M_w is 5.7.

Earthquakes after 1900 were only included if some independent (nongeologic) means was available to estimate magnitude. Moment estimates from waveform modeling were preferred to body-wave magnitudes where both were available. The six earthquakes prior to 1900 are particularly well documented, as described in Ⓔ the electronic supplement. Because L_E is known for these events and the uncertainty in M_w introduced by uncertain depth of faulting is less than 0.1, the measured slip in these events controls M_w. It follows that estimating M_w from L_E alone for these events is not circular. The rupture length is normally taken as the distance between the ends of primary coseismic surface rupture. The sum of the lengths of overlapping traces may be

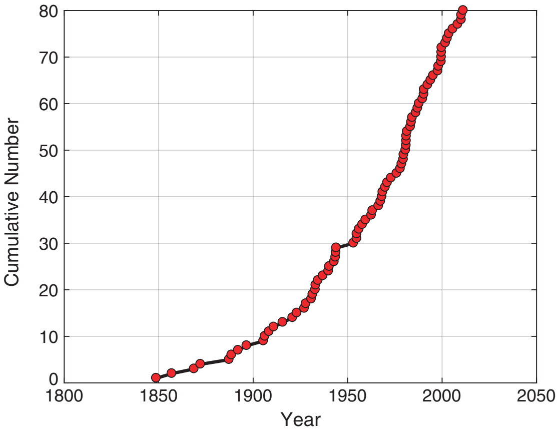

Figure 1. Cumulative number of events used in this analysis (Tables 1 and 2), shown as a function of time. The color version of this figure is available only in the electronic edition.

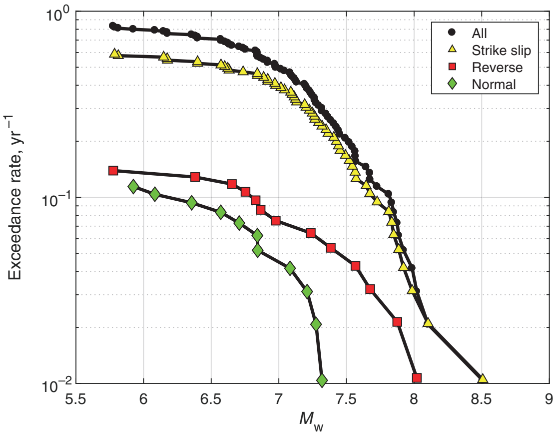

Figure 2. Event rates, as a function of magnitude and event types. The rates are estimated based on the approximation that the data represent about 100 yrs of seismicity, as discussed in the Data section. The color version of this figure is available only in the electronic edition.

used as the length in the analysis (e.g., event 53, Hegben Lake, 1959) where the overlapping portions were judged to contribute materially to the moment release. Rupture lengths based on aftershock distributions have generally been avoided, with the exception of six moderate strike-slip events, all in California. These were retained for continuity with AWS96 and for support of the regressions at moderate magnitudes. None control the results. Fault-slip rates are taken from offsets of geologic features 10–100 ka in age, where possible, to represent a stable recent slip-rate estimate. Fault-slip rates from paleoseismic offsets of one or a few individual earthquakes were avoided, because it is not clear how that activity would relate to the longer term average slip rate. Similarly, fault-slip rates from geodetic estimates were avoided where possible because they measure the current-day rate but may not represent the longer term average. Fault creep effects were considered, but no corrections were attempted in the database. First, creep is believed to affect only a few percent or less of events, and at a fraction of the full slip rate. Second, uncertainty in fault-slip rate will be seen below to have little effect on the regression.

Figure 1 shows the cumulative number of earthquakes used as a function of time. From 1954 to 2013, the rate of usable events is relatively steady, about 0.9 events per year. The rate is lower prior to ~1954 suggesting that the earlier historical record is less complete.

The earthquakes are separated into general categories of strike-slip, normal, and reverse faulting. Figure 2 shows the exceedance rates of considered earthquakes in each of these categories as a function of magnitude, both combined and separated by focal mechanism. To estimate the rates, the number of earthquakes for each of the curves was divided by 100 yrs. This is obviously an approximation, but considering Figure 1, the events prior to ~1910 may roughly compensate for the missing events since 1910. For instance, Figure 2 suggests that continental events that cause surface rupture with $M_w \geq 7.0$ have occurred at a rate of about 0.5 yr^{-1}, or roughly once every two years. The rates of strike-slip, reverse, and normal mechanisms are about 0.4, 0.075, and 0.045 yr^{-1}. Rounded to the nearest 5%, this implies that about 75% of those events were strike slip, about 15% had reverse mechanisms, and about 10% had normal mechanisms.

Figure 3 shows maps with locations of all events, using different symbols to distinguish among mechanisms. The insets show more details on locations of events from the western United States, the eastern Mediterranean region, and Japan.

Figure 4 plots the preferred slip rates versus the preferred rupture lengths. Figure 4a emphasizes the overall distribution of the data, while 4b highlights the 56 strike-slip faults, 4c highlights the 13 reverse faults, and 4d highlights the 11 normal faults. The combined data in Figure 4a are distinctly upper triangular. The points along the diagonal associate an increase in fault length with an increase in fault-slip rate, which in turn is likely a function of cumulative slip (e.g., Wesnousky, 1988, 1999) that does not depend on the mechanism. The data above the diagonal show that (1) the entirety of long faults and fault systems does not always break and that (2) small fast faults may exist. There are two alternatives to explain the lack of long ruptures on faults with low slip rates. The first could be purely statistical because events in the lower right corner of the plot could be too rare to be represented in the historical record. Alternatively, due to what Perrin *et al.* (2016) call "the competition between damage and healing processes," faults with slow slip rates might, during the interseismic period, be sufficiently affected by differential healing, influences from adjacent faults, or other processes that long ruptures on slow faults never occur.

Figure 4b–d emphasizes the data available to search for slip-rate dependency for the three fault types. Figure 4b

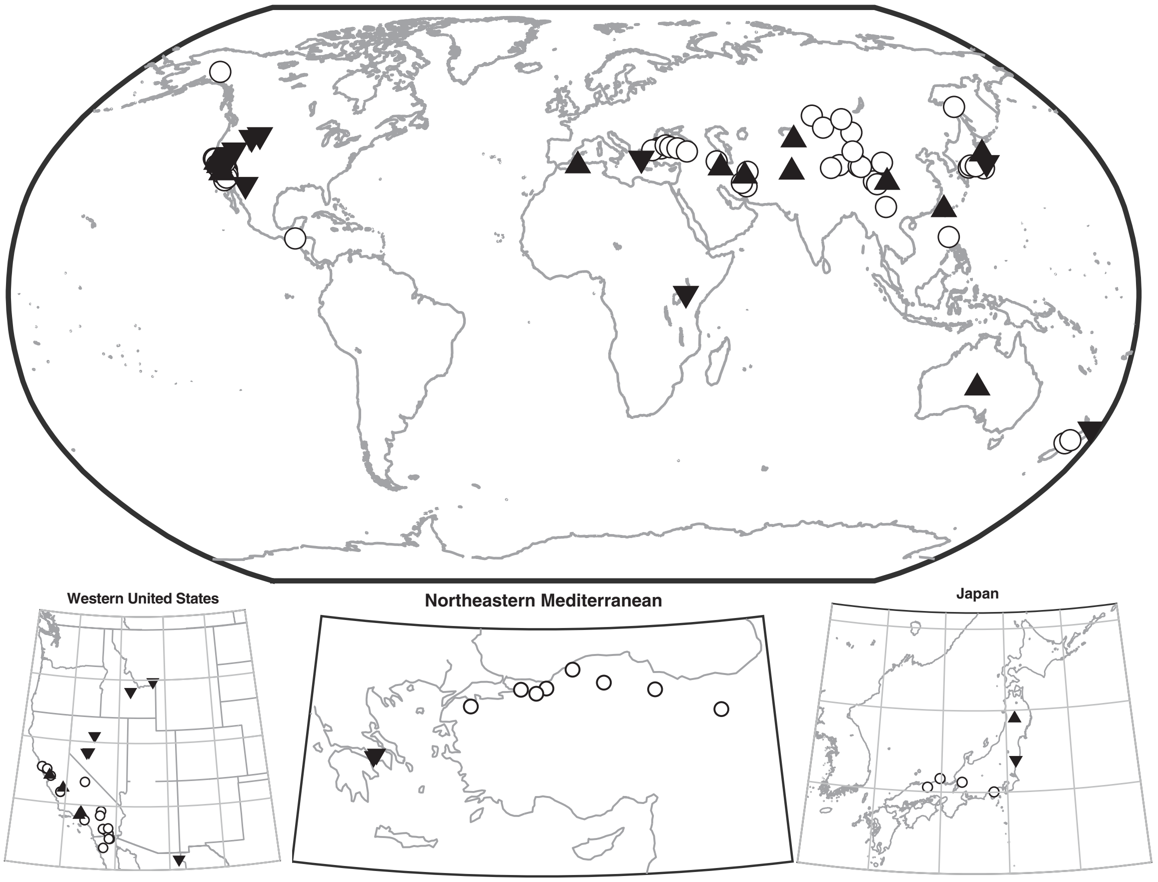

Figure 3. Locations of events considered in this study. Open circles show locations of events with a strike-slip mechanism. Triangles represent reverse events, and inverted triangles represent normal mechanisms.

shows a distribution of points spanning rupture lengths mostly between 20 and 400 km and slip rates between 0.3 and 30 mm/yr. Rupture lengths for reverse faults (Fig. 4c) range from 13 to 240 km although most are between 20 and 100 km. Slip rates for reverse faults are mostly between 0.4 and 4 mm/yr, with outliers at 0.005 and 12.9 mm/yr. Rupture lengths and slip rates for normal faults (Fig. 4d) range from 14 to 102 km and 0.08 to 2 mm/yr, but are unevenly distributed within these limits.

Modeling Approaches

The effect of slip rate is tested against three model shapes for the scaling relationship to confirm that it is not an artifact of a particular assumption for how magnitude depends on rupture length. The first M1 explores a linear regression of M_w with the logs of length and slip rate:

$$M_\mathrm{w} = c_0 + c_1 \log L_E + c_2 \log \frac{S_F}{S_0}, \tag{1}$$

in which L_E is the rupture length (measured along strike) of a specific earthquake; M_w is the reported moment magnitude for the respective earthquake (Kanamori, 1977); S_F is the slip rate of the fault on which the earthquake occurred determined from geological observation; S_0 is the average of the logs of all slip rates in the data set being considered (e.g., strike-slip faults, normal faults, etc.); and c_0, c_1, and c_2 are coefficients of regression to be determined. Mathematically, c_0 trades off with $-c_2 \log S_0$, which allows the parameter S_0 to be rounded to two significant digits. In this model, setting $S_F = S_0$ is mathematically equivalent to setting $c_2 = 0$ and thus also equivalent to the model approach used by Wells and Coppersmith (1994) and others who estimate a linear dependence of M_w on $\log L_E$ without including the slip rate on the fault. Two misfit parameters are considered. The first σ_{1L} is the standard deviation of the difference between observed and predicted magnitudes when $c_2 = 0$, so only L_E is used to estimate M_w, while σ_{1S} is the corresponding standard deviation when the slip-rate term in equation (1) is incorporated. A consequence of the assumed model M1 is

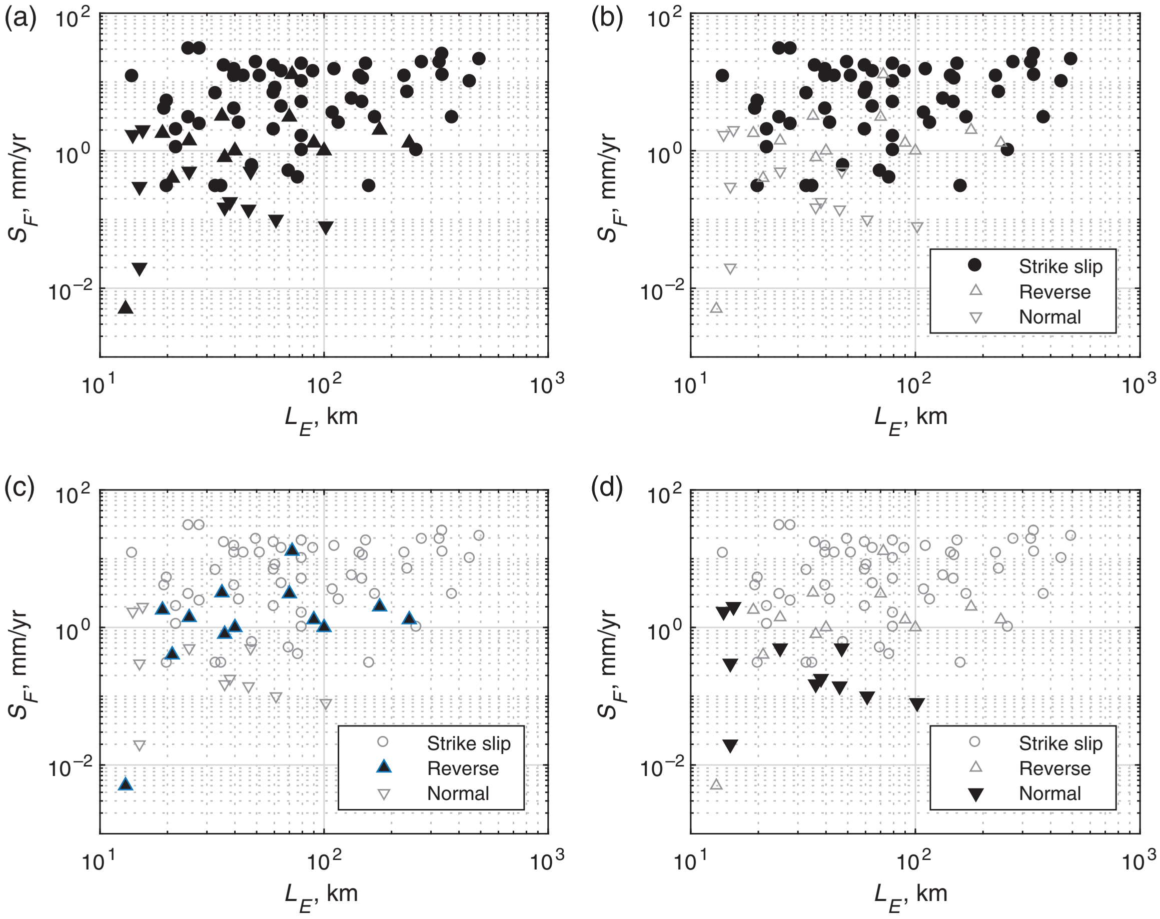

Figure 4. Rupture length–slip-rate distribution of the data in Tables 1 and 2. All points are shown combined in each part of the figure, (a) each fault type is given equal emphasis, (b) strike-slip faults are emphasized, (c) reverse faults are emphasized, and (d) normal faults are emphasized. The color version of this figure is available only in the electronic edition.

that unless c_1 fortuitously equals 2/3, stress drop increases for large earthquakes as a function of rupture length L_E, regardless of whether slip rate is included or not (Table A1).

The second M2 constrains the slope to give constant stress drop for small and large earthquakes with a slope change at the break-point magnitude M_{bp}. The stress drop for small and large earthquakes is allowed to differ:

$$M_{\mathrm{w}} = \begin{cases} M_{\mathrm{bp}} + c_{1C}\log\left(\frac{L_E}{L_{\mathrm{bp}}}\right) + c_2\log\left(\frac{S_F}{S_0}\right) & L_E < L_{\mathrm{bp}} \\ M_{\mathrm{bp}} + c_{1L}\log\left(\frac{L_E}{L_{\mathrm{bp}}}\right) + c_2\log\left(\frac{S_F}{S_0}\right) & L_E \geq L_{\mathrm{bp}}, \end{cases} \qquad (2)$$

in which $c_{1C} = 2$ and $c_{1L} = 2/3$ for rupture lengths that are less than or greater than L_{bp}, respectively, the rupture length where slope changes from 2 to 2/3. The three unknown parameters in model M2 are L_{bp} the rupture length where the slope changes from 2 to 2/3, M_{bp} the magnitude at that transition, and c_2 which is again the sensitivity of magnitude to fault-slip rate. Ruptures of length less than L_{bp} are considered to be a small earthquake and scale like a circular rupture in Table A1, implying that constant stress drop occurs when $c_{1C} = 2$. An earthquake with rupture length greater than L_{bp} is considered to be a large earthquake and corresponds to one of the models for a long fault in Table A1 (depending on fault mechanism), for which the value $c_{1L} = 2/3$ results in constant stress drop. However, equation (2) does not require the stress drop for the small earthquakes to be the same as the stress drop for large earthquakes. Equation (2) has the same number of unknown parameters to be determined from the data as equation (1). The two standard deviations of the misfit for model M2 are σ_{2L} and σ_{2S}, which correspond directly to the parameters σ_{1L} and σ_{1S} of model M1.

The third model M3 is derived from the model of Chinnery (1964) for a vertical strike-slip fault that ruptures the surface. It is assumed that stress drop for the top center of the fault in this model $\Delta\tau_C$ is constant across all rupture lengths and magnitudes:

$$M_{\mathrm{w}} = \begin{cases} 2\log L_E + \frac{2}{3}\log \Delta\tau_C + \frac{2}{3}\left(\log \frac{2\pi}{C_{LW}^2 C(\gamma)} - 16.1\right) + c_2 \log\left(\frac{S_F}{S_0}\right) & \frac{L_E}{C_{LW}} < W_{\max} \\ \frac{2}{3}\log L_E + \frac{2}{3}\log \Delta\tau_C + \frac{2}{3}\left(\log \frac{2\pi W_{\max}^2}{C(\gamma)} - 16.1\right) + c_2 \log\left(\frac{S_F}{S_0}\right) & \frac{L_E}{C_{LW}} \geq W_{\max}, \end{cases} \quad (3)$$

in which

$$C(\gamma) = 2\cos\gamma + 3\tan\gamma - \frac{\cos\gamma \sin\gamma(3 + 4\sin\gamma)}{(1 + \sin\gamma)^2}. \quad (4)$$

Details on the development of the model M3 equations are provided in the Appendix. The value γ is the angle from the top center of the fault to either of the bottom corners, that is, $\tan\gamma = 2W_E/L_E$, in which W_E is the down-dip width of the earthquake rupture. The model variables include four parameters. These are the aspect ratio of the fault for small ruptures $C_{LW} = L_E/W_E$, the stress drop $\Delta\tau_C$, the coefficient that quantifies the slip-rate dependence c_2, and the maximum fault width $W_{\max}$. Equation (3) assumes that the aspect ratio is constant for small earthquakes and that when the selected aspect ratio in combination with L_E implies a width greater than $W_{\max}$ the width is set to $W_{\max}$. For model M3, the two standard deviations of the misfit are σ_{3L} and σ_{3S}, corresponding to the parameters σ_{1L} and σ_{1S} of model M1. As written, the coefficients of the term in $\log L_E$ appear to be the same as in model M2, but for the long ruptures, γ depends on L_E, so the term with $C(\gamma)$ modifies the slope.

Model equations (1)–(3) require different strategies to obtain their unknown coefficients. The simplest way to find the unknown coefficients for equation (1) is using a linear least-squares regression, which minimizes the misfit of the prediction of M_{w} but does not account for uncertainties in L_E or S_F. AWS96 approached this difficulty by carrying out multiple regressions for points chosen at random within the range of allowed values of all three parameters, and then looked at the distribution of derived values of the coefficients of the regression. Alternative approaches to find the coefficients, described variously as "total least squares" or "general orthogonal regression" (e.g., Castellaro *et al.*, 2006; Castellaro and Bormann, 2007; Wikipedia article "Total Least Squares," see Data and Resources) were also considered for this analysis. The approach by AWS96 turned out to give the least biased results for a set of synthetic data with an uncertainty model that we considered to be realistic and consistent with the actual data, so their approach is also used in this study. The parameters for equation (1) were determined from 10,000 realizations of the randomized earthquake parameters to find the distributions of coefficients.

In implementing the AWS96 approach, M_{w}, L_E, and S_F are chosen at random from the range of uncertainties given in Ⓔ the electronic supplement. The probability distributions for the randomized parameters reflect that uncertainty ranges are not symmetrical around the preferred value. The preferred value is set to be the median. As an example, the probability distribution for the ith randomized value of L_E is as follows:

$$p(L_E) = \begin{cases} \frac{1}{(L_E^{\mathrm{pref}} - L_E^{\min})} & (\mathrm{caseA}) \\ \frac{1}{(L_E^{\max} - L_E^{\mathrm{pref}})} & (\mathrm{caseB}), \end{cases} \quad (5)$$

in which case A has probability of 0.5, case B has probability of 0.5, $L_E^{\min}$ and $L_E^{\max}$ are the minimum and maximum of the range on the rupture length, respectively, and L_E^{pref} is the preferred value. The seismic moment and slip rate are randomized using the same algorithm, and M_{w} is found from the randomized moment. The standard deviations of the misfit σ_{1L} and σ_{1S} are the average values from the multiple realizations.

Equation 2 has the additional complication of being nonlinear in L_{bp}. We approach the solution by reorganizing equation (2) as

$$M_{\mathrm{bp}} + c_2 \log\left(\frac{S_F}{S_0}\right) = M_{\mathrm{w}} - c_{1x} \log\left(\frac{L_E}{L_{\mathrm{bp}}}\right), \quad (6)$$

in which c_{1x} is either c_{1C} or c_{1L} depending on L_E. Assuming a value for L_{bp}, it is straightforward to find the unknown coefficients M_{bp} and c_2. We considered a set of closely spaced values of L_{bp} from the smallest to the longest rupture length in the data, and choose the value with the smallest total misfit. For each trial value of L_{bp}, we solved for the unknown coefficients 10,000 times with values of M_{w}, L_E, and S_F randomized as in equation (5), and our preferred model is the mean of the coefficients from the multiple realizations.

Model M3 (equation 3) has four unknown parameters, in which the effects of C_{LW} and $W_{\max}$ are nonlinear (Fig. A1). For this reason, a grid of values of C_{LW} and $W_{\max}$ was searched; there were 506 points on this grid. For each grid point, $\Delta\tau_C$ and c_2 were determined by linear least squares for 10,000 randomly chosen realizations of M_{w}, L_E, and S_F. The average values of $\Delta\tau_C$ and c_2 were found from the distributions of these realizations, together with the average values of σ_{3L} and σ_{3S}. This permitted creating a contour plots of σ_{3L} and σ_{3S} as a function of the trial values of C_{LW} and $W_{\max}$. The minima in σ_{3L} and σ_{3S} did not generally occur for the same combinations of C_{LW} and $W_{\max}$. Because the results of model M3 might potentially be used for faults where slip rate is unknown, we minimized σ_{3L}. The minimum in σ_{3L} is broad compared with the grid spacing of C_{LW} and $W_{\max}$, so the values that are used come as near as possible, within the minimum of σ_{3L}, to minimize σ_{3S} as well. The grid limits considered the maximum fault widths from 10 to 20 km for strike-slip faults, whereas for reverse and normal faulting the grid limits considered the maximum fault widths from 18 to 30 km. The larger widths were considered because of the suggestions of King and Wesnousky (2007), Hillers and Wesnousky (2008), and Jiang and Lapusta (2016) that a dynamic rupture in a large earthquake might reasonably extend

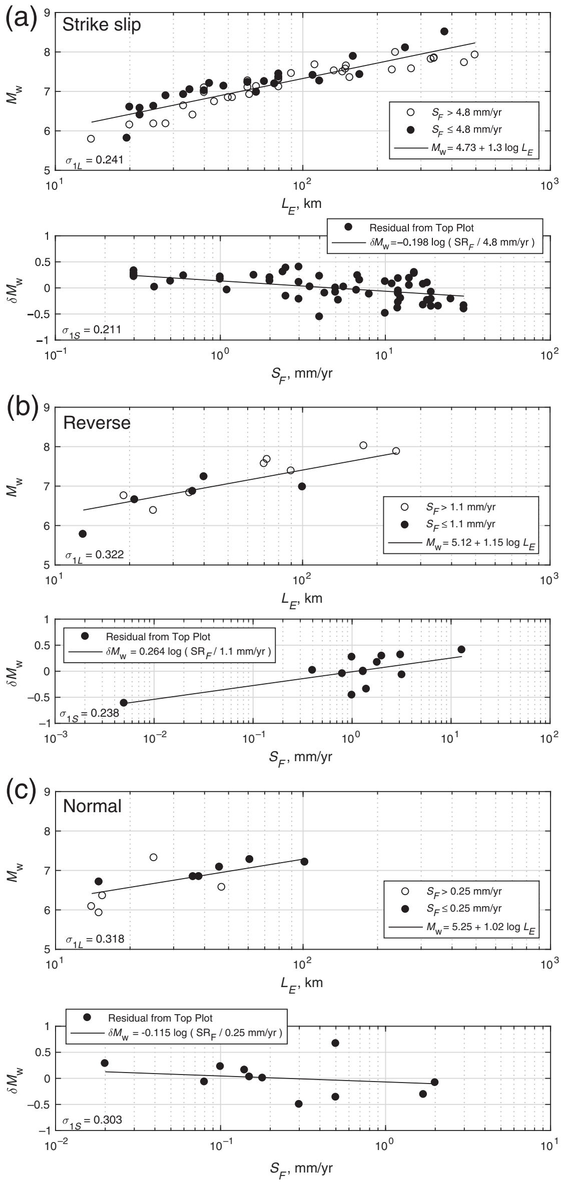

Figure 5. Model M1 (equation 1) for (a) strike-slip, (b) reverse, and (c) normal faults. For each mechanism, the upper frame shows M_w plotted as a function of L_E. Points are all the preferred values, as given in Tables 1 and 2. Solid points represent low slip-rate faults. The solid line uses coefficients given in Table 3 for $S_F = S_0$. The lower frame shows the residuals δM_w of the points in the upper frame from the solid line. The line in the lower frame shows the predicted effect of S_F based on the coefficients in Table 3, that is, $\delta M_w = c_2 \log(S_F/S_0)$. For strike-slip faults, the significant effect of fault-slip rate is seen in the clear separation of low and high slip-rate faults in the upper panel, and the negative slope of the fit to the residuals in the lower panel. For reverse and normal faults, the sparse data suggest a different trend in the residuals, indicating that mixing the three mechanism types is not appropriate.

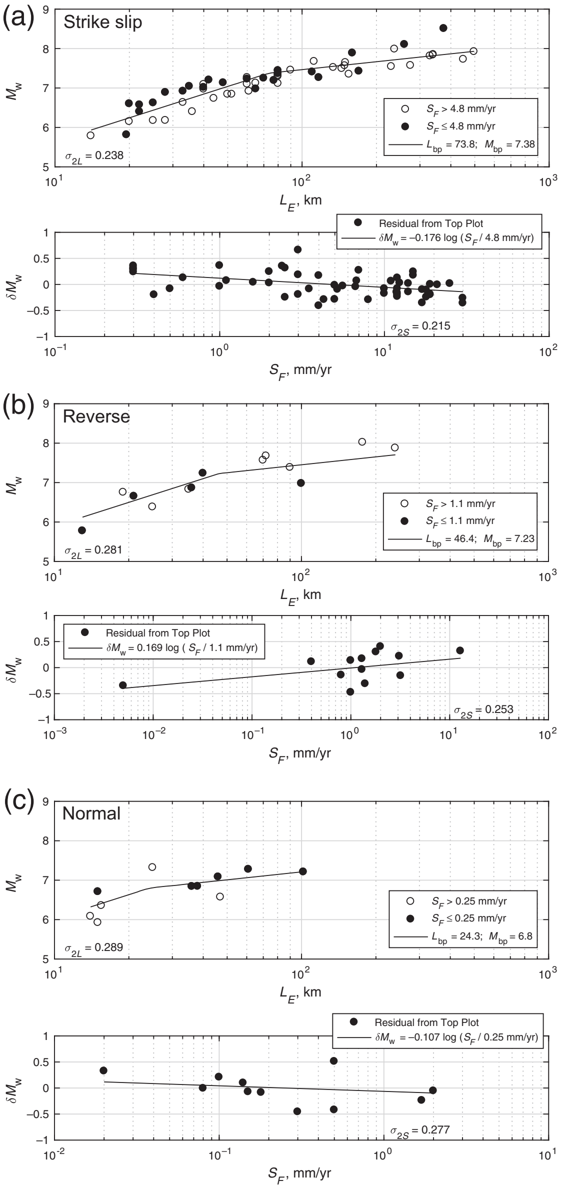

Figure 6. Model M2 (equation 2) for (a) strike-slip, (b) reverse, and (c) normal faults. Coefficients for the lines are given in Table 4. Other figure details are the same as in Figure 5.

deeper than the brittle crustal depths associated with microearthquakes.

Analysis Results

Figures 5–7 show results for models M1–M3, respectively, for strike-slip, reverse-, and normal-faulting earthquakes. For each mechanism, the curve in the upper frame shows predicted values of magnitude $\hat{M}_w$ for $S_F = S_0$. The

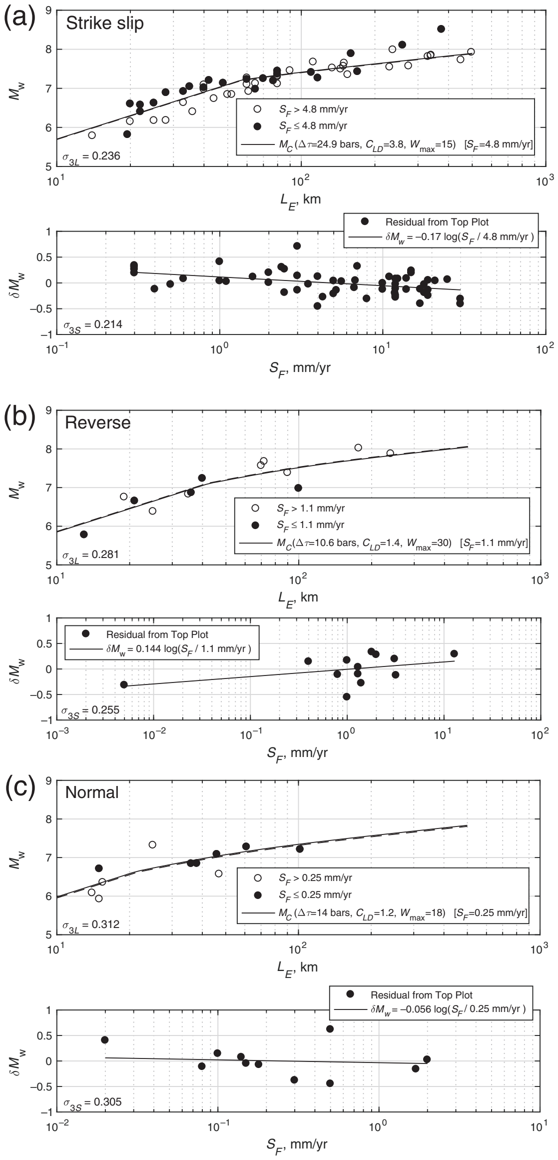

Figure 7. Model M3 (equation 3) for (a) strike-slip, (b) reverse, and (c) normal faults. Coefficients for the lines are given in Table 5. Other figure details are the same as in Figure 5.

lower frame shows the residuals from this prediction, defined as

$$\delta M_{wi} = M_{wi} - \hat{M}_{wi}, \tag{7}$$

for each considered earthquake, and the solid line is given by $\delta M_w = c_2 \log(S_F/S_0)$. Model coefficients and uncertainties in estimates of M_w for models M1–M3 are given in Tables 3–5, respectively.

Table 3

Coefficients for Model M1, Use in Equation (1), the Different Fault Types Considered Separately, and Earthquakes Listed in Tables 1 and 2

Parameter	Strike Slip	Reverse	Normal
c_0	4.73 ± 0.062	5.12 ± 0.11	5.25 ± 0.18
c_1	1.30 ± 0.031	1.15 ± 0.065	1.02 ± 0.12
c_2	−0.198 ± 0.023	0.264 ± 0.036	−0.115 ± 0.109
S_0 (mm/yr)	4.8	1.1	0.25
σ_{1L}	0.241	0.322	0.318
σ_{1S}	0.211	0.238	0.303

Table 4

Coefficients for Model M2, Use in Equation (2), the Different Fault Types Considered Separately, and Earthquakes Listed in Tables 1 and 2

Parameter	Strike Slip	Reverse	Normal
L_{bp}	73.8 ± 9.4	46.4 ± 6.4	24.3 ± 1.10
M_{bp}	7.38 ± 0.070	7.23 ± 0.091	6.80 ± 0.031
c_2	−0.176 ± 0.031	0.169 ± 0.042	−0.107 ± 0.091
S_0 (mm/yr)	4.80	1.1	0.25
σ_{2L}	0.238	0.281	0.289
σ_{2S}	0.215	0.253	0.277

Model M1: The Linear Model

The parameters for the linear models are given in Table 3. Figure 8 shows the distribution of coefficients found for 10,000 trials for strike-slip faults. The widths of these distributions are used to estimate the uncertainty in each coefficient. The coefficients c_0, c_1, and c_2 are found simultaneously, as opposed to a possible alternative approach, in which c_0 and c_1 could be found first, and then c_2 is determined by a second independent linear fit to the residuals.

For strike-slip events, which dominate the data, $c_2 = -0.198 \pm 0.023$ (Fig. 5a) so δM_w is observed to be a decreasing function of slip rate, similar to AWS96. The data with a reverse mechanism support δM_w increasing, rather than decreasing, with increased slip rate (Fig. 5b), whereas for the events with a normal mechanism the slip-rate dependence of δM_w is not distinguishable from zero (Fig. 5c). Considering the distribution of slip-rate data for reverse faults in Figure 5b, it may be observed that the finding of slip-rate dependence is the result of mainly a single outlier, the Marryat earthquake (M_w 5.8, event number 28 in Table 1) which is reported to have a slip rate of 0.005 mm/yr. Intracontinental events are included considering, based on Byerlys law, that the physics of rupture of crystalline rocks within the range of typical crustal compositions is not, *a priori*, different merely because the fault is located far from a plate boundary or that rock type might be different (e.g., Byerlee, 1978; Scholz, 2002). Also, the Marryat Creek event tends to decrease the slip-rate dependence of δM_w, as a consideration of the remaining points would reveal.

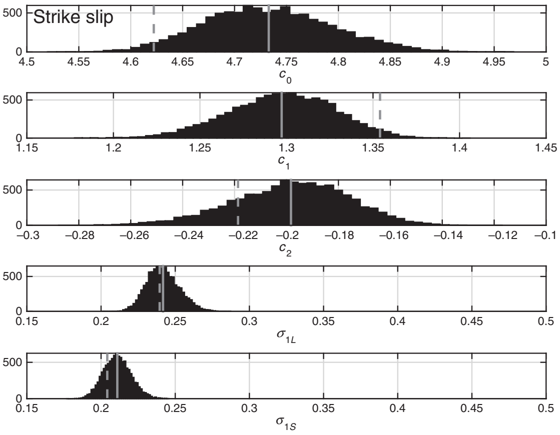

Figure 8. Coefficient distributions for the linear strike-slip model (M1, equation 1). The bar chart shows number of occurrences of parameter values among 10,000 realizations for randomly selected values of M_w, L_E, and S_F within the uncertainty range of each. The solid gray line shows the mean value of each parameter. The dashed gray line shows the value found for the preferred value of M_w, L_E, and S_F for each earthquake. The clear negative value of c_2 corresponds to decreasing relative magnitude predictions with increasing slip rate.

Nonetheless, the positive slope of δM_w in Figure 5b for reverse faulting is not a robust result.

Considering Figure 5, the results for the linear model provide an indication that it is not appropriate to combine different fault mechanisms in this type of regressions. The AWS96 model from all rupture mechanisms was $M_w = 5.12 + 1.16 \log L_E - 0.20 \log S_F$, which is only slightly different from the strike-slip case in Figure 5a. That result is consistent with the AWS96 model being dominated by strike-slip earthquakes, and thus demonstrates continuity with the previous study. However, results here separated by mechanism indicate that the slip-rate dependence in AWS96 is controlled by the behavior of strike-slip earthquakes, and not much affected by the normal mechanisms that show little or no slip-rate dependence, and the reverse mechanisms that potentially show a different dependence. Suppose as a thought experiment that the dip-slip cases have no slip-rate dependence, or in other words, that the variability with slip rate is pure noise. A strong strike-slip case plus some noise will still resolve to a decently significant trend even though we added only noise. In applying the combined regression to dip-slip faults, we may be projecting back from the strong case into the noise, and saying things about future dip-slip earthquake expectations that are not likely based on the available data.

Model M2: The Bilinear Model

Table 4 gives estimated coefficients for model M2 (equation 2), and Figure 6 illustrates the fit to the data. Without the slip-rate adjustment, the bilinear model fits the observed magnitudes as well or better than the linear model M1, as shown by similar or smaller values of σ_{2L} than the corresponding values of σ_{1L}. The results again show a dependence of magnitude on slip rate for strike-slip faults (Fig. 6a) but not dip-slip faults (Fig. 6b,c). The value of σ_{2S} is comparable to σ_{1S} for the strike-slip case but larger for the dip-slip faults. For the strike-slip case, the fit to the data in Figure 6a is better at large rupture lengths than in Figure 5a.

Model M3: The Constant Stress-Drop Model

Parameters for model M3 are given in Table 5, and the fit to the data is illustrated in Figure 7. Some features of Figure 7 are noteworthy. For the strike-slip case, the points for faults with low slip rates (solid points) are mostly above the average model, whereas points with high slip rates (open circles) are mostly below the average. This slip-rate dependence is reinforced in the lower frame of Figure 7a, where the slope of the linear fit to the residuals is more than five standard deviations of the slope different from zero. The variance reduction by the addition of the slip-rate term is statistically significant with 80% confidence, based on the F-test. The same remarks apply for models M1 (Fig. 5) and M2 (Fig. 6).

The strike-slip case in Figure 7a uses $W_{\max} = 15$ km, whereas Table 5 gives model M3 parameters for $W_{\max} = 20$ km as well. The data do not prefer either of these two models, as the curves and the misfits characterized by σ_{3L} and σ_{3S} are barely distinguishable, so the plot for the $W_{\max} = 20$ km model is not shown. For the 20 km wide strike-slip case, both σ_{3L} and σ_{3S} are smaller than the equivalent uncertainties in models M1 or M2. Although this improvement is small and statistically insignificant, it is encouraging that a model with constant stress drop achieves this result. Hanks and Bakun (2014) discussed the difficulties associated with several scaling models for long strike-slip faults, which fit the longest earthquakes either by increasing the rupture width by penetrating into the crust below the depths of microearthquakes or by increasing the stress drop. Although Hanks and Bakun (2014) consider the deep penetration of strike-slip faults below the depth of microearthquakes to be unlikely, we provide both models. Recent

Table 5

Coefficients for Model M3, Use in Equation (3), the Different Fault Types Considered Separately, and Earthquakes Listed in Tables 1 and 2

Parameter	Strike Slip (15 km)	Strike Slip (20 km)	Reverse	Normal
$\Delta\tau_C$ (bars)	24.9 ± 1.1	15.3 ± 0.7	10.6 ± 0.7	14.0 ± 1.5
C_{LW}	3.8	2.9	1.4	1.2
$W_{\max}$ (km)	15	20	30	18
c_2	−0.170 ± 0.029	−0.174 ± 0.029	0.144 ± 0.027	−0.056 ± 0.095
S_0 (mm/yr)	4.8	4.8	1.1	0.25
σ_{3L}	0.236	0.235	0.281	0.312
σ_{3S}	0.214	0.210	0.255	0.305

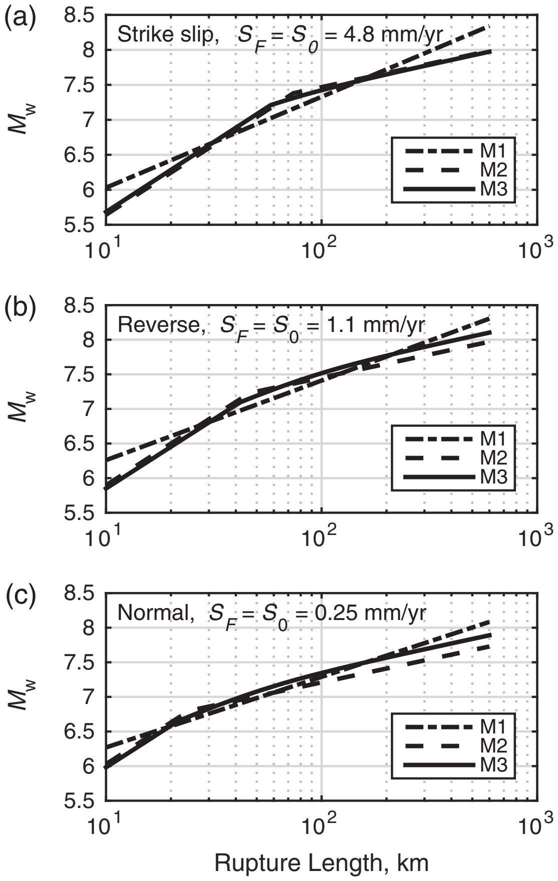

Figure 9. Comparisons of models M1, M2, and M3 for (a) strike-slip, (b) reverse, and (c) normal faults, using $S_F = S_0$ for each mechanism.

studies that favor deep penetration include Graves and Pitarka (2015) based on experience in modeling ground motions near the fault and Jiang and Lapusta (2016) based on the seismic quiescence of the ruptures of past large earthquake such as the 1857 earthquake on the San Andreas fault.

The ability to model the data using equation (3) unfortunately does not resolve the "no high stress drop/no deep slip enigma" articulated by Hanks and Bakun (2014), but rather pushes it into issues with the aspect ratio and the absolute value of the constant stress drop. The $W_{\max} = 15$ km model uses a large aspect ratio of $C_{LW} = 3.8$, compared with $C_{LW} = 2.9$ for the $W_{\max} = 20$ km model, or 2.4 at the transition to fix the width of 15 km in the Hanks and Bakun (2014) model. The higher aspect ratio for the $W_{\max} = 15$ km model would also imply that earthquakes such as the M_w 6.6 Superstition Hills event (number 25) or the M_w 6.2 Parkfield 1966 event (number 49) only penetrate from the surface to about 7 km depth. Also, the stress drop for the $W_{\max} = 15$ km model is rather high, $\Delta\tau_C \approx 25$ bars, considering that this corresponds to $\Delta\tau_S \approx 50$ bars (see the Appendix) in the more frequently used model of Kanamori and Anderson (1975). We suggest that variability of the aspect ratio must contribute to the uncertainties in these scaling relations at the lower magnitudes.

For the reverse-faulting data, we considered values of $W_{\max}$ up to 30 km because reverse faults can have low dips, and that upper limit is the preferred value. For normal faulting, we only considered the values of $W_{\max} > 18$ km, because constrained observations of normal faults imply that the fault width can be that wide (e.g., Richins *et al.*, 1987). For model M3 to fit the sparse normal-faulting data as well as model M2, we would need to use a much smaller value of $W_{\max}$.

Comparisons

Figure 9 compares the models for the three different types of mechanisms. Models M2 and M3 tend to resemble each other most closely, whereas model M1, being linear, tends to give larger magnitudes for long and short faults but smaller magnitudes in the center of the length range.

Discussion

The larger data set modeled here compared with AWS96 expands our understanding of slip-rate dependence for the scaling of magnitude and rupture length. Improvements in estimates of the magnitudes of earthquakes are realized with slip-rate dependence for strike-slip faults for all three models considered here. Thus, the slip-rate dependence in this case is not an artifact of the underlying scaling model. The distribution of data in $L_E - S_F$ space (Fig. 4b) gives further reason for confidence in the strike-slip case. On the other hand, individual models for reverse and normal faulting have, at best, an equivocal place for slip-rate dependence. This again is consistent with the uneven distribution of data on the plots of $L_E - S_F$ in Figure 4c,d. For models M1 and M2 of the normal-faulting events, but not for model M3, the sign of slip-rate dependence agrees with the strike-slip case. Thus, normal faulting could have slip-rate dependence nudging estimates toward smaller magnitudes for higher slip-rate faults but lacks sufficient data to prove it. The reverse-faulting events disagree even at the sign of the effect. The disagreement is present whether we retain either or both of the apparent outliers in Figures 5–7. Thus, based on the current data, we do not find support for the general reduction of magnitude with slip rate implied by the combined set regression of ASW96. It appears that the strength of the slip-rate effect among strike-slip events and their sheer numbers relative to dip-slip events overwhelm the ambiguous (normal) and contrary (reverse) data, leading to an apparently general slip-rate relationship among all data. Thus, our new data set contributes to the understanding that slip-rate dependence is dominantly a strike-slip fault effect that is not inconsistent with normal faulting, and not apparently consistent with reverse mechanism fault rupture. The data available to AWS96 did not permit this distinction.

If we are guided by studies of earthquake source physics, model M3 may be preferable to models M1 or M2. Specifically, the advantage would be the constant stress drop of earthquakes over the full range of magnitudes, consistent with, for example, Allmann and Shearer (2009). The slope of the linear model M1 with rupture length implies that stress drop increases significantly with rupture length for large earthquakes. The slopes of the bilinear model M2 are consistent with simple models for scaling with constant stress drop in the small and large earthquake domains, but the stress drops in the two domains are different. In addition, because the buried circular rupture model by construction does not reach the surface, its applicability to the short ruptures of model M2 is not obvious.

Constant stress-drop model M3 has the important advantage compared with dislocation models in an unbounded space in that it is explicitly designed for surface-rupturing earthquakes. For this reason, we might expect that it will perform well where magnitude scaling is required for calculation of synthetic ground motions (e.g., Goulet *et al.*, 2015). The Chinnery (1964) model has uniform slip with a singularity of stress drop near its edges, which enables a closed-form solution. Stress drop in actual earthquakes is a variable function of location on the fault, so single values are always averages. The Chinnery (1964) approach is probably as reasonable as others. The application of the same functional form for dip-slip earthquakes is entirely *ad hoc*, of course. Although it is more complicated, its consistency with a physical model with a constant stress drop commends it as a preferred regression. Compared with the better-known equations summarized by Kanamori and Anderson (1975), the stress-drop parameter in this model is smaller, emphasizing that average stress-drop estimates are model dependent.

The adjustment that decreases magnitude for high-slip-rate strike-slip faults implies that the stress drop on those faults is lower than on faults of the same length with lower slip rate. The finding is consistent with the observations of Kanamori and Allen (1986) and Scholz *et al.* (1986) that a longer healing time results in a larger stress required to initiate rupture and thus a higher stress drop. For normal or reverse faulting, the slip-rate dependence is low, and the slip-rate coefficient c_2 is indistinguishable from zero. The findings suggest that, if c_2 is not zero for these cases, then c_2 is positive for reverse-faulting earthquakes. This is contrary to the hypothesis of Kanamori and Allen (1986). We suggest that if this positive slope is confirmed with added data, the physical mechanism may be related to the dynamics of rupture. For a reverse fault, the dynamic stresses on a rupture propagating up-dip are tensile as rupture approaches the surface, so the coefficient of friction or cohesion on the fault is less relevant.

There are a number of future studies that should be performed to improve upon the results presented here. The first is to examine the consistency of the models, and especially model M3, with the observed fault displacement. If the results, based on the definition of seismic moment (equation A2), agree with seismic data, the scaling relationship presented here would be an alternative to the self-consistent scaling model of Leonard (2010, 2014) for earthquakes in continental crust.

The second issue that deserves attention is handling multisegment faults. We consider, for instance, the 1905 Bulnay, Mongolia, earthquake, which is the strike-slip point in Figures 5–7 at 375 km and M_w 8.5. The 375 km length is the distance from one end of the rupture to the other, and does not include a spur fault in between that is 100 km long. This event points out that the standard deviations σ_{xL} and σ_{xS} for all three models include the potential presence of spur or subparallel faults that do not increase the total end-to-end length of the rupture. Several other faults in Tables 1 and 2 have similar issues. A better understanding of how seismic moment is distributed on multiple segments and fault splays, as well as how best to measure the lengths of multiple segment ruptures and how to recognize these features ahead of the earthquake would help to reduce uncertainties in future studies of scaling relations. If the result is different from the approach used by Uniform California earthquake rupture forecast, v. 3 (UCERF3), it could have a direct impact on future seismic-hazard analyses.

Conclusions

The primary question asked by this research is if the introduction of slip rate on a fault helps to reduce the uncertainties in estimates of magnitude from observations of rupture length. We find that such a slip-rate dependence is reasonably well established for strike-slip cases: as the slip rate increases for any given fault length, the predicted magnitude tends to decrease. This result is robust in the sense that the slope of the residuals with slip rate is significantly different from zero, and the variance reduction is modestly significant for all three of the considered models relating rupture length and magnitude. For reverse- and normal-faulting mechanisms, on the other hand, our data do not demonstrate the presence of a significant slip-rate effect in the relationship between rupture length and magnitude. Compared with original results in AWS96, we now suggest slip rate be included only for strike-slip faults.

The constant stress-drop model presented here has potential for progress on a standing difficulty in ground-motion modeling of an internally consistent scaling of magnitude, length, down-dip width, and fault displacement. Current relations in which magnitude scales with length or area lead to unphysical stress drops or unobserved down-dip widths, respectively. By working from the model of Chinnery (1964), our constant stress-drop model has the advantage of starting with realistic physics including the stress effects of surface rupture. Work remains to be done in comparing displacements predicted from our model with observations, but the fact that it fits the current magnitude-length-slip-rate data as well or a bit better than the linear and bilinear models suggests that the constant stress-drop model is preferable to models that do not have this feature.

Data and Resources

The article "Total least squares" is available at https://en.wikipedia.org/wiki/Total_least_squares (last accessed February 2015).

Acknowledgments

The authors thank James Brune for many helpful discussions on this research project. The authors thank Tom Hanks, Ivan Wong, and two anonymous reviewers for very helpful reviews. This research was supported in part by the Southern California Earthquake Center (SCEC, Contribution Number 7485). SCEC is funded by National Science Foundation (NSF) Cooperative Agreement EAR-1033462 and U.S. Geological Survey (USGS) Cooperative Agreement G12AC20038. This research was supported primarily by the USGS, Department of the Interior, under USGS Award Number G14AP00030.

The views and conclusions contained in this document are those of the authors and should not be interpreted as necessarily representing the official policies, either expressed or implied, of the U.S. Government.

References

Abercrombie, R. (1995). Earthquake source scaling relationships from -1 to 5 M_L using seismograms recorded at 2.5-km depth, *J. Geophys. Res.* **100,** 24,015–24,036.

Allen, C. R. (1975). Geological criteria for evaluating seismicity, *Bull. Geol. Soc. Am.* **86,** 1041–1057.

Allmann, B. P., and P. M. Shearer (2009). Global variations of stress drop for moderate to large earthquakes, *J. Geophys. Res.* **114,** no. B01310, doi: 10.1029/2008JB005821.

Anderson, J. G. (1986). Implication of attenuation for studies of the earthquake source, *Earthquake Source Mechanics, Maurice Ewing Series 6*, Geophysical Monograph 37, American Geophysical Union, Washington, D.C., 311–318.

Anderson, J. G., S. G. Wesnousky, and M. Stirling (1996). Earthquake size as a function of fault slip rate, *Bull. Seismol. Soc. Am.* **86,** 683–690.

Baltay, A., S. Ide, G. Prieto, and G. Beroza (2011). Variability in earthquake stress drop and apparent stress, *Geophys. Res. Lett.* **38,** L06303, doi: 10.1029/2011GL046698.

Baltay, A., G. Prieto, and G. C. Beroza (2010). Radiated seismic energy from coda measurements and no scaling in apparent stress with seismic moment, *J. Geophys. Res.* **115,** no. B08314, doi: 10.1029/2009JB006736.

Biasi, G. P., and S. G. Wesnousky (2016). Steps and gaps in ground ruptures: Empirical bounds on rupture propagation, *Bull. Seismol. Soc. Am.* **106,** 1110–1124, doi: 10.1785/0120150175.

Blaser, L., F. Krueger, M. Ohrnberger, and F. Scherbaum (2010). Scaling relations of earthquake source parameter estimates with special focus on subduction environment, *Bull. Seismol. Soc. Am.* **100,** 2914–2926.

Bormann, P., and D. Di Giacomo (2011). The moment magnitude M_w and the energy magnitude M_e: Common roots and differences, *J. Seismol.* **15,** 411–427.

Bormann, P., M. Baumbach, G. Bock, H. Grosser, G. L. Choy, and J. Boatwright (2005). Seismic sources and source parameters, in *New Manual of Seismological Observatory Practice (NMSOP)*, P. Bormann (Editor), Deutsches GeoForschungsZentrum GFZ, Potsdam, Germany, 1–94.

Bormann, P., S. Wendt, and D. Di Giacomo (2013). Seismic sources and source parameters, in *New Manual of Seismological Observatory Practice 2 (NMSOP2)*, P. Bormann (Editor), Chapter 3, Deutsches GeoForschungsZentrum GFZ, Potsdam, Germany, 1–259.

Byerlee, J. D. (1978). Friction of rocks, *Pure Appl. Geophys.* **116,** 615–626.

Castellaro, S., and P. Bormann (2007). Performance of different regression procedures on the magnitude conversion problem, *Bull. Seismol. Soc. Am.* **97,** 1167–1175, doi: 10.1785/0120060102.

Castellaro, S., F. Mulargia, and Y. Y. Kagan (2006). Regression problems for magnitudes, *Geophys. J. Int.* **165,** 913–930, doi: 10.1111/j.1365-246X.2006.02955.x.

Chinnery, M. A. (1963). The stress changes that accompany strike-slip faulting, *Bull. Seismol. Soc. Am.* **53,** 921–932.

Chinnery, M. A. (1964). The strength of the Earth's crust under horizontal shear stress, *J. Geophys. Res.* **59,** 2085–2089.

Dieterich, J. H. (1972). Time dependent friction in rocks, *J. Geophys. Res.* **20,** 3690–3704.

Goulet, C. A., N. A. Abrahamson, P. G. Somerville, and K. E. Wooddell (2015). The SCEC broadband platform validation exercise: Methodology for code validation in the context of seismic-hazard analyses, *Seismol. Res. Lett.* **86,** 17–26, doi: 10.1785/0220140104.

Graves, R., and A. Pitarka (2015). Refinements to the Graves and Pitarka (2010) broadband ground-motion simulation method, *Seismol. Res. Lett.* **86,** 75–80, doi: 10.1785/0220140101.

Hanks, T. C., and W. H. Bakun (2002). A bilinear source-scaling model for M-logA observations of continental earthquakes, *Bull. Seismol. Soc. Am.* **92,** 1841–1846.

Hanks, T. C., and W. H. Bakun (2008). M-logA observations for recent large earthquakes, *Bull. Seismol. Soc. Am.* **98,** 490–494.

Hanks, T. C., and W. H. Bakun (2014). M-logA models and other curiosities, *Bull. Seismol. Soc. Am.* **104,** 2604–2610, doi: 10.1785/0120130163.

Hanks, T. C., and H. Kanamori (1979). A moment magnitude scale, *J. Geophys. Res.* **84,** 2348–2350.

Hillers, G., and S. G. Wesnousky (2008). Scaling relations of strike-slip earthquakes with different slip-rate-dependent properties at depth, *Bull. Seismol. Soc. Am.* **98,** 1085–1101, doi: 10.1785/0120070200.

Ide, S., G. C. Beroza, S. G. Prejean, and W. L. Ellsworth (2003). Apparent break in earthquake scaling due to path and site effects on deep borehole recordings, *J. Geophys. Res.* **108,** 2271, doi: 10.1029/2001JB001617.

Iida, K. (1959). Earthquake energy and earthquake fault, Nagoya University, *J. Earth Sci.* **7,** 98–107.

Jiang, J., and N. Lapusta (2016). Deeper penetration of large earthquakes on seismically quiescent faults, *Science* **352,** 1293–1297.

Kanamori, H. (1977). The energy release in great earthquakes, *J. Geophys. Res.* **82,** 2981–2987.

Kanamori, H., and C. R. Allen (1986). Earthquake repeat time and average stress drop, in *Earthquake Source Mechanics*, S. Das, J. Boatwright, and C. H. Scholz (Editors), Geophysical Monograph 37, 227–235.

Kanamori, H., and D. L. Anderson (1975). Theoretical basis of some empirical relations in seismology, *Bull. Seismol. Soc. Am* **65,** 1073–1095.

King, G. C. P., and S. G. Wesnousky (2007). Scaling of fault parameters for continental strike-slip earthquakes, *Bull. Seismol. Soc. Am.* **97,** 1833–1840.

Leonard, M. (2010). Earthquake fault scaling: Self-consistent relating of rupture length, width, average displacement, and moment release, *Bull. Seismol. Soc. Am.* **100,** 1971–1988, doi: 10.1785/0120090189.

Leonard, M. (2012). Erratum to "Earthquake fault scaling: Self-consistent relating of rupture length, width, average displacement, and moment release," *Bull. Seismol. Soc. Am.* **102,** 2797.

Leonard, M. (2014). Self-consistent earthquake fault-scaling relations: Update and extension to stable continental strike-slip faults, *Bull. Seismol. Soc. Am.* **104,** 2953–2965, doi: 10.1785/0120140087.

Perrin, C., I. Manighetti, J.-P. Ampuero, F. Cappa, and Y. Gaudemer (2016). Location of largest earthquake slip and fast rupture controlled by along-strike change in fault structural maturity due to fault growth, *J. Geophys. Res.* **121,** 3666–3685, doi: 10.1002/2015JB012671.

Richins, W. D., J. C. Pechmann, R. B. Smith, C. J. Langer, S. K. Goter, J. E. Zollweg, and J. J. King (1987). The 1983 Borah Peak, Idaho, earthquake and its aftershocks, *Bull. Seismol. Soc. Am.* **77,** 694–723.

Rolandone, F., R. Burgmann, and R. M. Nadeau (2004). The evolution of the seismic-aseismic transition during the earthquake cycle: Constraints from the time-dependent depth distribution of aftershocks, *Geophys. Res. Lett.* **31,** L23610, doi: 10.1029/2004GL021379.

Sato, R. (1972). Stress drop for a finite fault, *J. Phys. Earth* **20,** 397–407.

Scholz, C. H. (1982). Scaling laws for large earthquakes: Consequences for physical models, *Bull. Seismol. Soc. Am.* **72,** 1–14.

Scholz, C. H. (2002). *The Mechanics of Earthquakes and Faulting*, Second Ed., Cambridge University Press, Cambridge, United Kingdom, 471 pp.

Scholz, C. H., C. A. Aviles, and S. G. Wesnousky (1986). Scaling differences between large intraplate and interplate earthquakes, *Bull. Seismol. Soc. Am.* **76,** 65–70.

Shaw, B. E. (2009). Constant stress drop from small to great earthquakes in magnitude-area scaling, *Bull. Seismol. Soc. Am.* **99,** 871–875.

Shaw, B. E., and C. H. Scholz (2001). Slip-length scaling in large earthquakes: Observations and theory and implications for earthquake physics, *Geophys. Res. Lett.* **28,** 2995–2998.

Shaw, B. E., and S. G. Wesnousky (2008). Slip-length scaling in large earthquakes: The role of deep-penetrating slip below the seismogenic layer, *Bull. Seismol. Soc. Am.* **98,** 1633–1641.

Strasser, F. O., M. C. Arango, and J. J. Bommer (2010). Scaling of the source dimensions of interface and intraslab subduction-zone earthquakes with moment magnitude, *Seismol. Res. Lett.* **81,** no. 6, 941–950.

Tocher, D. (1958). Earthquake energy and ground breakage, *Bull. Seismol. Soc. Am.* **48,** 147–153.

Wells, D. L., and K. J. Coppersmith (1994). New empirical relationships among magnitude, rupture length, rupture width, rupture area, and surface displacement, *Bull. Seismol. Soc. Am.* **84,** 974–1002.

Wesnousky, S. G. (1988). Seismological and structural evolution of strike-slip faults, *Nature* **335,** 340–343.

Wesnousky, S. G. (1999). Crustal deformation processes and the stability of the Gutenberg-Richter relationship, *Bull. Seismol. Soc. Am.* **89,** 1131–1137.

Wesnousky, S. G. (2008). Displacement and geometrical characteristics of earthquake surface ruptures: Issues and implications for seismic-hazard analysis and the process of earthquake rupture, *Bull. Seismol. Soc. Am.* **98,** 1609–1632.

Wesnousky, S. G., C. H. Scholz, and K. Shimazaki (1983). Earthquake frequency distribution and the mechanics of faulting, *J. Geophys. Res.* **88,** 9331–9340.

Appendix

Fault-Scaling Relations

Basics

This article proposes models to estimate the moment magnitude of earthquakes based on observed surface rupture lengths and slip rates. The moment magnitude definition that we use is implicit in Kanamori (1977):

$$M_{\mathrm{w}} = \frac{2}{3}\left(\log M_0 - 16.1\right). \tag{A1}$$

The units of seismic moment M_0 are dyn·cm in equation (A1). This definition differs slightly from the equation used by Hanks and Kanamori (1979) but is the equation recommended for seismic network operations by the International Association of Seismology and Physics of the Earth's Interior since 2005 (see Bormann *et al.*, 2005, 2013; Bormann and Di Giacomo, 2011; and references therein), and thus is the relationship used by most seismic networks throughout the world. The seismic moment is defined as

$$M_0 = \mu A_E \bar{D}_E = \mu L_E W_E \bar{D}_E, \tag{A2}$$

in which μ is the shear modulus, A_E is the fault area ruptured in the earthquake, and $\bar{D}_E$ is the average slip over that area. For a fault that is approximately rectangular $A_E = L_E W_E$, in which L_E is the rupture length measured along strike and W_E is the down-dip rupture width.

Substituting equation (A2) into (A1), one obtains (for cgs units)

$$M_{\mathrm{w}} = \frac{2}{3}\log L_E + \frac{2}{3}\log W_E + \frac{2}{3}\log \bar{D}_E + \frac{2}{3}(\log \mu - 16.1). \tag{A3}$$

This justifies the models that relate magnitude to the log of fault length, width, and mean slip. Slopes different from 2/3 result from correlations among the fault parameters L_E, W_E, and $\bar{D}_E$. Wells and Coppersmith (1994) found that the model

$$M_{\mathrm{w}} = c_1 \log L_E + c_0 \tag{A4}$$

predicts magnitude from rupture length with a standard deviation of the misfit $\sigma_1 = 0.28$.

The possible dependence of stress drop or magnitude on slip rate was recognized by Kanamori and Allen (1986) and Scholz *et al.* (1986). With the addition of the slip-rate term, equation (A4) becomes, used by Anderson *et al.* (1996; hereafter, AWS96):

$$M_{\mathrm{w}} = c_0 + c_1 \log L_E + c_2 \log S_F. \tag{A5}$$

Testing for a logarithmic dependence on the geological fault-slip rate S_F can be motivated by findings in Dieterich (1972). In this article, equation (A5) is equivalent to model M1.

Constant Stress-Drop Scaling

The static stress drop $\Delta\tau_S$ is the average decrease in the shear stress acting on the fault as a result of the earthquake and is proportional to the ratio of average slip to a fault dimension. Seismic observations have found that the average value of $\Delta\tau_S$ is approximately constant (~4 MPa, ~40 bars) over a broad range of earthquake magnitudes (e.g., Kanamori and Anderson, 1975; Allmann and Shearer, 2009), although there is considerable scatter in these data. Seismic moment, and thus M_{w} through equation (A1), can be expressed as a function of fault dimension and stress drop, as recognized by Kanamori and Anderson (1975). Selected models are summarized in Table A1.

The equations in Table A1 indicate that constant stress drop implies the slope $c_1 = 2.0$ for small faults (first case 1) when L_E is equated to the diameter of the circular fault and $c_1 = 2/3$ for long faults (second and third cases). These observations motivate a bilinear approach to fit the data, which is model M2 in this article. The bilinear approach is formulated as follows:

Table A1

Models from Kanamori and Anderson (1975) for the Relationship of Fault Size, Stress Drop, and M_w

Case	M_0	Implied Magnitude Relations*
Buried, circular	$\frac{16}{7}\Delta\tau_S R_E^3$	$M_\mathrm{w} = \log A_E + \frac{2}{3}\log\Delta\tau_S + 3.0089$ If $L_E = 2R_E$: $M_\mathrm{w} = 2\log L_E + \frac{2}{3}\log\Delta\tau_S + 2.904$
Strike slip, long	$\frac{\pi}{2}\Delta\tau_S W_E^2 L_E$	$M_\mathrm{w} = \frac{2}{3}\log L_E + \frac{4}{3}\log W_E + \frac{2}{3}\log\Delta\tau_S + 3.1359$
Dip slip, long	$\frac{\pi(\lambda+2\mu)}{4(\lambda+\mu)}\Delta\tau_S W_E^2 L_E$	$M_\mathrm{w} = \frac{2}{3}\log L_E + \frac{4}{3}\log W_E + \frac{2}{3}\log\Delta\tau_S + 3.3141$

*$A_E = \pi R_E^2$, fault area in km^2; R_E, fault radius; W_E, fault width; and L_E, fault length in km, and $\Delta\tau_S$, stress drop in bars.

$$M_\mathrm{w} = M_\mathrm{bp} + c_{1C}\log\left(\frac{L_E}{L_\mathrm{bp}}\right) + c_2\log\left(\frac{S_F}{S_0}\right) \quad L_E < L_\mathrm{bp}$$
$$M_\mathrm{w} = M_\mathrm{bp} + c_{1L}\log\left(\frac{L_E}{L_\mathrm{bp}}\right) + c_2\log\left(\frac{S_F}{S_0}\right) \quad L_E \geq L_\mathrm{bp}, \qquad \text{(A6)}$$

in which the length L_bp is the length at which the length dependence of the scaling relationship changes from the small fault model with slope $c_{1C} = 2$ to the long fault model with slope $c_{1L} = 2/3$. The slip rate S_0 is a reference slip rate which can be chosen arbitrarily, but is conveniently chosen to be the log average slip rate in the data, so that setting $S_F = S_0$ gives the best fit when slip rate is unknown. The constant M_bp is the magnitude corresponding to a fault with length $L_E = L_\mathrm{bp}$ and slip rate $S_F = S_0$. Equation (A6) has three unknown coefficients (M_bp, L_bp, and c_2), which is the same number as in equation (A5).

However, there are issues with the applicability of the equations in Table A1. The foremost, for the long faults, is the width of the seismogenic zone. Table A1 shows that W_E is twice as influential as the fault length, so it needs to be considered carefully. One approach to estimate this width is to use the maximum depth of microearthquakes. By this approach, for strike-slip earthquakes the maximum depth of microearthquakes equates directly to an estimate of the fault width, whereas for a reverse or normal fault the dip is incorporated. The problem is that the maximum depth of seismogenic rupture in large earthquakes is difficult to observe. King and Wesnousky (2007) discuss this difficulty and present arguments for why the down-dip width might be larger in large earthquakes, at least up to some limit greater than that inferred from the depth range of small earthquakes, because rocks below the depths of mircoearthquakes might experience brittle failure under high strain rates. If the width increases in general for long ruptures, stress drop is no longer as high for these events because stress drop is inversely proportional to W_E, and furthermore the slope c_1 can no longer be reliably constrained by the models in Table A1. King and Wesnousky (2007) propose that this explains the proposal by Scholz (1982) that slip in large earthquakes is more nearly proportional to rupture length than to rupture width.

Another issue is that the first equation in Table A1 assumes that the circular fault is confined within the Earth and thus neglects free surface effects, while by definition all of the events considered in this study rupture the surface. This motivates the development of the model that is described in the next section.

Relations Based on Chinnery (1964)

Chinnery (1963, 1964) calculated a stress drop for a rectangular strike-slip fault that ruptures the surface. Unlike the circular slip model, the free surface in the Chinnery model is present for small earthquakes. His equations assume a uniform slip on the fault. Thus, the stress drop is variable over the fault and becomes singular at the edge of the fault. His equations give the stress drop on the surface at the midpoint of the rupture. Numerical solutions in Chinnery (1963) show relatively uniform stress drop over large portions of the fault. Chinnery (1963) thus suggests that the results are valid to represent the fault stress drop so long because the zone of slip fall-off is much smaller than the area of the fault. The key advantage provided by this approach is to provide a useful analytical solution.

For the rectangular fault with length L_E, width W_E, and aspect ratio $C_{LW} = L_E/W_E$, the stress drop in the Chinnery model $\Delta\tau_C$ at the midpoint at the surface is

$$\Delta\tau_C = \frac{\mu\bar{D}_E}{2\pi} C_1(L_h, W_E), \qquad \text{(A7)}$$

in which

$$C_1(L_h, W_E) = \left\{\frac{2L_h}{aW_E} + \frac{3}{L_h} - \frac{L_h(3a + 4W_E)}{a(a + W_E)^2}\right\}. \qquad \text{(A8)}$$

Note that $L_h = L_E/2$ and $a = (L_h^2 + W_E^2)^{1/2}$. Observe that C_1 has dimensions of 1/length, and thus C_1^{-1} is effectively the fault dimension that is used for calculating the strain. In other words, the strain change in the earthquake is $\sim\bar{D}_E C_1$. An equation for the seismic moment can be obtained by solving equation (A7) for $\bar{D}_E$ and substituting in equation (A2). The result is

$$M_0 = 2\pi\Delta\tau_C \frac{L_E W_E}{C_1(L_h, W_E)} \qquad \text{(A9)}$$

and thus

$$M_\mathrm{w} = \frac{2}{3}\log L_E + \frac{2}{3}\log\Delta\tau_C + \frac{2}{3}\log\frac{2\pi W_E}{C_1(L_h, W_E)} - \left(\frac{2}{3}\right)16.1. \qquad \text{(A10)}$$

Additional insight into the geometrical term can be obtained by observing that a is the length of the diagonal from the midpoint of the fault at the surface to either of the bottom corners. If the dip of this line is γ, then $\tan\gamma = W_E/L_h = 2/C_{LW}$, $L_h = a\cos\gamma$, $W_E = a\sin\gamma$, and one can rewrite

$$C_1(L_h, W_E) = \frac{1}{W_E} C(\gamma), \qquad \text{(A11)}$$

in which

$$C(\gamma) = 2\cos\gamma + 3\tan\gamma - \frac{\cos\gamma\sin\gamma(3 + 4\sin\gamma)}{(1+\sin\gamma)^2}. \quad \text{(A12)}$$

Thus, one can rewrite equation (A7) as

$$\Delta\tau_C = \frac{C(\gamma)}{2\pi}\mu\frac{\bar{D}_E}{W_E}. \quad \text{(A13)}$$

Solving equation (A13) for $\bar{D}_E$ and substituting into equation (A2) gives the moment of a vertical strike-slip fault that ruptures the surface as

$$M_0 = \frac{2\pi}{C(\gamma)}\Delta\tau_C L_E W_E^2. \quad \text{(A14)}$$

Because γ, and thus $C(\gamma)$, depends on the fault aspect ratio, equations (A9) or (A14), can be used to model a transition from small-earthquake behavior (e.g., the circular fault in Table A1) to a long-fault behavior. This article, similar to Hanks and Bakun (2002), maintains a constant aspect ratio as the fault length increases, until that aspect ratio implies that the fault width would exceed some maximum. For longer faults, the width is set to that maximum. Before reaching that maximum, γ and $C(\gamma)$ are constant, and

$$M_0 = \frac{2\pi}{C(\gamma)}\Delta\tau_C\frac{L_E^3}{C_{LW}^2} \quad \frac{L_E}{C_{LW}} < W_{\max}. \quad \text{(A15)}$$

For longer faults, for which the width is limited, equation (A14) becomes

$$M_0 = \frac{2\pi}{C(\gamma)}\Delta\tau_C L_E W_{\max}^2 \quad \frac{L_E}{C_{LW}} \geq W_{\max}. \quad \text{(A16)}$$

In this case, as the fault length increases while width is held constant, γ will be decreasing. For the limit of small γ (roughly $\gamma \lesssim 25°$), equation (A12) shows that $C(\gamma) \to 2$, so equation (A9) approaches

$$M_0 = \pi\Delta\tau_C L_E W_{\max}^2. \quad \text{(A17)}$$

Equation (A17) differs from the second case in Table A1 for the long strike-slip fault by a factor of 2 ($\Delta\tau_S = 2\Delta\tau_C$), in which the difference is due to the different boundary conditions used for the two solutions at depth.

From equations (A15) and (A16), converting to magnitude, the implied scaling relationship based on the Chinnery model is

$$M_\mathrm{w} = \begin{cases} 2\log L_E + \frac{2}{3}\log\Delta\tau_C + \frac{2}{3}\left(\log\frac{2\pi}{C_{LW}^2 C(\gamma)} - 16.1\right) & \frac{L_E}{C_{LW}} < W_{\max} \\ \frac{2}{3}\log L_E + \frac{2}{3}\log\Delta\tau_C + \frac{2}{3}\left(\log\frac{2\pi W_{\max}^2}{C(\gamma)} - 16.1\right) & \frac{L_E}{C_{LW}} \geq W_{\max}. \end{cases} \quad \text{(A18)}$$

Equation (A18) will be the third model M3 considered in this study, with the addition of a slip-rate contribution $+c_2\log(S_F/S_0)$, to the two branches of the equation. The unknown parameters in model M3 are $\Delta\tau_C$, C_{LW}, $W_{\max}$, and c_2. Thus, this model has four parameters to be determined, compared with three parameters in models M1 and M2. Figure A1 shows the effect of the three parameters $\Delta\tau_C$, C_{LW}, and $W_{\max}$ on magnitude predictions. The stress drop scales the entire curve upward. The aspect ratio C_{LD} adjusts the level of the magnitude for short rupture lengths. The maximum width affects the curvature and how rapidly the curve approaches the asymptotic slope of $(2/3)\log L_E$ for long rupture lengths.

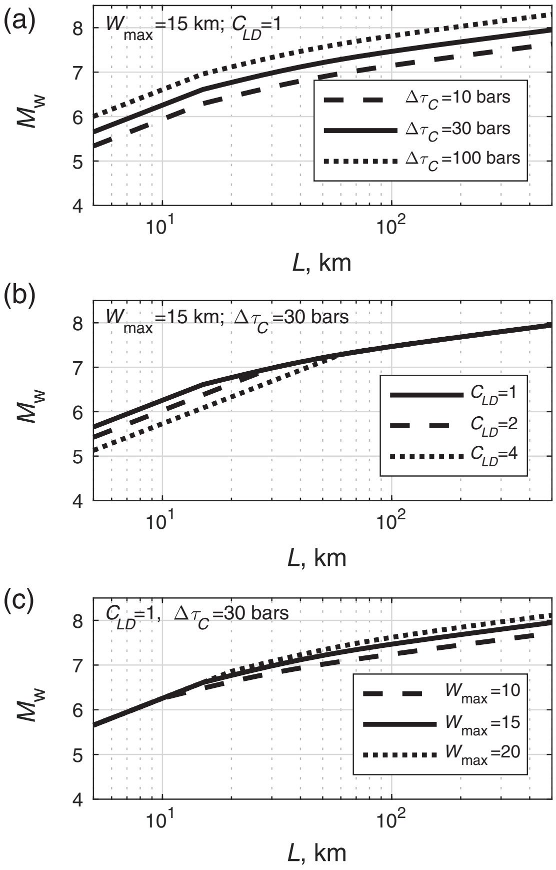

Figure A1. Model for M_w based on the Chinnery (1964) scaling as given in equation (A18). (a) Effect of changing the stress drop $\Delta\tau_C$. (b) Effect of changing the aspect ratio of the fault. (c) Effect of changing the limiting rupture width $W_{\max}$.

Other Models and Considerations

Sato (1972) overcomes the singularity introduced by Chinnery (1963, 1964) by assuming a smooth *ad hoc* slip function on a finite rectangular/elliptical-shaped fault, and for that function, calculating the average stress drop resulting from that slip function. Although the results are informative for source physics studies, the major disadvantages of this approach for our application are that the fault is embedded in a whole space, and there is no analytical solution comparable to equation (A7). Rather, the geometrical factor equivalent to $C(\gamma)$ can be computed numerically using equations in Sato (1972) or read from a figure in the paper. Considering these limitations, this model was not considered further.

Shaw and Scholz (2001) and Shaw and Wesnousky (2008) implement a numerical model for fault slip in a half-space with depth-dependent friction. They examine the statistics of events that rupture the surface. These papers are interesting for the finding that large surface-rupturing events also slip below the brittle crustal depths. The scaling found in the model has properties similar to the scaling in the Chinnery model. However, the scaling relationship that they determine has an *ad hoc* shape, and thus we preferred the analytical functional form of equation (A18). The physics-based solution of Chinnery was also preferred to a related constant stress-drop model by Shaw (2009). This model proposes three regimes of magnitude scaling from length based on intermediate length–width–displacement–scaling relations and heuristic arguments for transitions between them.

Rolandone *et al.* (2004) found some empirical evidence that might be interpreted to support the penetration of rupture below the brittle seismogenic layer in large earthquakes. They found that the maximum depth of aftershocks of the Landers earthquake were deeper immediately after the mainshock, and then the maximum depth returned to pre-earthquake levels over the next few years. This might be explained by high strain rates in the uppermost part of the ductile crust, as high strain rates favor brittle failure. However, postseismic strain rates in that depth range would be high even if seismic rupture of the mainshock did not extend that deep, so these observations allow, but do not require, dynamic rupture below the long-term average depth of microearthquakes.

Nevada Seismological Laboratory
University of Nevada
Reno, Nevada 89557
jga@unr.edu
stevew@seismo.unr.edu

Manuscript received 21 November 2016;

Measuring the Improvement in Synthetic Seismograms Using Shallow Velocity Profiles Obtained from Microtremor H/V Spectral Ratios

John Anderson and Hiroshi Kawase

October 28, 2018

Abstract

Our ultimate goal is to develop synthetic seismograms that outperform ground motion prediction equations through incorporation of the physics of wave propagation. The present model uses synthetic Green's functions generated for flat-layered geological structure. We test four generations of velocity models to generate synthetics for the M5.8 Fukushima-Hamadori earthquake of March 19, 2011. This is a shallow, normal-faulting earthquake that was a foreshock of the M6.7 Fukushima-Hamadori earthquake of April 11, 2011. This earthquake is strong enough to generate strong shaking with a high signal-to-noise ratio over a broad frequency band, but small enough to reduce the source complexity. Velocity model VM1 is given by JIVSM for the hypocenter of the earthquake. VM2 uses the same velocity model for all stations, but with improvements to the Q model for improved spectral matching. VM3 uses instead the JIVSM velocity model that is given for each station, with the improved Q model. VM4 substitutes a shallow velocity structure based on inversion of H/V from microtremors using the inversion method of Kawase et al. (2018). Overall, the quality of the synthetic seismograms, measured as the average standard deviation of Fourier and pseudoacceleration response spectra, improves modestly as the models advance from VM1 to VM4. The improvement is marked at some stations, but not at others. A challenge for future research is to better understand the physical factors behind these trends.

1 Introduction

Seismic risk analysis requires hazard estimates in the form of hazard curves and, increasingly, appropriate seismograms that are compatible with specific earthquakes on identified faults that might affect the site. This paper focuses on development of realistic synthetic seismograms that can serve as alternatives to past records.

In the process of developing a model for synthetic seismograms for engineering applications, the first question is the selection of an appropriate velocity model. The SCEC Broadband Platform, as described by Goulet et al. (2015), used regional models - one for northern California, one for the Mojave Desert, one for elsewhere in southern California, and two models to represent different regions in Japan. This project evaluates the benefits of going beyond regional models for the purposes of generating synthetic seismograms in two-dimensional structures.

We went through a number of iterations and model improvements. At the end, we selected four representative models to illustrate the effects of differences in the model concept. The result informs the trade-off between gathering more information and the reduction of sigma that can result from obtaining that information.

2 Procedure

2.1 The Earthquake

This case study considers the $M_W 5.8$ earthquake of March 19, 2011 (36.7837 N, 140.5715 E), in the region near the border between Fukushima and Ibaraki Prefectures . The focal mechanism of this event is normal faulting, on a fault with a southeast strike (141^o) dipping to the southwest (48^o). Figure 1 shows the location of the earthquake and it's aftershocks in eastern Japan, north of Tokyo. It was recorded by the Japanese K-NET and KiK-net strong motion network. Figure 1 locates the 42 stations within 200 km of the fault with estimated values of $V_{S30} > 500$ m/s, and used in this study.

2.2 Synthetic Seismograms

This project aimed to reproduce key charancteristics of the records at all 42 stations through the use of the composite source model system of generating synthetic seismograms. This code has been described by Anderson (2015). Synthetics at all frequencies are generated using the representation theorem. This requires a slip model for the source, and Green's functions to transmit the effect of the source slip to the station. This study focuses on the velocity model used to calculate the Green's functions. However, an elementary review of the source model will be helpful.

The source model consists of the superposition of subevents, where each subevent is modeled as the source of a "Brune pulse" (Brune, 1970). Thus each subevent has a virtual radius, r_i, a time constant $\tau_i = r_i / (2.34\beta)$, and a time function $\dot{M}_0(t) \sim \Delta\tau_s t e^{-t/\tau}$. The pulse size is normalized by a subevent stress drop, $\Delta\tau_s$ such that the time function integrates to the moment of a circular crack of that stress drop: $M_{0i} = \frac{16}{7}\Delta\tau_S r_i^3$ (Kanamori and Anderson, 1975). Each subevent has seismic magnitude $M_{Wi} = \frac{2}{3}(\log M_{0i} - 16.1)$ for moment in dyne-cm (Kanamori, 1977). The numbers and radii of subevents are chosen randomly from probability distributions that 1) satisfy a statistical Gutenberg-Richter relationship with $b = 1$, and 2) sum to the target seismic moment of the earthquake. The largest allowed subevent has $r_{max} = W_E/4$ where W_E is the narrowest width of the fault. Subevents are placed on the fault at random, but a circle with radius r_i cannot go outside of the fault limits. Each subevent starts at the time given by the distance from the hypocenter, divided by the rupture velocity. This model may break down for sites in the near field of the large subevents, but it generally seems to perform well. The total slip represented by the subevents, found by summing the slip of all the circular subevents in this study results in variable slip on the fault. From this slip, it is possible to find the “strong motion generating area”, and verify that it is consistent with the scaling of the Irikura recipe (Somerville et al., 1999). Furthermore, that slip distribution is consistent with the slip distribution reported by Kiram et al. (2016).

The Green’s functions are all generated using a Fortran code first written by Y. Zeng, but subsequently modified, following the method described by Luco and Apsel (1983). This method represents the Earth with flat layers, where each layer is characterized by the thickness, P-wave and S-wave speeds, attenuation quality factors Qp and Qs, and density. This study considers the effectiveness of four approaches to determine the velocity model, as summarized in Table 1. Figures 5 and 6 illustrate the differences the Q models in VM 1 and VM 2. The reasons for this change in the Q model will be pointed out in the discussion of the results.

Table 1: Characteristics of the velocity models considered in this study.

Model	Origin and Main Characteristics
VM 1	Obtained the velocity model for grid point nearest to the epicenter of the chosen earthquake from JIVSM, following instructions from H. Miyake: http://www.jishin.go.jp/main/chousa/12_choshuki/dat/nankai/lp2012nankaie_str.zip. This model for the crust was used exactly.
VM 2	Velocities are the same as VM1. Q model is modified from VM1. Shallow Qp=Qs, as given by the procedure in Anderson (2015). In the crustal waveguide (depth > 5 km), Qp=Qs=1000.
VM 3	Separate velocity model used for each site. Velocities are from JIVSM at each station location. Q is determined as in VM2.
VM 4	Like VM3, but shallow velocity structure was replaced with structure obtained from H/V ratios following the method of Ducellier et al. (2013) and Kawase et al. (2018).

3 Results

It is useful to begin the discussion of the synthetics with images of selected synthetics, compared to data. For this purpose, this paper will focus on the station IBRH16. As seen on Figure 2, this station is located southwest of the fault, on the hanging wall side of the fault, but beyond the vertical projection of the fault to the surface. Figures 7, 8, and 9 compare the observed and one of the model set of synthetic acceleration, velocity, and displacements. For each station, synthetics were calculated for 50 realizations of the source. The synthetics for these figures were computed using VM4. The data and synthetics have similar amplitudes and durations for all three components of the ground motion. They also appear to have similar frequency content, although that is difficult to judge from looking at the time series.

Figure 10 compares the observed Fourier amplitude at station IBRH16 to the average, over 50 realizations, of the source for VM1, VM2, VM3, and VM4. Figure 11 shows the equivalent for the pseudo-spectral acceleration (PSA). As a quick visual impression, VM4 appears to have generated the most similar Fourier spectra, particularly at frequencies near the frequency where the data spectrum peaks. We attribute the approximate match in frequencies of spectral peaks at about 4 Hz, 6 Hz, and 8 Hz to the improvements in the velocity model based on the H/V. VM1 also shows a peak at 6 Hz, which we attribute to coincidence, as VM2 and VM3 are much smaller in this range, and their spectra do not match. The VM1 spectrum is too high from ~12-25 Hz, which we attribute to the Q model. This is one illustration of why the Q model needs to have very low values near the surface, as in Figure 6 and is used for VM2, VM3, and VM4. The broad trend of the model spectra below 4 Hz is the same, as should be expected, but none of these models have a convincing match of the finer structure in this frequency range.

Comparing the observed PSA spectrum with the four models (Figure 11), the result of VM4 seems to provide the best match. At long periods, all four spectra converge as expected. At the short period side of the spectrum, VM4 comes closest to predicting the observed peak acceleration. The width and amplitude of the VM$ model peak is closer to matching the data than any of the others. VM2 and VM3 lack a peak in this period range. VM1 does have a peak that is similar to the data at Tn~0.2 s, but this model also has large peak between 0.05s and 0.1 s that is not present in the data.

Figure 12 shows the ratio of Data/Model for spectra such as those in Figures 10 and 11. This figure plots, on a logarithmic axis, the average spectral ratios for each of the 42 stations in Figure 1 based on the VM4 model as the denominator. For subsequent analysis, the residual is defined as the ln(data/model). At low frequencies / long periods, the residual converges to zero because that part of the spectrum is controled by the seismic moment of the source. The subevent stress drop for each velocity model was adjusted to give zero residual for Tn=0. This is not necessarily the optimal choice, but is useful to for the comparative purposes of this paper.

One test of the different velocity models is to see if there are trends in the residuals as a function of distance. Perusal of Figure 12 may show some trends, but it is easier to to see if spectral residuals at a specific frequency or period are plotted as a function of distance. This has been done, and Figure 13 shows the slopes, with their uncertainties, for each model at four frequencies. At 1 Hz and at ~3 Hz, the slopes are not zero, but a zero slope is within the one-sigma uncertainty range for all four models. At 10 Hz / 0.1 s, the residuals in the slope is significantly non-zero for VM1, but not for the other three models. Again, this unacceptable feature has been corrected by the change in the attenuation structure illustrated in Figures 5 and 6. At the longest periods shown (0.3 Hz / 3 s), all of the models have a significant tendency to have a larger residual at short distances, and a smaller residual at long distances.

Another way to compare the four velocity models is to compare the mean spectral residuals. This is shown in Figure 14. In this figure, the average response spectral period tends to be better for VM4 than any of the others. In the residuals for the Fourier spectrum, VM4 shows the largest deviation from 0.3-3 Hz, but tends to be better than the others at other frequencies. The corresponding standard deviations of the models, derived from the variability of station means as in Figure 12, is shown in Figure 15. Here, the differences seem small compared to the overall values. VM4 tends to be best from 1-10 Hz in the Fourier spectrum, and a corresponding period range in the response spectrum.

Figure 16 attempts to concisely summarize the observations in Figure 15. The misfit is the sum of the absolute values of the residuals in Figure 14, sampled on the log frequency / period axis scale. The standard deviation is the average of the standard deviations in Figure 15, sampled at equispaced points on the log frequency / period axis scale.. The relative values of the standard deviations indicate that the Fourier amplitude models based on the apropriate deep structure beneath the site is better than a single regional model, and that incorporating shallow site information is even better. The impact of including the shallow site information on the response spectrum does not show subsequent reduction of sigma.

4 Discussion / Conclusions

There are situations where broadband synthetic seismograms that satisfy the wave equation are useful and flat-layered velocity models are available but three dimensional models are not yet available. There are also situations where broadband ground motions in flat-layered models are sufficient for addressing specific scientific questions. This case study is relevant to those situations.

The broadest conclusion is that on average, it seems better to use a velocity model that is appropriate for the site, including near-surface velocities, if that is available. In the best case, a set of site-specific models like those used for VM4 might, hopefully, provide ground motion estimates with uncertainties that are comparable to determine single-station sigma in ground motion prediction equations. Figure 12 shows, however, that the standard deviations found using the synthetics have standard deviations of their estimated parameters that are considerably greater than the single-station sigma values found by Rodriguez-Marek et al. (2011) at KiK-net stations. Consistent with this observation, review of spectra on a site-by-site basis finds that the extent to which the models were improved in the shift from VM3 to VM4 is variable. A future challenge is to understand why these results are mixed, and consider how they can be improved to close the gap between the best models of synthetic seismograms and the results for single-station sigma.

The selected station, IBRH16, was chosen primarily because of it's location close to the fault off the hanging wall. Many urban areas near normal faults share that geometry. However, as a qualitative impression, in about a third of the cases, like IBRH16, VM4 was obviously best, in another third the spectral shapes were changed towards the observations and away from the other models, but the amplitude of the fit was off, and in about a third, model VM4 did not stand out from the other models. Indeed, it is clear in Figure 12 that there are some stations with conspicuously poor agreement with the model. We have observed, for instance, that some of the largest residuals are seen at stations in deep valleys near the west side of Honshu, within the volcanic range. It is known that Q is relatively low in that region, and perhaps also topography has an effect. This is one example where the physics affecting the ground motions is incompletely modeled in this study.

Another shortcoming in the physics included in the flat-layered model is seen in Figure 13, which indicates that the low frequency surface waves are not attenuating fast enough, on average. Indeed, displacement seismograms at stations beyond 150 km show strong surface waves that are not present in the data, and their Fourier spectra show peaks at ~0.2 Hz that are stronger than the data, It seems likely that scattering by near-surface complexity, that is not represented in the model, would reduce the amplitude of these surface waves. The very low Qp and Qs in the near-suface layers apparently does not cause these waves to attenuate strongly enough. This might alternatively be corrected with a frequency-dependent Qp and Qs, but that is not currently implemented in the Green's function calculations. There are uncomplicated patches to the present model. We have experimented with separate Green's functions generated with low Q, and combining them with the high-frequencies of the models shown here using match filters. The three-dimensional finite difference or finite element calculations also have the capability to model these low frequencies well, in those few regions where the velocity model is extremely well known. Nonetheless, this effect seems to indicate that special attention is needed at large distances.

As a summary, we do see applications for synthetic seismograms generated in flat-layered velocity structures. This case study, based on a subset of sites in Tohoku with Vs30>500 m/s shows both successes and opportunities for improvement. In this region with very complicated geology, the simple approximation of using a separate velocity structure appropriate for each site results in improvements in the standard deviations of the predictions compared to using a single regional velocity model. Detailed site-specific models of the shallow geological structure brought mixed success and a modest reduction of the standard deviation.

5 References

Anderson, J. G. (2015). The composite source model for broadband simulations of strong ground motions. Seism. Res. Lett. 86, 68–74.

Anderson, J. G., R. J. Brune, J. N. Brune and G. P. Biasi (2017). Wave propagation and source models for synthetic seismograms compatible with strong motion applications, Proceedings, 16th World Conference on Earthquake Engineering, Santiago, Chile, January 9-13, 2017, Paper No. 4023.

Brune, J. N. (1970). Tectonic Stress and the Spectra of Seismic Shear Waves from Earthquakes, J. Geopphys. Res. 75, 4997-5009.

Ducellier, A., H. Kawase and S. Matsushima (2013). Validation of a new velocity structure inversion method based on horizontal-to-vertical (H/V) spectral ratios of earthquake motions in the Tohoku area, Japan, Bull. Seism. Soc. Am. 103 (2A), 958-970.

Goulet, C. A., N. A. Abrahamson, P. G. Somerville, and K. E. Wooddell (2015). The SCEC Broadband Platform validation exercise: methodology for code validation in the context of seismic-hazard analyses, Seism. Res. Lett. 86, 17-26.

Kanamori, H. (1977). The energy release in great earthquakes, J. Geophys. Res. 82, 2981-2987.

Kanamori, H. and D. L. Anderson (1975). Theoretical basis of some empirical relations in seismology, Bull. Seism. Soc. Am. 65, 1073–1095.

Kawase, H., F. Nagashima, K. Nakano and Y. Mori (2018). Direct evaluation of S-wave amplification factors from microtremor H/V ratios: double empirical corrections to “Nakamura” method, Soil Dynamics and Earthquake Engineering (in press).

Kiran, K., S. Thingbaijam and P. M. Mai (2016). Evidence for truncated exponential probability distribution of earthquake slip, Bull. Seism. Soc. Am. 106, 1802-1816.

Luco, J. E., and R. J. Apsel (1983). On the Green’s function for a layered half-space, part I, Bull. Seismol. Soc. Am. 73, 909–929.

Rodriguez-Marek, A., G. A. Montalva, F. Cotton and F. Bonilla (2011). Analysis of single-station standard deviation using the KiK-net data, Bull. Seism. Soc. Am. 101, 1242-1258.

Somerville, P., K. Irikura, R. Graves, S. Sawada, D. Wald, N. Abrahamson, Y. Iwasaki, T. Kagawa, N. Smith, A. Kowada (1999). Characterizing crustal earthquake slip models for the prediction of strong ground motion, Seism. Res. Lett. 70, 59-80.

6 Figures

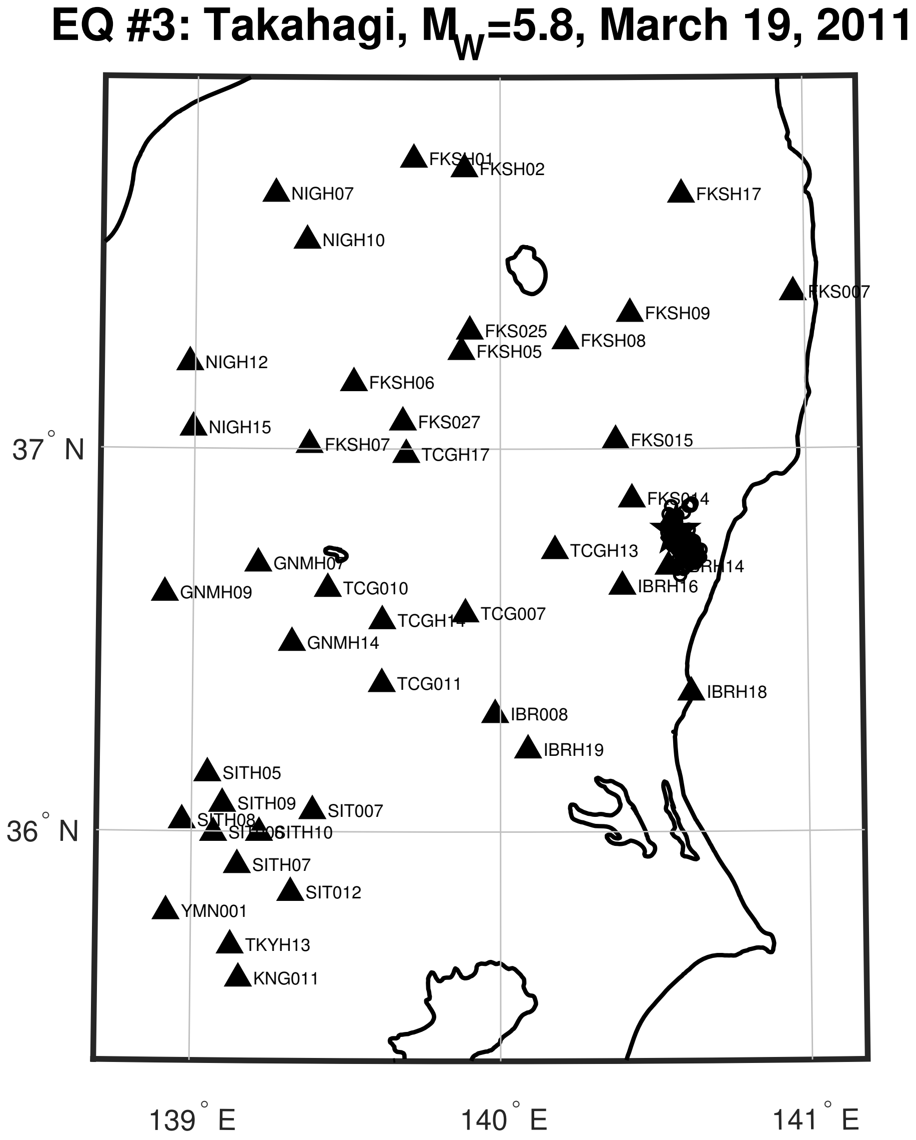

Figure 1: Location map: event and stations.

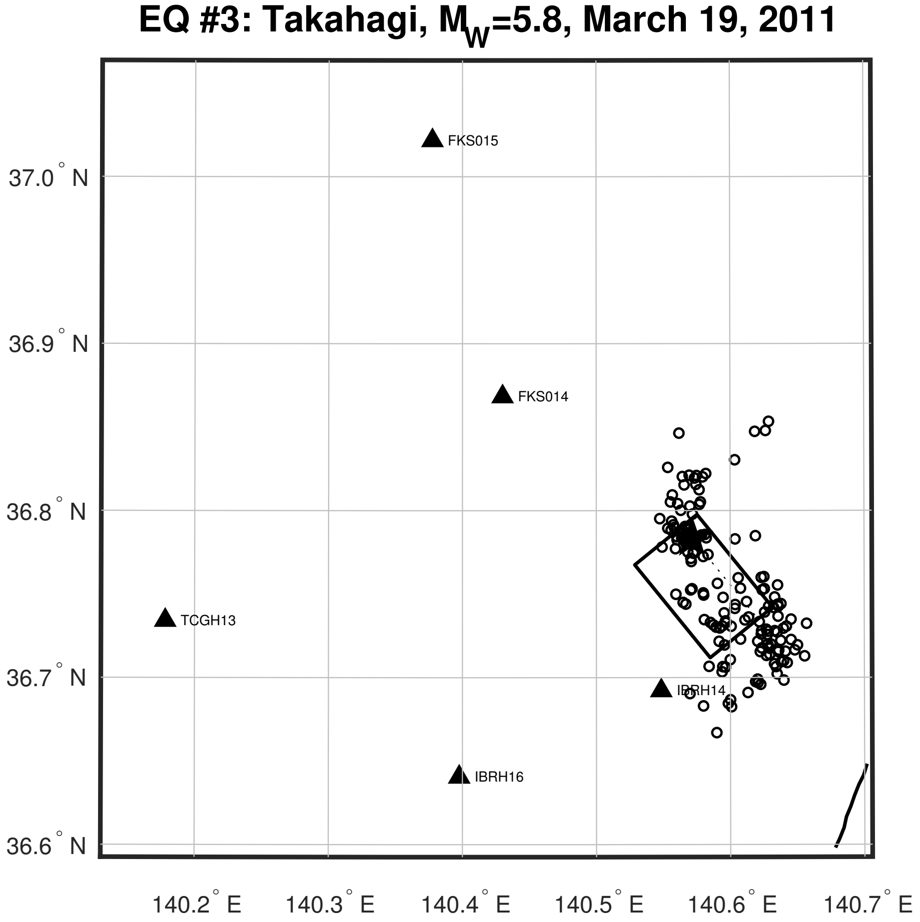

Figure 2: Detailed map of the epicentral region, showing nearby stations, epicenter of the main shock, immediate aftershocks, and the surface projection of the fault plane used to model the earthquake. The fault is square, 7.96 km on each side. The depth of the top edge is 4.0 km, and the hypocentral depth is 5.37 km. The fault strike is to the southeast, and it dips 48^o to the southwest.

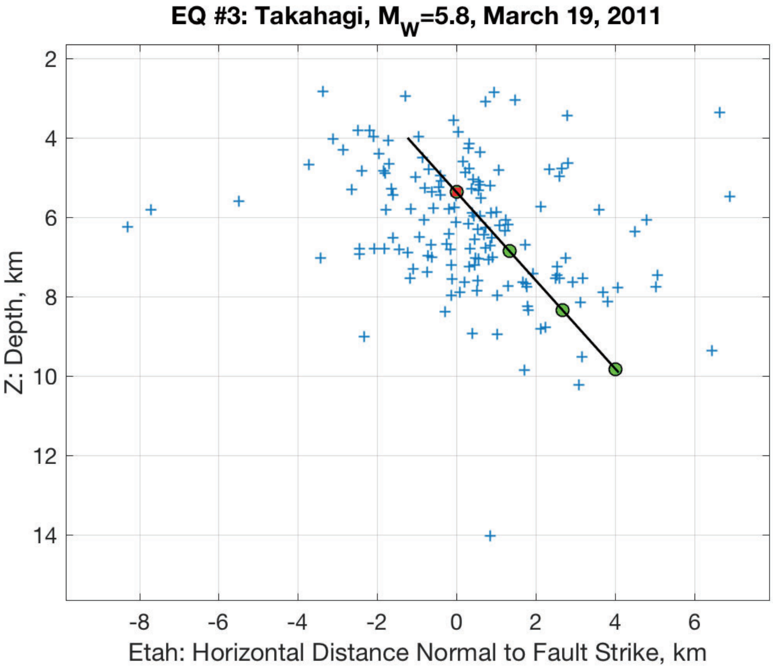

Figure 3: Cross-section view of aftershocks and the fault model. The view is towards the southeast.

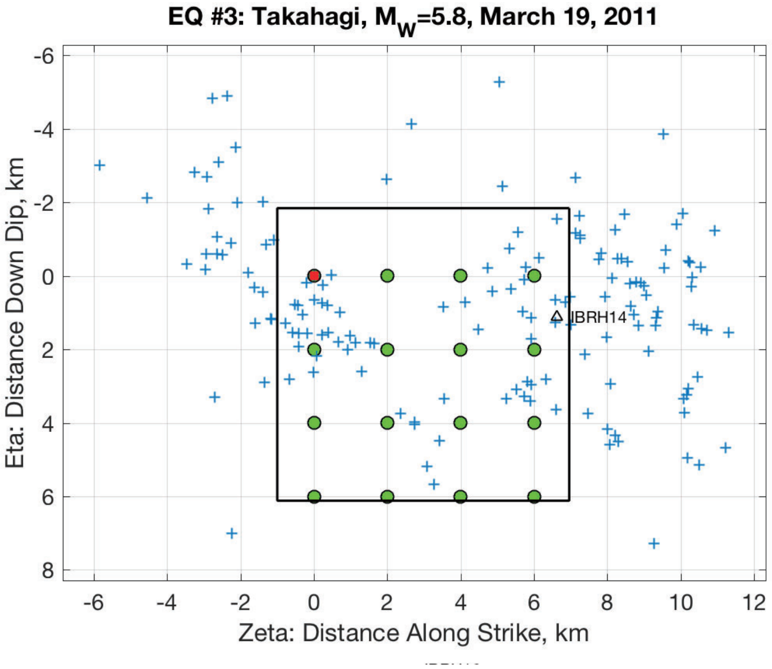

Figure 4: Earthquake hypocenter and aftershocks, projected onto the model fault plane. View is downwards, from the southwest.

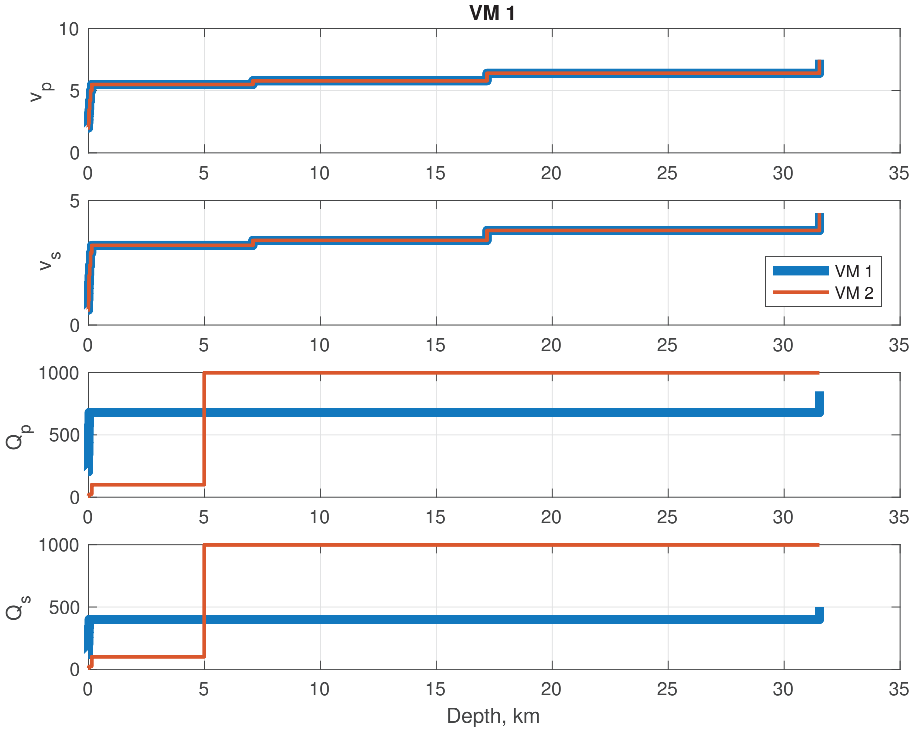

Figure 5: Velocity models compared to 35 km.

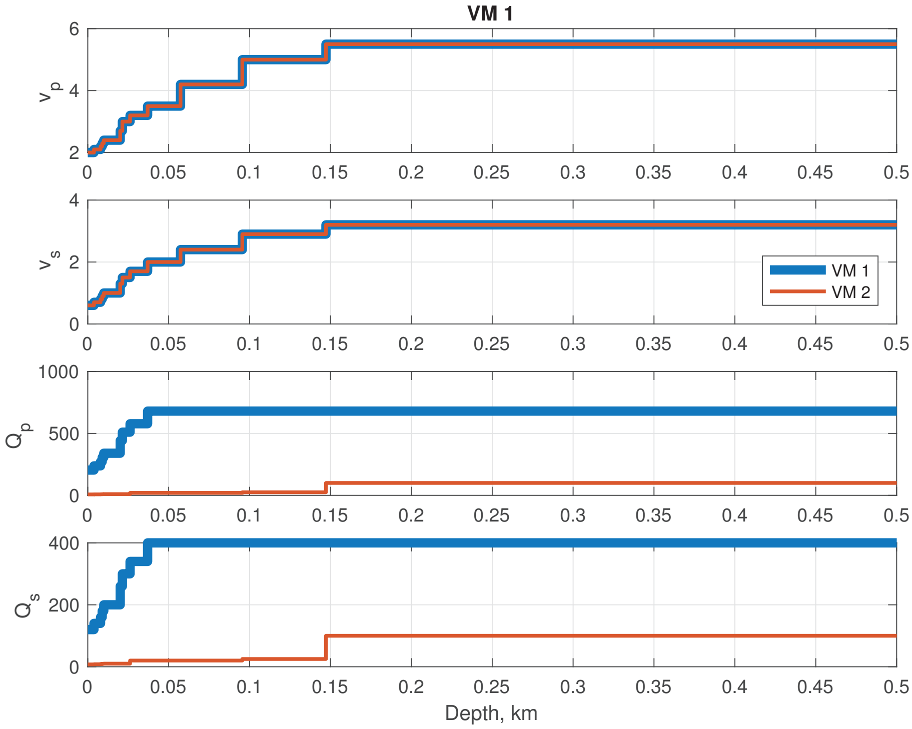

Figure 6: Velocity models compared to 0.5 km.

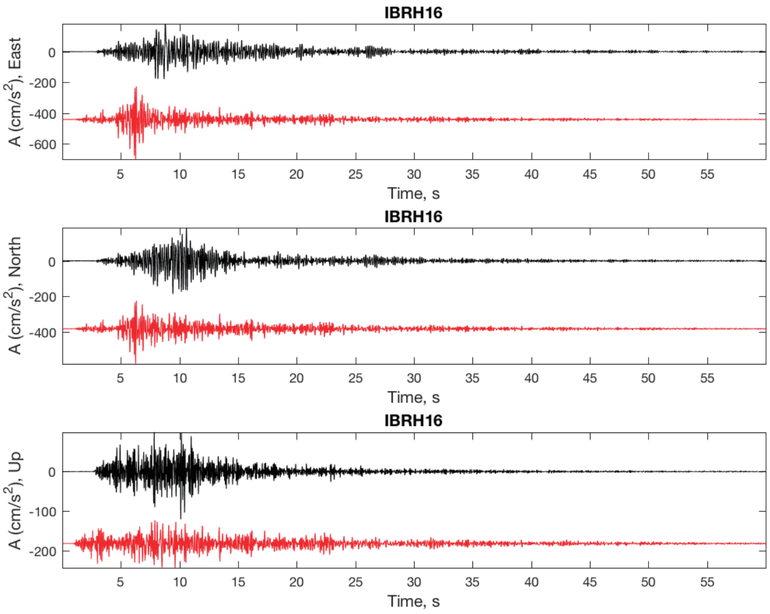

Figure 7: IBRH16 observed and synthetic accelerations, calculated with VM4.

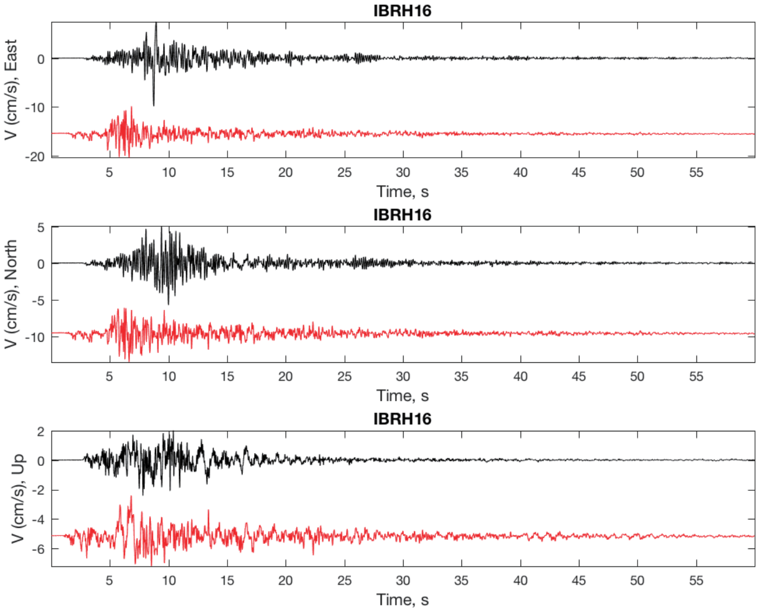

Figure 8: IBRH16 observed and synthetic velocities, calculated with VM4.

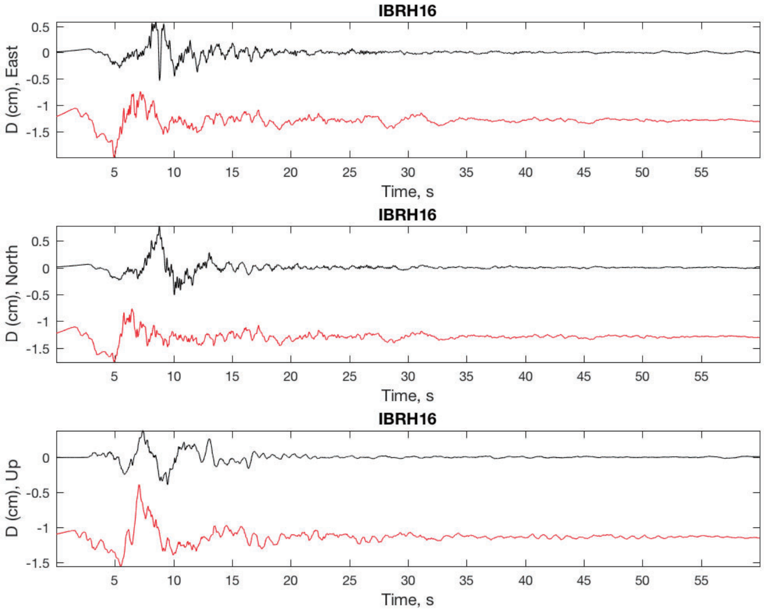

Figure 9: IBRH16 observed and synthetic displacements, calculated with VM4.

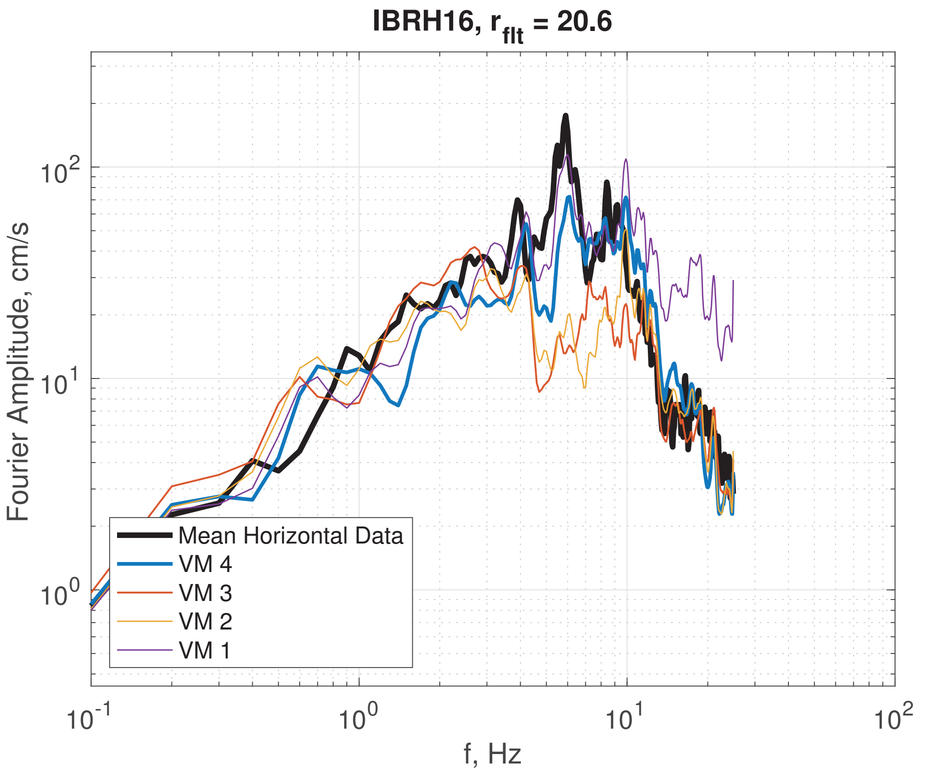

Figure 10: Observed Fourier amplitude spectra at station IBRH16, and average predictions from each velocity model. These spectra have been smoothed, and show the amplitudes of the vector sum of the horizontal components.

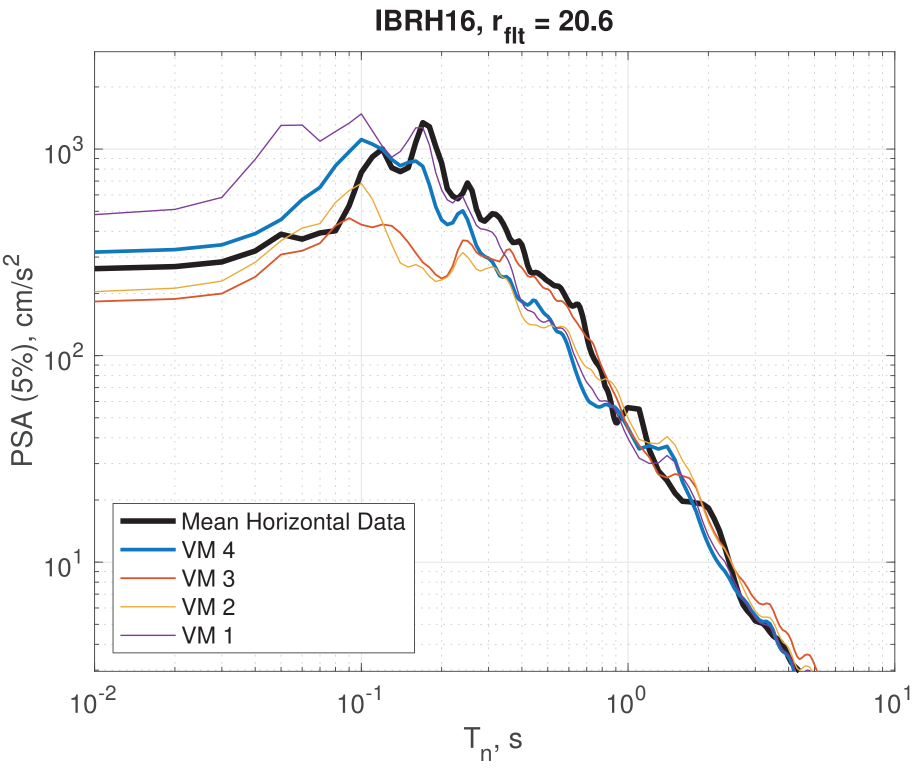

Figure 11: Equivalent of Figure 10 for the pseudo-acceleration response of data and average predictions from each velocity model.

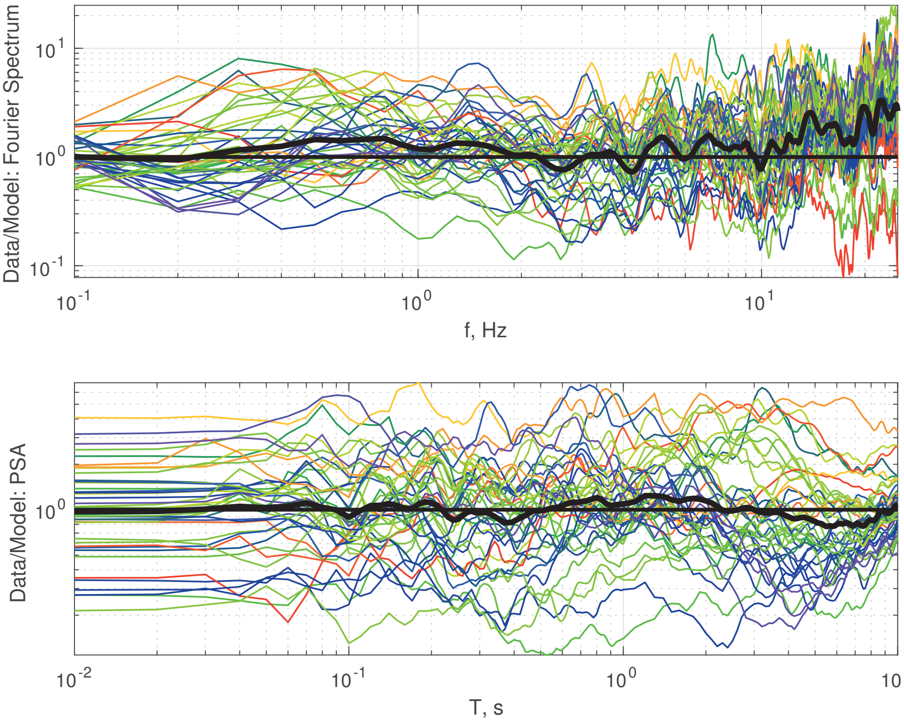

Figure 12: Average misfit, by station, relative to synthetic predictions from VM 4. The color of the line depends of the distance, r_{flt} from the station to the nearest point on the fault. Colors follow the colors of the spectrum, with red for the nearest station and violet for the farthest. The heavy black line is the 42 station average.

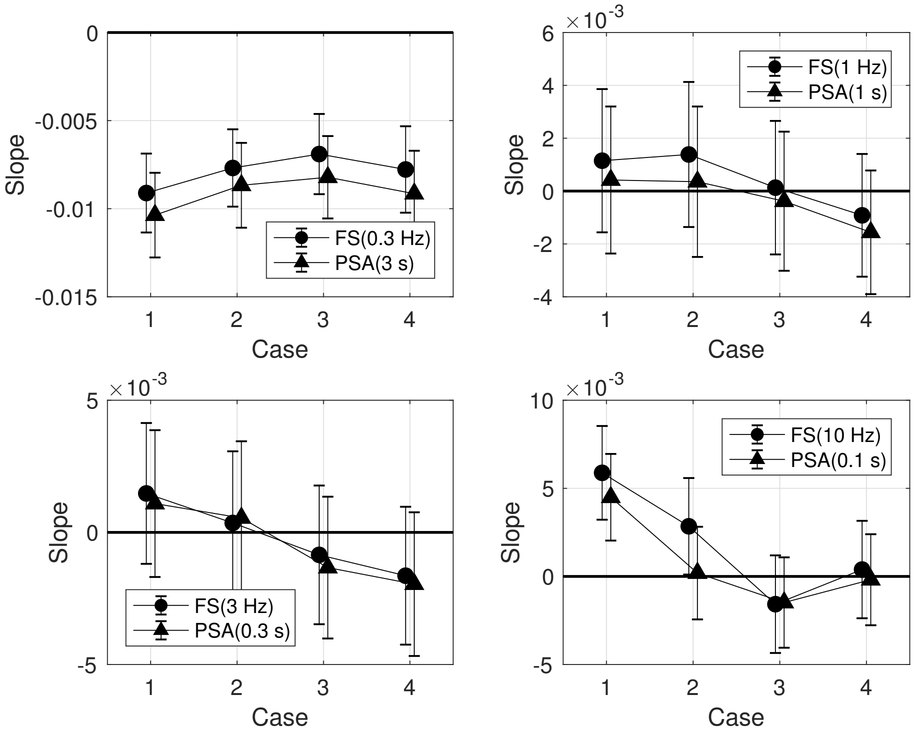

Figure 13: Residuals, by velocity model, as a function of distance at four different frequencies.

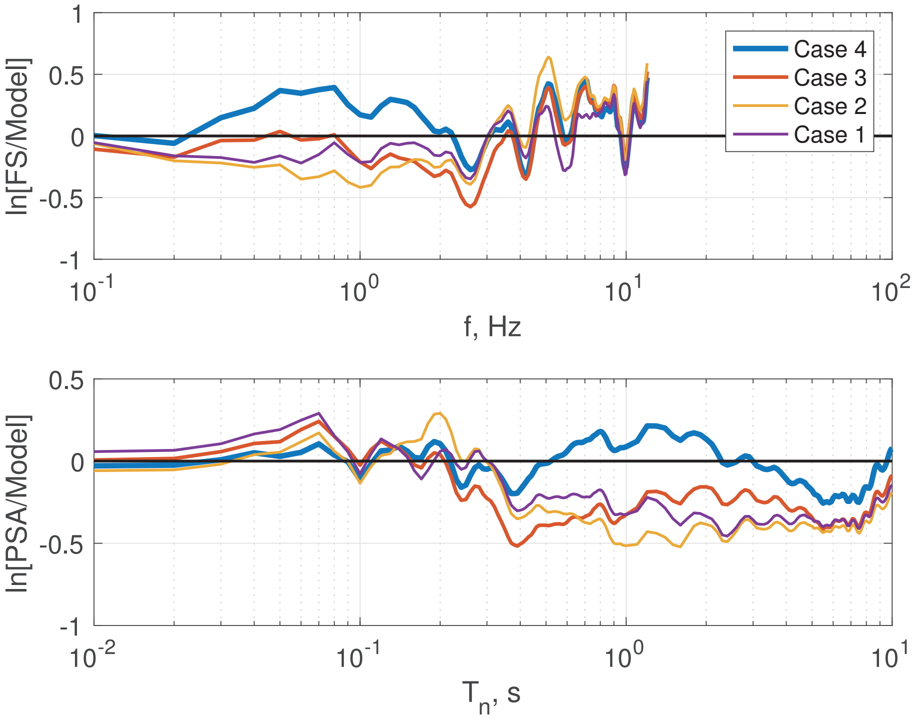

Figure 14: Effect of the velocity models on the mean residuals over 42 stations as a function of frequency for Fourier spectra (top) and by period for response spectra (bottom), by velocity model. The residuals for Fourier spectra are shown only to 12 Hz because we are not confident that the signal/noise ratio is adequate at all 42 stations.

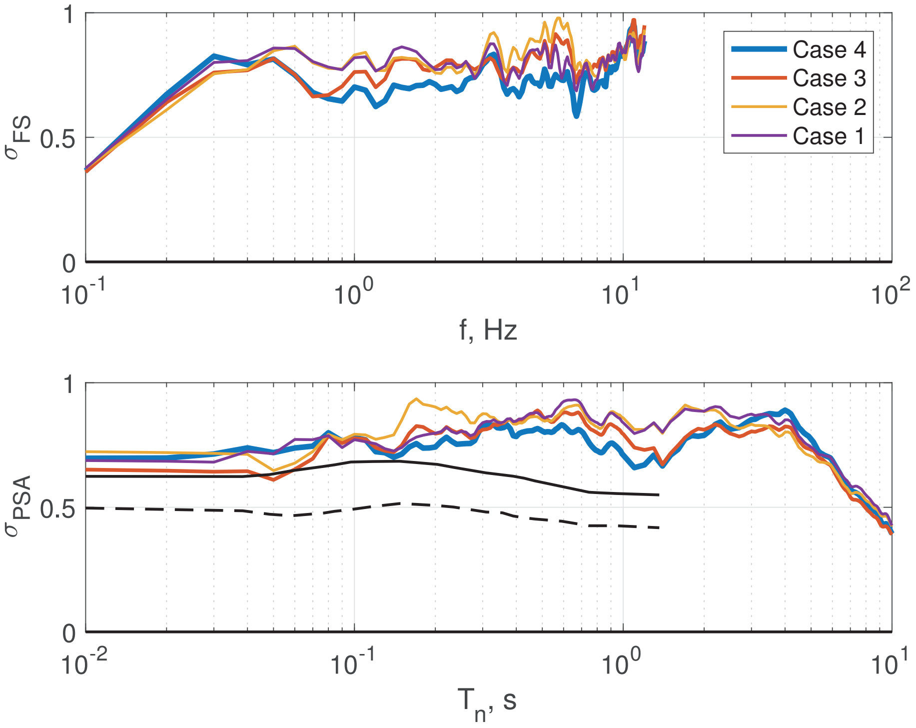

Figure 15: Effect of the velocity models on the standard deviation of residuals over 42 stations as a function of frequency for Fourier spectra (top) and by period for PSA (bottom), by velocity model. For PSA, the solid and dashed lines show values of ϕ and ϕ_{SS} , respectively the intraevent and single-station standard deviations measured at KiK-net stations, from Rodriguez-Marek et al. (2011).

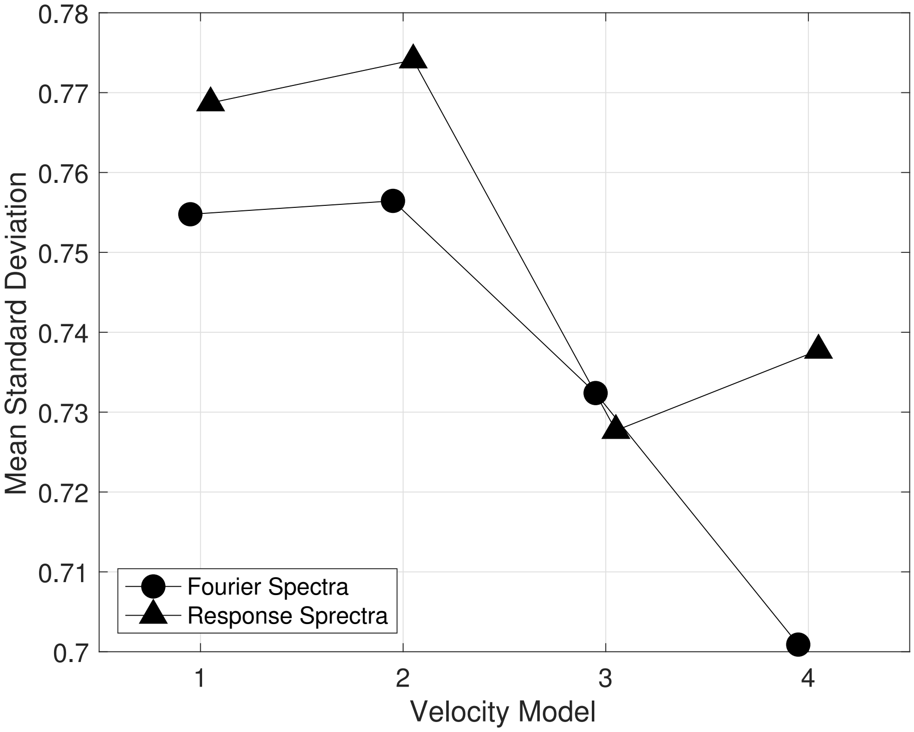

Figure 16: Effect of the velocity models on the mean standard deviation, the average over the spectrum of the standard deviations shown in Figure 15.